High-Impedance Quantum Circuits for Mesoscopic Physics

Geometric Superinductors and Insulating Josephson Chains

by

Andrea Trioni

August, 2025

A thesis submitted to the
Graduate School
of the
Institute of Science and Technology Austria
in partial fulfillment of the requirements
for the degree of
Doctor of Philosophy

Committee in charge:

Latha Venkataraman, Chair
Johannes M. Fink
Georgios Katsaros
Andrew P. Higginbotham

The thesis of Andrea Trioni, titled *High-Impedance Quantum Circuits for Mesoscopic Physics*, is approved by:

Supervisor: Johannes M. Fink, ISTA, Klosterneuburg, Austria

Signature: _____

Committee Member: Georgios Katsaros, ISTA, Klosterneuburg, Austria

Signature: _____

Committee Member: Andrew P. Higginbotham, James Franck Institute and Department of Physics, University of Chicago, Chicago, United States of America

Signature: _____

Defense Chair: Latha Venkataraman, ISTA, Klosterneuburg, Austria

Signature: _____

Signed page is on file

ISTA Thesis, ISSN: 2663-337X

ISBN: 978-3-99078-067-1

I hereby declare that this thesis is my own work and that it does not contain other people's work without this being so stated; this thesis does not contain my previous work without this being stated, and the bibliography contains all the literature that I used in writing the dissertation.

I accept full responsibility for the content and factual accuracy of this work, including the data and their analysis and presentation, and the text and citation of other work.

I declare that this is a true copy of my thesis, including any final revisions, as approved by my thesis committee, and that this thesis has not been submitted for a higher degree to any other university or institution.

I certify that any republication of materials presented in this thesis has been approved by the relevant publishers and co-authors.

Signature: _____

Andrea Trioni
August, 2025

Signed page is on file

Disclaimer on AI Assistance. *In the preparation of this thesis, large language models (ChatGPT) were used only in selected sections to assist with text refinement and clarity. All scientific content, data analysis, and conclusions were independently developed by the author. Any use of AI tools was limited to improving readability, grammar, and phrasing.*

Abstract

Quantum mechanics reveals a world that defies classical determinism, where uncertainty, superposition, and fluctuations are fundamental aspects. Engineering devices that harness these quantum features requires not only precision, but also a deep understanding of how they interact with their surrounding environment. Superconducting circuits, which exploit macroscopic quantum coherence in low-loss superconducting materials, provide a scalable platform for implementing such systems. Among the critical elements in these circuits, superinductors—high-impedance, dissipation-free inductive components—play a central role by suppressing charge fluctuations. They allow quantum states to be delocalized in phase space, protect qubits from environmental noise, and facilitate access to phenomena such as dual Josephson physics and ultra-strong coupling regimes.

This thesis explores two complementary implementations of high-impedance circuits: geometric superinductors, demonstrating that high impedance can be achieved beyond kinetic inductance, and Josephson junction chains, used to investigate both microwave mode properties and DC transport across the superconductor-to-insulator transition.

Part I addresses geometric superinductors. Contrary to the common belief that high-impedance superconducting circuits require kinetic inductance, we demonstrate that purely geometric designs can achieve characteristic impedance exceeding the resistance quantum. By exploiting mutual coupling between adjacent turns, coil-based inductors achieve enhanced self-inductance, creating a reliable platform for qubits and resonators. Modeling, simulation, fabrication, and characterization confirm that these elements behave as superinductor. With low loss, high linearity, and minimal stray capacitance, these elements are reproducible, free of uncontrolled tunneling events, and capable of strong magnetic coupling. This establishes geometric superinductors as robust, single-wave-function superconducting devices suitable for hardware-protected qubits and hybrid systems.

Part II presents classical numerical simulations of a Quantum Phase Slip circuit to study dual Shapiro steps. The circuit consists of an ideal Quantum Phase Slip element embedded in a resistive-inductive environment with a parasitic capacitance.

Part III extends the investigation of high characteristic-impedance circuit elements to one-dimensional Josephson junction chains, which act as a quantum simulator for many-body physics and the superconductor–insulator transition. Different devices are realized on both sides of the DC phase transition, showing either a supercurrent branch or Coulomb blockade at zero bias. The effect of the crossover on microwave modes, however, remains insufficiently investigated. Studying these modes provides insight into the interplay between disorder and phase-slip events. Small differences in circuit component sizes determine which side of the transition a device falls on, making these results relevant not only for fundamental understanding but also for the design of quantum devices, emphasizing the crucial role of the electromagnetic environment in stabilizing and controlling fragile quantum states.

Together, these results illustrate how carefully engineered high characteristic-impedance elements provide a link between macroscopic circuits and the inherently uncertain quantum world, enabling experiments that probe, control, and ultimately exploit quantum fluctuations for applications in quantum information, metrology, solid state physics and beyond.

Acknowledgements

Completing a Ph.D. is not a solitary climb; it is an expedition — long, technical, and often unforgiving. The path is rarely direct, and progress can feel invisible. Some days are pure slog, with your head down, taking one slow step at a time. Other days bring unexpected clarity, a moment of flow, a solved problem, or the quiet satisfaction of forward motion. And then there are the rope-team days, when you lean on your partners, belay their progress, check their knots, and remind one another to breathe. Deeply. 4-7-8.

Though the summit may be personal, the climb never is. My deepest acknowledgments go to all of you, my climbing partners!

Committee. Some opportunities shape you quietly, steadily, and over time. Working with Johannes Fink was one of those. From the first day, I knew I had found a project I truly loved and a mentor who trusted me enough to let me explore it freely. You gave me room to make mistakes, the support to keep going, and the resources to aim high. I still remember telling you that I applied to ISTA not for the place, but for the scientist behind the group. I stand by that. And even now, part of me still thinks I didn't deserve the opportunity, but you gave it anyway, and that made all the difference.

I was lucky to have, on my floor, a person who was consistently kind and approachable. Georgios Katsaros, your passion and dedication to work were a constant presence, and your door always seemed open even when you were just as busy. I'll never forget our Sunday afternoon table tennis trainings in Lab Building East, squeezing in a bit of movement during long cleanroom lag times in my first months. I still remember those moments with great joy. And you still owe me a rematch.

And then there are those who shift the way you see your work. Andrew Higginbotham, thank you for offering a fresh physics perspective to a PhD that had, until then, been largely engineering-driven and encounter a major roadblock. Your input complemented technical direction of this project with rich physics. More than that, your encouragement came exactly when it was most needed. It gave me momentum, confidence, and the feeling that the work truly mattered.

A special thanks to David Haviland, for me the godfather of high-impedance Josephson junction circuits, for serving as an external committee member during my qualifying exam. Our few discussions over the years were always insightful, providing valuable input and planting the seed for exploring the fascinating physics of Josephson arrays.

Finally, a thank you to Latha Venkataraman for kindly accepting the role of chair for my defense.

ISTA Facilities and Foundings. Every research journey is supported by a network of people whose work is behind the scenes but essential. A big thanks to Sandra Widdmann, HR, and

GradSchool for handling the paperwork and making the administrative side easier to navigate. I'm also grateful to the machine shop and electronics shop teams in particular Todor Asenov and Thomas Adletzberger whose expertise and practical solutions kept the experiments on track. And to the NFF staff, particularly the original team, Salvo Bagiante, Lubuna Shafeek, Juan Aguilera-Servin, Philipp Thaus, and the staff scientist Ivan Prieto-Gonzalez: thank you for being there with me in troubleshooting, advising, and sometimes just listening to my frustration. I know your job isn't easy, but your work made mine easier.

I also gratefully acknowledge the generous support of the NOMIS Foundation Project "Protected States of Quantum Matter" and the grant from the Beyond-C consortium. Their funding made this research possible and gave me the freedom to ask ambitious questions, and try to answer them.

Lab mates, colleagues, friends. Thank you all for the small, everyday gestures. In the end, those are what truly matter. Your scientific contributions live on in the methods, results, and analysis throughout this thesis. But this space is for the shared time and extraordinary moments after work or during a trip far way.

Matilda Peruzzo, thank you for being that rare kind of person, someone you genuinely look forward to working with each day. Sharing part of your project was one of the most rewarding parts of this journey. After you left, the Ph.D. was never quite the same.

With Shabir Barzanjeh, I shared calm, grounding hikes through the hills around campus. With Georg Arnold, it was sunny afternoons cheering for Mr. SkyBall at the beach volleyball world cup.

To Alfredo Rueda Sanchez, thank you for your ever-debatable theories on life and love, and for your great passion for physics. And to William Hease, for the long cooking sessions late in the day, always working toward the perfect Frasier recipe.

Elena Rechenko introduced me to the beauty of ballet, from Balanchine to Forsythe, and spent nights being inspired by Ekman's genius. Rishabh Sahu, thank you for the shared outdoor time on the bike and hours in the kitchen. Riya Sett, for being a supportive office mate and, together with Liu Qiu, for our coffee breaks, reading fortunes in the leftover grounds: will they ever come true?

To Farid Hassani, thanks for our board discussions, whether about protected qubits or chess positions. Lucky Kapoor's company carried me from South India to Disneyland Anaheim (Space Mountain!) and along alpine trails across France: we made it to La jonction!

To Thomas Werner, my favorite Burgenländer export — kind, sincere, and always welcoming. Alejandro Andrés Juanes, for the RV road trip across deserts, national parks, and alternative cities in Sunny California and for the Bacaro tour in Venice. Samarth Hawaldar, for the crowded, reach nights at the Musikverein.

Donald Swen and Uri Sharell were among the ISTerns I enjoyed spending time with the most. It means a lot that we're still in contact. To Areg Avantylian, thank you for sharing the excitement of the latest measurements on the JJ chain devices. And to Dante Loi, who made the brutally beautiful bouldering in Albarra truly unforgettable.

To Matthias Wulf, Martin Zemlicka, Carla Borja Espinosa, Jenny Sanchez Naranjo, Alinda Gerçek, Alesya Sokolova, Andrei Militaru, Christian Siegele, Erfan Riyazi, and all the other students whose names might not be listed here: I may not have the most postcard-like memories with each of you — yet — but you were part of this journey too.

And finally, Lena, Verena, and Elizabeth: thank you for our glittery meetings that brightened so many days.

And Everyone Else. Beyond the lab and beyond ISTA, there was a whole world that made this journey livable and often joyful. A big thank you to all my flatmates over the years for the space and moments shared. Greateful also for my climbing team and the Waves Vienna team: thank you for keeping me grounded with two of my greatest passions, climbing and music. It was often just exactly what I needed to reset. To my family, who supported me quietly and consistently from afar. And Vienna, for being the great city where I lived for all these years: I couldn't have asked for a better place to grow.

To everyone who contributed to this ascent: thank you for your role. We made it.

About the Author

Andrea Trioni earned a BSc in Physics Engineering from Politecnico di Milano. Before joining the ISTA Graduate School in September 2018, he completed two research internships: one at Paris Diderot University with Prof. Carlo Sirtori and another at ISTA with Prof. Johannes Fink. He joined the *QuantumIDs* group led by Prof. Fink in August 2019 and passed his qualifying exam in December 2020.

His main research interests focus on high-impedance superconducting circuits. He initially studied and developed the first geometric superinductor resonators, then moved on to one-dimensional Josephson junction arrays to investigate the interplay between superconductivity and insulating behavior.

Andrea was a teaching assistant for the *Quantum Optics with Atoms and Circuits* course during the spring semester of the 2022/2023 academic year.

During his PhD, he took part in the 2022 HIQCuing seminar in Manigod, organized by Ioan Pop's group, the 2023 workshop *The Physics of Disordered Superconductors and Their Application to Quantum Circuits* in Les Houches, and the *Charge-Phase Duality in Novel Superconducting Circuits* workshop held at the National Physical Laboratory in Teddington (London). He also presented his research at the APS March Meetings in Chicago (2022) and Anaheim (2025), as well as at the FisMat Workshop *Novel Schemes for Quantum Superconducting Hardware* in Venice (2025).

List of Collaborators and Publications

First author.

- M. Peruzzo*, A. Trioni*, F. Hassani, M. Zemlicka, and J. M. Fink. Surpassing the Resistance Quantum with a Geometric Superinductor. *Phys. Rev. Appl.*, 14:044055, Oct 2020. URL: https://link.aps.org/doi/10.1103/PhysRevApplied.14.044055, doi:10.1103/PhysRevApplied.14.044055

Co-author. Contributed to the development of the vapor HF etching process for releasing the silicon membrane.

- M. Peruzzo, F. Hassani, G. Szep, A. Trioni, E. Redchenko, M. Zemlicka, and J. M. Fink. Geometric Superinductance Qubits: Controlling Phase Delocalization across a Single Josephson Junction. *PRX Quantum*, 2:040341, Nov 2021. URL: https://link.aps.org/doi/10.1103/PRXQuantum.2.040341, doi:10.1103/PRXQuantum.2.040341
- F. Hassani, M. Peruzzo, L. N. Kapoor, A. Trioni, M. Zemlicka, and J. M. Fink. Inductively shunted transmons exhibit noise insensitive plasmon states and a fluxon decay exceeding 3 hours. *Nature Communications*, 14(1), July 2023. URL: http://dx.doi.org/10.1038/s41467-023-39656-2, doi:10.1038/s41467-023-39656-2
- M. Zemlicka, E. Redchenko, M. Peruzzo, F. Hassani, A. Trioni, S. Barzanjeh, and J. M. Fink. Compact vacuum-gap transmon qubits: Selective and sensitive probes for superconductor surface losses. *Phys. Rev. Appl.*, 20:044054, Oct 2023. URL: https://link.aps.org/doi/10.1103/PhysRevApplied.20.044054, doi:10.1103/PhysRevApplied.20.044054

Table of Contents

List of Figures

List of Tables

CHAPTER 1

Introduction

> “For me, quantum processes are a philosophical event. Meaning, they break with some of the most basic forms of experiencing and understanding reality that have defined the modern period. Things were either natural or technical; either alive or non-living; either human or machine; either being or thing. The beauty of quantum processes is that they are discontinuous with these binaries. They introduce us to the possibility of a world where these distinctions have no meaning. Quantum literally releases us from how we understood the world.”
>
> — *Tobias Rees*[1]

1.1 A World that defies determination

Unstable. Fragile. Elusive. Interconnected and, at times, unpredictable. A world vibrating at the threshold of what we can currently understand. At the smallest scales, where matter no longer follows the determinism of classical physics, a different language emerges, one that speaks in probabilities instead of certainties, in superpositions rather than predetermined states.

Beginning in the early 20th century, a series of experimental anomalies and theoretical breakthroughs gradually challenged Newtonian predictability. By the time Heisenberg [Hei25], Schrödinger [Sch26], and others shaped the mathematical formalism of quantum mechanics in the 1920s, it had become undeniable: reality, in its most elemental form, is not fixed but fluctuating. At the smallest scales, nature reveals a texture that is not smooth but granular. Particles do not follow predictable paths, but unfold in probabilities. They exist in multiple states at once, collapse under observation, influence each other across space with no apparent connection, leaping through barriers without warning. Presence and absence blur. These behaviors are not just mathematical oddities, they are foundational. They are how the world works, even if it resists our grasp.

[1] WE FELT A STAR DYING is an artistic installation by Laure Prouvost, born from her conversations with philosopher Tobias Rees and scientist Hartmut Neven, exploring the connection between quantum noise, quantum technologies, and the universe. Section 1.1 is inspired by this.
Laure Prouvost, WE FELT A STAR DYING, 21 February - 4 May 2025, Kraftwerk Berlin. Commissioned by LAS Art Foundation and co-commissioned by OGR Torino.

Particles don't just behave unpredictably, they emerge from and interact with a constantly fluctuating quantum field. What was once thought to be empty space is now understood as a dynamic field of quantum fluctuations, small, spontaneous, and omnipresent disturbances in energy. At our macroscopic scale, these fluctuations are usually masked by thermal noise and classical interactions, making them invisible in daily experience. But when we miniaturize our experiments, cool our systems to millikelvin temperature, and shield them from environmental noise, a threshold is crossed. The whispers of the quantum begin to surface.

At this threshold, superconducting Josephson circuits offer a platform for exploring the quantum–classical boundary. Built from macroscopic components, like wires, capacitors and loops, they resemble classical electrical circuits. Yet electricity flows without resistance, phase becomes quantized, and information can be encoded in fragile superpositions. Here, the quantum speaks. Loud.

However, the opportunity to access and manipulate these quantum states comes with significant challenges. Quantum systems are not robust in the way classical ones are. They are highly sensitive to external noise, with even minimal disturbances affecting their operation. Among these, charge noise is especially problematic. Random fluctuations in background charge can disrupt quantum coherence, corrupt stored information, and reduce system fidelity. These fluctuations do not only represent a technical detail; they are reflections of the deeper, stochastic nature of the quantum world. To suppress them is not just about refining hardware. It is to enter into a dialogue with nature's uncertainty. Designing quantum systems is an exercise in precision, but also in constraint: systems that work with, not against, the logic of indeterminacy. To engineer clarity in the presence of intrinsic noise is not an attempt to eliminate the quantum; it is an effort to stick together with it. We are no longer just observing the quantum world: we are building technologies that rely on it.

Quantum computing, in particular, has shifted this conversation from the abstract to the tangible. Devices based on superposition and entanglement promise to tackle problems that lie beyond classical reach. Yet, the same principles that give them their power also render them precariously unstable. This fragility is intrinsic to their operation: even at millikelvin temperatures, quantum fluctuations continue to play a role. In this sense, superconducting quantum circuits are more than just components, they are an interface between human-made systems and the quantum environment, a place where our designs must accommodate a world that, by its very nature, resists full control. Engineering them means dealing directly with the realities of quantum physics.

1.2 Macroscopic quantum phenomena and circuit QED

At first glance, it may seem counterintuitive that quantum mechanics, typically associated with atomic and subatomic scales, can influence the behavior of systems visible to the naked eye. There is no hard boundary separating the microscopic from the macroscopic; superconductivity, in particular, provides a clear demonstration of quantum effects manifesting in macroscopic systems. The remainder of the Chapter focuses on superconducting Josephson circuits, directly building on the discussion of superconductivity as a manifestation of quantum behavior in such systems.

1.2.1 Superconductivity

Discovered by Onnes in 1911 through experiments on mercury [Onn11], superconductivity is more than a low-temperature anomaly. It represents the emergence of a coherent quantum state, a condensate of paired electrons, the Cooper pairs, that move collectively without resistance.

Before the development of the microscopic BCS theory in 1957 by Bardeen, Cooper, and Schrieffer [BCS57a; BCS57b], a phenomenological framework had been introduced by Ginzburg and Landau [GL50]. Building on Landau's general theory of second-order phase transitions [Lan37], a pseudo-wavefunction $\Psi(\mathbf{r},t)$ was introduced as an order parameter to describe the superconducting state. This order parameter captures the macroscopic quantum nature of the condensate without the need for a detailed microscopic description.

The amplitude of Ψ corresponds to the local density of Cooper pairs $n(\mathbf{r},t)$ (number per unit volume), while its phase $\phi(\mathbf{r},t)$ governs the long-range coherence responsible for supercurrent flow. Instead of tracking individual electrons, the system is characterized by a collective wavefunction:

$$\Psi(\mathbf{r},t) = \sqrt{n(\mathbf{r},t)}\, e^{i\phi(\mathbf{r},t)}. \tag{1.1}$$

The later BCS theory confirmed this phenomenological picture by showing that electron pairing at low temperatures gives rise to a coherent quantum state well described by the Ginzburg–Landau formalism. Furthermore Gor'kov [Gor59] rigorously connected the two by deriving the Ginzburg-Landau theory as a limiting case of BCS.

Phase coherence across the material leads to the characteristic phenomena of superconductivity, which follow from the expression for the supercurrent density $\mathbf{J}_s(\mathbf{r},t)$. Within the Ginzburg–Landau framework, the supercurrent density is obtained by minimizing the Helmholtz free energy functional with respect to the vector potential $\mathbf{A}(\mathbf{r},t)$ which accounts for the coupling of the superconducting charges to the electromagnetic field. This results in the expression [Tin04][2]:

$$\mathbf{J}_s(\mathbf{r},t) = \frac{q\hbar}{i2m}\left(\Psi^*(\mathbf{r},t)\nabla\Psi(\mathbf{r},t) - \Psi(\mathbf{r},t)\nabla\Psi^*(\mathbf{r},t)\right) - \frac{q^2}{m}|\Psi(\mathbf{r},t)|^2\mathbf{A}(\mathbf{r},t), \tag{1.2}$$

where $q=-2e$ is the effective charge and $m=2m_e$ the effective mass of a Cooper pair, with e being the elementary charge and m_e the mass of a single electron. The vector potential $\mathbf{A}(\mathbf{r},t)$ is related to the magnetic field via $\mathbf{B}(\mathbf{r},t) = \nabla\times\mathbf{A}(\mathbf{r},t)$.

London Equations. By substituting the expression for the macroscopic wave function (Eq. 1.1) into Eq. 1.2, a simplified formula for the supercurrent density is obtained[3]:

$$\mathbf{J}_s(\mathbf{r},t) = \frac{\hbar q n_e(\mathbf{r},t)}{m}\left(\nabla\phi(\mathbf{r},t) - \frac{q}{\hbar}\mathbf{A}(\mathbf{r},t)\right), \tag{1.3}$$

where the term inside the parentheses corresponds to the gauge-invariant phase gradient and $n_e = 2n$ the superconducting electron density. When the phase is assumed uniform

[2] [Tin04] reports the expression for the supercurrent with the speed of light c appearing explicitly; this comes from the use of Gaussian (CGS) units rather than SI units. See also Ref. [Ann10]. Other references define Ψ with $\sqrt{\rho}$ (charge density) instead of $\sqrt{n}$ (pair density), which results in one fewer explicit factor of q in the supercurrent expression (Eq. 1.2).

[3] $\Psi^*(\mathbf{r},t)\nabla\Psi(\mathbf{r},t) - \Psi(\mathbf{r},t)\nabla\Psi^*(\mathbf{r},t) = in_e(\mathbf{r},t)\nabla\phi(\mathbf{r},t)$.

($\nabla\phi(\mathbf{r},t)=0$), the expression reduces further to:

$$\mathbf{J}_s(\mathbf{r},t) = -\frac{n_e e^2}{m_e}\mathbf{A}(\mathbf{r},t). \tag{1.4}$$

This relationship is known as the first London equation. Differentiating both sides with respect to time yields a relation between the time derivative of the supercurrent and the electric field $\mathbf{E}(\mathbf{r},t) = -\partial\mathbf{A}(\mathbf{r},t)/\partial t$:

$$\frac{\partial\mathbf{J}_s(\mathbf{r},t)}{\partial t} = \frac{n_e e^2}{m_e}\mathbf{E}(\mathbf{r},t). \tag{1.5}$$

This implies that a persistent supercurrent can flow without an applied electric field, meaning charge can move without resistance.

Taking the curl of the supercurrent density in Eq. 1.4 leads to the second London equation:

$$\nabla\times\mathbf{J}_s(\mathbf{r},t) = -\frac{n_e e^2}{m_e}\mathbf{B}(\mathbf{r},t). \tag{1.6}$$

This equation explains the phenomenon of perfect diamagnetism manifesting in the Meissner–Ochsenfeld effect [MO33] where magnetic fields are expelled from the material once cooled below its critical temperature. Consequently, the magnetic field inside the superconductor decays exponentially with distance $\mathbf{r}$ from the surface at $\mathbf{r}=0$:

$$\mathbf{B}(\mathbf{r},t) = \mathbf{B}(\mathbf{0},t)\; e^{-\mathbf{r}/\lambda_L}, \tag{1.7}$$

$$\lambda_L = \sqrt{\frac{m_e}{\mu_0 n_e e^2}}, \tag{1.8}$$

where λ_L is the London penetration depth.

In practical applications, zero resistance allows for persistent currents and low-loss operations, while perfect diamagnetism ensures tight confinement of magnetic flux within superconducting loops.

Flux Quantization. Because the superconducting wavefunction Ψ must be single-valued, its phase $\phi(\mathbf{r})$ must change by an integer multiple of 2π around any closed loop. This condition leads to the quantization of the fluxoid:

$$\Phi' = \Phi + \mu_0\lambda_L^2\oint\mathbf{J}_s(\mathbf{r})\cdot d\mathbf{r}, \tag{1.9}$$

where

$$\Phi = \oint\mathbf{A}(\mathbf{r})\cdot d\mathbf{r} \tag{1.10}$$

is the magnetic flux through the loop, $\mathbf{J}_s(\mathbf{r})$ is the supercurrent density, and λ_L is the London penetration depth. When the integration path lies deep inside a superconductor such that $\mathbf{J}_s(\mathbf{r})=0$, the fluxoid reduces to the magnetic flux Φ. In this case, the quantization of the fluxoid implies that the magnetic flux itself is quantized:

$$\Phi = m\cdot\Phi_0, \tag{1.11}$$

where m is an integer and $\Phi_0 = h/2e = 2.067833848\times10^{-15}\ \mathrm{Wb}$ is the magnetic flux quantum.

Experimental confirmation of flux quantization came from the observation of discrete changes in trapped magnetic flux [DN61], demonstrating that the total flux in a superconducting loop is set by screening currents to be an integer multiple of Φ_0, even in external fields. In circuit form

$$\Phi_{\text{total}} = \Phi_{\text{applied}} - LI, \tag{1.12}$$

where L is the loop's self-inductance and I the persistent supercurrent. This effect is central to single flux-quantum electronics [LS91; BLZ01] and superconducting devices such as DC-SQUIDs [MBM02] and flux qubits [MOL+99; OMT+99; SGJ+13].

Josephson Effects. The quantum phase of the superconducting wavefunction can directly affect measurable electrical properties, as predicted in Ref. [Jos62]. Two superconductors separated by a thin insulating barrier form a structure known as a Josephson junction. Each superconducting electrode is described by a macroscopic quantum wavefunction of the form in Eq. 1.1. Due to phase coherence, Cooper pairs can tunnel across the barrier, giving rise to the Josephson effects[4].

The first Josephson relation (or DC Josephson effect) describes the case with no voltage applied across the junction. If a finite phase difference $\varphi = \phi_R - \phi_L$ exists between the two superconductors, left (L) and right (R), a dissipationless supercurrent flows through the barrier according to

$$I_s = I_c \sin(\varphi), \tag{1.13}$$

where the critical current I_c is the maximum dissipationless current the junction can sustain without developing a voltage. The phase difference φ is gauge-invariant and defined as

$$\varphi = \phi_R - \phi_L - \frac{2e}{\hbar} \int_L^R \mathbf{A}(\mathbf{r}) \cdot d\mathbf{r}, \tag{1.14}$$

where $\mathbf{A}(\mathbf{r})$ is the electromagnetic vector potential within the barrier, and the integral is taken from one superconductor to the other. Although neither φ nor $\mathbf{A}$ is directly observable, their combination produces physically measurable effects.

The second Josephson relation (also known as AC Josephson effect) emerges when a voltage V is applied across the junction. In this scenario, the phase difference evolves in time according to:

$$\frac{d\varphi}{dt} = \frac{2eV}{\hbar}, \tag{1.15}$$

implying, if V is constant, a linear growth of $\varphi(t)$ with time. This time-dependent phase resembles the classical relation from Faraday's law, $V = -d\Phi/dt$, where Φ is the magnetic flux. The analogy suggests that the superconducting phase difference plays a role similar to that of magnetic flux in classical electrodynamics.

Substituting this time-dependent phase (Eq. 1.15) into the DC relation (Eq. 1.13) shows that the current becomes oscillatory at a frequency $f_J = \omega_J/(2\pi) = 2eV/h = 483.6 \times 10^{12}\ V\ (\text{Hz})$ which is directly proportional to the applied voltage, making the Josephson junction a voltage-controlled oscillator[5].

[4] For completeness, it is worth mentioning that the Josephson effects can be observed in various types of structures, which can be realized by introducing a "weak link" that interrupts the flow of supercurrent. The specific implementation determines the resulting current–phase relationship [GKI04]. In this discussion, we focus on the most common case: the superconductor–insulator–superconductor (SIS) Josephson junction.

[5] These considerations rely on the assumption that the voltage is independent of the current, i.e., that no resistive elements are present in the system. Applying a DC voltage of $10\ \mu\text{V}$ results in an oscillation frequency of roughly $5\ \text{GHz}$.

1.2.2 Macroscopic quantum nature of electrical circuits

Josephson junctions are essential to superconducting quantum circuits because they combine extremely low energy loss, preserving quantum coherence, with intrinsic nonlinearity.

In a circuit composed only of linear components such as inductors, capacitors, and resistors, the energy levels are equally spaced as in a harmonic oscillator, preventing to selectively address a single transition. Introducing a Josephson junction adds a nonlinearity that breaks this equal spacing, allowing the circuit's spectrum to be shaped so that two specific levels can be isolated and used as a qubit. A qubit is a controllable two-level quantum system that can exist in a superposition of its logical states, forming the fundamental building block of quantum computation. In superconducting implementations [KN19], the quantum state can be described in terms of either the number n of Cooper pairs that have tunneled through the junction or the phase difference φ across it. These satisfy the commutation relation $[\varphi, n] = i$, indicating that they are conjugate variables and that their values cannot be simultaneously specified with arbitrary precision. Rather than a drawback, this property is a powerful tool in qubit design: by tailoring the circuit parameters, one variable can be made highly certain, making the qubit largely insensitive to fluctuations in its conjugate partner. This ability to suppress noise channels allows to build protected quantum processors.

Given these features, Josephson circuits provide an ideal platform to explore a profound question posed by Leggett [Leg80] and others: to what extent can the laws of quantum mechanics, which govern the microscopic world, also describe macroscopic systems? In particular, they questioned whether observing quantized voltages and currents was enough to claim the presence of genuinely quantum phenomena, such as coherent superposition. The answers emerged through two key experiments, each demonstrating the quantum nature of φ and n, respectively.

Macroscopic Quantum Tunneling (MQT). A series of experiments in the early 1980s established the phase difference φ across a Josephson junction as a quantum variable. Measurements of current noise in resistively shunted Josephson junctions revealed that the noise spectrum was limited by quantum fluctuations rather than thermal noise, demonstrating that macroscopic circuit variables cannot be treated classically [KVHC82].

Direct evidence for MQT came from escape rate measurements in current-biased Josephson junctions [VW81]. In this regime, the phase φ behaves like a quantum particle trapped in a tilted washboard potential. At low bias currents, φ remains confined within a potential well; as the current increases, the barrier height decreases. At sufficiently low temperatures, the escape rate saturates instead of following thermally activated behavior, consistent with tunneling through the barrier.

Further experiments probed the quantum structure of the potential well using resonant microwave excitation. Spectroscopic measurements revealed discrete energy levels, directly demonstrating the quantization of the phase degree of freedom [MDC85]. The close agreement between measured tunneling rates and theoretical models, without adjustable parameters, provided further validation of the quantum nature of the phenomenon.

Taken together, these results [CCD+88] confirmed that φ is a genuine quantum variable, supporting the broader concept that macroscopic superconducting circuits can exhibit coherent quantum behavior.

Cooper Pair Box (CPB). Experimental work in the late 1990s demonstrated that the excess number of Cooper pairs n on a superconducting island behaves as a quantum variable. This was achieved using the CPB, a circuit consisting of a small superconducting island connected to a reservoir via a Josephson junction and coupled to a gate electrode through a capacitor. The electrostatic potential of the island, and thus the energy associated with different charge states, can be tuned via the gate voltage V_g, which controls the offset charge n_g.

In the regime where the charging energy dominates, the system's eigenstates correspond to discrete charge states that differ by one Cooper pair. The Josephson coupling introduces quantum coherence between these states, resulting in energy-level hybridization. Spectroscopic measurements revealed avoided level crossings as a function of n_g, directly confirming the coherent tunneling of Cooper pairs and the formation of quantum superpositions of charge states [NCT97; BVJ+98].

Subsequent time-domain experiments demonstrated Rabi oscillations [NPT99; MNAU02], Ramsey fringes, and energy relaxation [VAC+02], providing clear evidence that the charge number n, is a fully quantum degree of freedom in superconducting circuits.

Circuit Quantum Electrodynamics (cQED). cQED extended the principles of cavity QED [MD02] by integrating Josephson qubits, which acts as artificial atoms, with quantized microwave fields confined in high quality coplanar waveguide resonators. This architecture established a robust and scalable platform enabling strong coupling between qubits and resonators [WSB+04] as well as coherent light-matter interaction in the microwave regime [BHW+04; BGGW21].

In this setup, resonators have two principal purposes: they act as quantum buses that mediate coherent interactions between distant qubits, and they enable dispersive, quantum non-demolition (QND) readout [BHW+04; SWB+05], where the qubit state induces a measurable shift in the resonator frequency without destroying the state. This architecture addressed several limitations of earlier charge-based qubit designs. It allowed for high-fidelity control via microwave drives, fast and accurate qubit readout [WSB+04], and the implementation of entangling gates through photon-mediated interactions [MCG+07].

Beyond computation, cQED provides a versatile framework for microwave quantum optics. Experiments in this domain have demonstrated nonclassical photon state generation [HWA+08], quantum-limited amplification [MOH+15], and single-photon generation [HSG+07], key capabilities for quantum sensing and communication. Applications include QND detection of itinerant photons and the development of photon detectors for precision measurements and dark matter searches [DCH+21]. Recent advances include the use of resonators to encode bosonic logical qubits [JNG21], coupling superconducting circuits to spin systems [CLB+20], and exploring regimes of ultra-strong coupling [FKMDL+19]. In parallel, cQED has enabled analog quantum simulations of many-body systems by engineering Hamiltonians with tunable interactions and dissipation [HTK12].

Overall, superconducting quantum circuits studied within the cQED framework span a broad spectrum of research, from fundamental physics to practical technologies, leveraging the design flexibility of circuit-based quantum systems.

1.2.3 Effect of electromagnetic environment

Despite the progress enabled by cQED, decoherence, especially from charge fluctuations, remains a challenge. By introducing a large shunt capacitor in parallel to the single junction, the transmon qubit [KYG+07] achieves excellent protection against charge noise, though it remains susceptible to relaxation, ultimately limiting its coherence [GDPK+21]. This highlights the delicate balance between device design and environmental effects: to understand and optimize Josephson circuits, it is essential to view them not as isolated parts, but as quantum systems shaped by the interaction of their intrinsic properties with their electromagnetic environment.

The Josephson junction is similar to a living organism whose behavior results from the interaction between its internal structure, its genetic code, and its environment. Intrinsic properties like junction capacitance and critical current determine its fundamental characteristics by setting energy scales and quantum degrees of freedom, much like DNA defines an organism's potential. However, just as an organism's traits depend on its environment, a Josephson junction's quantum behavior is strongly influenced by its electromagnetic surroundings and the boundary conditions of the embedding circuit. In biology, this concept is known as phenotypic plasticity: the ability of a single genotype to give rise to different observable traits in response to environmental conditions. Similarly, in superconducting circuits, a fixed set of intrinsic parameters can lead to different quantum behaviors depending on the electromagnetic environment.

External influences on superconducting circuits are set by the environment's characteristic impedance, which determines how the junction interacts with electromagnetic modes through electric or magnetic coupling and whether charge or phase is the better-defined quantum variable. Fluctuations reflect how a quantum variable responds to external parameters, such as voltage or flux biases, and are closely related to the support of the circuit's wavefunction in that variable, which determines its sensitivity to environmental noise. Because of the Heisenberg uncertainty principle, wavefunction support in charge and phase cannot be made arbitrarily narrow simultaneously: confining it in one variable necessarily broadens it in the conjugate variable. At low impedance, as in phase qubits or macroscopic quantum tunneling experiments, the wavefunction is spread in the charge basis, producing a well-defined phase and making the circuit relatively insensitive to charge noise. By contrast, at high impedance, as in CPB experiments, the wavefunction is sharply peaked in charge, enhancing charge quantization but increasing susceptibility to charge fluctuations. Furthermore, the circuit layout, compact or extended, acts as a boundary condition for quantum fields, much like an organism's habitat shapes genetic expression.

These electromagnetic environments are engineered and tunable, allowing selective control over quantum modes. Thus, a Josephson junction's observable behavior depends not only on its intrinsic properties but also on its embedding within a deliberately designed electromagnetic ecosystem, reflecting the interplay of genetics and environment in biology.

1.3 This thesis: Engineering macroscopic quantum fluctuations

This thesis addresses how the quantum uncertainty principle between charge and phase manifests in high-impedance circuits, and the resulting consequences for their macroscopic behavior.

As introduced in Chapter 1, exploring these effects is particularly fascinating, as it bridges fundamental physics with practical device engineering challenges, offering valuable insights into how macroscopic quantum phenomena can be preserved and controlled in real, noisy environments.

Part I: Superinductor resonators. A key challenge in studying single-charge effects is realizing a high-impedance electromagnetic environment that suppresses charge fluctuations. It is commonly believed that the geometric inductance of superconducting circuits cannot exceed the vacuum impedance $Z_{\mathrm{vac}} = 377\ \Omega$ whereas surpassing the resistance quantum $R_Q = h/e^2 \approx 6.45\ \mathrm{k}\Omega$ would need to rely on kinetic inductance.

We challenge this assumption by exploring circuits with inductance coming only from their design geometry.

Chapter 2 provides a brief overview of common superconducting resonators, including their coupling mechanisms and resonance characteristics.

Chapter 3 is a concise literature review on superinductors, making a case for the purely geometric approach.

Chapter 4 presents the modeling, simulation, fabrication, and characterization of these spiral inductors. The successful demonstration of superconducting qubits built with these elements (Ref. [PHS+21; HPK+23]) validates this design strategy.

Part II: Phase-charge duality of Josephson-junction circuits. A challenge in understanding the quantum phase-slip (QPS) phenomenon and the Josephson junction's role as a self-dual circuit element is determining whether the environmental impedance alone can induce a quantum phase transition in a single junction. This question is central to advancing knowledge of circuits with symmetric charge and phase dynamics, the superconductor–insulator transition (SIT), and quantum current metrology.

We propose [Per21] to realize a high-impedance resistor–inductor circuit to investigate the dual Josephson physics and explore whether geometric inductance can mitigate some of the heating issues observed in previous studies besides providing an environment free of offset charges and phase slips by using a single continuous piece of metal.

Chapter 5 provides a concise review of Josephson junctions and phase-slip elements.

Chapter 6 presents preliminary modeling of the proposed circuit, with the specific goal of studying whether applying a voltage bias at different locations can enhance the amplitude of the first dual Shapiro step. However, due to unresolved fabrication and setup issues, the experimental data obtained so far remain limited and largely inconclusive.

Part III: Josephson chains across the superconductor-to-insulator transition. One-dimensional Josephson chains offer a versatile platform to study many-body physics and simulate theoretical models that are otherwise challenging to test experimentally. They implement the physics of the two-dimensional XY model and are expected to exhibit a quantum phase transition from a superconducting to an insulating state. In practice, however, effects such as finite size, nonzero temperature, and probing at nonzero frequency lead to deviations from the ideal theoretical behavior.

We study the fate of plasmonic microwave modes in a 1D Josephson chain showing insulating behavior at DC, aiming to understand how these modes evolve across the quantum phase transition.

Chapter 7 provides a short review of the one-dimensional physics accessible through Josephson junction chains, with particular emphasis on the Kerr effect and the dispersion relation that govern their nonlinear and collective behavior.

Chapter 8 presents experimental DC and RF measurements for Josephson chains designed on different sides of the phase transition. A definitive analysis of the observed phenomena cannot be provided at this stage, as cross-talk between the two devices makes it difficult to attribute specific modes unambiguously.

Part I

Superinductor resonators

CHAPTER 2

Fundamentals of superconducting resonators

Superconducting resonators in circuit quantum electrodynamics (cQED) enable precise control of electromagnetic fields at microwave frequencies. Unlike transmission lines, which support a continuum of traveling modes, resonators confine energy in a discrete set of standing-wave modes. This confinement allows for a strong and coherent exchange between the electric and magnetic field components at a single frequency. Thus, a resonator offers the advantage of confining the interaction to a single, or at most a few well-separated and well-defined modes, whereas coupling to a waveguide inevitably involves a continuum of modes, each of which interacts only weakly with external elements.

To evaluate and compare resonator designs, several figures of merit are typically introduced. The resonance frequency determines the fundamental mode and sets the timescale of energy oscillation. The quality factor quantifies the ratio of stored to dissipated energy per cycle, determining the lifetime of stored energy and the spectral width of the resonance. The characteristic impedance sets the voltage-to-current ratio and controls coupling to external circuitry, while the phase velocity determines the propagation speed of waves and the spacing of resonant modes. Finally, the coupling strength measures the rate of energy exchange between the resonator and external elements, be they other resonators, waveguides, or general quantum or classical circuit elements, thus determining the efficiency of coherent interactions.

Within cQED, resonators play diverse roles. They mediate interactions between qubits and microwave photons, enabling high-fidelity, nondestructive qubit readout via dispersive coupling [BHW+04]. They serve as quantum buses for generating entanglement [MCG+07], and as quantum memories by storing quantum states in long-lived modes [RPA+16]. Beyond computation, resonators are also used in microwave photonics, to control and route single photons within circuit networks [GKM+17], in parametric amplifiers to boost weak signals with minimal added noise [CBL07], and in quantum sensing and metrology to detect minute shifts in resonance frequency caused by environmental changes [SHS+07].

Resonator design is often classified by dimensionality. Structures whose physical dimensions are much smaller than the wavelength of their fundamental frequency are referred to as lumped-element resonators; from the perspective of the electromagnetic field, they behave as if they were zero-dimensional. By contrast, structures with dimensions comparable to or larger than the wavelength are categorized as distributed resonators, which are typically

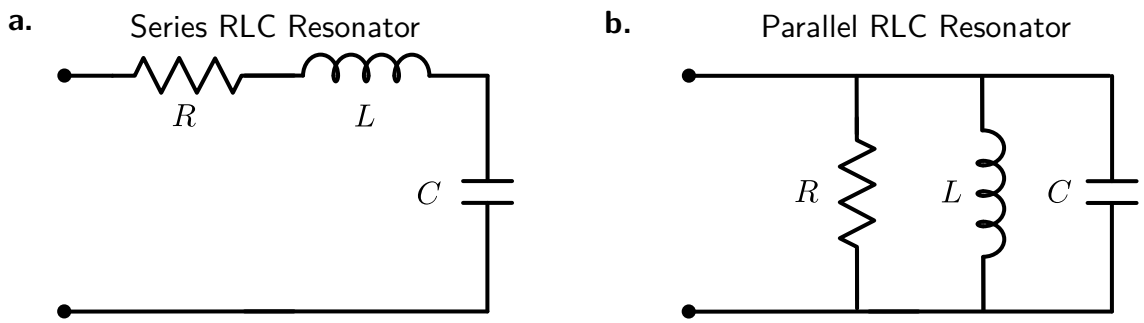

Figure 2.1: **Lumped-element RLC resonators. a.** Series configuration. **b.** Parallel configuration.

one-dimensional or three-dimensional depending on their geometry and the way the fields are confined.

This Chapter 2 covers essential aspects of the modeling, measurement theory and figures of merit of lumped-element and distributed resonators, which form the basis for understanding the geometric superinductors in Chapter 4 and the Josephson junction transmission line resonators in Chapter 8.

2.1 Lumped-element resonators

Lumped element resonators composed of discrete resistive R, capacitive C, and inductive L components have a resonance frequency determined solely by the circuit parameters, rather than geometric length[1]. This conceptual separation enables miniaturization, precise control, and design flexibility, making these resonators highly engineerable, tunable, and well-suited for integration. By contrast, in a conventional distributed element resonator, the fundamental frequency is directly linked to the physical length, and the impedance is also solely determined by the geometry. This makes it more difficult to decouple these aspects from the resonator's physical size (further details in Section 2.3).

Zero-dimensional microwave resonators are typically modeled using two canonical circuit configurations: series and parallel RLC resonators, as illustrated in Fig. 2.1 and summarized in Table 2.1 [Poz12].

2.1.1 The quantum LC harmonic oscillator

In the absence of dissipation, the most basic resonator consists of an inductor L and a capacitor C connected in a closed loop (Fig. 2.2.a). A current I through the inductor generates a magnetic flux $\Phi = LI$, resulting in a voltage drop $V = -L\dot{I}$. This voltage appears across the capacitor, inducing a charge $Q = CV$, with the current given by $I = \dot{Q}$.

The canonical momentum associated with Φ[2] is Q, and together they form the canonical coordinates of the Hamiltonian

$$H = \frac{Q^2}{2C} + \frac{\Phi^2}{2L}. \tag{2.1}$$

[1] In reality, all circuit components exhibit parasitic effects. For example, small capacitances between segments of an inductor slightly alter its behavior. Nevertheless, these deviations are typically minor, so the lumped-element approximation remains a reliable and practical tool for design and analysis.

[2] One node of the circuit is chosen as ground, and the node flux Φ is defined at the remaining node.

Parameters	Series RLC	Parallel RLC
Input Impedance	$Z_s = R + j\omega L - j\frac{1}{\omega C}$	$Z_p = \left(\frac{1}{R} + j\omega C - j\frac{1}{\omega L}\right)^{-1}$
Resonant Frequency	$f_0 = \frac{\omega_0}{2\pi} = \frac{1}{\sqrt{LC}}$	$f_0 = \frac{\omega_0}{2\pi} = \frac{1}{\sqrt{LC}}$
Internal Quality Factor	$Q_i = \frac{\omega_0 L}{R} = \frac{1}{\omega_0 RC}$	$Q_i = \frac{R}{\omega_0 L} = \omega_0 RC$

Table 2.1: **Comparison of series and parallel lumped-element RLC resonators.** Input impedance, resonant frequency, and internal quality factor are listed for both models.

Hamilton's equations directly reveal the harmonic nature of the circuit:

$$\dot{\Phi} = \frac{\partial H}{\partial Q} = \frac{Q}{C}, \quad \dot{Q} = -\frac{\partial H}{\partial \Phi} = -\frac{\Phi}{L}, \tag{2.2}$$

which lead to the standard harmonic oscillator equation

$$\ddot{Q} = -\frac{Q}{LC}, \tag{2.3}$$

with resonance frequency

$$f_0 = \frac{\omega_0}{2\pi} = \frac{1}{2\pi\sqrt{LC}}. \tag{2.4}$$

The circuit's characteristic impedance is

$$Z_C = \frac{V}{I} = \sqrt{\frac{L}{C}}, \tag{2.5}$$

relating the voltage and current amplitudes[3].

The classical Hamiltonian can be naturally extended to describe quantum behavior by promoting[4] the coordinates to operators that obey the corresponding canonical commutation relation

$$\hat{H} = \frac{\hat{Q}^2}{2C} + \frac{\hat{\Phi}^2}{2L}, \quad [\hat{\Phi}, \hat{Q}] = i\hbar. \tag{2.6}$$

Eq. 2.6 provides the complete Hamiltonian description of the superconducting LC circuit, which has the same form as the one-dimensional mechanical quantum harmonic oscillator Hamiltonian, with the correspondence $\hat{x} \leftrightarrow \hat{\Phi}$, $\hat{p} \leftrightarrow \hat{Q}$, and $m \leftrightarrow C$.

Accordingly, the energy levels of the quantum LC circuit are equally spaced, given by

$$E_n = \hbar\omega_0 \left(n + \frac{1}{2}\right), \quad n = 0, 1, 2, \ldots \tag{2.7}$$

where n is the eigenvalue associated with the photon number operator $\hat{n} = \hat{a}^\dagger \hat{a}$, and $\hat{a}$ and $\hat{a}^\dagger$ are the bosonic annihilation and creation operators, which respectively decrease or increase the excitation number of a quantum harmonic oscillator eigenstate.

[3] An inductor produces a voltage proportional to the time derivative of the current, $V = L\,\dot{I}$. Assuming a sinusoidal current at the resonance frequency, $I = I_0 \cos(\omega_0 t)$, the voltage amplitude is $V = \omega_0 L I_0$, which defines the characteristic impedance of the LC resonator as $Z_C = V/I_0 = \omega_0 L = \sqrt{L/C}$.

[4] For reviews on circuit quantization, see Refs. [VD17; BHW+04].

The charge and flux operators can also be written in terms of raising and lowering operators as

$$\hat{\Phi} = \Phi_{\mathrm{zpf}} \left(\hat{a}^\dagger + \hat{a} \right), \quad \Phi_{\mathrm{zpf}} = \Phi_0 \sqrt{\frac{Z_C}{4\pi R_Q}}, \tag{2.8}$$

$$\hat{Q} = iQ_{\mathrm{zpf}} \left(\hat{a}^\dagger - \hat{a} \right), \quad Q_{\mathrm{zpf}} = 2e \sqrt{\frac{R_Q}{4\pi Z_C}}. \tag{2.9}$$

where $R_Q = h/(2e)^2 \approx 6.45\ \mathrm{k\Omega}$ is the superconducting quantum of resistance. The zero-point fluctuations are defined as the root-mean-square (rms) values of the flux and charge operators in the ground state $|0\rangle$ of the quantum LC oscillator

$$\Phi_{\mathrm{zpf}} \equiv \sqrt{\langle 0|\hat{\Phi}^2|0\rangle}, \qquad Q_{\mathrm{zpf}} \equiv \sqrt{\langle 0|\hat{Q}^2|0\rangle}. \tag{2.10}$$

They represent the fundamental quantum uncertainties of the expectation value of the conjugate variables Φ and Q, imposed by the Heisenberg uncertainty principle. Physically, Φ_{zpf} corresponds to the rms magnetic flux value threading the inductor in the quantum ground state with no external excitations, while Q_{zpf} corresponds to the rms charge stored on the capacitor. These fluctuations are an unavoidable and intrinsic feature of the quantum ground state of the LC circuit under consideration.

The dimensionless ratio

$$\frac{\Phi_{\mathrm{zpf}}/\Phi_0}{Q_{\mathrm{zpf}}/(2e)} = \frac{Z_C}{R_Q}, \tag{2.11}$$

shows that the relative magnitude of flux and charge zero-point fluctuations is entirely determined by the characteristic impedance of the resonator. Low-impedance resonators ($Z_C \ll R_Q$) makes flux well defined at the expense of large charge uncertainty, whereas high-impedance resonators ($Z_C \gg R_Q$) suppress charge uncertainty at the cost of greater flux spreading. In this way, the circuit impedance determines along which conjugate variable the ground-state wavefunction has its narrower support, and consequently which variable remains delocalized.

Since the electromagnetic environment of a circuit typically has a low impedance of about $50\ \Omega$, modeling it as a noise source implies (Eq. 2.11) that the flux-noise amplitude is nearly two orders of magnitude smaller than the corresponding charge-noise amplitude[5]. This means that encoding quantum information in flux, rather than in charge, provides greater resilience to environmental noise.

This connection between impedance, noise, and conjugate-variable fluctuations can also be expressed in terms of the fundamental voltage and current fluctuations of the resonator. In the quantum regime, the relation $Z_C = \Delta\hat{V}/\Delta\hat{I}$ remains valid, with the zero-point voltage and current fluctuations given by

$$\Delta\hat{V} = \frac{Q_{\mathrm{zpf}}}{C} = \omega_0 \sqrt{\frac{\hbar Z_C}{2}}, \tag{2.12}$$

$$\Delta\hat{I} = \frac{\Phi_{\mathrm{zpf}}}{L} = \omega_0 \sqrt{\frac{\hbar}{2Z_C}}. \tag{2.13}$$

[5]Interestingly, this trend is also observed for other types of noise that are not of electromagnetic origin, such as $1/f$ noise. The $1/f$ flux-noise amplitude A_Φ is reported to lie within the range $10^{-6} - 10^{-5}\ \Phi_0$, which is roughly two orders of magnitude lower than the $1/f$ charge-noise amplitude A_e in $10^{-4} - 10^{-3}\ e$.

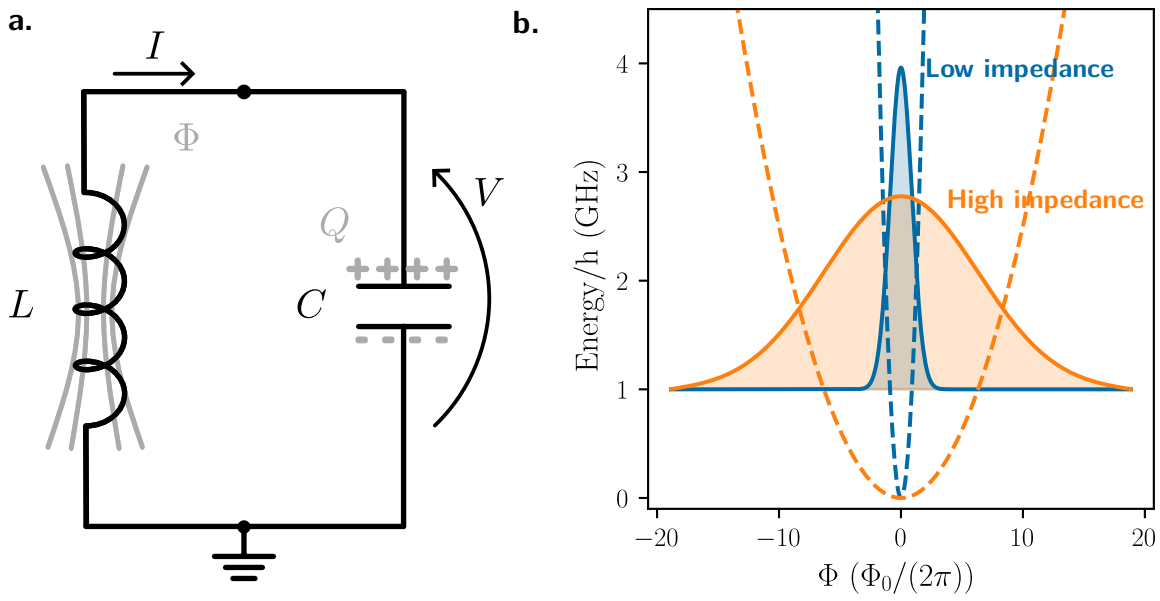

Figure 2.2: **Quantum fluctuations in an LC oscillator. a.** Schematic of an LC circuit indicating key variables: charge Q, flux Φ, voltage V, and current I. **b.** Flux representation of two LC oscillator states with identical resonance frequency but different characteristic impedance. Solid lines depict the corresponding ground-state wavefunction support, while dashed lines show the energy potential. Blue corresponds to low-impedance, and orange to high-impedance oscillators. Higher impedance leads to larger quantum fluctuations of the flux, resulting in broader wavefunction spreading.

For a fixed resonance frequency of $\omega_0 = 2\pi \times 5$ GHz, a low-impedance circuit with $Z_C = 50\ \Omega$ has quantum voltage and current fluctuations of approximately $\Delta\hat{V} \approx 1\ \mu$V and $\Delta\hat{I} \approx 30$ nA, respectively. In contrast, a high-impedance circuit with $Z_C = 10\ \text{k}\Omega$ exhibits larger voltage fluctuations $\Delta\hat{V} \approx 20\ \mu$V but smaller current fluctuations $\Delta\hat{I} \approx 2$ nA. Low-impedance resonators enhance inductive coupling, leading to well-defined flux and strong interaction with systems having small magnetic dipoles, whereas high-impedance resonators favor capacitive coupling, resulting in well-defined charge and strong interaction with systems possessing small electric dipoles [DGS07].

Beyond their role in determining voltage and current noise amplitudes, the impedance-dependent fluctuations also influence the shape of the quantum ground state. The ground-state wavefunction of the quantum harmonic oscillator is Gaussian in flux,

$$\Psi_0(\Phi) = \left(\frac{1}{2\pi\Phi_{\text{zpf}}^2}\right)^{1/4} e^{-\left(\frac{\Phi^2}{4\Phi_{\text{zpf}}^2}\right)}, \tag{2.14}$$

with its width set by the zero-point flux fluctuations. As the impedance increases, the wavefunction broadens in flux space, reflecting enhanced flux fluctuations (Fig. 2.2.b).

2.2 Transmission line

Transmission lines allow electromagnetic signals to propagate over distances much greater than their wavelengths, an important feature at high frequencies where lumped-element models fail as device dimensions approach the signal wavelength. Common transmission line geometries,

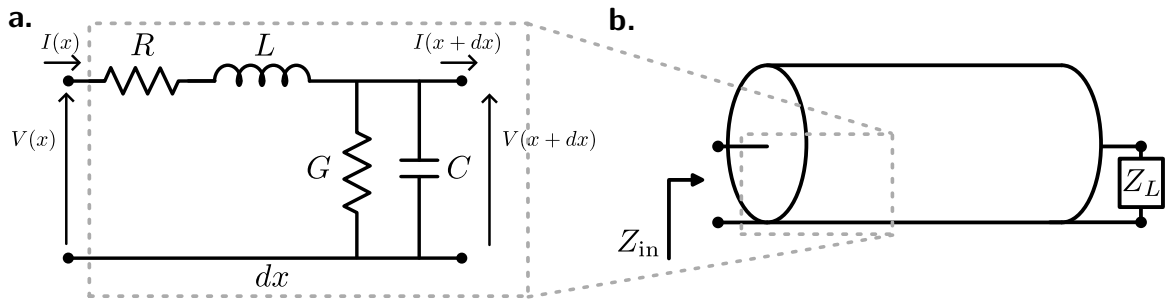

Figure 2.3: **Distributed-element model of a transmission line segment. a.** Lumped-element modeling of a transmission line segment dx. **b.** A load Z_L is connected to the transmission line. This allows interaction with the load over a long electrical distance or can be seen as modifying the line's electrical properties via the input impedance Z_{in}.

such as coaxial cables and coplanar waveguides, provide efficient ways for routing microwave signals to and from devices.

General Theory. A classical transmission line can be modeled as a continuous distribution of infinitesimal circuit elements per unit length: series inductance L, series resistance R, shunt capacitance C, and shunt conductance G, as illustrated in Fig. 2.3.a. The resistance R accounts for ohmic losses in the conductors, while the conductance G represents dielectric leakage through the insulating material.

Applying Kirchhoff's laws to an infinitesimal segment dx of the line yields the telegrapher's equations [Poz12]:

$$\frac{\partial V(x,t)}{\partial x} = -RI(x,t) - L\frac{\partial I(x,t)}{\partial t}, \tag{2.15}$$

$$\frac{\partial V(x,t)}{\partial x} = -GV(x,t) - C\frac{\partial I(x,t)}{\partial t}. \tag{2.16}$$

Considering a sinusoidal traveling wave with angular frequency ω, Eqs. 2.15, 2.16 become:

$$\frac{\partial V(x)}{\partial x} = -(R + j\omega L)I(x), \tag{2.17}$$

$$\frac{\partial I(x)}{\partial x} = -(G + j\omega C)V(x). \tag{2.18}$$

Differentiating these equations and substituting one into the other leads to wave equations for the voltage and current:

$$\frac{\partial^2 V}{\partial x^2} = \gamma^2 V(x), \tag{2.19}$$

$$\frac{\partial^2 I}{\partial x^2} = \gamma^2 I(x), \tag{2.20}$$

where the complex propagation constant γ is defined as

$$\gamma = \sqrt{(R + j\omega L)(G + j\omega C)} = \alpha + j\beta. \tag{2.21}$$

The real part α is the attenuation constant, which quantifies the exponential decrease in the amplitude of the wave as it propagates due to losses in the conductors (R) and the dielectric

(G). The imaginary part β is the phase constant, which specifies the rate of phase change along the line and therefore determines the wavelength and phase velocity of the wave.

The general solution for a traveling wave on the line is a superposition of forward- and backward-propagating waves:

$$V(x) = V_+ e^{-\gamma x} + V_- e^{\gamma x} \tag{2.22}$$

$$I(x) = \frac{V_+}{Z_C} e^{-\gamma x} - \frac{V_-}{Z_C} e^{\gamma x} \tag{2.23}$$

where V_+ and V_- are the amplitudes of the forward and reflected voltage waves, respectively. The characteristic impedance Z_C, defined by

$$Z_C = \sqrt{\frac{R + j\omega L}{G + j\omega C}}, \tag{2.24}$$

gives the ratio of voltage to current for traveling waves on the line.

Lossless case. Of particular importance is the lossless case, i.e. $R = G = \alpha = 0$. This is useful for modeling ideal systems or when losses are negligible compared to the reactive components of the line, as is the case for superconducting circuits at microwave frequency. It leads to a characteristic impedance formula indicating a purely reactive (non-dissipative) propagation. In a lossless transmission line, the input impedance depends on both the load impedance Z_L (Fig.2.3.b) and the physical length of the line ℓ, as well as on the frequency through $\beta = \omega\sqrt{LC}$ at which is probed. The phase velocity $v_p = 1/\sqrt{LC}$ indicates the speed at which a single-frequency signal component propagates along the line, which is constant in the ideal lossless case. A summary is reported in Table 2.2.

Parameter	**General Case**	**Lossless Case**
Characteristic impedance, Z_C	$\sqrt{\frac{R + j\omega L}{G + j\omega C}}$	$\sqrt{\frac{L}{C}}$
Propagation constant, γ	$\alpha + j\beta = \sqrt{(R + j\omega L)(G + j\omega C)}$	$j\beta = j\omega\sqrt{LC}$
Phase velocity, v_p	$\frac{\omega}{\beta}$	$\frac{1}{\sqrt{LC}}$
Wavelength, λ	$\frac{2\pi}{\beta}$	$\frac{2\pi}{\omega\sqrt{LC}} = \frac{v_p}{f}$
Input impedance, $Z_{\text{in}}(x = \ell)$	$Z_C \frac{Z_L + Z_C \tanh(\gamma\ell)}{Z_C + Z_L \tanh(\gamma\ell)}$	$Z_C \frac{Z_L + Z_C \tan(\beta\ell)}{Z_C + Z_L \tan(\beta\ell)}$

Table 2.2: **Transmission line parameters: general and lossless case.** The lossless case assumes $R = 0$ and $G = 0$, simplifying the expressions for the characteristic parameters.

At specific fractions of the wavelength λ, the input impedance Z_{in} simplifies in useful and intuitive ways (Table 2.3).

When the transmission line is a quarter wavelength long $\ell = \lambda/4$, it inverts the load impedance: $Z_{\text{in}} = Z_C^2/Z_L$. This means that a short circuit load $Z_L = 0$ appears as an open circuit $Z_{\text{in}} \to \infty$, while an open circuit load $Z_L \to \infty$ appears as a short circuit $Z_{\text{in}} = 0$.

For a half-wavelength line $\ell = \lambda/2$, the input impedance equals the load impedance $Z_{\text{in}} = Z_L$. At this length, the transmission line is effectively transparent in terms of impedance: it does not transform the load.

When the load matches the characteristic impedance of the line, i.e. $Z_L = Z_C$, the input impedance is $Z_{\text{in}} = Z_C$ and in this case there are no reflections, the wave is completely absorbed by the load, and power transfer is maximized.

Load	**any ℓ**	$\ell = \lambda/4$	$\ell = \lambda/2$
Generic Z_L	$Z_C \dfrac{Z_L + Z_C \tan(\beta\ell)}{Z_C + Z_L \tan(\beta\ell)}$	$\dfrac{Z_C^2}{Z_L}$	Z_L
Matched $Z_L = Z_C$	Z_C	Z_C	Z_C
Short $Z_L = 0$	$j \tan(\beta\ell)$	$\to \infty$	0
Open $Z_L \to \infty$	$-j \cot(\beta\ell)$	0	$\to \infty$

Table 2.3: **Input impedance for specific load and length conditions.** Input impedance Z_{in} of a lossless transmission line at specific length ℓ and termination condition Z_L.

2.3 Lossless transmission line resonators

A finite segment of a transmission line, when terminated with suitable boundary conditions, can behave as a one-dimensional resonator. Assuming a lossless transmission line with negligible attenuation ($\alpha \ll 1$)[6], and considering frequencies close to resonance ($|\omega - \omega_0| \ll \omega_0$) [CPP+22], three common types of transmission line resonators can be identified.

These transmission line resonators exhibit behavior analogous to lumped-element circuits. In particular, the short-circuited $\lambda/4$ and open-circuited $\lambda/2$ resonators are mapped to a parallel RLC circuit, while the short-circuited $\lambda/2$ resonator behaves like a series RLC circuit (see Table 2.4).

In all cases, the internal quality factor Q_i is given by the same expression:

$$Q_i = \frac{\beta}{2\alpha}, \quad \text{where} \quad \beta = \frac{2\pi}{\lambda}. \tag{2.25}$$

When the transmission line is open (or shorted) at both ends, the current (or voltage) must vanish at those boundaries. This implies a standing wave condition where the phase $\beta\ell = m\pi$, with m being an integer. In this configuration, the resonator supports modes that span half-wavelengths, resulting in resonant frequencies given by

$$f_{\lambda/2,m} = \frac{\omega_{\lambda/2,m}}{2\pi} = \frac{1}{2\pi}\frac{m\pi}{\ell}\sqrt{LC}, \quad m = 1, 2, 3, \ldots, \tag{2.26}$$

[6] I prefer to explicitly keep the α term here to clearly indicate where the correction is introduced, and also because omitting it would imply an infinite internal quality factor Q_i.

Parameter	$\lambda/4$ short	$\lambda/2$ open	$\lambda/2$ short
Z_{in}	$\dfrac{Z_C}{\alpha\ell + j\pi(\omega-\omega_0)/(2\omega_0)}$	$\dfrac{Z_C}{\alpha\ell + j\pi(\omega-\omega_0)/\omega_0}$	$Z_C\left(\alpha\ell + j\dfrac{\pi(\omega-\omega_0)}{\omega_0}\right)$
$f_0 = \dfrac{\omega_0}{2\pi}$	$\dfrac{1}{2\pi}\cdot\dfrac{\pi}{2\ell}\sqrt{LC}$	$\dfrac{1}{2\pi}\cdot\dfrac{\pi}{\ell}\sqrt{LC}$	$\dfrac{1}{2\pi}\cdot\dfrac{\pi}{\ell}\sqrt{LC}$
Q_i	$\dfrac{\beta}{2\alpha}$	$\dfrac{\beta}{2\alpha}$	$\dfrac{\beta}{2\alpha}$
R	$\dfrac{Z_C}{\alpha\ell}$	$\dfrac{Z_C}{\alpha\ell}$	$Z_C\alpha\ell$
L	$\dfrac{1}{\omega_0^2 C}$	$\dfrac{1}{\omega_0^2 C}$	$\dfrac{\pi Z_C}{2\omega_0}$
C	$\dfrac{\pi}{4\omega_0 Z_C}$	$\dfrac{\pi}{2\omega_0 Z_C}$	$\dfrac{1}{\omega_0^2 L}$

Table 2.4: **Lumped element modeling of transmission line resonators.** Formulas for modeling three common types of transmission line resonators as equivalent lumped element circuits: the quarter-wavelength short-circuited and the half-wavelength open-circuited as a parallel RLC circuit, and the half-wavelength short-circuited as a series RLC circuit. Ref. [CPP+22].

where ℓ is the length of the transmission line and L, C are the inductance and capacitance per unit length, respectively. These modes correspond to symmetric standing wave patterns with either voltage nodes (or anti-nodes) at the boundaries.

On the contrary, when one end of the transmission line is shorted and the other is open, the configuration supports standing waves with a quarter-wavelength mode structure. In this case, the resonant frequencies are:

$$f_{\lambda/4,m} = \frac{\omega_{\lambda/4,m}}{2\pi} = \frac{1}{2\pi}\frac{(2m+1)\pi}{2\ell}\sqrt{LC}, \quad m = 1, 2, 3, \ldots. \tag{2.27}$$

These modes produce patterns with a node at one end and an anti-node at the other. This type of resonance is particularly advantageous in practice, as it occupies only half the physical length of a $\lambda/2$ resonator. Moreover, the shorted end serves as a voltage node (and a current antinode), while the open end acts as a voltage antinode (and a current node). As a result, the resonator can couple capacitively at the open end and inductively at the shorted end, making it versatile for integration into superconducting circuits and other microwave systems.

Coplanar waveguide resonator. A coplanar waveguide (CPW) [GFB+08] consists of a narrow superconducting center conductor of width w, separated from two semi-infinite superconducting ground planes by gaps of width s. This geometry supports transverse electromagnetic (TEM) wave propagation, functioning similarly to a planar coaxial cable.

Typically, the CPW is fabricated on a dielectric substrate. The effective dielectric constant ε_{eff} experienced by the propagating mode lies between the substrate dielectric constant ε_{sub} and that of air (or vacuum), $\varepsilon_{\text{air}} = 1$, and depends on the CPW geometry, particularly w, s, and the substrate thickness. Although analytical formulas for ε_{eff} exist [GLK95], their accuracy

strongly depends on the ratio of substrate layer thicknesses to the CPW cross-section [CC97], and they often fail to provide reliable predictions [GFB+08].

Using conformal mapping techniques, the per-unit-length inductance L and capacitance C of the CPW are given by [GFB+08]

$$L = \frac{\mu_0}{4}\frac{K(k_0')}{K(k_0)}, \quad C = 4\varepsilon_0\varepsilon_{\text{eff}}\frac{K(k_0)}{K(k_0')}, \tag{2.28}$$

where $K(k)$ denotes the elliptic integral of the first kind. The arguments are defined as

$$k_0 = \frac{w}{w+2s}, \quad k_0' = \sqrt{1-k_0^2}. \tag{2.29}$$

The characteristic impedance Z_C can be expressed as

$$Z_C = \sqrt{\frac{L}{C}} = \frac{30\pi}{\sqrt{\varepsilon_{\text{eff}}}}\frac{K(k_0')}{K(k_0)}. \tag{2.30}$$

A coplanar waveguide can form a resonator by interrupting its center conductor. Open at both ends, it acts as a half-wavelength resonator; grounding one end creates a quarter-wavelength resonator.

2.4 Properties of resonance curves

The frequency response of an ideal resonator can be modeled as a damped harmonic oscillator, characterized by two fundamental quantities: the resonance frequency $f_0 = \omega_0/(2\pi)$ and the quality factor Q. Physically, the resonance frequency determines where the system naturally oscillates, while the quality factor quantifies how sharply the resonator stores energy relative to its losses.

2.4.1 Lorentzian response

The resonator's response to an external drive at angular frequency ω is described by its complex susceptibility $\chi(\omega)$:

$$\chi(\omega) \propto \frac{1}{(\omega-\omega_0)+i\kappa/2}, \tag{2.31}$$

where κ is the total energy decay rate of the resonator in angular frequency units. The power response is proportional to the magnitude squared of the susceptibility,

$$|\chi(\omega)|^2 \propto \frac{1}{(\omega-\omega_0)^2+(\kappa/2)^2}, \tag{2.32}$$

which forms a Lorentzian line shape centered at ω_0 with full width at half maximum (FWHM) κ. The photon lifetime inside the resonator is

$$\tau = \frac{1}{\kappa}, \tag{2.33}$$

and the quality factor is defined as

$$Q = 2\pi \times \frac{\text{energy stored}}{\text{energy lost per cycle}} = \frac{\omega_0 E}{P} = \frac{\omega_0}{\kappa}, \tag{2.34}$$

where E is the energy stored in the resonator and P is the power loss. Thus, higher Q corresponds to a narrower linewidth and longer photon lifetime.

2.4.2 Losses and coupling

The total decay rate κ can be decomposed into internal and external contributions:

$$\kappa = \kappa_i + \kappa_e \quad (\text{or } \kappa = \kappa_i + \kappa_{e1} + \kappa_{e2} \text{ for two-port systems}), \tag{2.35}$$

with corresponding quality factors

$$\frac{1}{Q} = \frac{1}{Q_i} + \frac{1}{Q_e}. \tag{2.36}$$

Internal losses. The internal quality factor Q_i captures intrinsic dissipation mechanisms:

$$\frac{1}{Q_i} = \frac{1}{Q_{\text{res}}} + \frac{1}{Q_{\text{diel}}} + \frac{1}{Q_{\text{rad}}} + \frac{1}{Q_{\text{other}}}. \tag{2.37}$$

The following terms describe the dominant factors contributing to internal losses.

Resistive losses (Q_{res}) [Sch07; dG14]. While superconductors are commonly associated with zero electrical resistance at DC, at higher frequencies they still exhibit an impedance that is not entirely reactive. This can be seen from the two-fluid model that treats the superconductor as a parallel combination of a lossless inductive channel (Cooper pairs) and a resistive channel (thermally excited or out of equilibrium quasiparticles). The surface resistance, proportional to the number of quasiparticles n_{qp}, decreases exponentially with temperature, $R_s(T) \propto n_{\text{qp}}(T) \propto e^{-\Delta/k_B T}$.

Dielectric losses (Q_{diel}). Dielectric substrates are characterized by a complex electric permittivity $\varepsilon = \varepsilon' + i\varepsilon''$, where the imaginary part ε'' describes energy dissipation. This dissipation is commonly expressed via the loss tangent

$$\tan\delta = -\frac{\varepsilon'}{\varepsilon''}, \tag{2.38}$$

which is directly related to the dielectric quality factor of the resonator:

$$Q_{\text{diel}} = \frac{1}{\tan\delta}. \tag{2.39}$$

At low temperatures and low drive powers (single-photon regime), the dominant source of dielectric loss in superconducting resonators comes from parasitic two-level systems (TLSs) [Mur21; ZRP+23; CMD+23], typically located at interfaces between the dielectric and the superconducting film. These TLSs can saturate either by raising the temperature or by increasing the energy stored in the resonator. Saturation reduces their ability to absorb energy, leading to a lower loss rate. Minimizing the electric field at metal–dielectric interfaces helps reduce TLS-related dissipation.

Radiative losses (Q_{rad}). Radiative loss occurs when energy escapes from the resonator into free space or coupled to higher-order modes in the surrounding environment instead of remaining confined within its structure. In coplanar waveguide resonators, this loss is generally very small due to the geometry: currents in the center conductor are largely canceled by opposing currents in the ground planes, resulting in a very low effective dipole moment. Consequently, typical CPW resonators exhibit extremely high radiation-limited quality factors [Maz05]. However, increasing the distance between the center conductor and the ground planes weakens this screening, allowing more energy to radiate away. These losses are usually minimized by careful packaging and design.

Other losses (Q_{other}). Additional contributions can arise from magnetic vortex motion, seam losses, imperfect grounding, and other secondary mechanisms.

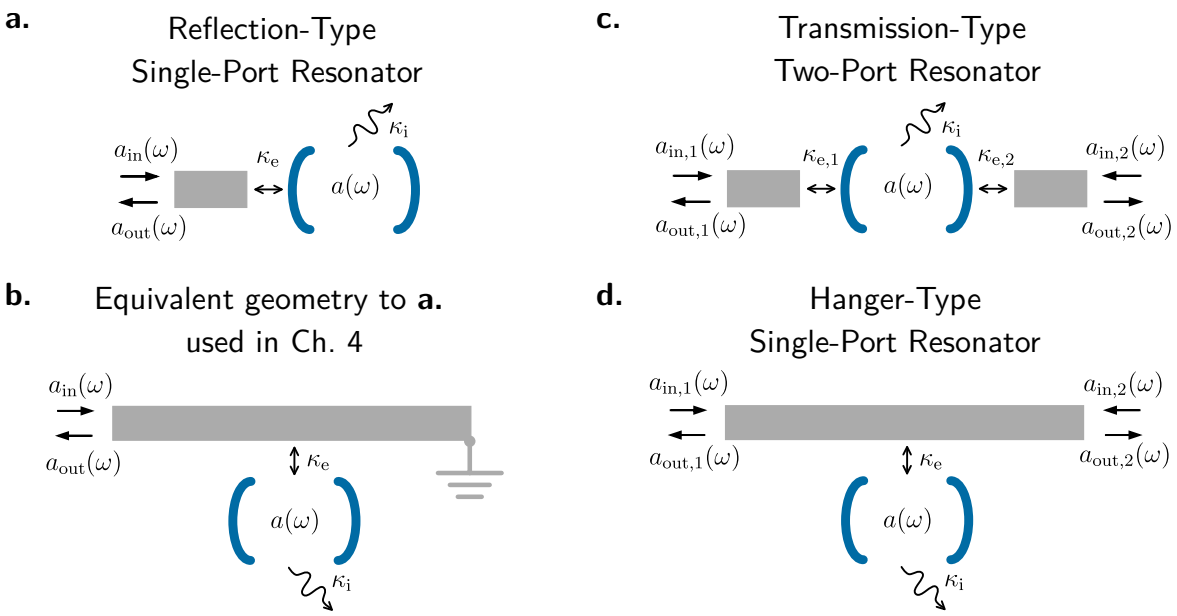

Figure 2.4: **Schematic of resonator coupling configurations. a.** and **b.** Reflection-type (single-port) resonators; **c.** Transmission-type (two-port), and **d.** Hanger-type (single-port) resonators.

External coupling. External losses correspond to energy leakage into measurement lines, quantified by κ_e and $Q_e = \omega_0/\kappa_e$. The ratio of external to internal decay rates

$$r = \frac{\kappa_e}{\kappa_i} = \frac{Q_i}{Q_e} \tag{2.40}$$

defines the coupling regime:

- Overcoupled ($r > 1$). Fast readout, high bandwidth, shorter photon lifetime.
- Critically coupled ($r = 1$). Maximizes power transfer; all incident power is dissipated internally at resonance.
- Undercoupled ($r < 1$). Minimizes coupling loss, preserves stored energy; ideal for quantum memory.

2.4.3 Scattering parameters

The transmitted or reflected power in a circuit network can be determined by analyzing the voltage amplitude and phase at the relevant ports, which are related through the scattering matrix that characterizes the interaction between incident and reflected voltage waves in a multiport network. Defining $\mathbf{V}^{\text{in}}$ as the incident (forward) wave and $\mathbf{V}^{\text{out}}$ as the outgoing (reflected/transmitted) wave, one writes

$$\mathbf{V}^{\text{out}} = \mathbf{S}\ \mathbf{V}^{\text{in}}. \tag{2.41}$$

The individual elements are defined as

$$S_{ij} = \frac{V_i^{\text{out}}}{V_j^{\text{in}}} \quad \text{with all other } V_k^{\text{in}} = 0 \ \ (k \neq j). \tag{2.42}$$

In many experiments, such as measurements of superconducting resonators, this reduces to the case of a two-port network.

In the quantum input–output formalism [GC85], the same description applies but with annihilation operators replacing classical voltage waves. The incoming and outgoing fields are denoted by a_{in} and a_{out} respectively (see Fig. 2.5), and satisfy

$$a_{\text{out}} = \mathbf{S}\ a_{\text{in}}. \tag{2.43}$$

The scattering coefficients are then given by

$$S_{ij} = \frac{a_{i,\text{out}}}{a_{j,\text{in}}}. \tag{2.44}$$

To understand the ideal response, three configurations are of interest. The following paragraphs are based on Gary Steele's Python notebook titled "Technical note about origins of Fano lineshapes and difficulty of extracting internal quality factors"[7].

Reflection-Type (Single-Port) Resonator. This corresponds to the case where a signal is applied to a single port, and the reflected response at the same port (S_{11}) is measured. The resonator acts as a mirror whose reflection coefficient depends on frequency [CPF+22] (Fig. 2.4.a and .b)

$$S_{11}(\omega) = 1 - \frac{\kappa_e}{i(\omega - \omega_0) + \kappa/2} \tag{2.45}$$

Near resonance, the reflection dips due to energy coupling into the resonator. The magnitude $|S_{11}|$ alone is not sufficient to distinguish undercoupling from overcoupling; the phase response (or polar representation) has also to be considered. In the complex plane, as the drive frequency is swept through resonance, S_{11} traces out a circle beginning at $(1, 0)$ and moving counterclockwise. If the circle does not enclose the origin, the resonator is undercoupled; if it does, the system is overcoupled. At critical coupling, the trajectory just touches the origin, and the phase becomes ill-defined. Looking at the real part $\Re(S_{11})$ also provides an indication of the coupling regime: undercoupling corresponds to $\Re(S_{11}) > 0$ everywhere; at critical coupling $\Re(S_{11})$ reaches zero at resonance; and in the overcoupled regime it becomes negative at resonance. On resonance, the reflection coefficient is purely real, $S_{11}(\omega_0) = 1 - 2\kappa_e/\kappa$ and so $\kappa_i = \kappa \cdot (1 + S_{11}(\omega_0))/2$. The total linewidth κ can be obtained independently from the full width at half maximum (FWHM) of either $\Re(S_{11})$ or $|S_{11}|^2$. In the reflection case, both f_0, κ_i and κ_e can be fitted, making the reflection measurement much more insightful than a transmission one.

Transmission-Type (Two-Port) Resonator. This case corresponds to a resonator placed between input and output ports. On resonance, the signal is mainly transmitted through the cavity [CPF+22][8] (Fig. 2.4.c)

$$S(\omega) = \begin{bmatrix} S_{11}(\omega) & S_{12}(\omega) \\ S_{21}(\omega) & S_{22}(\omega) \end{bmatrix} = \begin{bmatrix} 1 - \dfrac{\kappa_{e1}}{i(\omega - \omega_0) + \kappa/2} & \dfrac{\sqrt{\kappa_{e1}\kappa_{e2}}}{i(\omega - \omega_0) + \kappa/2} \\ \dfrac{\sqrt{\kappa_{e1}\kappa_{e2}}}{i(\omega - \omega_0) + \kappa/2} & 1 - \dfrac{\kappa_{e2}}{i(\omega - \omega_0) + \kappa/2} \end{bmatrix}, \tag{2.46}$$

[7] https://gitlab.tudelft.nl/steelelab/technical-note-fano/-/tree/7ccee74ba3c4508587f59068b454c4e019d5e777/

[8] Referred as "Necklace-type $\lambda/2$ resonator".

where $\kappa = \kappa_i + \kappa_{e1} + \kappa_{e2}$. This matrix captures both reflection at each port (diagonal terms) and transmission through the resonator (off-diagonal terms). Transmission shows a Lorentzian peak near resonance of magnitude set by the coupling efficiency κ_e/κ. On resonance, the total distance between the peak maximum and the 0 dB level is referred to as the insertion loss L_0. An ideal, uncoupled resonator cannot receive any signal, meaning $L_0 = -\infty$ dB, while a resonator with infinitely strong coupling behaves like a transmission line, exhibiting no loss, i.e. $L_0 = 0$ dB. In the general case [GFB+08]

$$L_0 = -20 \log_{10} \left(\frac{r}{r+1} \right) \text{ dB}, \tag{2.47}$$

with r the external to internal decay rates ratio in Eq. 2.40.

This configuration is commonly implemented with deliberately asymmetric couplings, i.e. a weakly coupled input port and a strongly coupled output port, so that most intracavity power is directed to the amplifier. Nevertheless, the symmetry of the scattering matrix ensures that $S_{21} = S_{12}$ even when $\kappa_{e1} \neq \kappa_{e2}$. The only fittable parameters in this formula are ω_0 and κ. Since the numerator is constant, it will be entirely masked by the amplification coefficient.

Hanger-Type (Single-Port) Resonator. This is effectively a side-coupled transmission resonator[9]: instead of reflecting everything back to the source, the resonator "hangs" off the feedline like a shunt element. In this case, the through transmission shows a notch (dip) at resonance [CPF+22][10](Fig. 2.4.d)

$$S(\omega) = \begin{bmatrix} S_{11}(\omega) & S_{12}(\omega) \\ S_{21}(\omega) & S_{22}(\omega) \end{bmatrix} = \begin{bmatrix} -\dfrac{\kappa_e/2}{i(\omega-\omega_0)+\kappa/2} & 1 - \dfrac{\kappa_e/2}{i(\omega-\omega_0)+\kappa/2} \\ 1 - \dfrac{\kappa_e/2}{i(\omega-\omega_0)+\kappa/2} & -\dfrac{\kappa_e/2}{i(\omega-\omega_0)+\kappa/2} \end{bmatrix}. \tag{2.48}$$

Here, $\kappa = \kappa_i + \kappa_e$, with a single external coupling rate to the bus waveguide. In this configuration the magnitude $|S_{21}|$ shows a dip similar to the reflection case, but with an important difference: the polar plot of S_{21} never encloses the origin. The transmission only vanishes in the limit of infinitely strong coupling. On resonance, $S_{21}(\omega_0) = 1 - \kappa_e/\kappa$ so that $\kappa_i = S_{21}(\omega_0) \cdot \kappa$. Also in this case, as for the reflection configuration, ω_0, κ_i and κ_e can be fitted.

2.4.4 Photon number

The average photon number $\langle n \rangle$ stored in a resonator mode is proportional to the energy stored divided by the photon energy $\hbar\omega$.

For a single-port resonator with input power P_{in} (in W) at frequency $\omega/2\pi$, the average intracavity photon number is given by

$$\langle n(\omega) \rangle = \frac{P_{\text{in}}}{\hbar\omega} \cdot \frac{4\kappa_e}{(\kappa_e + \kappa_i)^2 + 4(\omega - \omega_0)^2}; \tag{2.49}$$

for a double-port resonator driven on one port and with symmetric κ_e

[9] This is a single port resonator, but probed in a two port configuration.

[10] Referred as "Hanger-type $\lambda/4$ resonators"; the above relations also hold for a hanger-type $\lambda/2$ resonator.

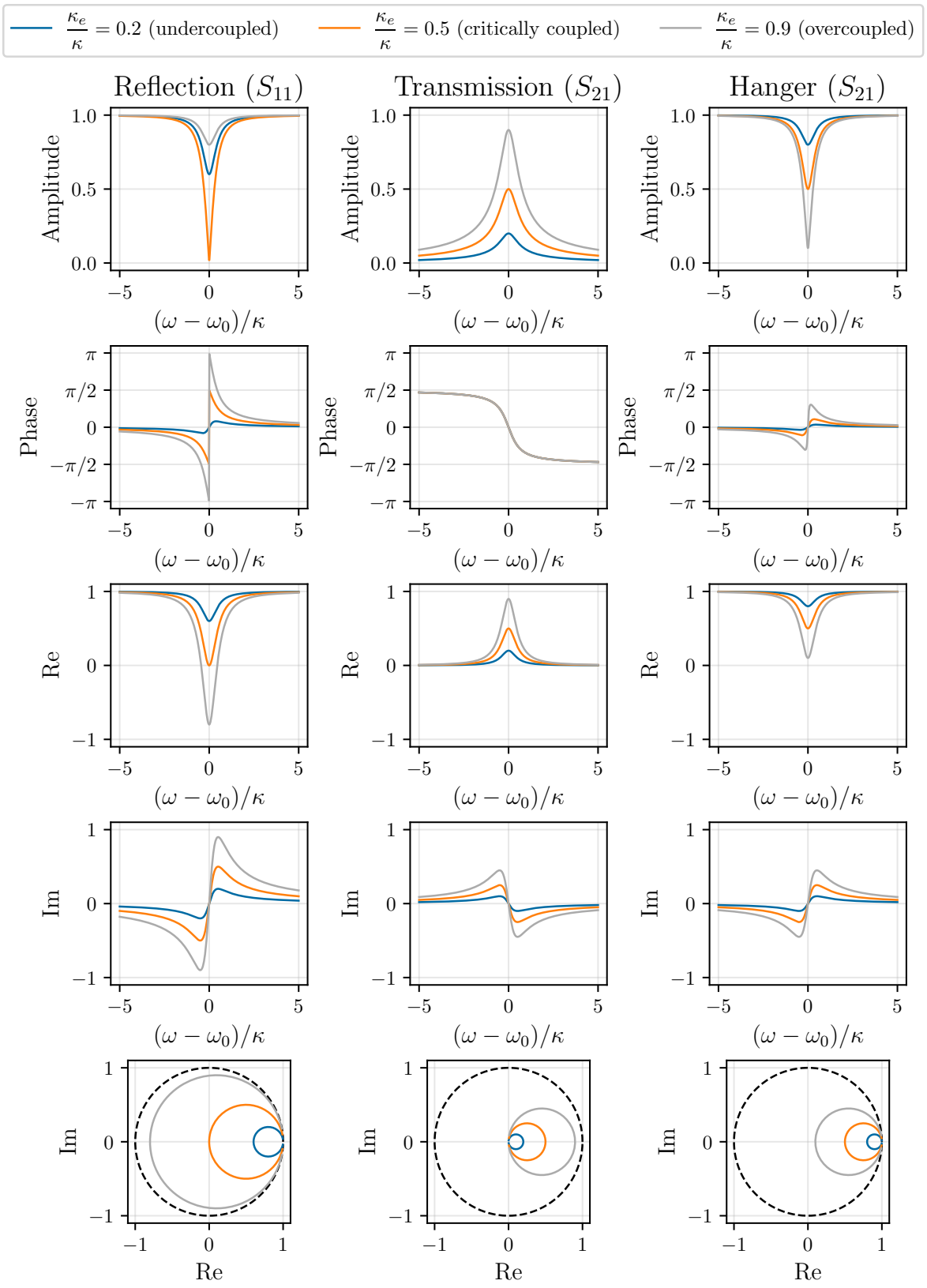

Figure 2.5: **S-parameter responses of microwave resonators.** Responses are shown for different resonator configurations and coupling regimes. Columns correspond to: Reflection resonator (S_{11}), Transmission resonator (S_{21}), and Hanger resonator (S_{21}). Reflection signals for the resonators in Transmission and Hanger configurations are simply $1 - S_{21}$. Rows show Amplitude, Phase, Real and Imaginary part plots. Three coupling regimes are illustrated: undercoupled ($\kappa_e/\kappa = 0.2$, blue), critically coupled ($\kappa_e/\kappa = 0.5$, orange), and overcoupled ($\kappa_e/\kappa = 0.9$, gray), with normalized frequency detuning $(\omega - \omega_0)/\kappa$ on the horizontal axis.

$$\langle n(\omega)\rangle = \frac{P_{\text{in}}}{\hbar\omega}\cdot\frac{\kappa_e}{(\kappa_e+\kappa_i/2)^2+(\omega-\omega_0)^2}; \tag{2.50}$$

and for a single-port resonator in hanger configuration

$$\langle n(\omega)\rangle = \frac{P_{\text{in}}}{\hbar\omega}\cdot\frac{\kappa_e}{(\kappa_e+\kappa_i)^2+4(\omega-\omega_0)^2}. \tag{2.51}$$

2.4.5 Impact of measurement setup on ideal lineshapes

Even when working with the symmetric resonance responses described above, experimental realities in cryogenic setups complicate the interpretation of measured data. Three common sources of deviation from the ideal case are discussed below.

Running phase. The resonator is never connected directly to the vector network analyzer (VNA), but instead through long coaxial cables. These cables introduce a frequency-dependent phase shift of the form $\phi = \omega t$, where t is the signal propagation delay. For a dispersionless cable, this delay can be approximated by $t = \ell/v_g$, with ℓ the physical cable length and v_g the group velocity of the electromagnetic mode in the cable. In the simplest case, the additional phase therefore increases linearly with frequency.

Unitary transmission. A more challenging issue arises from the often poorly known gain and loss in the microwave chain between the VNA and the device. Signal attenuation occurs at multiple stages: all coaxial cables introduce a few dB of loss, cryogenic cables can add temperature-dependent attenuation, and large amounts of intentional attenuation are placed on the input line to suppress room-temperature noise. On the return path, the signal passes through further elements such as cryogenic circulators, isolators, and one or more high-gain low-noise amplifiers. The microwave wiring is also interrupted repeatedly for thermalization, each break introducing connectors or fixed attenuators.

Because impedance matching is never perfect, these components produce weak standing waves along the line, causing frequency-dependent ripples in the measured transmission, around $1-4\ \mathrm{dB}$. As a result, the measured transmission baseline can fluctuate significantly, making it impossible to assign a precise value of "unity transmission".

In practice, the reference level is determined experimentally: for reflection and side-coupled configurations, the S-parameter measured far from resonance defines the normalization point. This method assumes that zero transmission is unaffected by the measurement chain, which is generally true if the setup introduces only loss and phase.

Crosstalk. In addition to overall gain and phase distortions, microwave setups often exhibit crosstalk between the input and output, which can mimic or distort the resonator response. In this case, part of the drive signal bypasses the resonator entirely and recombines with the cavity output, producing interference effects analogous to the classic Fano resonance [Fan61].

There are several physical origins for such unwanted signal leakage [RGS+23]:

- Reflections within the shared cable segment of a reflection measurement, i.e. between the device and the first circulator or directional coupler.

- Finite isolation of circulators, or limited directivity of directional couplers.
- Parallel electromagnetic pathways between input and output ports in side-coupled or end-coupled devices, e.g. slotline modes on-chip, box modes of the sample enclosure.

The general effect is that a small fraction of the input signal, of amplitude q relative to the cavity path, is added to the cavity output with an additional phase shift ϕ. If the device response is $S(\omega)$, then the measured signal takes the form [RGS+23]

$$S_{\text{meas}}(\omega) = A\left(be^{i\phi} + (1-b)S(\omega)\right), \tag{2.52}$$

where A is a normalization constant chosen such that $|S_{\text{meas}}| = 1$ far from resonance.

This coherent interference between the direct path and the resonator output is the origin of the asymmetric, Fano-like lineshapes often observed in practice. It also explains why simple normalizations are insufficient when crosstalk is significant: both the apparent unity level and the zero reference can be altered by parasitic paths.

Python libraryes to fit complex resonator scattering data are available, for instance, at Refs. [Pro15; Reg23].

CHAPTER 3

Superinductance

3.1 Introduction

The fine-structure constant is defined as $\alpha = e^2/(4\pi\varepsilon_0\hbar c_0) = Z_{\text{vac}}/(8R_Q) \approx 1/137$, with Z_{vac} the impedance of free space, and R_Q the superconducting resistance quantum and it is a dimensionless measure of the strength of the electromagnetic interaction. It quantifies how strongly charged particles couple to the electromagnetic field[1]. Because α is small, electromagnetic interactions are comparatively weak, which in superconducting circuits translates to a limit on the response of charge carriers to electric fields. Specifically, the small value of α restricts how rapidly current can change in response to voltage, setting a bound on the maximum geometric inductance L_g. Since the characteristic impedance of a circuit is given by $Z_C = \sqrt{L/C}$, a bound on L_g implies that the Z_C coming purely from the circuit geometry is limited as well, and in practice $Z_C \ll Z_{\text{vac}}$ (see Section 4.1 for a discussion of the subtleties and limitations of this statement).

Consequently, quantum circuits are typically found in a regime where the characteristic impedance is too small to suppress charge fluctuations. This means that charge is highly delocalized, while the conjugate variable, the superconducting phase, remains relatively well defined. Thus, the smallness of α underpins why superconducting circuits naturally tend to exhibit large charge fluctuations rather than phase fluctuations.

This imbalance poses a central challenge in quantum electronics: creating circuit environments that suppress charge fluctuations to stabilize quantum states, which requires specially engineered high-impedance elements. In practice, this means achieving a characteristic impedance much higher than the superconducting resistance quantum R_Q.

Early attempts to create high-impedance environments used on-chip resistors [KH91; LBZN03] and Josephson junction arrays operated in dissipative regimes [CGHH06b; CGHH06a], introducing dissipation and not effectively screening offset charges. The idea of a superinductance[2], i.e. a purely reactive component with high characteristic impedance, was practically realized only with the development of the fluxonium qubit in the group of M. Devoret in Yale [MKGD09; Man12; MPK+12], using a chain of Josephson junctions.

[1] The original physical interpretation of α is that it represents the ratio of the speed of an electron in the first Bohr orbit of a hydrogen atom to the speed of light in vacuum: "Das Verhältnis v_1/c nennen wir α" (the ratio v_1/c we call α) [Som21].

[2] The term was originally introduced in an unpublished work by A. Kitaev [Man12].

Definition. A superinductor is a passive, two-terminal electrical component that combines zero DC resistance with a characteristic impedance, at the frequency of interest, much larger than the resistance quantum:

$$R = 0, \quad |Z_C| \gg R_Q. \tag{3.1}$$

The impedance is purely reactive and given by $Z_C = iX = i\sqrt{L_{\text{tot}}/C_{\text{stray}}}$, where X is the system's reactance. The resistance quantum is defined as (see Section 2.1.1)

$$R_Q = \frac{\Phi_0}{2e} = \frac{h}{(2e)^2} \approx 6.45 \text{ k}\Omega. \tag{3.2}$$

In the context of quantum circuits, R_Q represents the natural resistance scale, determined by the ratio of the flux quantum Φ_0 to the Cooper pair charge $2e$. Notably, this quantum resistance is much larger than the vacuum impedance $Z_{\text{vac}} = \sqrt{\mu_0/\varepsilon_0} \approx 377\ \Omega$, which is defined by the ratio of the vacuum's magnetic permeability to its electric permittivity.

For practical applications, a superinductor must have a self-resonance frequency in the GHz range[3] to ensure the system stays in its ground state at millikelvin temperatures, which are typical operating conditions for quantum devices. It should have low loss and behave as a near-ideal, lumped, linear inductor throughout its operational bandwidth, even under strong driving to guarantee stable and predictable circuit performance. Additional desirable features include ease of fabrication and reliable operation under diverse conditions, such as strong magnetic fields applied in hybrid systems to control two-level systems.

Applications. The two main characteristics of a superinductor for practical applications are its ability to suppress charge fluctuations and to produce large voltage fluctuations. At first glance, these two requirements might seem contradictory, since suppressing charge fluctuations usually implies stabilizing the voltage, whereas producing large voltage fluctuations suggests the opposite. The key to resolving this apparent contradiction lies in the capacitance: in most relevant implementations, the capacitance associated with the superinductor is extremely small. Because the capacitance is so small, the relation $V = Q/C$ implies that even tiny charge fluctuations Q result in significant voltage fluctuations. Thus, while the inductive response of the superinductor suppresses the magnitude of charge fluctuations, the small capacitance converts those residual fluctuations into appreciable voltage variations. This is not a contradiction, but rather a direct consequence of operating in the regime of very low capacitance.

Hardware-protected qubits. To achieve high coherence in superconducting qubits, a successful strategy relies on sacrificing qubit anharmonicity by shunting the junction with a large capacitance, as in the transmon [KYG+07] and C-shunt flux qubit [YGK+16]. In these systems, dynamics are dominated by multi-Cooper-pair tunneling (Q_{zpf} is large), resulting in weak anharmonicity and suppressed sensitivity to charge noise. In contrast, the fluxonium qubit preserves strong anharmonicity by leveraging single-Cooper-pair charging effects, made possible through a different design strategy: shunting the junction with a large inductance rather than a large capacitance [KMDG09].

Because flux-based qubits couple to the environment through the phase operator, high coherence requires their quantum states to be delocalized in phase space, minimizing their

[3] This constraint provides insight into the typical inductance and capacitance values involved. Since the capacitance of a millimeter-long wire is on the order of picofarads, the required inductance falls within a few microhenries.

overlap with localized environmental noise. A large inductor allows this delocalization by raising the impedance of the circuit, reducing sensitivity to both phase noise and environmental coupling. At the same time, the inductive shunt suppresses charge sensitivity, providing a dual-protection mechanism for qubit coherence without compromising anharmonicity.

Hardware-protected qubits, such as fluxonium [GMDP+21], the 0–π qubit [GDPK+21], bifluxon [KHZ+20; MLC+24; ALK+24], $\cos(2\phi)$ [SKX+20], and $\cos(\mu\phi)$ elements [SVM+22], quasicharge qubits [PMN+20; PHS+21], and inductively shunted transmons [HPK+23], as well as emerging error-correction protocols [KBDG24; SSL+25], exploit symmetry and high impedance for intrinsic error suppression. These circuit implementations enable access to the dual Josephson physics regime [MH05; AIK+12; PCvHK25].

Dual Josephson physics. The behavior of Josephson junctions depends strongly on the surrounding electromagnetic circuit. In a low-impedance environment, fluctuations of the superconducting phase difference are small, and the system behaves in a mostly semi-classical way. When the impedance is high, these phase fluctuations grow, and the system starts to deviate from the semi-classical picture, opening the way to observing quantum effects that are dual to the standard Josephson effects [MN06].

In this situation, the low-energy spectrum of a Josephson junction can be modeled as a nonlinear capacitance that is periodic in charge; such a system is referred to as a quantum phase-slip element. Observing this behavior requires suppression of charge fluctuations, which is achieved by incorporating a superinductor in the circuit connected to the Josephsn junction. The large inductive reactance enables flux tunneling events that give rise to phase slips. At low enough bias frequencies, such as in DC measurements, quantum phase slips suppress charge transport, leading to insulating behavior in superconducting circuits [Sch83; Bul84; HKDC91; PPH+99] while at higher frequencies they can induce phase locking of Bloch oscillations to an external AC drive [AZL85; KH91]. Measuring the DC current–voltage characteristic in presence of an external frequency drive reveals quantized current values at integer multiples of the driving frequency, known as dual Shapiro steps [KH91; SKD+22; CCG+23; KKG+24; SKD+24]. This establishes a direct, quantized relationship between current and frequency, contributing to the closure of the metrology triangle [GS19]: in principle, all three electrical quantities, voltage, current, and frequency, can be defined through quantum effects, enabling consistency tests of their interrelations [SAK+24].

Coupling to hybrid systems [XAYN13; BGMP20; CLB+20]. Incorporating a superinductor into a resonator allows the design of compact, high-impedance microwave modes that exhibit large vacuum voltage fluctuations per photon $V_{\mathrm{zpf}} \propto \sqrt{Z_C}$ (Eq. 2.12). These fluctuations enhance the coupling strength to systems with intrinsically small electric dipole moments or weak field overlap, such as polar molecules[4] [RDD+06; ADD+06], quantum dots [VDCK15; SBS+16; SSK+17; MBP+18; JRBE+25], electron on superfluid helium [SFD+10; KYS19; KGB+25], and mechanical degrees of freedom [AAWP+18; AWB+20]. Building on the general principle that high-impedance resonators enhance vacuum voltage fluctuations and thus coupling to hybrid systems, the focus now shifts to more specific applications. In particular, increased impedance can be exploited to enhance the direct coupling strength g in parametric interactions, the dispersive interaction χ in the off-resonant regime, and the cooperativity $\mathcal{C}$ governing quantum transduction efficiency.

[4] In Ref. [DM04] the energy splitting between the two quantum states in an RF-SQUID qubit is described as bearing a close resemblance to the dynamics of the ammonia molecule, where a similar tunnel splitting effect occurs.

Parametric interactions, used to create time-dependent and tunable couplings, can benefit from increased impedance. In these schemes, a circuit parameter such as inductance or capacitance is modulated by a secondary system or external drive. For example, in a capacitor C with a mechanically movable electrode, mechanical displacement can shift a cavity's frequency $\omega_0(x)$, creating a coupling of the form $g_0(\hat{a}+\hat{a}^\dagger)(\hat{b}+\hat{b}^\dagger)$, where $g_0 = (\partial\omega_0/\partial x)x_{\mathrm{zpf}}$ is the frequency shift resulting from a displacement associated with half a photon [FKP+16]. Here, $\partial\omega_0/\partial x \propto \omega_0/C$, which is maximized. fixed the frequency, by increasing the inductance, and consequently the characteristic impedance. Higher impedance allows even minute physical displacements (or flux modulations [XHF+19]) to induce significant interactions.

When the detuning between a system and an electromagnetic field greatly exceeds their coupling strength, the interaction is described by the dispersive regime: two quantum systems interact without exchanging real excitations, instead influencing each other through virtual processes. This interaction is captured by the term $\chi\hat{a}^\dagger\hat{a}\hat{b}^\dagger\hat{b}$, where χ represents the dispersive coupling strength. The magnitude of χ scales as $\chi \propto g^2/\Delta$ [BGGW21], with g the coupling rate and Δ the detuning between system frequencies. Since $g \propto \sqrt{Z_C}$[5], high impedance directly enhances χ. This is critical for enabling quantum non-demolition measurements and frequency-based readout mechanisms in hybrid systems, particularly where bringing the subsystems into resonance is not possible due to coherence constraints or thermal population issues.

Also in the context of quantum transduction, i.e. the coherent transfer of quantum states between different frequency domains, an important requirement is to achieve strong coupling between subsystems that often have mismatched characteristics. The efficiency of transduction is governed by the cooperativity $\mathcal{C} = g^2/(\kappa\gamma)$, where κ and γ are the decay rates of the resonator and the hybrid element, respectively. In many cases, $\mathcal{C} \ll 1$ due to inherently weak g. High-impedance resonators can increase g, thus enhancing $\mathcal{C}$ and improving transduction efficiency [SHR+22]. Additionally, maintaining resonator linearity is important when applying strong pump fields, as it allows a large number of photons to drive the system without shifting the resonance or introducing nonlinear effects.

Ultra-strong coupling physics. The interaction strength between a qubit and a resonator is a critical parameter that determines the speed of gate operations and the fidelity of readout. In the ultrastrong coupling regime (typically $g/\omega_0 \gtrsim 0.1$ [BGS+17a; BGS+17b; FDLR+19; FKMDL+19; Red22]), standard Jaynes-Cummings approximations no longer hold, enabling processes that violate excitation number conservation. As a result, the ground state of the system can contain virtual excitations. This opens the possibility to study rapid and robust quantum information processing, enhanced nonlinear optical effects, and various new quantum phenomena hardly achievable with other platforms [JXGRR16; FKMDL+19; TCCGdPM+25].

3.2 Implementation

To achieve a high characteristic impedance, a circuit must combine large inductance with minimal parasitic capacitance. Superinductors, to meet these requirements, can be realized through various approaches, each enhancing inductance beyond that of a standard electrical circuit. Examples include arrays of Josephson junctions connected in series, superconducting

[5] The interaction is of the dipole type, where V_{zpf} represents the electric field amplitude associated with a single photon. The coupling strength g is proportional to V_{zpf}, which in turn scales with the resonator impedance as $V_{\mathrm{zpf}} \propto \sqrt{Z_C}$ (see Eq. 2.12).

materials with high kinetic inductance, and miniaturized aluminum spirals suspended on a silicon membrane. Complementary techniques for reducing parasitic capacitance further improve performance, enabling the full realization of high-impedance behavior.

3.2.1 Ways to increase the inductance

Most traditional inductors rely on magnetic self-inductance (geometric inductance, L_g), which originates from Faraday's law and is related to the magnetic energy generated by the current flow. For a straight conductor, L_g scales linearly with length ℓ and only logarithmically with wire radius r [Ros08][6]:

$$L_g = \frac{\mu_0}{2\pi}\ell\left[\ln\left(\frac{2\ell}{r}\right) - 0.75\right], \tag{3.3}$$

with typical values being on the order of $\sim 1\ \mathrm{pH}/\mu\mathrm{m}$ [Ann10].

An alternative is to use kinetic inductance L_k, which arises from the kinetic energy of charge carriers. In nanoscale wires, L_k scales with length ℓ and inversely with cross-section area A, besides depending on the material properties.

In a normal metal, electrons do not respond instantaneously to an applied electric field. When the field oscillates at a frequency f, the electrons need time to accelerate and change direction. If the frequency becomes high enough, specifically when $f > 1/\tau$, where τ is the momentum relaxation time (how long an electron typically moves before scattering), this lag becomes significant. In typical metals at room temperatures, $\tau \sim 10^{-14}\ \mathrm{s}$ [KZA+20], so the corresponding frequency threshold is in the THz range [Ann10], meaning kinetic inductance only matters at very high frequencies. In superconductors, scattering is negligible, and as a result resistance vanishes and the kinetic inductance becomes significant at any frequencies [Mes69], making it a crucial effect for superconducting circuits. This lag effectively stores energy in the motion of charge carriers, analogous to how energy is stored in a moving mass.

Typical values for L_k depend on the material and can go up to $\sim 1\ \mathrm{nH}/\mu\mathrm{m}$.

The next paragraphs will explore various strategies to enhance inductance, including leveraging the Josephson inductance, employing kinetic inductance in disordered materials, and using the geometric inductance of planar spiral structures.

Josephson junction chains. Given their fundamental role in superconducting qubits, Josephson junctions are often arranged in a series of large junctions to form superinductors. The Josephson inductance L_J is a nonlinear inductance coming from the voltage–current relation intrinsic to the Josephson effects and it is given by

$$L_J(\varphi) = \frac{\Phi_0}{2\pi(J_c \cdot A)\cos(\varphi)}, \tag{3.4}$$

where Φ_0 is the flux quantum, $I_c = J_c \cdot A$ is the critical current and φ is the superconducting phase difference across the junction. L_J can be seen as a lumped inductance due to Cooper pair tunneling across a junction whose value depends on junction parameters such as the critical current density J_c and the junction area A.

When designing an array of N identical junctions with total inductance $L_{\mathrm{J,chain}} = N \cdot L_J$, the goal is to have the highest inductance per junction, within the linear inductive regime

[6] For very high frequencies, skin effects causes the factor 0.75 to approach 1.

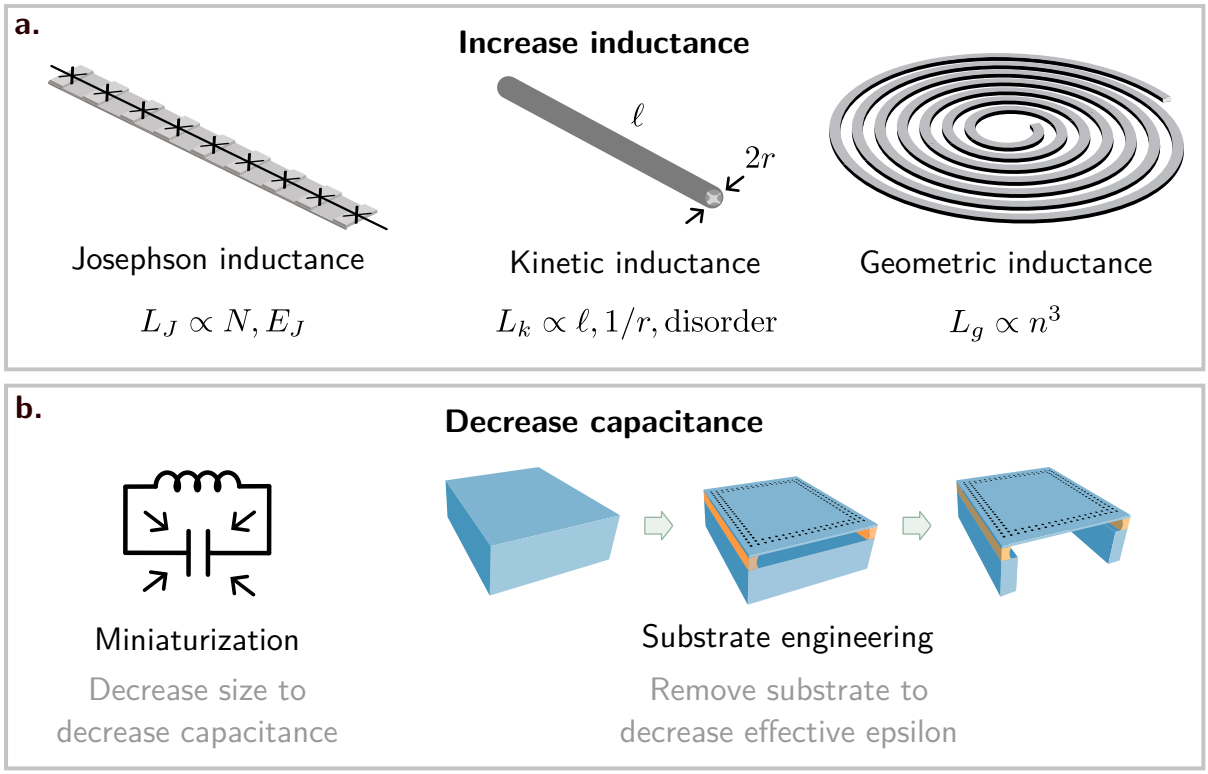

Figure 3.1: **Strategies for increasing characteristic impedance in resonant circuits.** Characteristic impedance scales as $Z_C \propto \sqrt{L/C}$, highlighting the need to maximize inductance L and minimize capacitance C. Panel **a.** illustrates increasing inductance through Josephson inductance $L_J \propto N, E_J$, where N is the number of junctions and E_J the Josephson energy, kinetic inductance L_k, which depends on carrier inertia and conductor geometry, and geometric inductance $L_g \propto n^3$, with n being the number of spiral turns. Panel **b.** shows capacitance reduction by miniaturizing circuit dimensions to lower geometric capacitance and substrate engineering that replaces high-permittivity materials (ε) with air or vacuum ($\varepsilon \approx 1$) to reduce stray capacitance.

and with the fundamental mode of the chain far from the operating frequencies [Ear19]. Increase L_J comes at the cost of stronger nonlinear behavior, which is influenced by the junction's physical dimensions: smaller junctions restrict supercurrent flow more, amplifying this effect. Optimizing junction size therefore involves a trade-off between inductance and linearity. Alternatively, one can increase the number N of junctions in a chain, though this lowers the fundamental resonance frequency and limits the range over which the device acts as an ideal inductor.

A way to estimate the nonlinearity is by evaluating the expected phase-slip rate [RHDP+24], which provides an upper bound on how frequently quantum phase slips may occur across a junction. For a chain, in the limit $E_J \gg E_C$ this rate is given by [MLG02]:

$$\Gamma_{\text{QPS}} = 4N\sqrt{\pi}\left(E_J^3 E_C\right)^{1/4} \exp\left(-8\sqrt{\frac{E_J}{E_C}}\right), \tag{3.5}$$

where $E_J \propto A$ and $E_C \propto 1/A$ are the Josephson and single electron charging energies of an individual junction, respectively. Fig. 3.2 shows Γ_{QPS} as a function of E_J and E_C. To preserve a linear inductive response, the junction area is chosen large enough to suppress phase slips; a common rule of thumb is $E_J/E_C > 20$, the transmon regime. Moreover, linearity

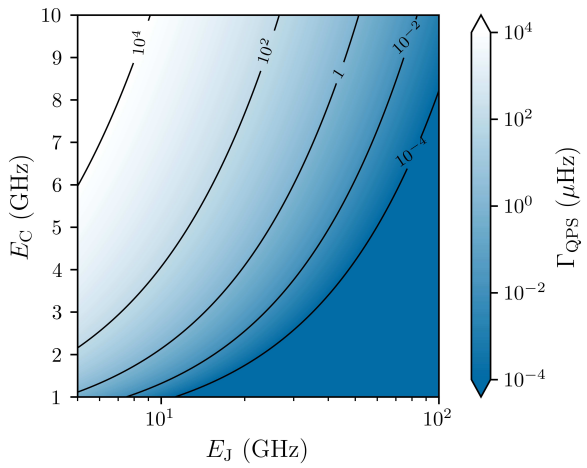

Figure 3.2: **Quantum phase-slip rate as a function of Josephson and charging energies.** The phase-slip rate is plotted as a function of Josephson energy E_J and charging energy E_C, with isolines indicating constant rates.

can also be compromised when a Josephson junction is embedded in a superconducting loop, with a geometric inductance comparable to the junction's Josephson inductance. In this case, the screening currents in the loop strongly affect the junction phase, making the flux–phase relation multivalued. This results in undesirable hysteresis, where the state of the circuit depends on its history rather than only on the applied flux. Another measure of nonlinearity is given by the Kerr coefficients. These parameters characterize the frequency shift of a resonator mode due to photon occupation, either within the same mode (self-Kerr) or in a different mode (cross-Kerr). They are particularly useful for understanding nonlinear phenomena such as bistability in Josephson junction arrays [MGM+18].

In early fluxonium implementations [MKGD09], the Josephson junction chain was short enough to be treated as a lumped-element inductor. However, increasing the inductance by lengthening the chain shifts its modes to lower frequencies, making their influence non-negligible: this can have deleterious effect on fluxonium readout [SRCR25] and coherence [VC15].

The main results in the literature on Josephson junction chains as low-loss high inductance elements are Refs. [MPK+12; BSI+12; PMN+20; JCN+25; M+25].

Using arrays of DC-SQUIDs [ELJ+13] or a DC-SQUID composed of Josephson junction chains [Wes20], both relying on the idea of achieving a diverging inductance for specific external flux values, does not work in practice because of phase slips. In the former case, this is explained by the fact that E_J/E_C effectively becomes small with increasing flux, leading to a higher phase-slip rate and thus jeopardizing the whole approach. similar reasoning applies to the latter case as well.

Ref. [NB17] presents a theoretical analysis of the low-frequency impedance of a Josephson junction chain with spatially varying parameters. When junction areas are varied, the optimal configuration, meaning the one that maximizes the total inductance of the chain without reducing the low-frequency window where the chain behaves as an inductor, remains a spatially uniform chain. However, using DC-SQUIDs with differing loop areas, which allows inductance tuning via an applied magnetic field, shows some improvement, although this advantage decreases as the chain length increases.

High kinetic inductance material. The kinetic inductance of a superconducting nanowire can be determined by equating the kinetic energy of all Cooper pairs in the wire to the magnetic energy stored in an equivalent inductor [ASF+10]

$$n \cdot \ell w t \cdot \frac{1}{2} m v^2 = \frac{1}{2} L_k I^2, \tag{3.6}$$

leading to the expression for the kinetic inductance as:

$$L_k = \left(\frac{m_e}{2e^2 n}\right) \cdot \left(\frac{\ell}{wt}\right), \tag{3.7}$$

where m_e is the electron mass, e is the electron charge, and n represents the Cooper pair density. The second term is a geometric factor that depends on the wire's length ℓ, width w, and thickness t.

A convenient way to express the kinetic inductance is in terms of inductance per square [Tin04]

$$L_{k,\square} = \frac{\hbar R_\square}{\pi \Delta(0)}, \tag{3.8}$$

where $R_\square$ is the sheet resistance in the normal state, $\Delta(0) = 1.76\ k_B\ T_C$ the superconducting energy gap at zero temperature and the number of squares is represented by the factor ℓ/w.

The two terms in brackets in Eq. 3.7 are the two independent knobs to boost the impedance.

Increasing the length ℓ, while reducing the width w and thickness t of the nanowire, raises its inductance. However, a longer wire also increases capacitance (even if not as much as the kinetic inductance), and thinner, narrower films are more susceptible to material inhomogeneities.

Charge carrier density n is an intrinsic property of the material of choice. Increasing disorder, n reduces the superfluid stiffness near the disorder-driven superconductor-to-insulator transition (SIT) and can lead to the appearance of subgap delocalized modes and increased microwave-frequency dissipation [FI18; SPG+25]. Several material commonly used for such applications include: niobium nitride (NbN)[7], titanium nitride (TiN), niobium-titanium nitride (NbTiN) and granular aluminium (grAl). Additionally, materials known as dirty superconductors, characterized by high impurity content and belonging to the type-II class, typically exhibit reduced n and thus higher kinetic inductance [SPG+25].

Kinetic inductance is also sensitive to temperature. At low temperatures, where n is maximal, L_k reaches its minimum value. As the temperature approaches the critical temperature T_C, the Cooper-pair density vanishes and L_k diverges. Physically, this reflects the fact that with fewer charge carriers available, each carrier must move faster to sustain a given current, and since the kinetic energy grows with the square of velocity, the effective inductance increases sharply. The kinetic inductance is modeled within the BCS framework [ASF+10] as

$$L_k = \frac{\ell}{w} \frac{R_\square \hbar}{\pi \Delta(T)} \coth\left(\frac{\Delta(T)}{2k_B T}\right), \tag{3.9}$$

$$= L_k(0) \frac{\Delta(0)}{\Delta(T)} \coth\left(\frac{\Delta(T)}{2k_B T}\right). \tag{3.10}$$

[7] Special mention for the atomic layer deposited NbN thin films [LZA+17; KZL+21], that allowed the observation of dual Shapiro steps for the first time.

To obtain the temperature dependence of the superconducting gap $\Delta(T)$, one must solve the BCS gap equation numerically [Tin04], but various approximations can be found, such as [She66]

$$\Delta(T) = \Delta(0) \cdot \sqrt{\cos\left(\frac{\pi}{2}\left(\frac{T}{T_C}\right)^2\right)}, \tag{3.11}$$

or [KCB+24]

$$\Delta(T) = \Delta(0) \cdot \sqrt{1 - \left(\frac{T}{T_C}\right)^4}. \tag{3.12}$$

with $\Delta(0) = 1.76\ k_B\ T_C$.

In addition to temperature, the Cooper pair density also depends on the applied current. This nonlinearity is often described by a power series expansion [ASB89; Ann10; SKE+21; GPK+22]:

$$L_k(I) = L_k(0) \cdot \left[1 + \left(\frac{I}{I^*}\right)^2 + \ldots\right]. \tag{3.13}$$

The geometry and intrinsic properties of the superconductor determine the value of I^*. At currents approaching the nonlinear current I^*, there is a marked decrease in n [APE03], resulting in a corresponding increase in L_k. This current-induced nonlinearity causes a downshift in the resonant frequency of superconducting resonators and can lead to resonance bifurcation. Interestingly, this effect enables parametric amplification, allowing weak signals to be amplified with high gain and minimal added noise [VEK+16].

Mechanical strain, tensile or compressive, can significantly alter superconducting nanowire properties by modifying lattice parameters and electron–phonon coupling. Experiments on Al, NbN, and hybrid semiconductor–superconductor nanowires report strain-induced shifts in T_C [AGL+19], I_C and phase-slip rates, effects amplified by the high surface-to-volume ratio and mechanical compliance of nanowires.

Superconducting nanowires are widely used in Kinetic Inductance Detectors (KIDs) for astronomy [d'A14] and quantum information [FSM+24], where their sensitivity to quasiparticles allows monitoring the purity of the microwave environment and protecting qubit coherence. This high sensitivity arises from the fact that current in nanowires is carried by Cooper pairs (superfluid) and thermally excited quasiparticles (normal fluid). At low temperatures, Cooper pairs dominate, giving near-zero resistance, but increasing temperature breaks pairs, reducing the superfluid density and increasing quasiparticle contributions, which in turn affects L_k and the nanowire's response. Materials used for KIDs, including WSi [MVS+13; L+25], are being actively considered for optimizing performance.

The phase-slip rate in a kinetic-inductance material with moderate disorder is approximately given by [AGZ08; AIK+12]:

$$\gamma_{\mathrm{QPS}} \approx \frac{\Delta(T)}{\hbar}\frac{R_Q}{R_\xi}\frac{\ell}{\xi}\exp\left[-A\frac{R_Q}{R_\xi}\right], \tag{3.14}$$

where $\Delta(T)$ denotes the superconducting energy gap, R_ξ is the resistance of a wire segment of length ξ, ℓ is the total wire length, R_Q represents the quantum of resistance, and A is a dimensionless numerical factor. It increases linearly with the wire length, but it is exponentially

sensitive to the resistance R_ξ. Utilizing this property, it is possible to engineer a highly inductive wire with minimal phase slips by making the wire sufficiently long, which is beneficial for realizing large kinetic inductance in a fluxonium circuit. However, this strategy requires consideration of the inductor's chain modes.

In very strongly disordered superconductors, electrons form localized pairs even without global superconducting coherence, and superconductivity emerges only through Cooper pair hopping between these localized states [AIK+12].

L_g from self-coupling of adjacent turns. Another method to increase the inductance is to exploit the coil geometry: it offers a distinct advantage over a straight wire or meander: it exploits the mutual inductance between adjacent turns to enhance the total inductance, thereby increasing the impedance without increasing the physical length of the wire. In contrast, a straight wire or simple meander relies solely on the geometric inductance of its length, which is typically much smaller. More details in Subsections 4.2.3 and 4.6.3.

3.2.2 Ways to decrease the capacitance

While increasing the inductance is the standard approach to raise a circuit's characteristic impedance, an alternative is to reduce its capacitance. For a straight wire of length ℓ, the capacitance C is given by

$$C \approx \frac{\pi \varepsilon_{\text{eff}}}{\log\left(d/r\right)} \ell. \tag{3.15}$$

It scales linearly with length and inversely with the logarithm of the distance to ground d, and also depends on the effective dielectric permittivity ε_{eff}; r is the wire radius. The two approaches considered are modifying the geometry, to ultimately decrease ℓ and d, and engineering the substrate, to reduce ε_{eff}.

Decrease circuit footprint. Capacitance is influenced by both materials and geometry, as it depends on how electric fields are distributed between conductors. When the size is reduced, the surface area and field spread decrease, reducing the stored energy and thus lowering capacitance. To minimize stray capacitance, both between parts of the superinductor and between the superinductor and ground, wires should be kept short and positioned away from the ground.

The main results reported in the literature on reducing capacitance and optimizing superinductor design are summarized in Refs. [Ear19; KLK+20; PTH+20; KSP+25; M+25].

Ref. [KLK+20] optimizes grAl meander inductors by varying the period Δb and aspect ratio b/h, where b and h are the lateral and longitudinal dimensions of the meander, respectively. The longitudinal dimension h corresponds to the orientation of the longer strips. Interestingly, square-shaped meanders do not maximize the resonance frequency f_0. While a square shape minimizes capacitance to ground for a given area, increasing the strip length h increases inter-strip capacitance. This trade-off leads to minimal stray capacitance when $b > h$. For the parameters simulated in Ref. [KLK+20], the optimized meander achieves a self-resonance frequency approximately twice that of a straight nanowire with the same total length and inductance.

Ref. [KSP+25] studies ring resonators made from grAl meanders, where capacitance is reduced by shrinking the outer radius. Approximating the ring as a coplanar capacitor, the capacitance

scales with the plate width and thus also with the inner radius: minimizing it therefore lowers the capacitance. Using the smallest possible meander pitch also contributes to reducing the overall capacitance of the resonator.

Ref. [PTH+20] shows that the capacitance of planar spiral inductors with filling factor approaching one scales as the external radius when the ground is far away. More details in Subsection 4.6.4.

In Refs. [Ear19; M+25], arranging the junctions into a compact vertical chain rather than a horizontal one significantly reduces the device footprint. This vertical stacking offers a more scalable alternative to other methods, such as suspending Josephson junction chains several micrometers above the substrate to replace the dielectric environment with vacuum.

Decrease electrical permittivity of the substrate. Even with careful design, inductance and capacitance typically scale together with wire length. Suspending the device from the dielectric substrate can reduce the capacitance without significantly affecting the inductance.

This strategy is fundamentally limited by the dielectric constant of vacuum, $\varepsilon_r = 1$. Typically, circuits are fabricated on a silicon substrate with $\varepsilon_r = 12$, and assuming that half of the electric field resides in air and half in the substrate, the effective dielectric constant is approximately $\varepsilon_{\text{eff}} = 6.5$. The resulting improvement in impedance scales as $\sqrt{\varepsilon_{\text{eff}}}$, which yields a maximum gain of only about 2.5.

Refs. [PTH+20; PMN+20; JCN+25] explore this approach.

Ref. [PMN+20] implemented suspended Josephson junction chains lifting off several micrometers above the substrate, but with one end still attached to it. By replacing the dielectric environment with vacuum, this configuration reduces the parasitic capacitance by a factor of $\sim \varepsilon_r/2$, where ε_r denotes the substrate's relative permittivity. It requires a fabrication process that is mechanically delicate and technically demanding, making the approach difficult to scale and integrate.

As highlighted in Ref. [JCN+25], the fabrication process used in Ref. [PMN+20] can lead to additional loss mechanisms or inadvertently damage surrounding components. Conventional etching techniques, such as XeF_2 etching, lack selectivity, suspending all aluminum structures, and are incompatible with widely used superconducting materials like Nb, Ta, TiN, and NbN. In contrast, selective substrate etching enables the suspension of specific components in aluminum-based planar superconducting circuits. A key advantage of this approach is its precision: individual regions can be etched while the majority of the silicon surface remains unetched and pristine. By analyzing the device's frequency spectrum, a mean reduction of approximately 74% in capacitance to ground is observed as a result of the etching process.

A process similar to that described in Ref. [JCN+25] was tested by me in 2022 to evaluate the feasibility of fabricating SQUID chains with a small single junction at the center, as studied in Ref. [WH03], on a SOI substrate. The motivation for this approach was to decrease the capacitance to ground of the chain by suspending it. The release test was successful, although no further optimization was carried out beyond the initial attempt. Fig. 3.3.a shows an optical image of a device suspended on a silicon membrane pierced with holes to allow the removal of the underlying silicon dioxide. Fig.s 3.3.b-.f present SEM images of similar devices, in which nearly the entire membrane has been etched away, leaving only the minimal area surrounding the SQUID chain intact. Devices with 15, 65, and 105 DC-SQUIDs were fabricated, incorporating either one or twenty single junctions at the center. The yield of the

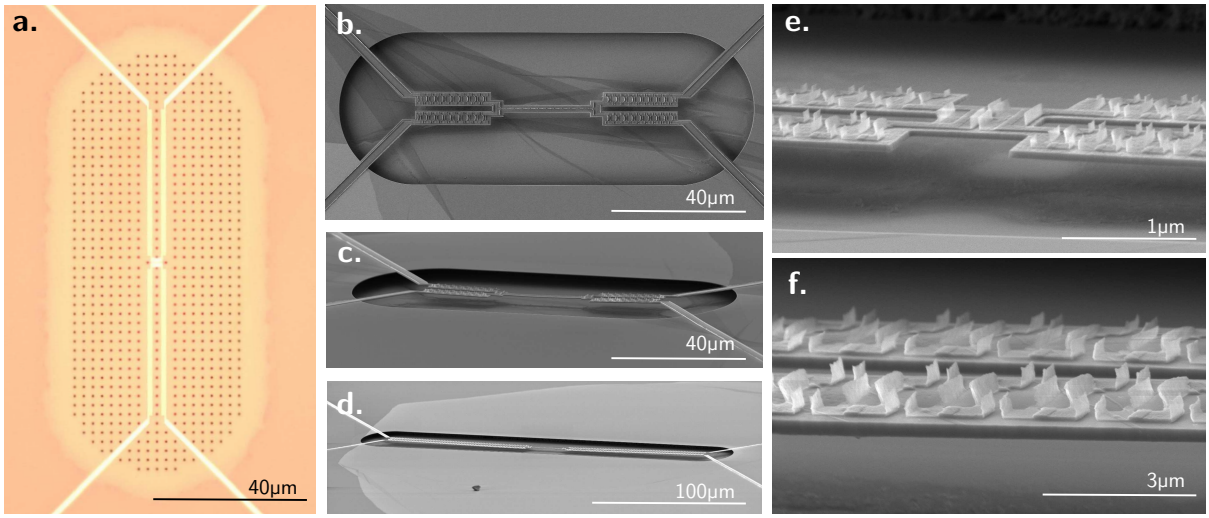

Figure 3.3: **Suspended DC-SQUID arrays. a.** Optical image of a DC-SQUID array on a silicon membrane. The dots correspond to holes in the Si membrane that allow HF vapor to penetrate and remove the underlying 3 μm of SiO_2. **b.**,**c.** SEM images of a suspended DC-SQUID array with 25 DC-SQUIDs per arm and 20 single junctions. **d.** SEM image of a suspended DC-SQUID array with 105 DC-SQUIDs per arm and 20 single junctions. **e.**,**f.** Zoomed-in SEM images of the suspended Si membrane.

suspended membranes was 100%, although other fabrication issues were present in the devices. The nanofabrication process is basically the same described in Section 4.4.3 and Appendix D and E for the membrane.

Ref. [PTH+20], using an SOI substrate, is able to decrease the ε_{eff} by a factor of 3, removing the silicon dioxide with vap-HF and the Si substrate with Bosh etching process. Details in Appendix D and E.

3.3 Conclusion

Returning to one of the original motivation behind the development of superinductors, the fluxonium qubit was proposed as a circuit in which a Josephson junction is shunted by a large inductance. This design relies on the property that a continuous piece of superconducting metal maintains a uniform voltage in the presence of static electric fields. In contrast to flux qubits composed of multiple superconducting islands, the fluxonium architecture proposed a single metallic loop interrupted by a single Josephson junction. The large inductance of the loop would serve as the shunt, and the single-piece structure would naturally suppress sensitivity to low-frequency charge noise.

In practice, the geometric inductance of a simple superconducting loop was thought to be insufficient for achieving the desired circuit parameters. To realize the necessary inductive energy scale, early fluxonium implementations introduced a superinductor formed from a long chain of Josephson junctions. Although this introduces many discrete islands into the circuit, the strong coupling between them allows the chain to behave collectively as a single superconducting element. This maintains the essential charge-noise protection originally anticipated, while enabling the large inductance required for fluxonium operation [MY20].

This chapter has reviewed the various superinductor designs developed to meet these requirements. A list of superinductors used in fluxonium experiments is available on this online

repository https://github.com/probvar/FluxoniumDB by Paul Varosy.

Chapter 4 revisits the initial premise that a purely geometric inductor could suffice as the fluxonium shunt. Although initially set aside due to limitations in achievable inductance, recent approaches based on geometric spiral inductors (developed in the groups of Oskar Painter [FKP+16], Gary Steele [GKD+19], Fabien Portier [MPP+22] and others) suggest that this route is indeed feasible.

CHAPTER 4

Geometric superinductance resonators

> “Die Spirale ist das Symbol des Lebens und des Todes. Die Spirale liegt genau dort, wo die leblose Materie sich in Leben umwandelt. Es ist meine Überzeugung, und ich glaube, es ist auch religiös verankert, und auch Wissenschaftler können es bestätigen, daß das Leben irgendwie einmal beginnen muß und man sich aus der leblosen Masse entwickelt hat, und das geschieht in Form einer Spirale.
>
> The spiral is the symbol of life and death. The spiral lies at that very point where inanimate matter is transformed into life. It is my conviction that this has a religious basis, and the scientists confirm it too, that life must begin somewhere and that development from a lifeless matter has taken the form of a spiral.”
>
> — *Friedensreich Hundertwasser*[1]

Contributions and acknowledgments. *I acknowledge the support from the NFF at ISTA, in particular Salvatore Bagiante, Juan Aguilera Servin, Lubuna Shafeek, and Philipp Taus for their assistance in setting up the fabrication, a large part of this result. Staff scientist Ivan Prieto Gonzalez contributed to the development of the Bosch etching recipe. Matilda Peruzzo implemented the measurement setup and performed part of the data analysis. Farid Hassani applied the Black-box quantization method to the simulations and contributed to valuable discussions. This chapter is based on Ref. [PTH+20].*

It is widely believed that high-impedance circuits cannot be achieved with geometric inductance alone. This belief is rooted in a misunderstanding of fundamental electromagnetic constraints. In standard circuits, inductance and capacitance originate from magnetic and electric fields stored in the surrounding space, within the turns of inductors and between plates of capacitors. When such fields reside in vacuum, the circuit's characteristic impedance is ultimately limited by the electromagnetic properties of free space, the vacuum electric permittivity ε_0 and magnetic permeability μ_0, which fix the impedance near the vacuum impedance $Z_{\mathrm{vac}} = \sqrt{\mu_0/\varepsilon_0} \approx 377\ \Omega$.

This is true for straight wires, for which the capacitance and inductance scale in the same way with wire length. However, by changing the geometry, particularly by coiling the conductor,

[1] Hundertwasser, Friedensreich. "Die Spirale." Hundertwasser, 1974, https://hundertwasser.com/texte/the_spiral.

the scaling between inductance and capacitance can be altered, allowing a substantial increase in impedance.

4.1 The common misconception about geometric inductance

Typical electrical circuits are conductive paths that carry signals relative to a common reference point, the ground. At first approximation, these paths can be seen as a simple network of straight wires. To analyze signal behavior at high frequencies or over long distances, these interconnections are modeled as transmission lines.

Two parallel straight wires of radius r, separated by a distance $d \ll \lambda$ much smaller than the wavelength of the probing signal, behave as a transmission line when shorted at one end and open at the other. They can be modeled as a series of infinitesimal LC segments. The per-unit-length inductance l and capacitance c in vacuum are given by [Poz12][2]:

$$l \approx \frac{\mu_0}{\pi} \log\left(\frac{d}{r}\right), \tag{4.1}$$

$$c \approx \frac{\pi \varepsilon_0}{\log\left(\frac{d}{r}\right)}. \tag{4.2}$$

The characteristic impedance of the system is then:

$$Z_C = \sqrt{\frac{l}{c}} = Z_{\text{vac}} \cdot \frac{1}{\pi} \log\left(\frac{d}{r}\right). \tag{4.3}$$

Ref. [Man12] discusses both the low-frequency and resonant regimes to highlight a key point: electromagnetic circuits are fundamentally constrained by the vacuum's properties, regardless of operating frequency or circuit design.

As derived in Section 2.2, the input impedance for a lossless transmission line of length corresponding to a fundamental resonant frequency $f_{\lambda/4} = \omega_{\lambda/4}/2\pi$

$$Z_{\text{in}}(x = \lambda/4, \omega) = iZ_\infty \tan\left(\frac{\pi}{2\omega_{\lambda/4}}\omega\right), \tag{4.4}$$

with the wave impedance[3]

$$Z_\infty = \sqrt{\frac{l}{c}} = Z_{\text{vac}} \cdot \frac{1}{\pi} \log\left(\frac{d}{r}\right). \tag{4.5}$$

When a transmission line is driven at frequencies much lower than its fundamental resonance $\omega \ll \omega_0$, it acts like a lumped-element inductor, with the energy stored mainly in the magnetic

[2]The exact expression for the unit-length inductance l capacitance c are given in Appendix C.

[3]Wave impedance generally depends on frequency and also varies along the length of the transmission line where it is measured. When probed at the end of a wire of length $\lambda/4$, the wave impedance matches the characteristic impedance, given by $Z_C = \sqrt{l/c}$.

field between the wires. Even in this quasi-static limit, the inductance is not arbitrary; it is determined by the geometry and the vacuum permeability μ_0. The effective inductance of a $\lambda/4$ open-circuited transmission line at low frequency is

$$L_{\text{eff}} = \frac{\pi}{2}\frac{Z_\infty}{\omega_0} \tag{4.6}$$

where $Z_\infty = \sqrt{l/c}$, with $l \propto \mu_0$ and $c \propto \varepsilon_0$. Thus, L_{eff} is ultimately limited by the electromagnetic properties of vacuum.

As the frequency approaches resonance ($\omega \approx \omega_0$), standing waves form along the line. The system now behaves as a distributed electromagnetic structure. The input impedance becomes very large (ideally infinite for a lossless line). The behavior mimics a parallel LC resonator. The impedance at resonance is given by

$$Z_C = \frac{4}{\pi}Z_\infty \tag{4.7}$$

Again, the wave impedance Z_∞, which is tied to μ_0 and ε_0, sets the scale. Both low-frequency and resonant behavior reflect the fundamental limits imposed by vacuum. In reality this is even worse because electrical circuits do not exsiste in free space but resides on dielectric and as a consequence the effective permettivity $\varepsilon = \varepsilon_0\varepsilon_r$. Also magnetic materials are not suitable with superconducting linear circuits, and as a consequence $\mu = \mu_0$.

To increase impedance, increasing d or decreasing r would help. Decreasing r has some technological limitations, so it is common to think about increasing wire separation. Once the spacing between the wires becomes comparable to the wavelength, the system begins to radiate energy into free space. This radiation effectively introduces a real component to the input impedance, often referred to as the radiation resistance, $R_{\text{rad}} = \Re[Z(\omega)]$, which arises from classical electric dipole radiation theory. It can be approximated by

$$R_{\text{rad}} \approx Z_{\text{vac}}\left(\frac{\omega_0}{\omega}\right)^4. \tag{4.8}$$

At low frequencies, radiation is negligible, but as the operating frequency approaches resonance, the system becomes increasingly coupled to free space, effectively behaving as if it were terminated by the vacuum impedance.

The conclusion of these didactic examples is that *Nature hates superinductance* [Man12], that is, with minimal effort, the impedance of a typical circuit remains far below the superinductive regime. This conclusion is correct. However, the subsequent claim that purely geometric methods cannot produce superinductors and that kinetic inductance is the only viable path [MKGD09; Man12; MPK+12; WO19; KLK+20], is unjustified.

The apparent inadequacy of geometric inductance is not fundamental, but rather a misinterpretation of standard transmission-line theory. The rest of the chapter challenges this common belief by demonstrating that superinductive behavior can, in fact, be achieved through purely geometric design. This not only provides new perspective on the physical nature of inductance but also suggests new opportunities for realizing superinductive elements with less sensitivity to charge disorder and potentially improved coherence.

The key lies in the mutual inductance between adjacent turns of a miniaturized 2D solenoid.

4.2 Modeling

This analysis is based on the distributed electrodynamics and resonance modeling of planar spiral resonators described in Refs. [MFK+14; MAA+15]. The inductance is determined using the empirical expression of Ref. [Moh99], with the more recent analytical formulation of Ref. [HW21] included for completeness.

Definition. The spiral geometry is described in polar coordinates $\{r, \theta\}$ by

$$r(\theta) = \alpha R_e \theta, \tag{4.9}$$

where r is the radius, θ is the polar angle, and R_e is the external radius of the spiral. The radius increases linearly from the center $(r = 0)$ at $\theta = 0$ to the outer edge $(r = R_e)$ at $\theta = 2\pi n$, where n is the number of turns. The parameter α is defined as

$$\alpha = \frac{p}{2\pi R_e} = \frac{1}{2\pi n}, \tag{4.10}$$

with p denoting the spacing between adjacent turns. Thus, α represents the radial advance of the spiral per unit angle. Smaller α corresponds to more turns and denser packing (large n, small p); while larger α corresponds to fewer turns or looser spacing.

4.2.1 Resonant frequency

In a simplified description, a spiral can be modeled as a straight transmission line of effective length ℓ, wound into a spiral geometry. For open boundary conditions at both ends, the resonance frequencies f_m satisfy the standard transmission-line relation (Eq. 2.26)

$$f_m = m \cdot f_0, \quad m = 1, 2, 3, \ldots \tag{4.11}$$

with the fundamental frequency

$$f_0 = \frac{c}{2\ell}. \tag{4.12}$$

Here, $c = c_0/\sqrt{\varepsilon_0 \varepsilon_r}$ is the speed of light in the medium, and the effective length is approximated by

$$\ell \approx \frac{\pi R_e^2}{p}, \tag{4.13}$$

where R_e is the outer radius of the spiral and p is the pitch, i.e., the spacing between adjacent turns. The exact formula for the length can be found in the Appendix A.

Assuming a uniform transmission line, the standing-wave current distribution as a function of arc length s can be written as

$$I_m(s) = I_0 \sin\left(m \frac{\pi s}{\ell}\right). \tag{4.14}$$

Expressing the distribution in terms of the radial coordinate r gives

$$I_m(r) = I_0 \sin\left(m \frac{\pi r^2}{R_e^2}\right). \tag{4.15}$$

This simplified formulation provides an intuitive and analytically convenient description; however, it does not account for the geometry of the spiral and the electromagnetic coupling between adjacent turns, which can be essential for accurately capturing the full resonator behavior.

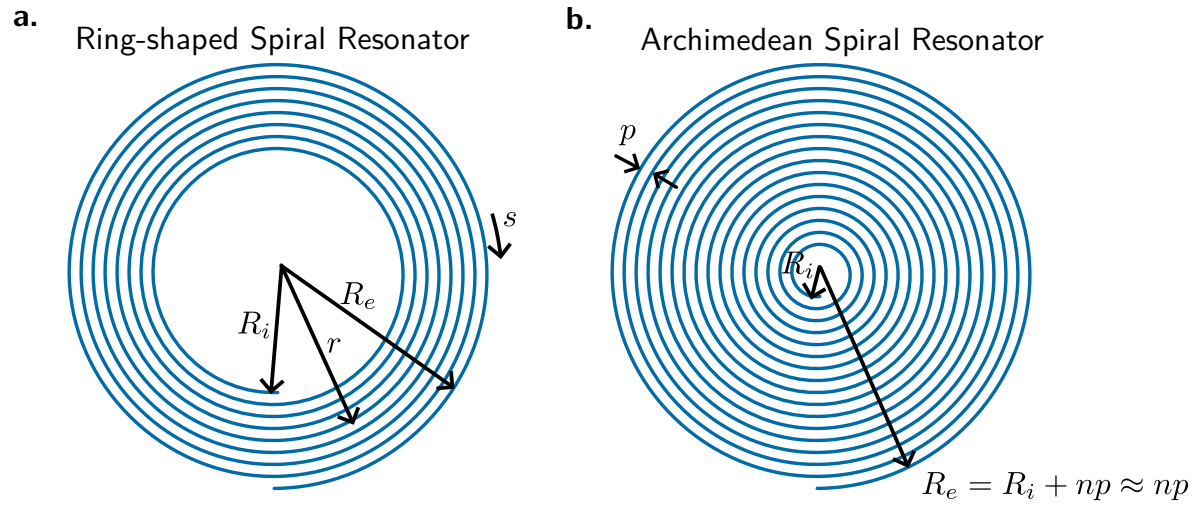

Figure 4.1: **Spiral resonator geometries.** Sketch of **a.** a ring-shaped spiral resonator, where the internal radius R_i is comparable to the external radius R_e, and **b.** an Archimedean spiral resonator, where $R_e \gg R_i$.

Ring-shaped spiral resonator. The following is based on Ref. [MFK+14]. As already said, a conventional one-dimensional transmission line with two open ends exhibits resonance frequencies that form a harmonic series, $f_m = m \cdot f_0$ for $m = 1, 2, 3, \ldots$. In contrast, planar ring-shaped spiral resonators (Fig. 4.1.a), where the inner radius is comparable to the outer radius, display a different spectrum. Their resonance frequencies follow an odd-integer sequence, $f_m = (2m-1) \cdot f_0$, yielding modes such as f_1, f_3, f_5, and so on. This odd-harmonic pattern is typically observed in resonators that are open at one end and short-circuited at the other.

The expression for the current distribution along the unwrapped spiral can be found in Ref. [MFK+14].

The spiral spectral behavior can be attributed to strong electromagnetic coupling between adjacent turns, which effectively reduces the phase velocity and lowers the fundamental frequency to approximately $f_0 \approx c/(4\ell)$. This makes the spiral operate as a compact quarter-wavelength resonator, supporting only odd harmonics $(f_1, f_3, f_5, \ldots)$. At higher frequencies, the coupling weakens, and the resonator transitions back to the behavior of a straight conductor, with harmonics approaching a regular integer series. Moreover, the model provides physical insight into the spatial structure of the resonant modes. It explains the non-uniform spacing between standing wave maxima as a result of spatially varying phase velocity along the spiral. Similarly, the variation in the amplitude of these maxima is attributed to the non-uniform characteristic impedance, both consequences of the spiral geometry.

Archimedean spiral resonator. The following is based on Ref. [MAA+15]. Compared to a ring-shaped spiral, the Archimedean spiral has a much smaller internal radius, allowing the turns to occupy almost the entire available area, which results in a filling factor close to one (Fig. 4.1.b).

The resonant frequencies of an Archimedeal spiral resonator are the solutions of the following transcendent equation

$$S(a) - \pi = 0 \tag{4.16}$$

where

$$S(a) = \sum_{m=1}^{\infty} \frac{(-1)^m \; m \; \beta(m)}{-m^2 + a} \tag{4.17}$$

with

$$a = \frac{\omega^2 R_e^2}{4\pi^2 c^2 \alpha^2}^{4} \tag{4.18}$$

$$\beta(m) = \int_0^1 \frac{K(v)}{g_1(v)} v^{-2} \sin(\pi m v) \; dv \tag{4.19}$$

$$K(v) = R_e v \int_0^{\infty} J_1\left(\sqrt{v}\; x\right) J_1(x) \; dx \tag{4.20}$$

$$g_1(v) = R_e \sqrt{v} \int_{\sqrt{v}}^{\infty} du \int_0^{\infty} J_1(ux) \; J_1(x) \; dx. \tag{4.21}$$

In Eq. 4.18, $\omega/2\pi$ is the frequency, R_e is the external radius of the spiral, $c = c_0/\sqrt{\varepsilon_{\text{eff}}}$ is the speed of light in the medium, and $\alpha = p/(2\pi R_e) = 1/(2\pi n) \ll 1$ a parameter with p the distance between adjacent turns and n the number of turns. In Eq.s 4.20 and 4.21 J_1 is the Bessel function of the first kind.

Eq 4.17 is solved numerically using a root finding method. The Mathematica code is shown in Appendix. B. Given the solution a^*, the fundamental frequency is

$$f_g = \frac{1}{2\pi} \sqrt{\frac{a^* c^2 \alpha^2}{R_e^2}} \tag{4.22}$$

leading to

$$f_g = \xi \frac{c_0}{\sqrt{\varepsilon_{\text{eff}}}} \frac{2p}{\pi (2R_i + 2np)^2}, \tag{4.23}$$

where $\xi = \sqrt{a^*} = 0.81$[5] is a shape-dependent factor, n the number of turns, p the pitch (wire width plus spacing), R_i the internal radius (assumed to be $R_i \ll R_e$), ε_{eff} is the effective relative permittivity, and c_0 is the speed of light in vacuum.

4.2.2 Inductance

The geometric inductance of a spiral can be approximated using the current-sheet model [Moh99]

$$L_g = \mu_0 n^2 d_{\text{av}} \left[\ln\left(\frac{2.5}{\rho}\right) + 0.2\rho^2 \right], \tag{4.24}$$

[4] I believe that the expression for a in Ref. [MAA+15] is incorrect, with a factor of $(2\pi)^2$ missing, whereas it is correct in the preprint [MAA+14].

[5] The value of $\xi = 0.81$ is close, but not exactly the same as the one reported in the `.html` code in `view-source:https://smm.misis.ru/spiral/`, where $\xi = 0.81876$ for the fundamental mode and $2.0357, 2.90048, 4.03697, 4.92102, 6.03659, 6.93143, 8.03592, 8.93801, 10.0352$ for the modes up to the tenth. The discrepancy likely arises because the code I used truncates the summation in Eq. 4.17 at 1000, rather than summing to infinity.

where μ_0 is the vacuum permeability, n is the number of turns, $d_{\text{av}} = (d_{\text{in}} + d_{\text{out}})/2$ is the average diameter (with $d_{\text{in}} = 2R_i$ and $d_{\text{out}} = 2R_e$), and $\rho = (d_{\text{out}} - d_{\text{in}})/(d_{\text{out}} + d_{\text{in}})$ is the fill factor of the coil. For the geometries considered here, $\rho \approx 1$, and since $d_{\text{out}} \propto n$, the inductance scales approximately as $L_g \sim n^3$.

Ref. [HW21] presents an alternative method for calculating the self-inductance of an Archimedean spiral coil. This method is derived analytically by solving Neumann's integral formula, unlike many conventional methods that are empirical, like Eq. 4.24. The modeling approach involves calculating the mutual inductance between the spiral coil and a duplicate of itself, shifted by a distance equal to the wire's diameter. The resulting formula is a double integral that is solved numerically:

$$L = \frac{\mu_0}{4\pi} \iint_{2\pi n} \frac{k d\theta_1 d\theta_2}{\sqrt{(R_i + a\theta_1)^2 + (R_i + a\theta_2)^2 - 2k + w^2}}, \tag{4.25}$$

where $k = (R_i + a\theta_1)(R_i + a\theta_2)\cos(\theta_2 - \theta_1)$, n the number of turns, R_i the internal radius, w the wire width, $a = p/(2\pi)$ the pitch factor and θ_1, θ_2 the polar angle of the spiral and its duplicate.

This was published after our work on the geometric superinductor and should be carefully tested to check its consistency with both simulations and the empirical formula. It is reported here for completeness.

4.2.3 The proof of principle

Using the relationships for the fundamental frequency (Eq. 4.23) and geometric inductance (Eq. 4.24) of a planar spiral resonator, it can be shown that such a structure can outperform a straight wire and surpass the quantum resistance limit, while maintaining operation in the gigahertz frequency range.

In the regime where the number of turns is large ($n \gg 1$) and the spiral is fully wound ($\rho \approx 1$), the fundamental resonance frequency scales as $f_g \sim n^{-2}p^{-1} \sim \ell^{-1}$, consistent with the behavior expected from distributed-element systems. An approximate expression for the length of a circular spiral, ℓ, modeled as a series of concentric circles, is:

$$\ell \approx \sum_{i=1}^{n} 2\pi r_i = \sum_{i=1}^{n} 2\pi i p = 2\pi p \sum_{i=1}^{n} i = 2\pi p \cdot \frac{n(n+1)}{2} \approx n^2 p \tag{4.26}$$

where $r_i = i \cdot p$ with $i = 1, 2, 3, \ldots$ is the radius of each turn. The complete expression of ℓ is reported in Appendix A.

When modeled as an LC resonator, the spiral's characteristic impedance $Z_C = \sqrt{L_g/C} = 2\pi f_0 L_g$, indicating a linear scaling of characteristic impedance with the number of turns ($Z_C \sim n$). The parasitic capacitance follows $C \sim np$, scaling in first approximation with the coil's overall radius.

These scaling trends are illustrated in Fig. 4.2.a, which compares the impedance and resonance characteristics of straight wires and spiral coils. Although both configurations show a similar inverse dependence of resonance frequency on total length ($f_0 = c_0/2\ell$), the coil exhibits an impedance that increases with length as $Z_C \sim \sqrt{\ell/p}$[6]. This enables the coil to exceed the impedance cap of a straight wire, supporting the realization of superinductors that function in the GHz regime.

[6] Ref. [PTH+20] contains a typographical error, stating that $Z_C = 2\pi f_g L_g \sim \sqrt{\ell}/p$.

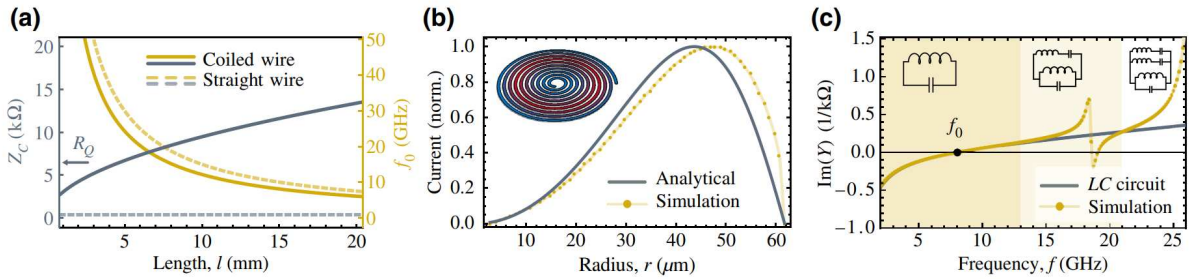

Figure 4.2: **Coils modeling. a.** Characteristic impedance Z_C (blue) and first resonance frequency f_0 (yellow) are compared for a straight wire ($d/w = 10$, dashed) and a planar coil ($p = 1$ μm, $\rho = 1$, solid) in vacuum ($\varepsilon_{\text{eff}} = 1$). The blue dashed curve corresponds to the wire impedance, while the blue solid curve represents the coil impedance ($Z_C = 2\pi f_g L_g$, with f_g and L_g from Eqs. 4.23 and 4.24). For coil lengths $\ell > 4.78$ mm, Z_C exceeds $R_Q \approx 6.45$ kΩ, while the resonance frequency (yellow solid line) falls slightly below 25.4 GHz. Both the coil frequency (Eq. 4.23) and the $\lambda/2$ wire resonator frequency $f_0 = c_0/2\ell$ scale with length, the coil case including a multiplicative factor due to enhanced inductance. **b.** Normalized current distribution for a coil with $p = 1$ μm, $n = 60$, and $d_{\text{in}} = 6$ μm. Simulated data points (yellow, line as a guide to the eye) align closely with the analytical $\lambda/2$ resonator model (blue). The inset illustrates current amplitude, with red corresponding to maxima and blue to minima. To first order, the spiral resonator behaves as a distributed $\lambda/2$ resonator. **c.** Admittance spectrum of the same coil in vacuum. Simulated points are shown in yellow. The first resonance frequency corresponds to the zero crossing (black dot). The blue curve is the LC model admittance, using L_g from Eq. 4.24, which matches the simulated response at low frequencies (dark yellow region). At higher frequencies, additional resonances appear and can be modeled by the equivalent circuits sketched in the insets. Around f_0 the coil acts as an ideal LC resonator, while at lower frequencies it approximates a pure inductor.

4.3 Simulations

Round archimedean spirals were studied in this thesis. The choice of this geometry, instead of square coils, which are regularly used at Caltech [FKP+16] and in other works [GKD+19], was motivated by the possibility of having an analytical model for the fundamental frequency, as well as the fact that the circle can achieve higher impedance for the same length compared to any other geometry. The drawback is a longer simulation time compared to the square coils[7], which is why it was not used in subsequent devices [PHS+21; HPK+23].

A total of one hundred and four spiral resonators were successfully measured, each with distinct resonant frequencies. Simulations were essential to determine the number of turns needed to keep all coils within the measurable frequency range of the current setup. Due to the high computational demand, a simplified model of the real device and coupling geometry was used, as can be seen in Fig. 4.3.a.

The main goal was to extract the resonance frequency. Additional parameters that can be obtained include the external quality factor Q_e, capacitance, and inductance for each coil. The latter two parameters require a slightly different type of simulation performed, as noted in Subsection 4.3.2.

[7]The reason is that the finite element method discretizes the geometry using square mesh cells, which do not conform naturally to curved edges. As a result, accurately representing the round Archimedean spiral requires a finer mesh, increasing the number of elements and, consequently, the computational time.

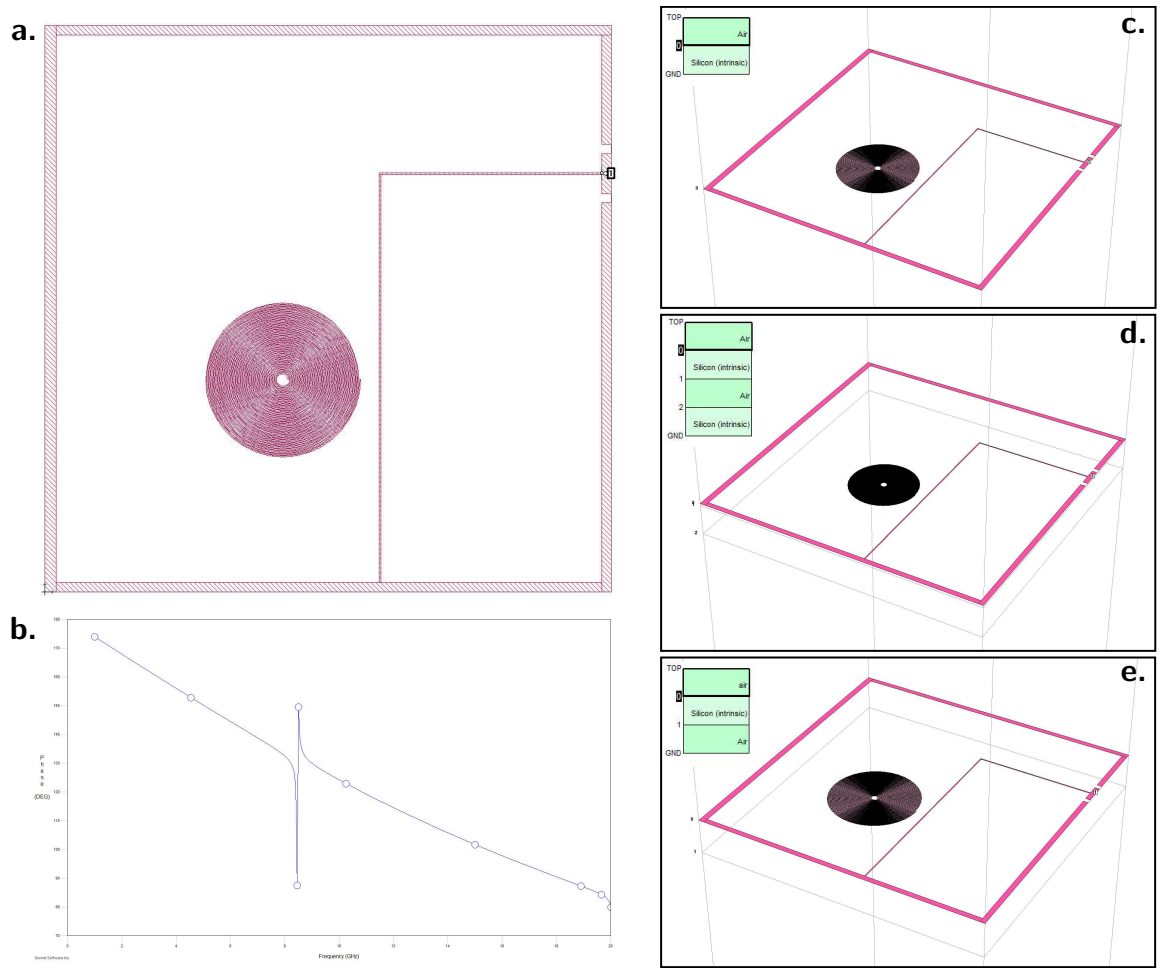

Figure 4.3: **Sonnet simulations of spiral resonators. a.** Single-port setup with a $50\ \Omega$-matched port and minimal ground metal. **b.** Example phase response of S_{11}. **c.** Silicon substrate ($\varepsilon_r = 11.9$, $500\ \mu\mathrm{m}$ thick) with vacuum above. **d.** SOI stack: $220\ \mathrm{nm}$ Si / $3\ \mu\mathrm{m}$ vacuum / $725\ \mu\mathrm{m}$ Si. **e.** BE-SOI stack: $220\ \mathrm{nm}$ Si / $728\ \mu\mathrm{m}$ vacuum.

The electromagnetic behavior of each resonator was simulated using the commercial software Sonnet https://www.sonnetsoftware.com/, specialized for high-frequency planar circuits. Additional simulations performed with Ansys are reported in Ref.[HB24] by Farid Hassani, and simulations using Comsol are detailed in an internal QuantumIDS report by Maria Zelenayova and Martin Zemlicka.

4.3.1 Resonance frequency and coupling

Each spiral geometry was simulated within a single-port setup (Fig. 4.3.a). Due to memory and time constraints, the ground metal was minimal. The feedline width was set to $1\ \mu\mathrm{m}$, and the excitation port defined as $50\ \Omega$-matched to minimize reflections at the port.

The simulations assumed a silicon substrate with relative permittivity $\varepsilon_r = 11.9$ and vacuum above ($\varepsilon_r = 1$). The dielectric layer below thickness was chosen to be $500\ \mu\mathrm{m}$ for the Si substrate (Fig. 4.3.c), $220\ \mathrm{nm}$ Si/$3\ \mu\mathrm{m}$ vacuum/$725\ \mu\mathrm{m}$ Si for the SOI (Fig. 4.3.d) and $220\ \mathrm{nm}$ Si/$728\ \mu\mathrm{m}$ vacuum for the BE-SOI (Fig. 4.3.e). All metal layers were treated as perfect conductors, and dielectric losses were neglected. The dielectric layer above is set to vacuum, $500\ \mu\mathrm{m}$.

Resonance frequencies were identified from the jump in the phase of S_{11} (Fig. 4.3.b) while Q_e values were extracted using standard fitting techniques. The cell size division was set to $0.25/0.15/0.1/0.075$ μm for $1/0.5/0.3/0.2$ μm pitch coils respectively. For the lowest pitch, this is at the border of a continuous layer of metal but it was necessary to have results in reasonable time (for the lowest pitch, constantly above 10 hours per resonance). The filling type was set to "Conformal".

In Ref. [Kis13], similar simulations were performed for single and double-spiral coils. Double-spiral coils, with same frequency and coupling geometry, were found to exhibit higher resonance frequencies and larger coupling quality factors Q_e than single Archimedean spirals of the same outer radius and coupling geometry. This behavior is explained by inductance effects: in a double-wound spiral, current flows inward and then outward, leading to partial cancellation of magnetic fields, a reduced net inductance, and thus a higher resonance frequency. The spatial voltage distribution further contributes. For an open-ended $\lambda/2$ transmission line resonator, voltage peaks at both ends and minimizes at the center. In a double-wound design, both spiral ends are equidistant from the feedline, giving a smaller voltage gradient and weaker coupling. In contrast, a simple spiral has one end much closer to the feedline, creating a larger voltage gradient and stronger electromagnetic coupling, which lowers Q_e.

In Ref. [Kis13] were employed a faster approach [WMRG14] based on introducing an internal (virtual) port in the Sonnet model and determining f_0 and Q from the input impedance at that port, and a technique for visualizing current distributions using a high-reactance “sense metal plane” above the resonator, where the simulated current is proportional to the local field strength.

4.3.2 Inductance and capacitance

To verify the analytical formulas introduced earlier, the inductance and capacitance were also extracted directly from simulation. This serves as an independent check to ensure agreement between the analytical model and the simulated response The inductance and capacitance were extracted by adding an ideal capacitor in parallel to the coil in the simulation. Sweeping the value of this capacitor shifts the resonant frequency; using just two values of the parallel capacitor and the corresponding simulated resonance frequencies allows solving a system of equations to extract the unknowns, L_g and C. More details in Ref. [Per21].

4.3.3 Ansys simulations and black-box quantization

In Fig. 4.2.c, the simulated frequency-dependent admittance of a spiral coil shunted by a single lumped port is compared with that of an ideal LC circuit, $Y(f) = i2\pi fC + 1/(i2\pi fL)$. The first zero crossing corresponds to the coil's fundamental resonance. The capacitance can be extracted [NPV+12; HB24] from the derivative of the imaginary part of the admittance at the resonance frequency: $C = (1/4\pi)\ \ d\,\mathrm{Im}[Y(f)]/df|_{f=f_0}$. Using this method, we find an inductance of approximately $L_g = 1/(C(2\pi f_0)^2) \approx 163$ nH, in good agreement with Eq. 4.24, which predicts $L_g \approx 173$ nH. Consistent results are also obtained by extracting f_0 and its slope with respect to capacitance, df_0/dC, from the simulated S_{11} parameter of a weakly coupled wave port, as mentioned in Subsection 4.3.2. This approach yields $L_g \approx 180$ nH.

The two admittance curves in Fig. 4.2.c align well within the dark shaded region, beyond which additional LC branches improve the model accuracy across a broader frequency range. This validates the use of an ideal LC oscillator model for the coil up to and beyond its

first resonance. Furthermore, below its fundamental frequency, the coil exhibits a negative imaginary admittance, confirming its role as an ideal inductor. All subsequent discussions in this work refer to the frequency regime in which this LC approximation holds.

This is a reassuring outcome, since conclusions about the high impedance of the devices are based on the inductance calculated using Eq. 4.24, which cannot be measured directly. This assumption was later independently confirmed by fitting the inductive energy E_L extracted from qubit spectroscopy measurements [PHS+21; HPK+23].

4.3.4 Current and field distributions

Fig. 4.2.b illustrates the distributed-resonator nature of the spiral coil through its radial current profile, obtained via finite-element-method (Sonnet) simulations. This is compared to the current distribution of a straight $\lambda/2$ open-ended transmission line, $I(r) = I_0 \sin[\pi(2r/d_{\text{out}})^2]$, which does not include mutual inductance between turns. At the fundamental mode, the current density peaks at the center ($\ell/2$) and vanishes at the ends, consistent with the FEM results. Closed-form expressions are provided in Refs. [MFK+14; MAA+15]. Also Ref. [TSH+25] reports a current distribution.

4.4 Device nanofabrication

Most of the following fabrication process are based on knowledge Johannes Fink acquired during his time at Caltech in the Painter Lab[8]. These methods were later adapted and re-established in the newly opened nanofabrication facility at ISTA in 2017, where I was among the first users. While many of the parameters set are based in the underlying physics, chemistry, and engineering principles of the tools and processes, others have proven effective through experience. Nevertheless, the so-called "black magic" that takes place inside the ISO 7 cleanroom works reliably and has become an essential part of the scientific workflow, particularly in the context of this project. Even without full control over every parameter, the process shows high yield and repeatability. The successful fabrication of a hundred and four devices stands as proof.

The devices presented in this section are fabricated on three different substrates: high-resistivity silicon (Si), silicon-on-insulator (SOI), and back-etched silicon-on-insulator (SOI-BE). Each substrate requires a specific sequence of nanofabrication steps, adapted to realize the desired geometry, suit the application, and fulfill design constraints. A summary of the main fabrication steps together with an SEM picture of the coil resonators are presented in Fig. 4.4.a and Fig. 4.4.b-.c, respectively.

4.4.1 Basic toolkit

Working in a cleanroom requires a highly systematic and disciplined approach. Precision, consistency, and attention to detail are essential, not just to improve the chances of success, but to prevent small oversights from turning into costly failures. Even with careful procedures, things can go wrong, but a methodical process makes it easier to identify issues, trace errors, and refine techniques over time. It's an exercise in patient. Even if the machines perform most tasks automatically, constant vigilance is necessary to act promptly if something deviates

[8] Good reference, especially for the etching of Silicon, is [Hil13]. The rest of the section follows some methodologies therein.

from expectations: this can save days of work. Many aspects remain like black boxes, which can be frustrating. However, if a device with a correct design is fabricated carefully, it will significantly simplify the later characterization.

Other basic tools needed before starting any process include stainless steel ESD (Electrostatic Discharge) tweezers with interchangeable tips. These tips should be replaced when they start scratching or showing signs of wear due to exposure to chemicals and high temperatures. I had two pairs: one "clean" pair reserved for processes not involving metals, and one "dirty" pair used during liftoff. Additionally, I had a pair made of Teflon specifically for HF-related processes.

I used different sets of Pyrex glass graduated beakers for nearly every step in the fabrication process. These were designated for clean ACE and IPA (where "clean" means no liftoff metal was involved immediately before), developer, liftoff, dirty ACE and IPA (rinsing after liftoff), and water. Teflon beakers were reserved for processes involving MF319 developer and buffered HF. The glass beakers were rinsed with IPA before and after each process, making sure to clean all internal walls and the upper rim; the beaker for ACE rinsed only with ACE. They were also cleaned regularly, approximately every six months, in the cleanroom dishwasher. If not used for a long time, it is recommended to clean them thoroughly before reuse. Glassware is often cleaned by solvent washing, followed by a rinse in deionized (DI) water, a mild acid clean, another DI rinse, and finally nitrogen blow-drying. Although I never performed this cleaning procedure myself, I was told it makes a difference, particularly if the smallest particles can cause problems in the process. If any beaker comes into contact with gold particles, it must be cleaned separately from all other equipment to prevent contamination.

A diamond scriber is a useful tool for pre-scratching chips intended for cleaving. To cleave, place a wedge underneath the chip and press down with the tweezers after making the incision. This can cause the chip to break into many pieces and damage the tips of the tweezers. Take special care and wear goggles.

4.4.2 High-resistivity silicon substrate

The table below lists the fabrication steps for the devices on a silicon substrate, which represents the most straightforward process among those used. Important processes are discussed in more detail in the paragraphs following the table. Gray text indicates optional cleaning steps. The values provided serve as a useful starting point but should be adjusted based on the current condition and calibration of the tools.

Process	Steps	Notes
Wafer preparation	Tape Dice	See Wafer preparation.
Substrate cleaning	ACE, 21°C, uc power 9, 5 min IPA, 21°C, uc power 9, 5 min N2 blow dry Plasma ashing BOE, tank, 10 sec DI Water, beaker, 5 sec DI Water, tank, 5 sec N2 blow dry	See Substrate cleaning.
Spin and bake e-beam resist	Prebake, 120°C, 1 min	See Spin coating and baking of e-beam resist.

	Spin, CSAR AR-P 6200.13, 6 krpm, 1 min (acceleration 1.5 krpm/s) Bake, 160°C, 2 min	
E-Beam flow prep	CAD file preparation Beamer flow file preparation	See E-beam flow file preparation.
E-beam patterning	Coils, 0.8 or 1 nm beam, dose 300-330 μC/cm^2 with PEC Couplers, 10 nm beam, dose 250-270 μC/cm^2 with PEC CPW and Ground plane, 100-250 nm beam, dose 250-270 μC/cm^2 with PEC	See E-beam patterning.
Development	AR 600-549, 21°C, 1 min IPA, 21°C, 30 sec N2 blow dry	See Development.
Evaporation	Cleaning Ti gittering, 5 min, 0.2 nm/s Al evaporation, 100 nm, 1 nm/s	See Metal evaporation.
Liftoff	NMP, in a beaker immersed in a water bath on a hot plate at 145°C, 1 h NMP, in a beaker immersed in a water bath on a hot plate at 145°C, 1 h ACE, 21°C, 30 sec IPA, 21°C, 30 sec N2 blow dry	See Metal liftoff.

Wafer preparation. The process starts with a polished $525\ \mu\mathrm{m}$ thick, high resistivity ($> 20\ \mathrm{k\Omega \cdot cm}$), Si <100> wafer, purchased from the company TopSil. We covered both sides with a tape and dice the wafer in $10\ \mathrm{mm} \times 10\ \mathrm{mm}$ chips.

Substrate cleaning. This step prepares the substrate chip for resist application. After wafer dicing, chips often retain traces of protective materials such as adhesive films or residual photoresist. To ensure good resist adhesion, the substrate is first cleaned using a standard solvent procedure (ACE and IPA with mechanical agitation in an ultrasonic bath), followed, if necessary, by plasma ashing (Table 4.2). A subsequent dip in buffered oxide etch (BOE), followed by a DI water rinse, removes the native silicon oxide. This also produces a hydrogen-terminated surface, which is hydrophobic and temporarily passivated against oxidation in air. This surface condition improves the quality of both substrate–air and substrate–metal interfaces. Teflon tweezers and beakers should be used for all steps involving HF.

Spin coating and baking of e-beam resist. CSAR[9] is used as the electron-beam resist due to its high resolution, good selectivity against silicon plasma etching and lower required exposure dose, which enables faster patterning. Before applying the resist, the substrate is placed on a hot plate to evaporate any residual moisture and to bring it to a uniform starting temperature. The resist is applied using a vacuum chuck spinner[10], with the chip centered

[9] https://www.allresist.com/wp-content/uploads/sites/2/2016/12/allresist_produktinfos_ar-p6200_englisch.pdf

[10] Before starting, test the spin coater to ensure the vacuum pump is functioning, as dried resist can clog the chuck and reduce suction. If needed, clean the chuck with acetone and a needle.

Process	Time (s)	Power (W)	Pressure (mBar)	Flow (sccm)
for Cleaning	300	240	0.5	12.5
after Development	15	45	0.5	8

Table 4.2: **Process parameters for O_2 plasma ashing.**

to ensure symmetric spinning and uniform resist distribution. Using a clean, nitrogen-dried glass pipette, three to four drops of CSAR resist are deposited at the center of a 10×10 mm chip in one continuous flow, avoiding air bubbles. Never double-dip the pipette into the resist bottle to prevent contamination. Avoid contact with the bottle rim and sidewalls.

Spinning CSAR at 6000 rpm yields a layer approximately 330 nm thick. After spinning, the chip is baked on a hot plate (placed on an Si wafer, uncovered) to harden the resist. Once removed, the chip should cool for a few minutes in a clean, covered container before proceeding. CSAR is a positive-tone resist. Resist uniformity can be inspected with an optical microscope using both bright-field and dark-field illumination. It is important to check for trapped air bubbles, surface scratches, or irregularities at the resist edge, as these defects can affect subsequent steps like exposure or etching.

E-beam flow file preparation. The layout of the device was initially scripted in Matlab to automatically generate all coils and launchers, using code adapted from earlier work at Caltech. A more flexible approach uses the Python library `gdspy`[11] to script the layout using a hierarchy of `Cell` objects containing geometric primitives like polygons and paths, organized by layer. Shapes can be transformed via translation, rotation, or mirroring. The library supports Boolean operations, layout visualization via `gdspy.LayoutViewer`, and direct export to GDSII. An example is given in Ref. [Red22]. To compensate for overdosing and development effects, the coil layout uses a width-to-spacing ratio of $30\% : 70\%$, which shifts to approximately $50\% : 50\%$ after processing. This is the most stable configuration: a larger width can cause collapse of the "negative coil" resist during development, while excessive spacing increases the risk of breaks in the resulting narrow wire. The final layout is exported and opened in AutoCAD, where layer names are manually assigned. The file is saved in a `.dxf` format with encoding compatible with subsequent processing and imported into BEAMER.

BEAMER is a software developed by GenISys that converts layout files into exposure data (`.gpf`) for electron-beam lithography. It performs fracturing, the process of breaking down complex shapes into basic geometries compatible with the electron-beam writer, and applies corrections for tool artifacts, proximity effects, and process variations. The sequence of processing steps in BEAMER is called "flow".

Import Module. The `.dxf` file with the layout is loaded in the import module, where the dimensional tolerances are set to very fine values (by default 1 nm), well below the EBPG's resolution, to ensure that software settings do not limit the layout feature size.

Heal Module. A healing operation removes overlapping geometry that would otherwise cause double exposure. The Heal module automatically eliminates redundant regions using default settings.

Export Module.The final stage of the workflow exports the fractured layout into a format compatible with the EBPG system (`.gds`). A predefined tool configuration must be selected,

[11] https://github.com/heitzmann/gdspy by Lucas H. Gabrielli.

Parameters	GND, CPW	Coupling line	Coils
PEC	Yes	No	Yes
Max number of dose classes	256	-	256
Min dose factor	0.1	-	0.1
Resolution (= Beam step size)	0.050 μm	0.010 μm	0.001 μm
Fracture mode	LRFT	LRFT	LRFT
Field ordering	Fixed	Floating	Floating
Feature order	No Compaction	No Compaction	No Compaction
Beam Current	250 nA	10 nA	0.8-1 nA
Dose	250-270 μC/cm^2	250-270 μC/cm^2	300-330 μC/cm^2

Table 4.3: **E-beam parameters for coils on Si substrate.**

here "5200/5000+ 20bit HS 100kV", which includes all relevant hardware parameters. The writing resolution is set based on the smallest feature size and desired dose; it also defines the beam step size accordingly.

This resolution setting determines the maximum field size writable without stage movement, limited to $1040\ \mu\mathrm{m} \times 1040\ \mu\mathrm{m}$. Since individual coils fit within this range, we constrain each pattern to a single field to avoid stitching, using the "floating" field option. Larger structures like the ground plane require "fixed" field placement.

The fracture mode controls how the layout is decomposed into shapes the EBPG can interpret. Available modes include "large rectangle fine trapezoid" (LRFT), "conventional", and "curved". Most configurations yield comparable results.

The resulting `.gpf` folder is synchronized with the e-beam workstation, where `.cjob` files are generated for exposure.

E-beam patterning. The electron beam pattern generator (EBPG) utilizes the `.gpf` file to expose the resist-coated chip by delivering a controlled electron dose, i.e. a specific charge per unit area, to chemically modify the resist. The optimal dose depends on multiple factors, including the resist type and thickness, substrate material, feature size, and overall pattern geometry.

To calibrate and refine this value, a dose test is routinely written right before starting the fabrication of the sample. This involves patterning identical structures multiple times across the chip, each with a slightly different dose. Dose test steps and number of replicas depends on requirements, but at least 10 steps, with $10\ \mu\mathrm{C}$ increment for CSAR. Insufficient dosing results in incomplete development, where some resist remains. Conversely, excessive exposure causes overdevelopment, enlarging and rounding out sharp features beyond their intended dimensions.

The choice of electron beam current is influenced by both the required feature resolution and the pattern density defined in the `.gpf` file. Higher resolution patterns necessitate smaller beam currents to prevent beam deflection from exceeding the system's speed limits and causing dose errors. Writing at up to $100\ \mathrm{MHz}$ is technically possible, even if not recommended.

Larger beam currents enable faster writing, making them suitable for patterning large open areas. However, smaller beam currents offer finer resolution and smaller spot sizes, which are essential for high-precision features with step sizes as small as $2.5\ \mathrm{nm}$. In practice, a $300\ \mathrm{pA}$

beam, yielding a spot size of roughly $4\ \mathrm{nm}$, is commonly used, as it provides a good balance between speed and resolution and represents the performance limit of the current tool.

Development. We use AR600-549, a proprietary developer from "Allresist", to process the exposed resist. The chip is gently agitated in the developer, held by tweezers at the edges. Fresh developer is replaced after processing approximately 4 chips. Following development, the chip is rinsed for 30 seconds using ACE and then IPA. After rinsing, the chip is dried with nitrogen.

The resist is sensitive to environmental moisture, which can cause it to swell and alter its properties over time, potentially damaging fine features and degrading pattern fidelity. To minimize this risk, it is a good thing to develop chips after exposure and proceed to BOE etching within a few days and immediately before the metal evaporation.

Metal evaporation. Metal evaporation is performed immediately after development to minimize oxide growth on the substrate surface. To enhance this step, a descumming step at the plasma asher (Table 4.2) or an ICP-RIE directional oxygen clean can be applied beforehand (parameters provided in Table 4.6), followed by a buffered HF (BHF) dip.

The sample is then mounted into an ultra-high vacuum (UHV) evaporator system from Plassys. The system consists of three interconnected chambers. The first is a load lock chamber, used for rapid sample insertion and evacuation. It is connected via a mechanical arm to the oxidation chamber, where gas inlets (oxygen and argon) are available. In this chamber, the sample can be rotated and tilted in all directions, and a shutter is used to shield the sample from unwanted metal deposition. The oxidation chamber is connected by a valve to the evaporation chamber, which houses multiple crucibles mounted on a rotating stage. The user can select the desired crucible, and a laser beam can be focused and precisely positioned on the target.

Before aluminum deposition, a thin titanium layer is first evaporated while the sample is protected by vertically tilting the substrate holder. This process coats the chamber walls with titanium, which acts to trap residual oxygen. As a result, the vacuum improves by approximately an order of magnitude, reaching down to the $10^{-8}\ \mathrm{Torr}$ range.

Metal liftoff. For each sample, the metal liftoff process involves two beakers filled with NMP (N-Methyl-2-pyrrolidone), followed by rinsing in acetone and IPA. The NMP is preheated in a water bath. After soaking the sample for about one hour in the first beaker, aggressive pipetting is used to break and remove the metal film.

The sample is then transferred to a second NMP beaker to dissolve any remaining resist. If pipetting alone is not sufficient, it typically indicates suboptimal pattern design, exposure dose, or development quality. A mild sonication step can be introduced if necessary, but this may degrade the device's quality factor due to rough sidewalls or dislodged metal flakes caused by poor adhesion. Shallow beakers are preferable for strong pipetting, as they allow access from multiple angles. Before drying, the sample can be stored in a shallow layer of IPA and inspected under an optical microscope. Once dried, any remaining metal residues that were not lifted off and have redeposited onto the substrate will likely be impossible to remove by re-immersion in solvent. Therefore, care must be taken during the liftoff process. Use the appropriate tweezers dedicated for this step, and process the sample in a designated "dirty" beaker to avoid contamination of clean tools and materials.

4.4.3 Silicon-on-insulator (SOI) substrate

Process	Steps	Notes
Wafer preparation	Outsourced	See SOI wafer prep.
Layer 1: Markers and Holes		
Substrate cleaning	ACE, 21°C, uc power 9, 5 min IPA, 21°C, uc power 9, 5 min N2 blow dry	Cleaning same as for Si substrate.
Spin and bake e-beam resist	Prebake, 21°C, 1 min Spin, CSAR AR-P 6200.13, 6 krpm, 1 min (acceleration 1.5 krpm/s) Bake, 160°C, 1 min	
E-beam flow prep	CAD file preparation Beamer flow file preparation	
E-beam patterning	Markers and holes, 0.8 or 1 nm beam, dose 300-330 μC/cm^2 with PEC	
Development	AR 600-549, 21°C, 1 min IPA, 21°C, 30 sec N2 blow dry	
Silicon etching	Cleaning: Oxygen plasma, 5 min Conditioning: Mixed-nano, 15 min Etching: Mixed-nano, 110 sec Cleaning: Oxygen plasma, 15 min	See SOI RIE.
Resist stripping	NMP, in a beaker immersed in a water bath on a hot plate at 145°C, 1 h ACE, 21°C, uc power 9, 5 min IPA, 21°C, uc power 9, 5 min N2 blow dry	
Layer 2: Circuit		
See Si recipe		
Membrane release	Baking, 120°C, 1 min vapor HF	See Membrane release.

Wafer preparation. The process starts with a silicon-on-insulator (SOI) wafer from Soitec, with a device layer Si thickness $220\ \mathrm{nm}$, buried oxide (BOX) layer $3\ \mu\mathrm{m}$, handle Si thickness $725\ \mu\mathrm{m}$, crystal orientation $< 1,0,0 >$, resistivity $\rho = 5 - 15\ \mathrm{k\Omega \cdot cm}$, diced into die of $10\ \mathrm{mm} \times 10\ \mathrm{mm}$. Silicon-on-insulator (SOI) allows for the fabrication of suspended nanoscale structures by removing or undercutting the buried oxide beneath the silicon device layer. Its processing methods are well established in both industry and research, making it a practical choice of substrate.

E-beam patterning. For details about the parameters for the markers and holes on SOI substrate, see Table 4.5.

Silicon RIE. Etching is a process used to selectively remove material in a controlled manner, leaving behind a desired pattern defined by an etch mask. The system used in this work is an inductively coupled plasma reactive ion etching (ICP-RIE) tool from Oxford Instruments.

Parameters	Markers, Holes
PEC	No
Max number of dose classes	-
Min dose factor	-
Resolution (= Beam step size)	0.005 μm
Fracture mode	LRFT
Field ordering	Floating
Feature order	Array Compaction
Beam Current	0.8-1 nA
Dose	300-330 $\mu C/cm^2$

Table 4.5: **E-beam parameters for etched markers and holes on SOI substrate.**

Parameters	O_2 Descumming	Mixed Nano
Chiller Temperature (°C)	20	20
Backside He Pressure (Torr)	8	10
O_2 Flow (sccm)	20	0
SF_6 Flow (sccm)	0	10
C_4F_8 Flow (sccm)	0	12
LPS - low pressure setpoint (mTorr)	30	5
RF Power (W)	50	30
ICP Power (W)	0	400

Table 4.6: **Process parameters for ICP RIE.** O_2 Descumming is an ICP process to remove resist residues before the coil evaporation, while Mixed Nano is for Si etching.

In this system, an etch gas is introduced and ionized, producing reactive ions that either chemically react with the sample surface or are accelerated toward it to physically sputter material or both. One of the key features of the ICP-RIE tool is the decoupling between plasma generation and ion acceleration. This allows for independent control of the ion density and the ion energy. The ion density is controlled by the ICP power, while the energy with which the ions bombard the sample is set by the RF forward power.

The process is governed by three main parameters. First, the ICP power determines the amount of gas ionized into plasma, thereby setting the plasma density. Second, the RF forward power accelerates the ions toward the sample surface and contributes to the energy transferred during the etch. Third, the gas chemistry determines etch selectivity, material compatibility, and sidewall passivation.

The DC bias, defined as the voltage drop between the plasma and the substrate stage, is a critical parameter because it directly reflects the energy with which ions strike the sample. Etch recipes often aim for a target DC bias, and the RF forward power is adjusted accordingly to reach this value.

The gas flow rate and chamber pressure together set the total amount of gas available in the etch environment. In this process, the chamber pressure is maintained at 15 mTorr, providing a balance between mean free path, plasma stability, and etch directionality.

To ensure effective thermal management during the etch, helium is supplied as a backside cooling gas. Helium backing provides good thermal contact between the sample and the carrier wafer, allowing for stable and repeatable etching conditions. Plasma generation consumes

a significant amount of electrical power, much of which ends up as heat. Maintaining the correct helium backing pressure and flow rate is therefore essential to prevent overheating and preserve etch fidelity.

The chips are mounted onto a carrier wafer using thermal paste. A small amount of paste, typically a dab in the center and one on each corner, is sufficient to secure the chips while also improving thermal conduction to the helium-cooled wafer chuck. Care must be taken to avoid overflow of the paste, which could affect the etch uniformity or contaminate the chamber.

Because high-frequency electrical power is used to generate and maintain the plasma, impedance matching between the power source and the plasma load is critical. A mismatch can cause reflected power, which not only reduces efficiency but could also damage the equipment. An automatic matching unit (AMU) is used to dynamically adjust internal capacitors to minimize reflection by matching the impedance.

Once the plasma is ignited, it emits a visible glow which can be observed through a viewport. This glow provides a visual confirmation of plasma ignition and is useful as a diagnostic to identify potential issues in the early stages of the etch.

The etch process used here follows a pseudo-Bosch strategy, alternating between etching and passivation phases to achieve more vertical profiles.

For silicon etching, sulfur hexafluoride ($\mathrm{SF_6}$) is the primary etchant. When ionized, $\mathrm{SF_6}$ dissociates into reactive species such as SF_x and fluorine ions ($\mathrm{F^-}$). Fluorine chemically reacts with silicon to form volatile byproducts such as $\mathrm{SiF_4}$, which are removed from the chamber via pumping. Without directional ion bombardment, fluorine leads to isotropic etching due to its high diffusivity and reactivity. However, by accelerating heavier ions like $\mathrm{SF_5^+}$ toward the substrate, the process also includes physical milling, introducing a degree of anisotropy.

To further enhance directionality and minimize lateral etching, an inhibitor gas such as octafluorocyclobutane ($\mathrm{C_4F_8}$) is introduced. Upon ionization, this gas produces fragments like $\mathrm{CF_2}$, which deposit a polymer-like layer on all surfaces, providing sidewall passivation. The ion bombardment preferentially removes this layer from horizontal surfaces, allowing vertical etching to proceed while protecting the sidewalls. However, the addition of $\mathrm{C_4F_8}$ typically reduces the overall etch rate, as fluorine and carbon can recombine into stable compounds like $\mathrm{CF_4}$, lowering the concentration of free reactive species.

Membrane release. The HF (hydrofluoric acid) etch mechanism is a critical process in nanofabrication, primarily used to remove silicon dioxide ($\mathrm{SiO_2}$) layers. In this reaction, hydrofluoric acid reacts with $\mathrm{SiO_2}$ in the presence of a catalyst to form volatile byproducts such as silicon tetrafluoride ($\mathrm{SiF_4}$) or hexafluorosilicic acid ($\mathrm{H_2SiF_6}$) along with water ($\mathrm{H_2O}$). The reactions are

$$\mathrm{SiO_2 + 4HF \rightarrow SiF_4 + 2H_2O}$$

$$\mathrm{SiO_2 + 6HF \rightarrow H_2SiF_6 + 2H_2O}$$

A catalyst is required to dissociate HF and initiate etching. Fluorine substitutes into the silicon dioxide network, breaking $\mathrm{Si-O}$ bonds and forming $\mathrm{SiF_4}$. Water generated from the reaction also acts as a catalyst. Although the chemical reaction itself is independent of the etch chamber configuration, the overall etch mechanism and etch rate are highly dependent on the chamber setup.

4.4.4 Back-etched Silicon-on-insulator (SOI-BE) substrate

Process	Steps	Notes
Wafer preparation	Outsourced	See SOI-BE wafer prep.
Layer 1: Markers and Holes		
See SOI recipe.		
Layer 2: Circuit		
See Si recipe until liftoff, no vapor HF release yet.		
Layer 3: Back etching		
Spin and bake protective layer	Spin, LOR 5B, 4 krpm, 1 min (acceleration 1.5 krpm/s) Bake, 160°C, 1 min Repeat 3 times	
Spin and bake bottom	Flip chip Spin, PMMA 950k 4%, 4 krpm, 1 min (acceleration 1.5 krpm/s) Bake, 170°C, 3 min	
E-beam flow prep	CAD file preparation Beamer flow file preparation	
E-beam patterning	All chip except cutouts, 250 nm beam, dose 700 μC/cm^2 without PEC	
Development	water:IPA ratio 1:3, 2 min IPA, 10 sec	
Evaporation	Cr, 50 nm, 1 nm/s	
Liftoff	ACE, in waterbath, 40°C, 1 h	
Bosch etching	Cleaning: Oxygen plasma, 5 min Conditioning Etching Cleaning: Oxygen plasma, 15 min	See Si Bosch etching.
Resist stripping	NMP, in a beaker immersed in a water bath on a hot plate at 145°C, 1 h ACE, 21°C, uc power 9, 5 min IPA, 21°C, uc power 9, 5 min N2 blow dry	
Membrane release	No Baking vapor HF	See Membrane release.

Wafer preparation. The thickenss of the SOI wafer used for this process is $200\ \mathrm{nm}$.

Bosch Si etching. The Bosch DRIE method, originally tailored for micro-electromechanical systems (MEMS), operates through a cyclic two-step process: alternating isotropic etching of silicon using sulfur hexafluoride ($\mathrm{SF_6}$) and conformal passivation using a fluorocarbon gas such as octafluorocyclobutane ($\mathrm{C_4F_8}$). The etching cycle anisotropically removes silicon due to directional ion bombardment, while the deposition cycle forms a protective polymer layer on the sidewalls. This results in vertically etched trenches with high aspect ratios.

A hallmark of the Bosch DRIE process is the scalloped morphology that emerges on etched sidewalls, arising from the repeated alternation between etching and passivation. This scalloping

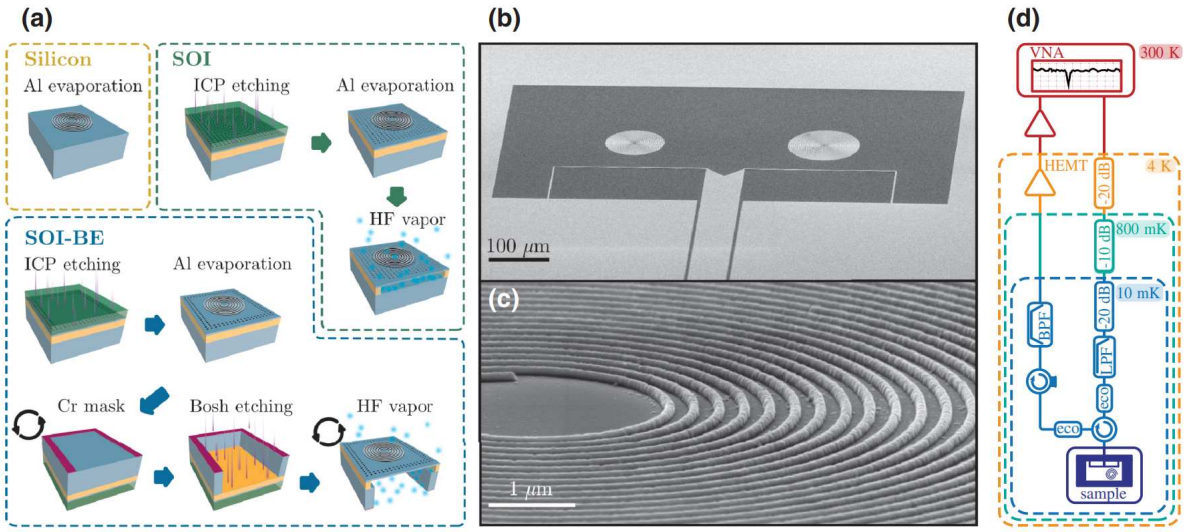

Figure 4.4: **Nanofabrication and measurement setup. a.** Key nanofabrication steps for the different substrates. **b.** SEM image of coil resonators inductively coupled to a shorted coplanar waveguide feedline. **c.** Magnified SEM view of an aluminum coil resonator with $300\ \mathrm{nm}$ pitch on SOI-BE. **d.** Schematic of the measurement setup: the sample is wire-bonded to a printed circuit board, enclosed in a copper package, and cooled to $10\ \mathrm{mK}$ in a dilution refrigerator. Magnetic and radiation shields surround the box. The input from the vector network analyzer (VNA) is attenuated by about $82\ \mathrm{dB}$ (including cable losses and attenuators), filtered by a low-pass filter (LPF), and routed through a circulator. ECCOSORB filters are placed at the input and output of the circulator. The transmitted signal passes through an additional circulator for isolation, then a band-pass filter (BPF), before being amplified by a cryogenic HEMT amplifier followed by room-temperature amplifiers.

becomes a significant issue at the nanoscale due to its pronounced surface roughness. However, this nano-scalloping can be systematically controlled by tuning process parameters such as chamber pressure, radio frequency (RF) power, gas flow composition, and most critically, the timing balance between etch ($\mathrm{SF_6}$) and passivation ($\mathrm{C_4F_8}$) phases. By optimizing the ratio and duration of these cycles, it becomes possible to engineer smooth profiles with precise reproducibility.

Using the patterned resist as a mask, the subsequent Bosch DRIE step allows for the etching of high-aspect-ratio structures. For details see Appendix E.

Membrane Release. For details see Appendix D.

4.5 Experimental methods

4.5.1 Cryo setup

Superconducting devices are designed to have their fundamental frequency f_0 in the microwave range, typically between $4 - 12\ \mathrm{GHz}$. To control the quantum phenomena and suppress thermal excitation, they need to be cooled below $1.2\ \mathrm{K}$, the critical temperature of aluminum, the material from which all these circuits are made. Additionally, lower temperatures also ensure a low thermal population, so that $T \ll hf_0/k_B \approx 480\ \mathrm{mK}$ at $10\ \mathrm{GHz}$. This requires all devices to be operated in a dilution refrigerator.

To achieve millikelvin temperatures, immersing the device into a bath of liquid helium is not enough: it boils at $4\ \mathrm{K}$, and by pumping to lower its vapor pressure, temperatures around $1.2\ \mathrm{K}$ can be reached. To go lower, more advanced cryogenic systems are required. The BlueFors LD-250 dilution refrigerator is an example. This dry cryostat uses a mechanical pulse-tube cooler to establish the $4\ \mathrm{K}$ stage. From there, a closed-cycle mixture of $^3\mathrm{He}$ and $^4\mathrm{He}$ allows dilution cooling down to approximately $10\ \mathrm{mK}$. The cryostat is composed of several subsequent plates at different temperatures, nominally $295\ \mathrm{K}$ (RT), $50\ \mathrm{K}$, $4\ \mathrm{K}$, $0.8\ \mathrm{K}$ (still), $0.1\ \mathrm{K}$ (cold plate, CP) and $10\ \mathrm{mK}$ (mixing chamber, MXC). The cryostat used is nicknamed "Fermi".

4.5.2 Measurement setup

Apart from low temperatures, cQED experiments require control over microwave signals: to reach the single-photon regime necessitates to minimize thermal and electronic noise, so special attention needs to be placed for thermal anchoring, magnetic shielding, high-frequencies filtering, low-noise amplification. A sketch of the setup is shown in Fig. 4.4.d.

Input line. The devices are mounted on the MXC plate at $10\ \mathrm{mK}$, and are connected through coaxial microwave lines to the room temperature elctronics. These coaxial lines enter the fridge via hermetic vacuum feedthroughs and are anchored at each temperature stage using attenuators and mounting blocks to minimize heat transfer and prevent thermal radiation from reaching the qubit stage. Since all signals originate at room temperature, they carry significant Johnson-Nyquist noise. Attenuators are placed at multiple stages rather than concentrating them at the $10\ \mathrm{mK}$ stage, since they dissipate power and could cause local heating: the location of the attenuators need to take into account the cooling power at each stage. Proper attenuation at the coldest stage is necessary to prevent thermal noise from warmer stages reaching the sample. Each attenuator introduces noise corresponding to its temperature, so the final attenuation stage at $10\ \mathrm{mK}$ is critical. $50\ \mathrm{dB}$ attenuators were located as $20\ \mathrm{dB} - 10\ \mathrm{dB} - 20\ \mathrm{dB}$ at $4\ \mathrm{K} - 800\ \mathrm{mK} - 10\ \mathrm{mK}$, respectively. Including cryostat ($\sim 20\ \mathrm{dB}$) and room temperature cables ($\sim 13\ \mathrm{dB}$), for a total of $\sim 83\ \mathrm{dB} \pm 5\ \mathrm{dB}$ attenuation at $8\ \mathrm{GHz}$.

In addition to attenuation, all input lines are filtered to reject noise coming from frequencies outside the measurement band. Two input lines are implemented, with identical attenuator and filter configurations, low-pass filter with $12\ \mathrm{GHz}$ cutoff from K&L Microwave. Eccosorb-filters are in-house made and detailed in Ref. [Red22] and take care to filter frequencies above $50\ \mathrm{GHz}$ where the commercially available filters don't operate anymore. For a similar reason, the inner side of the MXC copper shield is painted with Stycast shielding, following the approach described in Ref. [HGWC86].

After the filters, the signal passes through one of circulators, to allow the reflection measurement, allowing to isolate the sample from amplifier noise. The signal then enters a 6-port coaxial switch (Radiall), which allows for the selection among six different samples during a single cooldown.

Output line. On the output side, the reflected signals, often on the order of a few single-photon events, must be amplified by factors up to 10^8 to be detectable. This is achieved through a cryogenic and room-temperature amplifiers.

Before reachign the HEMT at the $4\ \mathrm{K}$ stage the signal the signal passes through 2 isolators Memstar for the $4-8\ \mathrm{GHz}$ range and LNF for the $8-12\ \mathrm{GHz}$ and a bandpass filter together with an Eccosorb filter to prevent amplifier noise from entering through the output.

A High Electron Mobility Transistor (HEMT) amplifier is located at the $4\ \mathrm{K}$ stage. it contributes noise equivalent to 7–10 photons and $40\ \mathrm{dB}$ gain.

Inter-stage connections use stainless steel, which has low thermal conductivity. The output cable from the $50\ \mathrm{K}$ stage to room temperature is made from a combination of stainless steel and beryllium copper. Within the $10\ \mathrm{mK}$ stage, where high thermal conductivity and low signal loss are both required, copper cables are used. Components such as attenuators, circulators, and filters are thermally anchored to the mixing chamber plate to ensure they are well thermalized and do not introduce heat to the stage.

4.5.3 Chip layout and packaging

These resonators were distributed across several samples and measured over different cooldowns, with each chip containing sixteen resonators of varying numbers of turns and pitch. All resonators were coupled, grouped in pairs, to eight feedlines, which taper and split in the middle into two parts (See Fig. 4.4.b). For each coupler, the two resonators were intentionally designed to have significantly different resonance frequencies. The distance from the outermost turn of each coil to the feedline was kept constant. Simulations in Ref. [Per21].

The sample is mounted in a box made of oxygen-free high-conductivity copper, featuring a cutout beneath the chip to suppress parasitic box modes and shift them above $12\ \mathrm{GHz}$. The box is sealed with a lid, made out of the same material, to shield the device from external RF radiation. The boxes are made at the ISTA Machine Shop.

To interface the sample with the rest of the experimental setup, a printed circuit board (PCB) is mounted with screws on the bottom half of the box. The PCB hosts four 50 Ω coplanar waveguides and is fabricated on AD1000 Rogers laminate by an external manufacturer. It includes a central cutout to accommodate the chip. Surface-mounted MMPX connectors are soldered at the outer edge of the PCB.

The chip is glued to the rim of the cutout using four small drops of silver paste at the corners. Excess paste should be avoided, as it may spread into the gap between the chip and PCB, potentially overflowing and causing shorts. Once the paste has dried, wire bonds are made between the on-chip coplanar transmission lines and ground planes and the corresponding PCB pads, using aluminum wires.

To suppress slot-line modes, on-chip bonds are added across the launcher. These have a triangular shape. Three aluminum wires are used to connect the launcher to the PCB CPW, and as many as possible are used to bridge the ground planes. The bonds should be low inductance and form low arcs, not too tall, so as to avoid contact with the lid and minimize coupling to flux noise.

Once the sample is mounted, connected, and the box closed with screws, care is taken to ensure the lid presses securely on the MMPX connectors and that all components are properly aligned, without any strain applied: this could rip off the connector. Electrical connection is then verified by checking that there is a finite (non-zero) resistance between the central conductor and ground, confirming that there are no shorts.

In all of the samples the waveguide is shorted to ground near the device for inductive coupling. Resistance measurements between the PCB conenctor and ground will result in a resistance of $50 - 100\ \Omega$.

Finally the box hosts threads on the side and on the bottom so that can be mounted on a cold finger at the MXC plate of the dilution refrigerator.

4.6 Measurement results

One hundred and four resonators were measured using a Vector Network Analyzer (VNA). The single-port coupling reflection coefficient S_{11}, which includes both the real (in-phase) and imaginary (quadrature) components of the reflected signal, was recorded as a function of frequency and input power.

The collected data were fitted using an analytical model introduced in Ref. [Gao08], which extends the standard Lorentzian response to account for imperfections commonly encountered in experimental setups. The fitting function is given by:

$$S_{11}(f) = A_0 e^{-i(\phi + 2\pi f \tau)} \left(1 - \frac{2Q_i - 2iQ_iQ_e\ \delta f/f_0}{(Q_i + Q_e) + 2iQ_iQ_e(f - f_0)/f_0}\right), \tag{4.27}$$

where the A_0 is an amplitude that captures the overall gain and attenuation in the measurement chain (dimensionless measurement baseline), ϕ accounts for a static phase offset, while τ introduces a frequency-dependent phase correcting for signal delay accumulated in the coaxial cables. Q_e and Q_i represent the external and internal quality factors, respectively, with Q_e related to losses due to coupling to the environment and Q_i to intrinsic dissipation within the resonator. The resonance frequency is denoted by f_0, and δf is an asymmetry parameter introduced to fit resonance features that deviate from a purely symmetric (Lorentzian) shape. Such distortions are often due to circuit imperfections or reflections in the measurement setup (see Subsection 2.4.5) [Fan61; RGS+23].

4.6.1 Resonant frequencies

This subsection presents a detailed summary of the resonance frequencies measured for all coils. Fig. 4.5 shows the fundamental resonance frequencies f_0

$$f_0 = \frac{\omega_0}{2\pi} = \frac{1}{2\pi\sqrt{L_{\text{tot}}C}}, \tag{4.28}$$

as a function of the number of coil turns n for each pitch p and substrate. The solid lines correspond to fits based on the Eq. (4.23) for f_g, the purely geometric resonance frequency, adjusted to include a correction accounting for the kinetic inductance L_k. This leads to a modified expression for the resonance frequency

$$f_0 = f_g(n, p, R_i, \varepsilon_{\text{eff}}) \cdot \sqrt{\frac{L_g(n, p, R_i)}{L_g(n, p, R_i) + L_k}}, \tag{4.29}$$

where R_i is the internal radius[12]. The only fitting parameter in this model is the effective dielectric permittivity ε_{eff}, which enters through f_g: its fitted values are reported in Table 4.8 for the

[12] $R_i^{\text{Si}} = 5\ \mu\text{m}$ ($p = 1\ \mu\text{m}$); $2.5\ \mu\text{m}$ ($p = 0.5\ \mu\text{m}$) and $1.5\ \mu\text{m}$ ($p = 0.3\ \mu\text{m}$). $R_i^{\text{SOI}} = 3\ \mu\text{m}$. $R_i^{\text{SOI-BE}} = 3\ \mu\text{m}$.

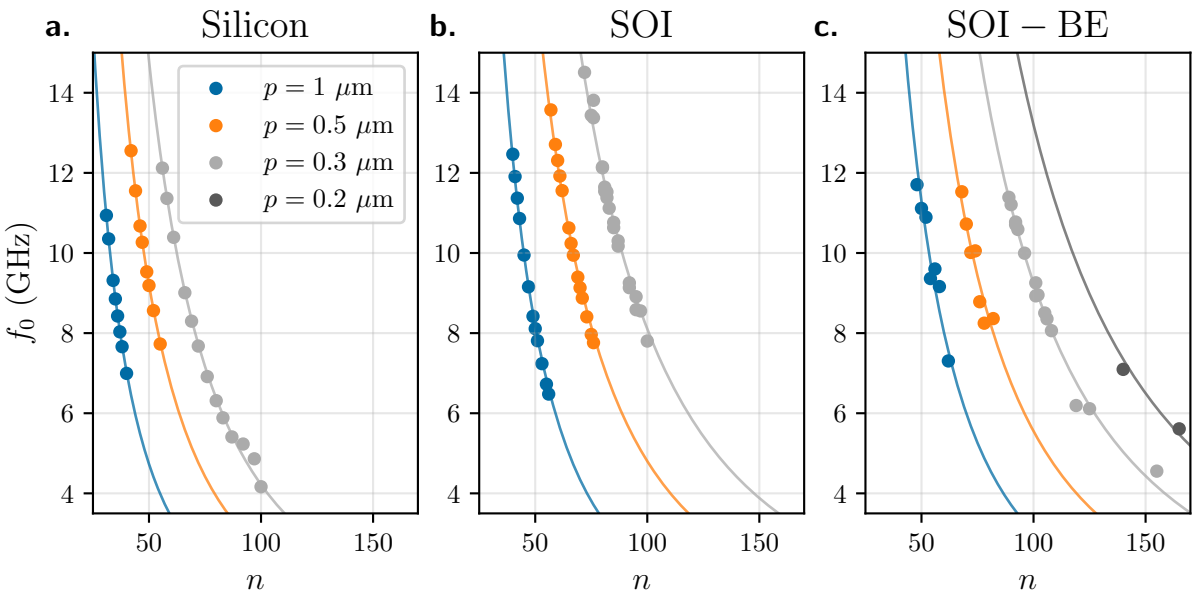

Figure 4.5: **Resonance frequency scaling of coil resonators.** Fundamental resonance frequency f_0 as a function of the number of coil turns n for each substrate. Solid lines represent fits to the modified resonance frequency model given by Eq. (4.29), which incorporates a correction for the kinetic inductance.

three different substrate. L_g is calculated using the analytical expression in Eq. (4.24), while L_k is determined from temperature-dependent measurements analyzed using the Mattis–Bardeen formalism (see Subsection 4.6.3).

Most of the measured resonance frequencies lie within the setup's readout ranges of $4-8$ GHz and $8-12$ GHz. Some frequencies extend slightly beyond these bands, but the signal-to-noise ratio remained sufficient for reliable detection.

The fundamental frequency scales as $f_0 \propto 1/n^2$.

Linearity vs power. To analyze the resonator nonlinearity, the system can be modeled as a simple nonlinear oscillator with a self-Kerr interaction term:

$$H = \hbar \cdot 2\pi f_0 \cdot \hat{a}^\dagger \hat{a} - \frac{1}{2}\hbar \cdot 2\pi K_{11} \cdot \left(\hat{a}^\dagger \hat{a}\right)^2, \tag{4.30}$$

where f_0 is the fundamental resonance frequency, $\hat{a}$ and $\hat{a}^\dagger$ are the bosonic annihilation and creation operators, and K_{11} is the self-Kerr nonlinearity coefficient in Hz.

Fig. 4.6.b shows the resonance frequency shift $\Delta f = f_0(\langle n_{\mathrm{ph}} \rangle) - f_0(n_{\mathrm{ph,min}})$, with $n_{\mathrm{ph,min}} = 14.4$, as a function of the average photon number $\langle n_{\mathrm{ph}} \rangle$ in a resonator on SOI-BE substrate with $n = 155$, $p = 0.3$ μm and outer diameter $2 \cdot R_e = 105$ μm. The photon number is swept by varying the input power from -40 dBm to $+10$ dBm. Taking into account an input line attenuation of -81.232 dB (plus an additional -20 dB attenuation at room temperature), the corresponding photon population measured spans from approximately 14 to 2×10^6. The resonance frequency remains nearly unchanged up to approximately 1.5×10^4 photons. At higher photon numbers, it begins to drift and the resonance profile deviates from a Lorentzian shape (curves in Fig. 4.6.a), indicating the onset of nonlinear effects and possible local suppression of superconductivity. In this regime of large photon numbers, the effect of

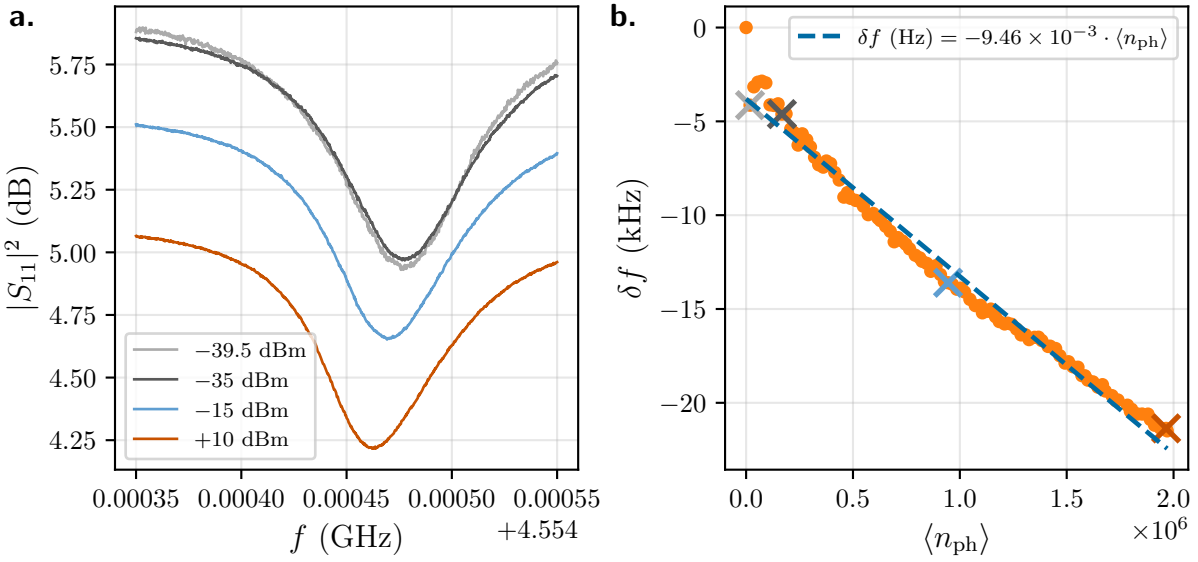

Figure 4.6: **Coil resonator linearity. a.** Resonance line shapes measured at various input powers, showing increasing distortion at high photon numbers. For powers of -15 dBm and $+10$ dBm, the response deviates from a Lorentzian profile. **b.** Resonance frequency shift $\Delta f = f_0(\langle n_{\mathrm{ph}} \rangle) - f_0(n_{\mathrm{ph,min}})$ as a function of average photon number $\langle n_{\mathrm{ph}} \rangle$, extracted from the same device, a coil resonator with $n = 155$ turns, pitch $p = 0.3$ μm, and outer diameter $2 \cdot R_e = 105$ μm , fabricated on an SOI-BE substrate. The frequency remains stable up to about 10^4 photons, beyond which it begins to shift linearly. A linear fit yields a frequency shift of 9.46 mHz per photon.

the nonlinearity becomes comparable to the resonator linewidth. Also, the baseline drops, indicating saturation of the output amplifier.

The average photon number at resonance is calculated using Eq. 2.49

$$\langle n_{\mathrm{ph}} \rangle = \frac{P_{\mathrm{in}}(\mathrm{W})}{h f_0} \cdot \frac{4\kappa_e}{(\kappa_i + \kappa_e)^2}, \tag{4.31}$$

where P_{in} is the input power, in W, at the resonator, f_0 is the resonance frequency, and $\kappa_e = 2\pi f_0/Q_e$, $\kappa_i = 2\pi f_0/Q_i$ are the external and internal decay rates in rad/s, respectively.

The nonlinearity is quantified by the resonance frequency shift per photon, $\Delta f/\langle n_{\mathrm{ph}} \rangle$. A linear fit to the data yields

$$\Delta f = f_0(n_{\mathrm{ph}}) - f_0(n_{\mathrm{ph,min}}) = 9.46 \text{ mHz/photon}, \tag{4.32}$$

corresponding to a self-Kerr coefficient of

$$K_{11} \approx 0.3 \text{ mHz}. \tag{4.33}$$

The shift varies slightly between different coils and is difficult to measure accurately, as the large photon numbers required to resolve it can induce superconducting breakdown.

The extremely low self-Kerr nonlinearity measured in these planar coils is unmatched by other reported superinductors, supporting their classification as highly linear components. By comparison, higher values of K_{11} have been reported in other high impedance platforms: grAl

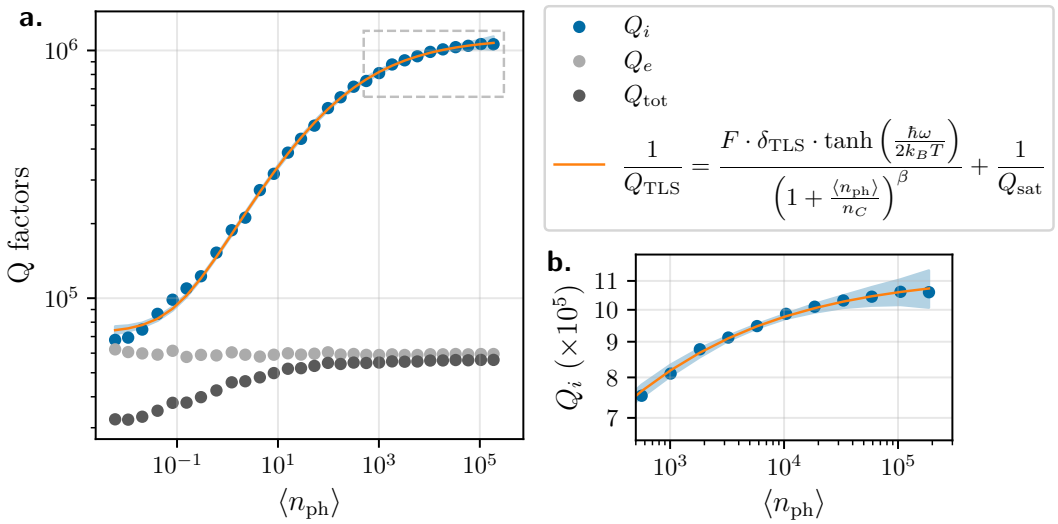

Figure 4.7: **Internal quality factor vs. intraresonator photon number. a.** Measured Q_i of a representative overcoupled coil (pitch $p = 300$ nm, $n = 155$ turns, $Q_e = 6 \times 10^4$ on SOI-BE) as a function of the mean intraresonator photon number n_{P}. Blue dots are values extracted from Lorentzian fits, and the shaded band represents the 90% confidence interval. The yellow line is a fit to a TLS model. **b.** Close-up of the internal quality factor near saturation.

resonators exhibit K_{11} values ranging from 7 to 95 Hz [KSP+25], and from 10^{-2} to 10^6 Hz per photon [MGK+18] depending on film thickness and resistivity. NbN and TiN resonators show self-Kerr nonlinearities in the range of 10 to 10^5 Hz per photon [FAdP+23]. However, impedance values are not always specified, making direct comparison less straightforward. For the Josephson junction chain in Ref. [MPK+12], the expected value was $K_{11} = 10$ MHz, while for the suspended Josephson junction chains in Ref. [JCN+25], it was measured to be $K_{11} = 9$–17.5 kHz.

4.6.2 Quality factor

A characterization of the linewidth was performed on the same reference coil resonator fabricated on SOI-BE substrate as in Subsection 4.6.1-linearity vs power. As a reminder, the device has a pitch of 300 nm and consists of 155 turns, resulting in a fundamental resonance frequency at 4.55 GHz and a calculated geometric inductance of 933.9 nH (Eq. 4.24). This resonator is a representative example among SOI-BE coils and was measured inside two radiation shields (most of the resonators were not). It was also fabricated with an optimized vapor-phase hydrofluoric acid release process (Test 13 in Appendix D), which is crucial to avoid fluorination of aluminum and a clean undercut to reduce dielectric losses from the SiO_2 residues on the membrane interface.

The complete power- and temperature-dependent behavior of a resonator mode can be accurately captured by a model that includes three loss mechanisms [CMD+23]: two-level systems (Q_{TLS}), equilibrium quasiparticles (Q_{QP}), and a power- and temperature-independent loss channel (Q_{sat}) that sets the limit for Q_i at high microwave powers,

$$\frac{1}{Q_i} = \frac{1}{Q_{\mathrm{TLS}}(n_{\mathrm{ph}}, T)} + \frac{1}{Q_{\mathrm{QP}}(T)} + \frac{1}{Q_{\mathrm{sat}}}. \tag{4.34}$$

Power dependent behavior. Fig. 4.7 presents the internal quality factor Q_i as a function of the average intraresonator photon number $\langle n_{\mathrm{ph}} \rangle$. The high-power saturation is consistent with losses caused by TLSs, which typically arise from surface defects or dangling bonds. As the mean intraresonator photon number increases, the TLS bath saturates, reducing dielectric loss and thus increasing the internal quality factor Q_i.

The data is fitted using the TLS loss model present in Ref. [Gao08]:

$$\frac{1}{Q_{\mathrm{TLS}}(n_{\mathrm{ph}})} = \frac{F \cdot \delta^0_{\mathrm{TLS}} \cdot \tanh\left(\frac{\hbar\omega}{2k_B T}\right)}{\left(1 + \frac{n_{\mathrm{ph}}}{n_C}\right)^{\beta}} + \frac{1}{Q_{\mathrm{sat}}}, \tag{4.35}$$

where F is the filling factor of the TLS material, i.e. the fraction of the electric field in the lossy material, δ^0_{TLS} is the intrinsic TLS loss tangent $\delta^0_{\mathrm{TLS}} = 1/Q_{\mathrm{TLS},0}$, n_C is the critical photon number required to saturate TLS, β is a phenomenological exponent describing the saturation behavior, and Q_{sat} represents the loss floor due to residual mechanisms such as quasiparticles[13] or radiation.

For the device under study, $\beta = 0.4$ and deviates from the canonical $\beta = 0.5$, suggesting weak TLS correlations [BSK+17]. The fit also yields an effective TLS loss tangent of

$$F \cdot \delta_{\mathrm{TLS}} = 1.3 \cdot 10^{-5} \tag{4.36}$$

and a saturation quality factor

$$Q_{\mathrm{sat}} \approx 1.1 \cdot 10^{6}. \tag{4.37}$$

The device with the best performances has a tighter pitch of $200\ \mathrm{nm}$, on SOI-BE, and shows an order of magnitude lower TLS loss, comparable to state-of-the-art millimeter-sized coplanar waveguide resonators fabricated on high-quality sapphire substrates [MNB+12].

Additionally, stronger capacitive coupling to the feedline (corresponding to smaller external quality factors Q_e) was noticed to have a correlation with reduced internal quality factor Q_i. However, when Q_e exceeds approximately 5×10^4, the high-power Q_i consistently surpasses 10^6. A detailed overview of the measured quality factors across devices is in Table 4.9.

In a comparative study [TSH+25] of superconducting resonator geometries, it was demonstrated that Archimedean spiral resonators fabricated from titanium nitride (TiN), significantly outperform conventional coplanar waveguide resonators. The spiral resonators exhibited intrinsic quality factors approaching 10^7 at the single-photon level, representing a two- to fourfold enhancement over their CPW counterparts. This improvement is primarily attributed to the spiral geometry, which, as confirmed through COMSOL simulations, promotes a more uniform distribution of the electromagnetic field. Such field homogeneity reduces participation of lossy interfaces and minimizes dielectric loss from TLSs.

Despite these advantages, the outer regions of the spiral present more complex field distributions that warrant further detailed modeling. To support performance analysis, the study also introduces an analytical expression for the voltage distribution along the spiral. This model enables efficient and accurate computation of the electric field profile, essential for participation ratio evaluations and loss predictions. The spiral resonators employed in the study featured larger physical dimensions and pitch than those typically explored here, yet still maintained high characteristic impedance values near $1\ \mathrm{k}\Omega$.

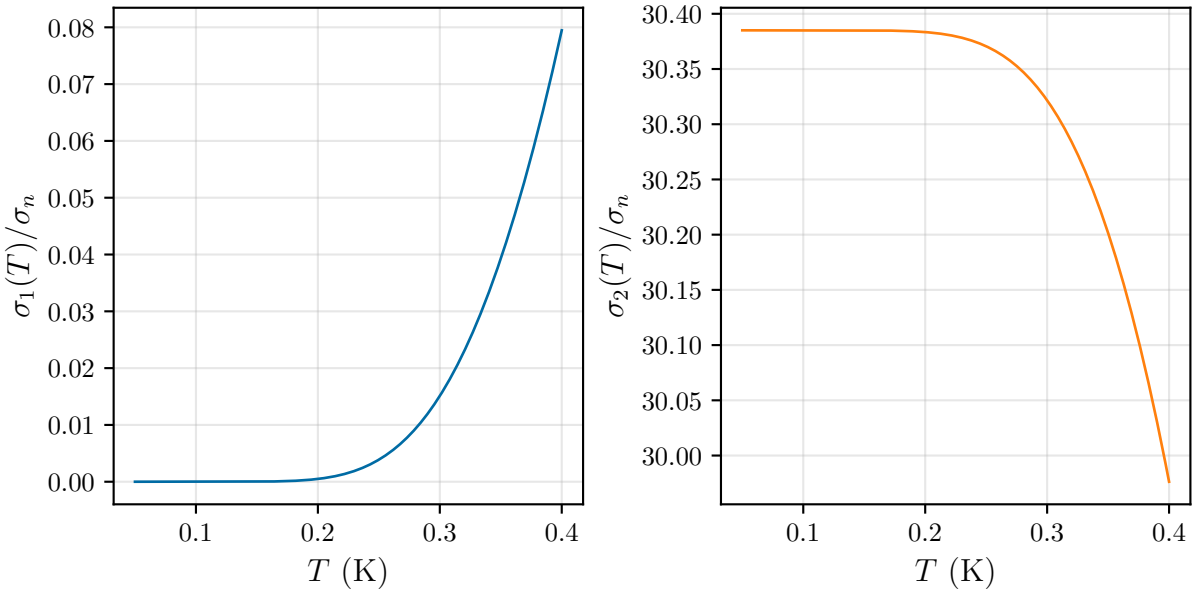

Figure 4.8: **Temperature dependence of complex conductivity. a.** Calculated real component of the complex conductivity, σ_1, following Eq. 4.38. **b.** Calculated imaginary component of the complex conductivity, σ_2, following Eq. 4.39. Both plots are calculated for the coil on SOI-BE with $f_0 = 4.55$ GHz, made out of aluminum $T_C = 1.2$ K.

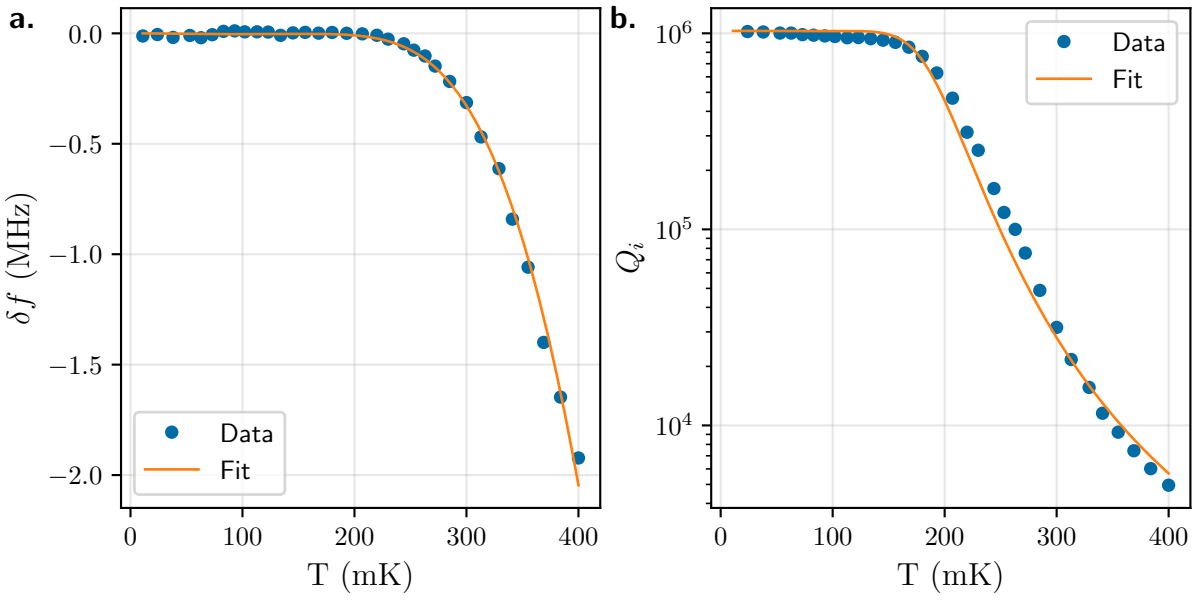

Figure 4.9: **Temperature dependence of resonator properties.** Measured values for a representative overcoupled coil resonator ($p = 300$ nm, $n = 155$, $Q_e = 6 \times 10^4$) on an SOI-BE substrate. **a.** Resonance frequency shift as a function of temperature, with dots representing measured data and the line showing a fit to the BCS model, yielding a kinetic inductance $L_k = 58.0$ nH. **b.** Internal quality factor Q_i versus temperature for the same device; the line is the BCS fit.

Temperature dependence. Measurements performed as a function of temperature show that increasing the fridge temperature results in a decrease of both resonance frequency and internal quality factor (see Fig. 4.9). This behavior arises from the temperature-dependent surface resistance and reactance of the superconductor, as expected from the complex conductivity $\sigma(T) = \sigma_1(T) - i\sigma_2(T)$ introduced in Ref. [GT57]. In the limit of $hf \ll \Delta(0)$ and $k_B T \ll \Delta(0)$, that is, the microwaves and thermal excitations are low energy compared to the superconducting gap, the superconductor behaves as if it is in its ground state, with negligible quasiparticle excitations. The temperature dependence of the conductivity is expressed by the Mattis-Bardeen relations [GZV+08; Gao08]

$$\frac{\sigma_1(T)}{\sigma_n} = \frac{4\Delta(0)}{hf} e^{-\frac{\Delta(0)}{k_B T}} \sinh\left(\frac{hf}{2k_B T}\right) K_0\left(\frac{hf}{2k_B T}\right), \tag{4.38}$$

$$\frac{\sigma_2(T)}{\sigma_n} = \frac{\pi\Delta(0)}{hf}\left[1 - 2e^{-\frac{\Delta(0)}{k_B T}} e^{-\frac{hf}{2k_B T}} I_0\left(\frac{hf}{2k_B T}\right)\right], \tag{4.39}$$

where σ_1 and σ_2 are the real and imaginary part of the conductivity, σ_n is the normal-state conductivity, Δ the superconducting energy gap, and I_0 and K_0 are the zeroth-order modified Bessel functions of the first and second kind, respectively.

The real component $\sigma_1(T)$ corresponds to losses from quasiparticles, which lead to energy dissipation in the resonator, while the imaginary component $\sigma_2(T)$ reflects the inductive response of the superconducting Cooper pairs. This inductive contribution determines the superconductor's ability to store and transfer energy without dissipation and is directly linked to its kinetic inductance L_k.

Fig. 4.8 presents the calculated real and imaginary components of the complex conductivity as functions of temperature. At low temperatures, the available thermal energy is insufficient to break a significant number of Cooper pairs, resulting in only a small population of quasiparticles. Since $\sigma_1 \propto n_{\mathrm{qp}} \propto e^{-\Delta/k_B T}$, its value remains extremely small as $T \to 0$, where $\Delta(T) \to \Delta(0)$. This behavior arises because $\Delta(0)$ is much larger than $k_B T$, suppressing quasiparticle generation. As the temperature increases, more quasiparticles are excited, leading to a corresponding rise in σ_1. In contrast, Fig. 4.8.b shows a decreasing trend for σ_2. This can be understood from the relation $L_k \propto 1/\sigma_2$: with increasing temperature, the higher quasiparticle density enhances the kinetic inductance, which in turn reduces σ_2.

The surface complex conductance governs the frequency and quality factor shifts, expressed by the Mattis-Bardeen formulas [GZV+08], where the relative resonance frequency shift δf and inverse internal quality factor Q_i are given by:

$$\frac{\delta f(T)}{f(0)} = -\frac{\alpha\gamma}{2}\frac{\delta\sigma_2(T,\Delta)}{\sigma_2(T,\Delta)}, \tag{4.40}$$

$$\delta Q_i^{-1}(T) = \alpha\gamma\frac{\delta\sigma_1(T,\Delta)}{\sigma_2(T,\Delta)}. \tag{4.41}$$

The parameter $\alpha = L_k/(L_g + L_k)$ represents the kinetic inductance fraction and $\gamma = -1$ for thin-film aluminum. The superconducting gap $\Delta(0)$ is taken as the bulk value, appropriate for the $100\ \mathrm{nm}$ film thickness used here [CEP69].

[13] Comparing Eq. 4.35 to the more general Eq. 4.34, the Q_{QP} term is included in Q_{sat} one because not power dependent.

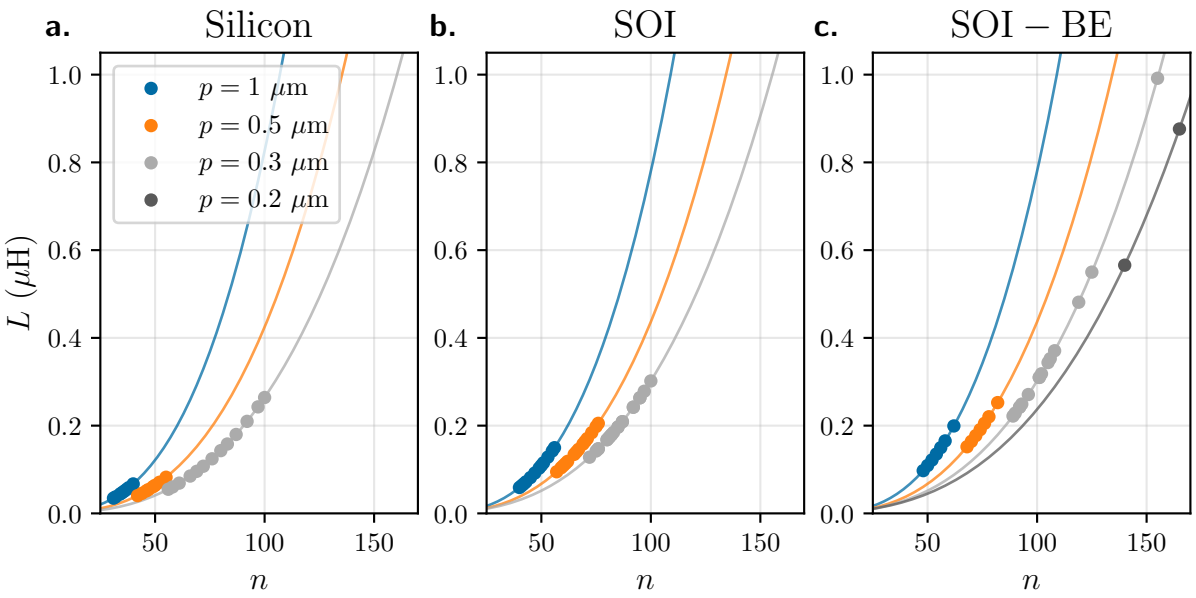

Figure 4.10: **Inductance scaling of coil resonators.** Total inductance L as a function of the number of coil turns n for each substrate. Solid lines represent the sum of the geometric contribution L_g (Eq. 4.24) and the kinetic contribution L_k (Eq. 4.42).

4.6.3 Inductance

The geometric inductance, obtained from Eq. 4.24, is shown in Fig. 4.10.From the temperature dependence analysis, the kinetic inductance was determined to be $L_k = 58.0\ \mathrm{nH}$, corresponding to 5.9 % of the total inductance. Using the relation

$$L_k = \mu_0 \lambda_{\mathrm{L}}^2(0) \frac{\ell}{wh}, \tag{4.42}$$

where μ_0 is the vacuum permeability, and ℓ, w, and h are the length, width, and thickness of the superconducting wire, respectively, we infer a London penetration depth of $\lambda_{\mathrm{L}}(0) = 147\ \mathrm{nm}$. This value is substantially higher than the bulk value for aluminum ($\sim 15\ \mathrm{nm}$), which is attributed to the thin-film geometry ($100\ \mathrm{nm}$ thickness) of the metal [Gao08]. This effective penetration depth is subsequently used to calculate kinetic inductance corrections across all devices in this study.

The total inductance $L_{\mathrm{tot}} = L_g + L_k$ spans from approximately $35\ \mathrm{nH}$ to $992\ \mathrm{nH}$.

4.6.4 Effective permittivity and capacitance

Fitting the measured resonance frequencies with Eq. 4.29 it is possible to extract the values of $\varepsilon_{\mathrm{eff}}$ for the different substrates as reported in Table 4.8.

For the Silicon substrate, the effective permittivity can be approximated by the simplified conformal mapping expression $\varepsilon_{\mathrm{eff}} \approx (\varepsilon_{\mathrm{Si}} + \varepsilon_{\mathrm{air}})/2 = 6.5$, which is remarkably close to the value obtained from fitting. In contrast, the SOI-BE substrate exhibits an $\varepsilon_{\mathrm{eff}}$ close to unity, indicating an environment dominated by vacuum and very low-permittivity material beneath the coil, i.e. just the $200\ \mathrm{nm}$ thick Si membrane.

The coil capacitance C ranges between $0.88\ \mathrm{fF}$ and $7.71\ \mathrm{fF}$ (Table 4.9). The values of the capacitance are obtained from substituting the equation of the total inductance ($L_{\mathrm{tot}} = L_g + L_k$)

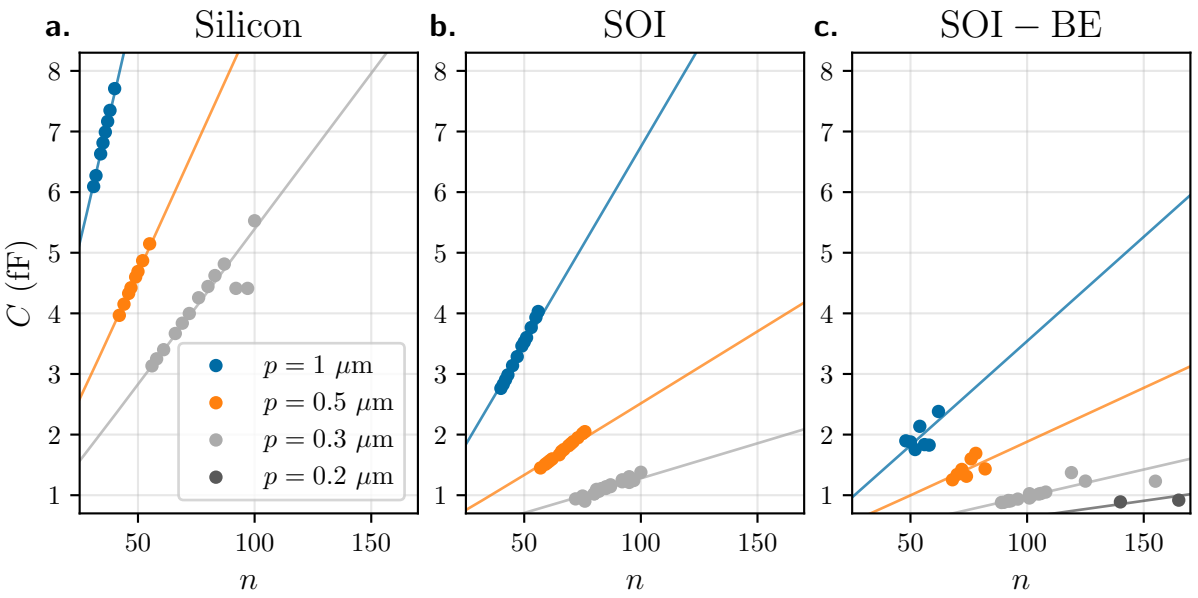

Figure 4.11: **Capacitance scaling of coil resonators.** Effective capacitance C as a function of the number of coil turns n for each substrate. Data points are obtained from the measured resonance frequency f_0, using $f_0 = 1/(2\pi\sqrt{(L_g + L_k)C})$ with L_g and L_k given by Eqs. 4.24 and (4.42), respectively. Solid lines correspond to capacitances extracted from $f = 1/\left(2\pi\sqrt{(L_g + L_k)C}\right)$, where f is taken from Eq. 4.29.

Substrate	ε_{eff}
Silicon	6.89 ± 0.09
SOI	2.04 ± 0.93
SOI-BE	1.25 ± 0.19

Table 4.8: **Effective permittivity of different substrates.** Extracted values of effective permittivity (ε_{eff}) for various substrates.

into Eq. 4.28 of the fundamental resonance frequency and knowing the geometry of the coil and the measured resonant frequency. The values are reported in Fig. 4.11 for the three substrates.

Fig. 4.12.a provides a comparison illustrating the effects of reducing the effective permittivity ε_{eff} on the coil capacitance C. As expected, decreasing ε_{eff} reduces the capacitance, while the inductance remains constant because all substrates have relative permeability $\mu_r = 1$. We observe a linear scaling of C with the coil radius $r \approx np$, consistent with the previously derived proportionality $C \sim np$. Although the majority of coils in this study has a fixed inner radius of approximately $3\ \mu\text{m}$, in the regime of large filling factor ρ and large turn number $n \gg 1$, the approximation $r = np$ becomes accurate. Consequently, a coil's self-capacitance can be estimated simply from its outer radius, which highlight the advantages of device miniaturization.

To quantify the suppression of capacitance due to substrate effects, we extract the slope $\mathrm{d}C/\mathrm{d}r$ for each combination of pitch p and substrate type, resulting in nine gradient values. These gradients are found to be largely independent of pitch and are therefore averaged to yield a single value per substrate, as reported in Fig. 4.12.a. An exception is observed for the SOI substrate, which exhibits a pronounced pitch dependence (see inset of Fig. 4.12.a). This

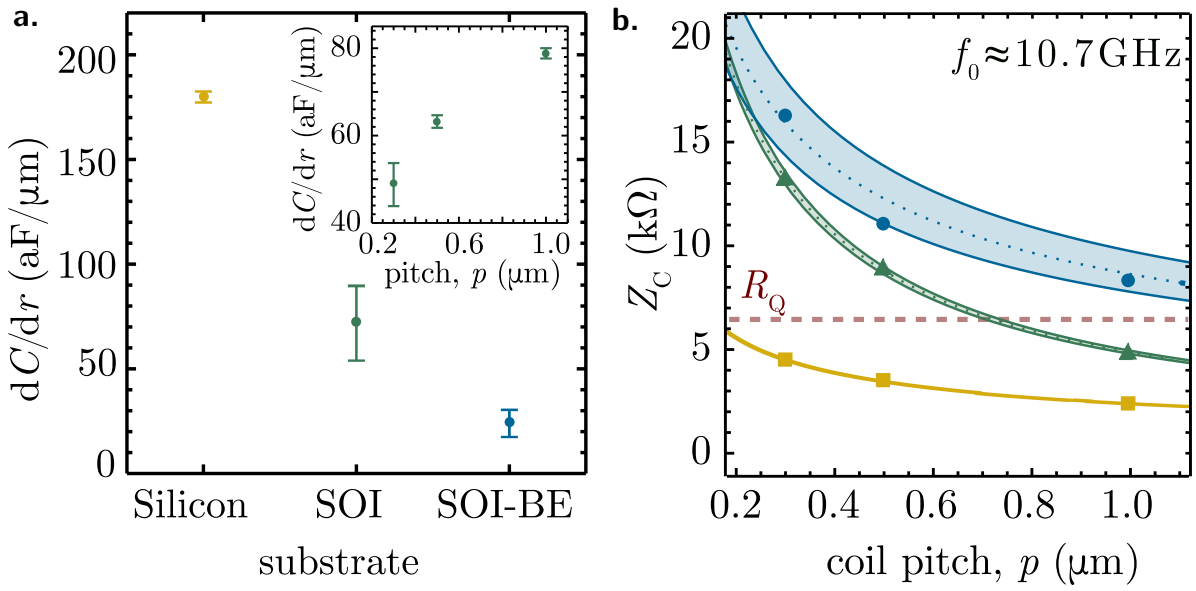

Figure 4.12: **Substrate-dependent capacitance and impedance trends. a.** Extracted capacitance per unit radius for three substrates. Dots indicate the average capacitance added by increasing the coil radius by 1 μm, with the larger error bar for SOI reflecting pitch dependence shown in the inset. **b.** Characteristic impedance as a function of coil pitch at $f_0 \approx 10.7$ GHz. Dashed lines show impedance scaling for each substrate (silicon in yellow, SOI in green, SOI-BE in blue) using the average ε_{eff} from Fig. 4 fits. Bands reflect permittivity uncertainty; for SOI, strong pitch dependence is included via quadratic interpolation.

behavior arises because coils with larger pitch have increased physical size and thus a broader electric field distribution. Given that the SOI substrate is not electrically homogeneous, a larger coil pitch leads to a greater fraction of the electric field penetrating into the high-permittivity silicon handle wafer, thereby increasing ε_{eff}. This spatial field distribution is the primary source of the larger uncertainty (90% confidence interval) in ϵ_{eff} reported earlier.

The spatial extent and vertical decay of the electric field also explain why changing the substrate from bulk silicon to SOI provides a larger capacitance suppression compared to transitioning from SOI to SOI-BE, as seen in Figs. 4.12.a and 4.12.b. This is because the electric field is most concentrated near the coil and decays rapidly with vertical distance. By removing the 3 μm silicon layer directly beneath the coil (as in SOI-BE), the strongest part of the electric field resides in vacuum, resulting in significant capacitance reduction. Simulations indicate that this suppression effect saturates for vacuum gaps around 20 μm, depending on coil geometry.

4.6.5 Characteristic impedance

Fig. 4.13 illustrates the characteristic impedance Z_C, calculated using the relation

$$Z_C = 2\pi f_0 (L_g + L_k), \tag{4.43}$$

where L_g and L_k are determined from Eqs. 4.24 and 4.42, respectively, and f_0 corresponds to the measured resonance frequencies (Fig. 4.5). These are represented as data points along with their respective fits (lines) from the first panel. The fits show excellent agreement with the experimental data across all substrates.

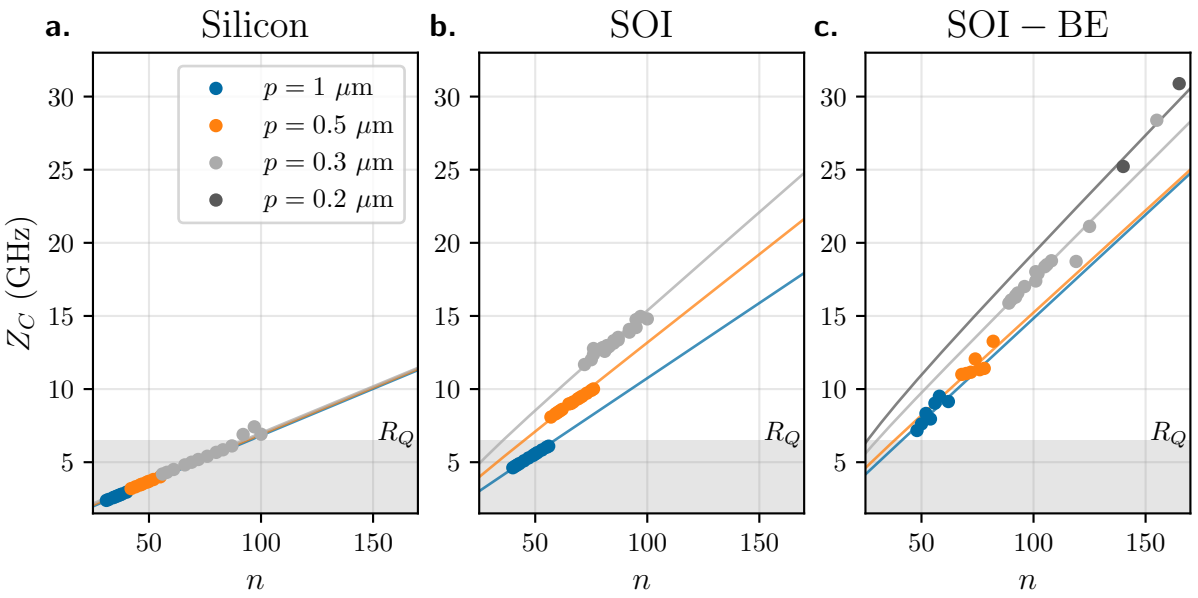

Figure 4.13: **Characteristic impedance scaling of coil resonators.** Characteristic impedance Z_C as a function of the number of coil turns n for each substrate. Data points (dots) are obtained from Eq. 4.43. The solid lines, calculated using Eq. 4.43, are not direct fits to Z_C but are derived from the fitted models of f_0 (Eq. 4.29) and L_k (Eq. 4.42) and the expression of L_g (Eq. 4.24).

It is important to note that the model for f_g proposed in Ref. [MAA+15] has an estimated uncertainty of up to 10%, which likely contributes to the observed variation in ϵ_{eff}. Furthermore, our model does not explicitly include parasitic capacitances or mutual inductances arising from the coupling wire or the surrounding ground planes, which can induce minor shifts in the resonant frequency, typically negative for parasitic capacitances and positive for mutual inductances [HRA+16]. Nonetheless, finite-element method (FEM) simulations suggest that such coupling-related frequency shifts remain below 1%, validating the robustness of our model. We also confirm that the measured resonances correspond to the fundamental mode, since wave-port coupled FEM simulations predict f_0 values within 20% of the measured data, an agreement that improves further when the kinetic inductance contribution is included.

The data presented in Fig. 4.12.b show the characteristic impedance Z_C of coils with similar fundamental frequencies $f_0 = (10.7 \pm 0.3)$ GHz. The observed increase in Z_C with decreasing pitch ($Z_C \propto p^{-1/2}$) arises because fixing the resonance frequency effectively fixes the wire length. For a fixed length, coils with smaller pitch accommodate more turns, yielding higher inductance and reduced coil radii, which in turn lowers parasitic capacitance. Both effects contribute to an enhanced characteristic impedance. The dashed lines correspond to analytical predictions derived from Eqs. 4.24, 4.42, and 4.29, with shaded bands representing uncertainties in ε_{eff}. For the SOI substrate, ϵ_{eff} was interpolated across pitches, leading to a slightly modified curve shape and narrower error bands. For the other substrates, curves are plotted using average ε_{eff} values.

Overall, these findings highlight the critical role of substrate engineering and coil geometry in optimizing the microwave properties of on-chip superconducting resonators.

Substrate	p [μm]	diameter [μm]	f_0 (GHz)	L_g [nH]	L_k [nH]	C [fF]	Z_C [kΩ]	V_{ZPF} [μV]	$Q_i^{\mathrm{low}}(\times 10^5)$	$Q_i^{\mathrm{high}}(\times 10^5)$
Silicon	1	72 - 90	10.94 - 7.00	32.04 - 62.90	2.71 - 4.27	6.09 - 7.71	2.39 - 2.95	24.39 - 17.34	0.70 - 1.70	1.93 - 15.4
	0.5	47 - 60	12.05 - 7.73	35.85 - 74.77	4.66 - 7.62	4.30 - 5.15	2.89 - 3.81	30.46 - 22.30	0.26 - 1.44	3.04 - 17.5
	0.3	36.6 - 63	12.12 - 4.17	47.15 - 240.68	7.88 - 23.46	3.13 - 5.53	4.19 - 6.91	35.80 - 15.80	0.36 - 6.06	0.71 - 50.0
SOI	1	86 - 118	12.47 - 6.48	55.08 - 142.34	3.92 - 7.40	2.76 - 4.03	4.62 - 6.09	38.67 - 23.08	0.05 - 1.08	0.33 - 30.2
	0.5	63 - 82	13.57 - 7.76	86.47 - 190.97	8.39 - 14.26	1.45 - 2.05	8.09 - 10.01	55.69 - 35.43	0.12 - 1.15	0.18 - 5.51
	0.3	49.2 - 66	14.52 - 7.80	113.97 - 276.27	14.13 - 25.59	0.94 - 1.38	11.68 - 14.80	71.59 - 43.31	0.02 - 0.37	0.22 - 0.82
SOI-BE	1	102 - 130	11.71 - 7.31	91.93 - 190.32	5.53 - 8.99	1.90 - 2.38	7.17 - 9.15	45.22 - 31.88	0.16 - 0.51	0.20 - 0.92
	0.5	74 - 88	11.53 - 8.36	140.29 - 236.08	11.60 - 16.44	1.25 - 1.43	11.00 - 13.27	55.17 - 43.95	0.08 - 0.71	0.27 - 1.73
	0.3	59.4 - 99	11.39 - 4.55	201.19 - 933.91	20.69 - 57.85	0.88 - 1.23	15.88 - 28.38	65.49 - 35.01	0.04 - 0.17	0.10 - 0.35
									0.24 - 1.66	1.11 - 10.9
	0.2	62 - 72	7.09 - 5.61	515.00 - 807.51	50.76 - 68.62	0.89 - 0.92	25.22 - 30.89	51.41 - 44.99	1.57 - 7.51	4.67 - 21.4

Table 4.9: **Parameter summary of measured geometric superinductor resonators.** f_0 are from measurements. L_g and L_k from Eqs. 4.24 and 4.42 respectively. C and Z_C are calculated assuming the LC-behavior. Q_i^{low} and Q_i^{high} are from the fundamental resonance fit at low and high intra-resonator photon numbers. The grayed values refer to devices measured with additional radiation shielding, weaker coupling strengths (high Q_e) and optimized VHF release.

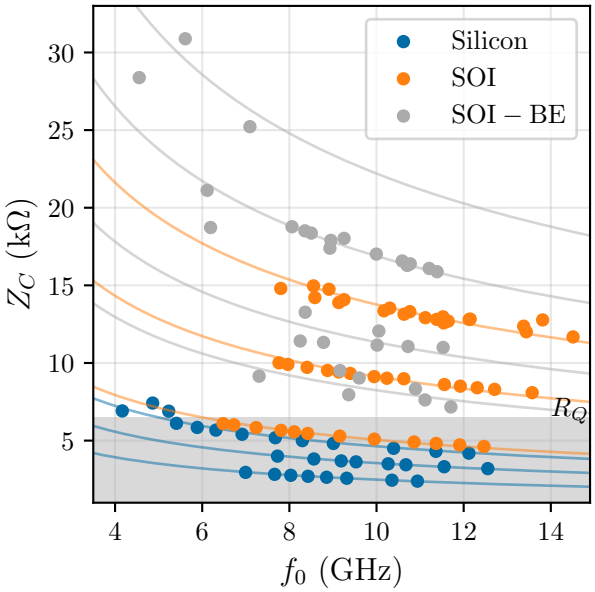

Figure 4.14: **Summary of coil resonators: Z_C vs. f_0.** Characteristic impedance Z_C plotted against the fundamental resonance frequency f_0 for all coils across all substrates. The gray area at the bottom marks the low-impedance regime, below the resistance quantum $R_Q \approx 6.45$ kΩ. Data points lying above this area demonstrate that the devices satisfy the superinductor criterion ($Z_C > R_Q$) while maintaining fundamental frequencies in the GHz range.

4.7 Outlook

4.7.1 Summary of findings

The results of this chapter demonstrate that planar aluminum coils suspended on a silicon membrane can operate as linear, high-impedance, low-loss superinductors, with resonance frequency above 4 GHz and with 95 % of the inductance coming from the geometry of the circuit. In particular, the fact that the calculated characteristic impedance of these devices can reach $Z_C = 30.89$ k$\Omega \approx 5 \cdot R_Q$ demonstrates that the common misconception, that geometric inductors are fundamentally limited by the vacuum impedance $Z_{\mathrm{vac}} = 377\ \Omega$, is incorrect. This result shows that Z_C can in fact exceed Z_{vac} by nearly two orders of magnitude. Such a

finding is exceptional both from a fundamental perspective and for practical applications.

An intriguing perspective is provided by the fact that geometric superinductors, unlike devices based on kinetic inductance, being made from a single uninterrupted aluminum wire, are based on a single superconducting wavefunction. This is usually what theorists wish to realize because it provides a clean, well-defined circuit element from the modeling point of view, thus ruling out the possibility of uncontrolled phase and charge tunneling events. Moreover, the fact that these resonators maintain linear behavior at high photon numbers allows them to be treated as linear inductors when operated below their self-resonance frequency.

The demonstrated quality factors of $Q_i \approx 8 \cdot 10^5$ at the single-photon level makes these devices suitable for quantum information processing. This is remarkable considering the small gap dimension between adjacent turns, down to $100\ \mathrm{nm}$. Additionally, because of their compact size, an advantage in terms of integration, these resonators produce significant zero-point voltage fluctuations in the range $V_{\mathrm{ZPF}} \approx 15 - 70\ \mu\mathrm{V}$.

Complementing the experimental results, analytical formulas are provided for nearly all electrical characteristics, enabling straightforward and rapid modeling of these devices. An estimate of the effective dielectric constant is also obtained from a fit to the measurement data.

A complete summary of the results is presented in Table 4.9.

4.7.2 Limitations and improvements

The devices presented here represent both a proof of principle and the first implementation of geometric superinductors. Only minimal optimization was performed, as the primary goal was to demonstrate feasibility rather than maximize performance. As illustrated by the devices measured with double magnetic shielding, optimized vapor HF recipe, and reduced coupling strength (gray in Table 4.9), the quality factor can already be improved. This highlights the considerable room for further optimization and the possible directions to explore. Although the results are promising, several challenges remain.

One issue is the high susceptibility to flux noise due to the coil's long wire [PHS+21]. This is particular detrimental for qubit performances. Ref. [BDV+20] studied more than 50 flux qubits with different SQUID geometry parameters and observed a linear dependence of the flux noise power on the SQUID perimeter (rather than its area), inverse wire width and inverse film thickness. These results are consistent with a $1/f$ flux noise model involving magnetic two-level system defects located at the interfaces of the SQUIDs loop.

The origin of the $1/f$ noise is not fully understood. Ref. [KSB+16] shows that adsorbed molecular O_2 is a dominant contribution. As suggested there, one possible direction is to apply appropriate surface treatments or improve the sample vacuum environment. Complementarily, another approach would be to prevent oxide formation by encapsulating with noble metals that do not form a native oxide [CSM+25].

Replacing lift-off techniques with dry etching has been shown to improve the circuit quality factor by an order of magnitude [HB24]. The main reason is that lift-off leaves metal residues and particles between the turns of the coil, degrading the quality factor, whereas coils fabricated with dry etching yield much cleaner devices. Replacing lift-off techniques with dry etching also makes it possible to further increase the characteristic impedance, enabling tighter coil pitches and higher inductance for a given length. An additional advantage of etching over lift-off lies in the fabrication yield: whereas lift-off can lead to complete device failure due

to broken wires, etching typically results only in shorted adjacent turns, reducing the total number of turns but still yielding a functional device.

An alternative way to increase the impedance is to raise the fundamental frequency for the same geometry by grounding one end of the coil, typically the outer end, to avoid the need for a connection at the center. This effectively changes the resonator from a $\lambda/2$ to a $\lambda/4$ mode. For the same inductance, this modification doubles both the fundamental frequency and the characteristic impedance. A potential drawback, however, is that the wire must be extended to reach a remote ground, which is necessary to keep the parasitic capacitance low and thus prevent a reduction in impedance.

Another approach is to replace aluminum with materials with significant kinetic inductance, which can greatly increase the impedance. The trade-off is a reduction of the fundamental resonance frequency and a diminished benefit of tight coil packing when aiming to remain in the GHz regime.

A further complication arises when these devices are incorporated into loops, since the central part of the coil must remain accessible. This requires additional fabrication steps to implement aluminum bridges, beneath which the wire can exit from the coil center [PHS+21; HPK+23]. Such bridges, however, increase the circuit capacitance and thereby reduce the impedance. An alternative to aluminum bridges is to evaporate the wire emerging from the center in a separate layer directly on top of the underlying coil, as demonstrated by Farid Hassani in our group. In this approach, the natural oxidation of the bottom aluminum prevents shorts simplifying the fabrication step, but the parasitic capacitance increases even more than with air bridges, because the spacing between the two wires is few nanometers, compared to few microns for air bridges.

4.7.3 Applications

An overview of applications of the superinductors can be found in the paragraph "Application" in Section 3.1. Further details on the intended applications of the coils are provided in the paragraphs below.

Protected qubits. The first obvious application of a new superinductor is to make qubits, in particular high-impedance ones like fluxonium. The ideal inductively shunted qubit gains protection from the fact that a single piece of superconductor, the inductor, avoids voltage drops in the presence of an external static electric field. A geometric superinductor qubit realized by a single junction embedded in a high-impedance loop (the coil) should therefore be insensitive to low-frequency charge noise. Until now, the common idea was that achieving high impedance necessarily required moving away from geometric implementations; instead, kinetic inductance materials or Josephson-junction arrays were employed. This approach, even if it seems counterproductive to incorporate a large number of islands, still approximates a unique piece of metal as long as the islands are coupled together sufficiently strongly.

This approach naturally avoids the problem of charge offsets, which can lead to unwanted phase or charge tunneling in multiterminal qubits. Furthermore, the coils enable strong coupling to other resonators or qubits without significantly increasing parasitic capacitance, with values on the order of tens to hundreds of MHz achieved using capacitances as small as $1-2$ fF. This is made possible by the compact size and high impedance of both the qubit and the resonator, a feature that supports large capacitive coupling in the light-fluxonium and quasi-charge regimes, and is crucial for error-protected readout and control architectures.

The first generation of geometric superinductor qubits was demonstrated in Ref. [PHS+21]. An alternative approach, making use of inductive shunting and a careful choice of qubit energies without requiring high impedance, is presented in Ref. [HPK+23].

Finally, because of their reproducibility, these inductors are excellent candidates for realizing 0–π qubits, which require strict symmetry among circuit components to reach the deeply protected regime. Exploratory directions are presented in Ref. [HB24].

Dual Shapiro steps. Another typical application of a superinductor is its use in circuits designed to study single-charge phenomena. A common configuration is a weak link (either a nanowire or a single Josephson junction) embedded in a linear high-impedance environment to probe dual Josephson physics. A specific focus in this context is the observation of Coulomb blockade of current in DC and dual Shapiro steps when an AC signal is additionally applied. These dual steps, i.e., the flat regions appearing in the device's I–V curve, have positions determined solely by fundamental quantum constants and the frequency of the applied drive. Achieving steps with high flatness could provide a platform to define the Ampere directly, without relying on the Volt. Early attempts in this direction are reported in Ref. [Per21]: the coils offer a promising path to explore these phenomena because they avoid charge disorder that can localize on different superconducting grains or islands in disordered or Josephson-junction materials.

Coupling to spin qubits. In circuit QED, a quantum device like a quantum dot can be coupled to a microwave resonator, often a finite-length transmission line. This setup enables non-demolition qubit readout when the qubit is far detuned from the cavity, and qubit control via photons when near resonance. Fast operation requires strong coupling, achievable through high-impedance cavities using metamaterials (e.g., SQUID arrays) or LC resonators. The large voltage fluctuations achievable with coil resonators, due to their intrinsic low stray capacitance, make them promising components in hybrid quantum implementations.

During my research rotation in the Nanoelectronics Lab at ISTA under the supervision of Prof. Georgios Katsaros, we explored this direction by designing a geometry to couple spin qubits via a spiral resonator (Fig. 4.15). The goal was to access the midpoint of the coiled wire, where a voltage antinode forms, without disturbing the fundamental resonator mode or voltage distribution, in order to couple to a spin qubit. Niobium was chosen as the superconducting material because it is more resilient to magnetic fields than aluminum, which are required for the manipulation of the quantum dot. The coils were fabricated on silicon using a lift-off process, which is relatively uncommon for niobium.

Splitting a single n-turn coil into two $n/2$-turn coils significantly reduced the inductance and, consequently, the achievable impedance, although values on the order of a few kiloohms were still attainable.

Due to time constraints, the resilience of these resonators to magnetic fields was not tested, and this research direction was not further pursued within the Nanoelectronics group after my rotation.

A similar effort is being currently pursued by the group of M. Blok at the University of Rochester, whose first publication characterizes the magnetic field resilience of niobium-based devices [MKM+25]. This approach uses high-impedance etched niobium spiral resonators to couple with quantum dot spin qubits, with the goal to enable strong spin–photon interactions for long-range spin coupling and hybrid quantum operations.

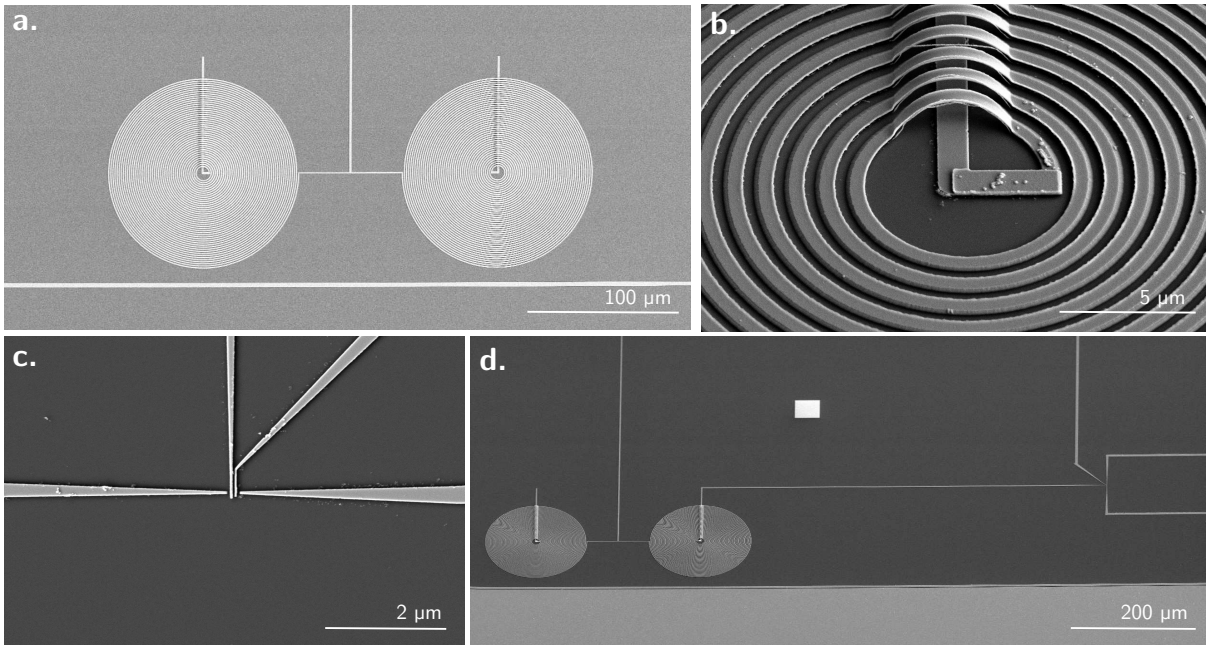

Figure 4.15: **Double spiral-coil resonators for hybrid quantum architectures. a.** SEM image of a double-coil resonator coupled to a feedline. A narrow wire between the coils represents a gate connected to the resonator center, allowing access to the voltage antinode without disturbing the fundamental mode. **b.** Air bridges and aluminum patch connecting different aluminum layers. **c.** Gate electrodes patterned to mimic the geometry of a future spin–qubit device (no quantum dot is present). **d.** SEM overview of the complete circuit.

Other applications. The strategies developed to achieve high impedance in planar aluminum coils, namely, miniaturization, mutual coupling between adjacent turns, and substrate engineering, can also be applied to enhance the impedance of other types of superinductors, for instance the one in Ref. [KSP+25]. These techniques offer a versatile toolkit for tailoring inductive elements across a range of quantum circuits.

High-impedance microwave resonators have found applications in optics-to-microwave transduction [FKP+16; Kal] due to their combination of high impedance and linearity under a driven pump. Their ability to slow down light can also be exploited in metamaterial designs, enabling engineered dispersion and enhanced light-matter interactions [MKF+18].

Similar coils were used to image the anisotropic nonlinear Meissner effect in a cuprate superconductor [ZGK+13], and the coil design is also well suited for related studies, such as Andreev bound states, as demonstrated in Ref. [ZBS+18].

A recent collaboration (Fig. 4.16) with the group of Prof. Mikko Möttönen at Aalto University, within the framework of the Quantum-Circuit Refrigerator (QCR) project, has demonstrated that the requirements on noise power can be significantly relaxed by driving a resonator coupled to the QCR, compared to off-resonant driving at the QCR input. Further reductions in required noise power could be achieved by increasing the resonator impedance and mode frequency, which enhances multiphoton-assisted tunneling in the QCR [KVMM24].

The operation of the QCR relies on photon-assisted electron tunneling, traditionally activated by a bias voltage across the NIS junctions. An alternative approach uses a radio-frequency drive applied to a supporting mode, enabling multiphoton tunneling that absorbs photons from both the primary and supporting modes. High-impedance resonators are crucial in this

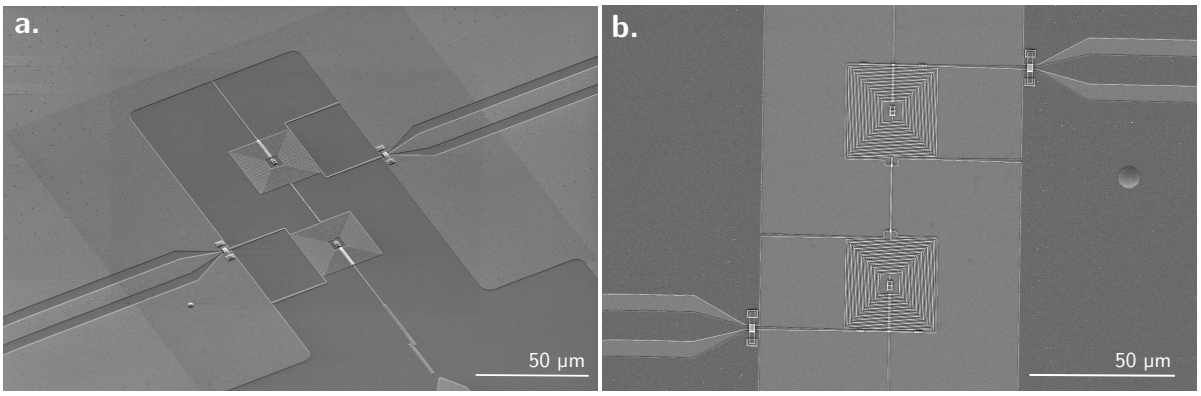

Figure 4.16: **Resonators for the QCR project. a.** SEM image of the full resonator, including the auxiliary structure used to connect the SIN junction. **b.** Another tested coupling geometry.

scheme, as they enhance the interaction between the resonator modes and the tunnel junctions, reducing the required drive power and facilitating efficient multiphoton-assisted tunneling even in the single-photon regime of the primary mode [VSJ+21; MVV+22; VMT+24].

Part II

Phase-charge duality of Josephson-junction circuits

CHAPTER 5

Josephson junction and QPS element

5.1 Josephson junction overview

Josephson junctions are fundamental elements in superconducting electronics, exhibiting rich quantum behavior due to coherent tunneling of Cooper pairs. This chapter provides an overview of their essential properties, associated energy scales, the RCSJ model, and the influence of thermal fluctuations.

5.1.1 Josephson relations and characteristic energies

In superconductors, the collective quantum state of Cooper pairs is described by a macroscopic wave function $\Psi(x) = |\Psi(x)|e^{i\phi(x)}$, as introduced in Subsection 1.2.1. When two superconducting regions, characterized by phases ϕ_1 and ϕ_2, are weakly linked via a thin insulating barrier, quantum tunneling of Cooper pairs becomes possible. This structure is known as a Josephson junction.

Remarkably, even in the absence of an applied voltage, a current can flow through the junction due to the phase coherence of the superconducting wave functions. This phenomenon is known as the DC Josephson effect. The supercurrent I_s across the junction is given by the current-phase relation:

$$I_s = I_c \sin(\varphi) \tag{5.1}$$

where I_c is the critical current, the maximum supercurrent the junction can sustain without developing a voltage. It depends on temperature T, the normal-state resistance R_N, and the superconducting gap $\Delta(T)$ as expressed by the Ambegaokar-Baratoff formula [AB63a; AB63b]:

$$I_c = \frac{\pi\Delta(T)}{2eR_N} \tanh\left(\frac{\Delta(T)}{2k_BT}\right). \tag{5.2}$$

The temperature-dependent superconducting energy gap is approximated by:

$$\Delta(T) \approx \Delta(0) \tanh\left(1.74\sqrt{\frac{T_C}{T} - 1}\right), \tag{5.3}$$

with $\Delta(0) \approx 1.76 k_B T_C$ the zero-temperature gap and T_C the critical temperature, for aluminum $T_C^{\mathrm{Al}} = 1.176$ K.

When a constant voltage V is applied across the junction, the phase difference φ evolves in time according to:

$$\frac{d\varphi}{dt} = \frac{2e}{\hbar}V = \frac{2\pi}{\Phi_0}V, \tag{5.4}$$

where $\Phi_0 = h/(2e)$ is the magnetic flux quantum.

Substituting this time-dependent phase (Eq. 5.4) into the current-phase relation (Eq. 5.1) yields an alternating current with frequency:

$$f_J = \frac{\omega_J}{2\pi} = \frac{2eV}{h} = \frac{V}{\Phi_0}, \tag{5.5}$$

which typically lies in the microwave regime. The corresponding conversion factor is approximately $483.6\ \mathrm{GHz/mV}$. This phenomenon is known as the AC Josephson effect.

Taking the time derivative of the supercurrent gives:

$$\frac{dI_s}{dt} = I_c\cos(\varphi)\cdot\frac{d\varphi}{dt} = I_c\cos(\varphi)\cdot\frac{2\pi}{\Phi_0}V. \tag{5.6}$$

This expression resembles the voltage-current relation for an inductor, $V = L(dI/dt)$, implying that the Josephson junction behaves as a nonlinear inductor with Josephson inductance

$$L_J = \frac{\Phi_0}{2\pi I_c\cos(\varphi)} = L_{J0}\cdot\frac{1}{\cos(\varphi)}, \tag{5.7}$$

where $L_{J0} = \Phi_0/(2\pi I_c)$ is the minimum linear inductance.

It is important to note that L_J diverges as $\varphi \to \pi/2 + n\pi$, and becomes negative in the range $\pi/2 + 2\pi n < \varphi < 3\pi/2 + 2\pi n$. This nonlinearity plays a crucial role in superconducting quantum circuits and can lead to rich dynamics in systems based on Josephson junctions.

Josephson coupling energy. The potential energy associated with a purely tunneling element is not stored in a magnetic field, as it is for a geometric inductor, but is instead associated with the motion of Cooper pairs. The instantaneous power delivered to the junction is given by $P(t) = I_s(t)V(t)$. Substituting the Josephson relations (Eqs. **??**) into the expression for energy

$$U_J = \int_0^{t_0} I_c\sin(\tilde{\varphi}(t))\cdot\frac{\Phi_0}{2\pi}\frac{d\tilde{\varphi}}{dt}\,dt, \tag{5.8}$$

and changing the variable of integration from time to phase

$$U_J = \frac{\Phi_0 I_c}{2\pi}\int_0^{\varphi}\sin(\tilde{\varphi})\,d\tilde{\varphi} = \frac{\Phi_0 I_c}{2\pi}(1-\cos(\varphi)), \tag{5.9}$$

leads to the standard form:

$$U_J(\varphi) = E_J(1-\cos(\varphi)), \tag{5.10}$$

where the Josephson energy is defined as:

$$E_J = \frac{\hbar I_c}{2e} = \frac{\Phi_0 I_c}{2\pi} = \frac{\hbar^2}{4e^2 L_{J0}} \approx \frac{\Delta(0) R_Q}{2R_N}. \tag{5.11}$$

Here, $\Phi_0 = h/2e$ is the magnetic flux quantum, L_{J0} is the zero-bias Josephson inductance, $R_Q = h/(2e)^2$ is the superconducting resistance quantum, $\Delta(0)$ is the superconducting energy gap at zero temperature, and R_N is the normal-state resistance of the junction. The final equivalence uses the Ambegaokar–Baratoff relation. This allows for a quick estimation of the Josephson energy using a simplified and practical formula:

$$E_J/h \approx 140\,\mathrm{GHz} \cdot \mathrm{k\Omega}/R_N. \tag{5.12}$$

This energy characterizes the coupling strength between the two superconductors: a larger E_J, i.e. thinner barrier and larger contact area, implies stronger phase locking and a more robust supercurrent.

Charging energy. The second important energy scale arises from the capacitive charging of the junction. The electrostatic energy stored due to a net charge Q on one side of the junction is given by:

$$U_C = \frac{Q^2}{2C}. \tag{5.13}$$

Assuming the charge is quantized in units of $2e$ (due to Cooper pairs), so that $Q = n \cdot 2e$, the expression becomes:

$$U_C = \frac{(n \cdot 2e)^2}{2C} = E_C (2n)^2, \tag{5.14}$$

where the charging energy is defined as:

$$E_C = \frac{e^2}{2C}. \tag{5.15}$$

This energy quantifies the cost of adding a single electron to the junction and opposes Cooper pair tunneling by favoring charge localization.

Competing energy scales. The behavior of a Josephson junction is governed by the competition between E_J and E_C: if $E_J \gg E_C$, phase coherence dominates, and the junction exhibits superconducting behavior with well-defined phase φ and delocalized charge. If $E_C \gg E_J$, charge localization occurs, suppressing tunneling; the junction behaves more like an insulator due to Coulomb blockade.

In the quantum regime, the phase $\hat{\varphi}$ and number $\hat{n}$ of Cooper pairs are conjugate variables obeying:

$$[\hat{\varphi}, \hat{n}] = i, \tag{5.16}$$

with the associated uncertainty relation:

$$\Delta\varphi \cdot \Delta n \geq \frac{1}{2}. \tag{5.17}$$

This duality underlies the competition between E_J and E_C: a precise number of Cooper pairs ($\Delta n \to 0$) implies an undefined phase ($\Delta\varphi \to \infty$), corresponding to an insulating state. Conversely, a well-defined phase allows a delocalized number of pairs, supporting coherent tunneling and superconductivity.

5.1.2 Josephson junction dynamics: current- and voltage-biased models

While the basic Josephson relations describe the behavior of an ideal junction, a more comprehensive model is necessary to accurately represent real junctions. The resistively and capacitively shunted junction (RCSJ) model, introduced independently by Stewart and McCumber [Ste68; McC68], incorporates the influence of both quasiparticle tunneling and capacitive effects. In this model, the physical Josephson junction is represented as an equivalent circuit consisting of an ideal Josephson element in parallel with a resistor R and a capacitor C.

The ideal element accounts for the supercurrent following the Josephson current-phase relation $I_s = I_c \sin(\varphi)$, Eq. 5.1; the resistor models the dissipative quasiparticle current $I_n = V/R$ that appears in the presence of a voltage V, while the capacitor introduces the displacement current $I_d = C\ dV/dt$, originating from the junction's intrinsic capacitance.

The RCSJ model shows that the phase dynamics in a Josephson junction are rich and nonlinear. The choice between current- or voltage-bias models, along with the damping regime, determines whether the junction behaves more like a switch (underdamped), a linear resistor (overdamped), or a microwave oscillator (voltage-biased).

Two common modes of operation are considered: current bias and voltage bias.

Current-biased model. In the current-bias configuration, an external current source is applied to the junction. Hence, the total current bias I_{bias} through the junction becomes

$$I_{\text{bias}} = I_s + I_n + I_d = I_c \sin(\varphi) + \frac{V}{R} + C\frac{dV}{dt}. \tag{5.18}$$

By applying the AC Josephson relation (Eq. 5.4), the current is expressed in terms of the phase difference:

$$I_{\text{bias}} = I_c \sin\varphi + \frac{\hbar}{2eR}\frac{d\varphi}{dt} + \frac{\hbar C}{2e}\frac{d^2\varphi}{dt^2}. \tag{5.19}$$

Multiplying through by $\hbar/2e$, and recognizing the Josephson coupling energy (Eq. 5.11), we obtain:

$$\left(\frac{\hbar}{2e}\right)^2 C\frac{d^2\varphi}{dt^2} + \left(\frac{\hbar}{2e}\right)^2 \frac{1}{R}\frac{d\varphi}{dt} + \frac{d}{d\varphi}\left[-E_J\cos\varphi - \frac{\hbar I_B}{2e}\varphi\right] = 0. \tag{5.20}$$

Eq. 5.20 has the same structure of the classical equation of motion for a particle of mass $m = (\hbar/2e)^2 C$ subjected to a potential $U(\varphi)$ and damping:

$$m\frac{d^2\varphi}{dt^2} + \eta\frac{d\varphi}{dt} + \frac{dU}{d\varphi} = 0, \tag{5.21}$$

where the damping coefficient is given by $\eta = (\hbar/2e)^2(1/R)$, and the effective potential is

$$U(\varphi) = -E_J\cos\varphi - \frac{\hbar I_{\text{bias}}}{2e}\varphi = -E_J\left(\cos\varphi + \frac{I_{\text{bias}}}{I_c}\varphi\right). \tag{5.22}$$

This mechanical analogy leads to the concept of the tilted-washboard potential, where the phase φ plays the role of a coordinate for a fictitious particle. When $I_{\text{bias}} = 0$, the potential is symmetric and periodic. The particle rests in a potential well minimum and oscillates around it with the so-called Josephson plasma frequency:

$$f_p = \frac{\omega_p}{2\pi} = \frac{1}{2\pi} \cdot \frac{1}{\sqrt{L_{J0}C}} = \frac{1}{2\pi} \cdot \left(\frac{2eI_c}{\hbar C}\right)^{1/2} = \frac{1}{2\pi} \cdot \left(\frac{2\pi I_c}{\Phi_0 C}\right)^{1/2}, \tag{5.23}$$

where $L_{J0} = \Phi_0/2\pi I_c$ (Eq. 5.7) is the Josephson inductance.

As the bias current increases, the cosine potential becomes tilted. At $I_{\text{bias}} = I_c$, the minima vanish and the phase particle is free to accelerate down the potential, resulting in a non-zero time derivative of φ and, by Eq. 5.4, a finite voltage appears across the junction.

Upon decreasing the current, the system does not immediately return to the zero-voltage state. Instead, the particle may retrap into a potential well at a current $I_r < I_c$, depending on the competition between its inertia and the damping. A high capacitance corresponds to a large effective mass and allows the particle to carry significant kinetic energy, thereby reducing the probability of retrapping. On the contrary, strong damping (low R) reduces kinetic energy, favoring retrapping at higher currents.

To describe the damping regime quantitatively, Stewart and McCumber introduced the dimensionless Stewart–McCumber parameter β_c:

$$\beta_c = \frac{2\pi I_c R^2 C}{\Phi_0}. \tag{5.24}$$

This parameter contains the relative influence of inertia (via C) and damping (via R). The junction is said to be overdamped when $\beta_c \ll 1$, and underdamped when $\beta_c \gg 1$.

Fig. 5.1 shows the IV characteristics for the two damping regimes. In the overdamped regime, the transition from zero to finite voltage occurs smoothly at $I = I_c$, and the voltage returns to zero at the same current as it is reduced. There is no hysteresis. In contrast, the underdamped regime exhibits hysteresis: the system switches to the resistive state at I_c, but retrapping occurs only when the current is significantly reduced, sometimes down to zero.

The retrapping current in the underdamped limit can be estimated as

$$I_r = \frac{4I_c}{\pi Q}, \tag{5.25}$$

where the quality factor Q is defined by

$$Q = \sqrt{\beta_c}. \tag{5.26}$$

This expression can be derived by equating the energy dissipated by the particle between two maxima of the potential with the energy it gains from the tilt [Tin04].

Voltage-biased model. In the voltage-bias configuration, an external voltage is applied across the junction. According to the AC Josephson relation (Eq. 1.15), the phase increases linearly in time: $\varphi(t) = \varphi_0 + \omega_J t$, where $\omega_J = 2eV_{\text{bias}}/\hbar$ is the Josephson angular frequency (Eq. 5.5).

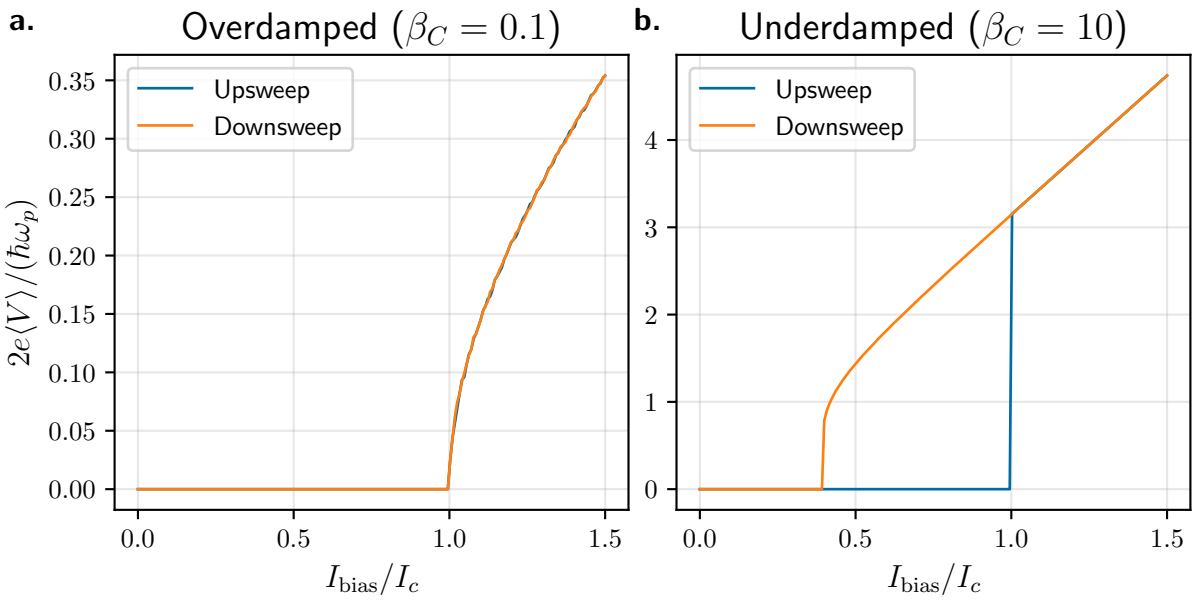

Figure 5.1: ***I*-*V* response of current-biased Josephson junctions.** Current-voltage characteristics for **a,** an overdamped ($\beta_c \ll 1$) and **b.** underdamped ($\beta_c \gg 1$) current-biased Josephson junction. Hysteresis is evident in the latter case.

The supercurrent then oscillates as:

$$I_s(t) = I_c \sin(\omega_J t + \varphi_0). \tag{5.27}$$

This leads to an AC current at frequency $\omega_J/(2\pi)$, which can couple to external circuits and produce measurable microwave radiation.

To model the fact that quasiparticle conduction is negligible for sub-gap voltages and rises for $V \gtrsim \Delta/e$, a smooth step (sigmoid[1]) function $s(V)$ which transitions from 0 to 1 near a threshold voltage $V_s \approx 2\Delta/e$ is introduced [CCG+23]:

$$s(V) = \frac{1}{1 + \exp\Big[-(V - V_s)/\delta\Big]}, \tag{5.28}$$

where δ is a small smoothing parameter (on the order of sub-gap broadening or thermal energy). $s(V)$ varies continuously from 0 for $|V| < 2\Delta$ to 1 for $|V| > 2\Delta$, practically gradually suppressing the Josephson supercurrent I_s while activating the resistive part I_n.

The quasiparticle current is then modelled as

$$I_n^{\mathrm{eff}}(V) = \frac{V}{R_N}\, s(V), \tag{5.29}$$

replacing the simple linear term V/R_N.

A physically meaningful DC voltage bias must include the source/environment impedance. For a bias voltage V_{bias} in series with a source resistance R_s the node equation is

$$\frac{V_{\mathrm{bias}} - V(t)}{R_s} = I_c \sin\varphi(t) + \frac{\Phi_0}{2\pi R_N}\dot{\varphi}(t)\; s(V(t)) + C\frac{\Phi_0}{2\pi}\ddot{\varphi}(t) + I_F(t). \tag{5.30}$$

[1] As long as the transition is sufficiently sharp, the specific shape of the function s has no influence on the I–V response [CCG+23].

Substituting $V(t) = (\Phi_0/2\pi)\dot{\varphi}(t)$ and collecting terms gives the second-order ODE for $\varphi(t)$:

$$\left(\frac{\Phi_0 C}{2\pi}\right)\ddot{\varphi} + \left(\frac{\Phi_0}{2\pi}\right)\dot{\varphi}\left(\frac{1}{R_N}s(\dot{\varphi}) + \frac{1}{R_s}\right) + I_c \sin\varphi = \frac{V_{\text{bias}}}{R_s} + I_F(t). \tag{5.31}$$

Two limiting and instructive cases are important:

(i) Ideal (zero-impedance) voltage source, $R_s \to 0$. Formally $V(t) = V_{\text{bias}}$ is enforced, hence

$$\dot{\varphi}(t) = \frac{2\pi}{\Phi_0}V_{\text{bias}} \equiv \omega_J, \qquad \varphi(t) = \varphi_0 + \omega_J t. \tag{5.32}$$

The instantaneous supercurrent oscillates as

$$I_s(t) = I_c \sin(\varphi_0 + \omega_J t), \tag{5.33}$$

with Josephson frequency $\omega_J = 2\pi V_{\text{bias}}/\Phi_0 = 2eV_{\text{bias}}/\hbar$. The time-average of the pure supercurrent vanishes, $\langle I_s\rangle_T = 0$ for any long averaging time T, unless phase locking or rectification occurs. Thus the DC (time-averaged) current reduces to the quasiparticle contribution:

$$\left\langle I \right\rangle \;=\; \left\langle I_s \right\rangle \;+\; \frac{V_{\text{bias}}}{R_N}\, s(V), \tag{5.34}$$

for $R_s \to 0$ and in the absence of fluctuations or locking phenomena. Physically this means negligible DC current below the gap and quasiparticle current above it.

(ii) Finite source impedance (practical voltage bias). When R_s is finite the junction sees a drive term V_{bias}/R_s and additional damping through $1/R_s$. The equation above then admits nontrivial phase dynamics: the phase is not strictly linear in time, the supercurrent can develop a nonzero time-average through rectification and partial locking with the environment, and displacement currents may contribute transiently. Numerical integration of the ODE is required to obtain $\varphi(t)$ and the time-averaged current $\langle I\rangle$.

Over-coupled / overdamped: total damping is large (small Stewart–McCumber parameter β_C or effectively low quality factor Q). The phase velocity $\dot{\varphi}$ quickly relaxes toward the value set by the bias; Josephson oscillations are heavily damped and have small amplitude. Under voltage bias with a finite R_s the junction shows a stable, nearly linear averaged I–V: for $V_{\text{bias}} < V_s$ the averaged current is suppressed (sub-gap), and for $V_{\text{bias}} \gtrsim V_s$ the averaged current follows the qp law V_{bias}/R_N (modulated smoothly by s). Any rectified supercurrent or Shapiro-like locking is weak because dissipation suppresses coherent oscillations.

Under-coupled / underdamped: damping is weak (large β_C, high Q). The phase has significant inertia and the Josephson oscillations can have large amplitude. Under voltage bias this leads to strong AC supercurrents at ω_J, significant higher harmonics, and an increased tendency to exchange power with the environment. Consequences for the averaged I–V include: (i) suppression of the averaged qp-like current at some voltages due to nonlinear averaging of the large oscillations, (ii) the possibility of self-rectification and generation of a nonzero $\langle I_s\rangle$ (producing features that deviate from the simple qp step), and (iii) sensitivity to small environmental resonances that can produce steps, kinks or instability. In extreme cases, an underdamped junction driven by a DC voltage with negligible series impedance may show runaway currents unless the external circuit provides load or dissipation.

5.1.3 Thermal fluctuations in the RCSJ model

Thermal fluctuations have so far been neglected, an assumption valid when $k_B T \ll 2E_J$ [Tin04]. For a realistic description of Josephson junction dynamics at finite temperatures, however, such fluctuations must be included.

Within the RCSJ framework, noise sources are incorporated via an additional fluctuating current $I_f(t)$, modifying the bias relation to

$$I_{\text{bias}} = I_s + I_r + I_d + I_f, \tag{5.35}$$

so that the effective potential becomes

$$U(\varphi) = -E_J \left(\cos\varphi + \frac{I_{\text{bias}} - I_f}{I_c} \varphi \right). \tag{5.36}$$

This additional fluctuating term introduces a random tilt to the tilted-washboard potential. The consequence of this stochastic tilt is that the phase particle can occasionally escape over the nearest potential maximum, resulting in a phase slip of $\pm 2\pi$. When no external current is applied, and the potential is strictly horizontal, these thermal fluctuations cause the particle to escape left or right with equal probability. As a result, the time-averaged voltage remains zero.

In underdamped junctions, the presence of thermal noise reduces the observed critical current. The reason is that the phase particle may escape from the potential well and gain momentum even before reaching I_c, causing the junction to switch prematurely into the resistive state. Addittionally, thermal fluctuations can also assist in retrapping the particle, leading to an increased retrapping current I_r.

In the overdamped regime, the behavior differs significantly. Here, thermal fluctuations can still drive the phase particle over the potential barrier, resulting in a 2π phase slip. However, due to strong damping, the particle rapidly loses kinetic energy and settles into the next well rather than continuing to accelerate, as it would in the underdamped case. This behavior gives rise to a diffusive motion across the potential landscape, characterized by a finite average velocity. Consequently, a small but nonzero average voltage appears across the junction, even below the nominal critical current I_c. The I–V curve under these conditions becomes rounded at low voltages, and the critical current is suppressed.

This thermally activated behavior was studied theoretically by Yu. M. Ivanchenko and L. A. Zil'berman [IZ69] and, independently by V. Ambegaokar and B. I. Halperin [AH69] who analyzed the dynamics of small Josephson junctions subjected to strong damping and thermal noise. odeling $I_f(t)$ as a Markovian process and applying the Fokker–Planck formalism, they obtained an analytic expression for the thermally averaged Cooper-pair current,

$$I(V_{\text{BIZ}}) = I_0 \, \Im \left[\frac{I_{1-i\beta\hbar V_{\text{BIZ}}/2eR_B}(\beta E_J)}{I_{-i\beta\hbar V_{\text{BIZ}}/2eR_B}(\beta E_J)} \right], \tag{5.37}$$

where $I_\nu(z)$ denotes the modified Bessel function of the first kind with complex order ν, $\beta = 1/k_B T$ is the inverse temperature, R_B is a series resistance, and V_{BIZ} represents the total bias voltage across the junction plus resistor. The intrinsic current I_0 is not the measurable critical current but rather the theoretical maximum for the Josephson coupling. The junction voltage is

$$V_{\text{IZ}} = V_{\text{BIZ}} - R_B I. \tag{5.38}$$

The resulting I–V curves exhibit a supercurrent peak near zero voltage that replaces the noiseless supercurrent branch. This prediction was later confirmed experimentally [SJC+01].

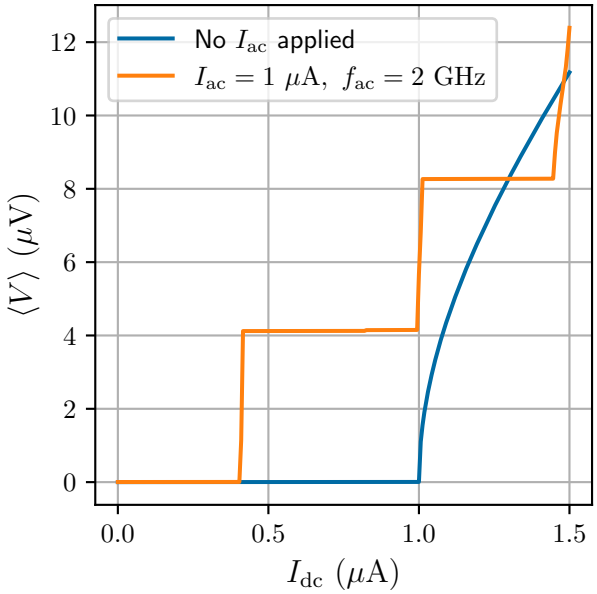

Figure 5.2: ***I*-*V* characteristics of a current-biased Josephson junction showing Shapiro steps under AC drive.**

5.1.4 DC and AC biased Josephson junctions

This Subsection follows the notes https://physics.umd.edu/courses/Phys798S/AnlageSpring16/Lecture%2024%20Summary.pdf by Prof. Steven Anlage.

We now consider a Josephson junction subjected to both a DC and an AC bias.

Shapiro steps in a current-biased junction. In the current bias configuration,

$$I_{dc} + I_{ac}\sin(\omega_{ac}t) = I_c \sin\varphi + \frac{\Phi_0}{2\pi R_N}\frac{d\varphi}{dt} + C\frac{\Phi_0}{2\pi}\frac{d^2\varphi}{dt^2}. \tag{5.39}$$

The AC current has two main effects on the junction

The oscillating AC component effectively shakes the "washboard" potential, causing the phase particle to escape over the potential barrier slightly earlier than it would under purely DC bias. This reduces the apparent critical current.

Consider the junction in the running state, where $d\varphi/dt \neq 0$. The phase particle moves along the tilted washboard, periodically speeding up and slowing down due to the AC drive. Although the motion is not strictly sinusoidal, it is periodic. The average angular velocity of the phase particle is $\langle d\varphi/dt \rangle = 2\pi/T$, where T is the period of the motion. Resonance occurs when the AC drive frequency ω_{ac} matches this periodicity. In this condition, the AC source can "phase-lock" to the junction motion, leading to energy absorption at discrete voltages, known as Shapiro steps (Fig. 5.2). The steps appear at

$$\langle V_n \rangle = n\frac{\hbar\omega_{ac}}{2e}, \quad n = 1, 2, \ldots \tag{5.40}$$

and correspond to the phase particle traversing multiple 2π periods per AC cycle.

Shapiro steps in a voltage-biased junction. While voltage biasing a junction is experimentally challenging, it simplifies theoretical analysis. Consider a voltage bias

$$V(t) = V_{\mathrm{dc}} + V_{\mathrm{ac}} \cos(\omega_{\mathrm{ac}} t). \tag{5.41}$$

Integrating the AC Josephson relation

$$\frac{d\varphi}{dt} = \frac{2e}{\hbar} V(t) \tag{5.42}$$

gives the gauge-invariant phase

$$\varphi(t) = \varphi(0) + \frac{2e}{\hbar} V_{\mathrm{dc}} t + \frac{2eV_{\mathrm{ac}}}{\hbar\omega_{\mathrm{ac}}} \sin(\omega_{\mathrm{ac}} t). \tag{5.43}$$

Define the Josephson frequency as

$$\omega_J = \frac{2eV_{\mathrm{dc}}}{\hbar}. \tag{5.44}$$

In the resistively shunted junction (RSJ) model, neglecting the capacitor, the total current is

$$I(t) = \frac{V(t)}{R} + I_c \sin\left[\varphi(0) + \omega_J t + \frac{2eV_{\mathrm{ac}}}{\hbar\omega_{\mathrm{ac}}} \sin(\omega_{\mathrm{ac}} t)\right]. \tag{5.45}$$

and can rewritten as[2]

$$I(t) = \frac{V(t)}{R} + I_c \sum_{n=-\infty}^{\infty} (-1)^n J_n\left(\frac{2eV_{\mathrm{ac}}}{\hbar\omega_{\mathrm{ac}}}\right) \sin\left[\gamma(0) + (\omega_J - n\omega_{\mathrm{ac}})t\right]. \tag{5.46}$$

Taking the time average of $I(t)$, one finds that the average current $\langle I \rangle$ is nonzero only when the resonance condition $\omega_J = n\omega_{\mathrm{ac}}$ is satisfied. These resonances produce the voltage steps (Shapiro steps) in the IV characteristic:

$$\langle V_n \rangle = n \frac{\hbar\omega_{\mathrm{ac}}}{2e}. \tag{5.47}$$

The width of these steps depends on the amplitude of the AC voltage V_{ac} through Bessel functions J_n, and their appearance follows a non-monotonic pattern as V_{ac} is increased. The metrological voltage standard are based on this physical phenomena.

5.2 QPS element overview

One of the defining features of superconductivity is its ability to carry electrical current without resistance. This property arises from the macroscopic quantum nature of the superconducting state, which is described by the Ginzburg-Landau theory through a complex-valued order parameter $\Psi(x) = |\Psi(x)|e^{i\phi(x)}$ interpreted as a macroscopic wavefunction (Subsection 1.2.1). Because this phase $\phi(x)$ is coherent across the entire sample, currents can flow without dissipation.

[2] Using the Jacobi-Anger expansion $\sin(a + b\sin\theta) = \sum_{n=-\infty}^{\infty} (-1)^n J_n(b) \sin(a - n\theta)$.

However, this ideal dissipationless state is not entirely immune to disturbances. Even well below the critical temperature, critical current or critical magnetic field, fluctuations can locally disrupt the superconducting phase. These fluctuations may arise from two fundamental sources: thermal fluctuations, due to finite temperature, and quantum fluctuations, due to zero-point motion at absolute zero.

The effect of such fluctuations is the occurrence of phase slips. A phase slip is a topological event in which the phase of the order parameter changes by 2π

To visualize this, consider the polar representation of $\Psi(x)$ in the complex plane. As the phase $\phi(x)$ varies smoothly along space, the tip of $\Psi(x)$ traces out a continuous spiral, a helical trajectory, around the origin. Coherence corresponds to an unbroken, uniform helix of constant amplitude. A strong enough fluctuation can distort this trajectory, introducing a discontinuity that breaks the smooth winding. To restore a well-defined, continuous order parameter, the system undergoes a phase slip: the trajectory reconnects after passing through the origin, with the phase shifted by 2π. The temporary suppression of $\Psi(x)$ at the core of the slip is essential to preserve the single value and continuity of the complex order parameter throughout the process. Each 2π phase winding corresponds to a quantized unit of current, so a change in winding number alters the supercurrent.

According to the second Josephson relation, a time-dependent phase change implies a voltage pulse. Thus, each phase slip generates a brief voltage spike. If such events occur repeatedly, they manifest as a finite resistance, In equilibrium positive and negative phase slips occur with equal probability, leading to zero net voltage. However, under a bias current, the energy landscape becomes tilted, favoring phase slips in one direction. This results in a net phase drift over time and hence a measurable voltage drop, introducing resistance into the system.

TAPS: thermally activated phase slips. Thermally activated phase slips describe transitions between metastable current-carrying states in a superconducting wire due to thermal fluctuations. When the thermal energy $k_B T$ exceeds the energy barrier ΔF separating these states, the system can overcome the barrier, resulting in a sudden 2π phase jump and a transient suppression of the superconducting order parameter. These events introduce a measurable resistance below the critical temperature T_C, even though the medium is otherwise superconducting.

Different approaches have been developed to estimate the resistance due to thermally activated phase slips. Little [Lit67] introduced a phenomenological model based on temporary normal regions, which reproduces the expected Arrhenius behavior but lacks microscopic justification. Langer and Ambegaokar [LA67], later extended by McCumber and Halperin [MH70] (LAHM theory), applied time-dependent Ginzburg–Landau theory to derive the free-energy barrier and nucleation rate, providing a more systematic framework but predicting an unphysical vanishing resistance as $T \to T_C$. Golubev and Zaikin [GZ08] addressed this issue with a field-theoretical approach, modifying the prefactor to remain finite near T_C and thereby achieving better agreement with experimental data.

QPS: quantum phase slips. At low temperatures, thermal fluctuations become negligible, and yet, in very narrow superconducting wires, phase slips can still occur. These are known as quantum phase slips (QPS), where the superconducting phase tunnels through the energy barrier separating metastable states instead of being thermally activated. QPS are inherently quantum in nature and remain active even as $T \to 0$, leading to finite resistance or even insulating behavior in superconducting nanowires well below T_C.

The origin of QPS lies in the conjugate relationship between phase $\hat{\Phi}$ and charge $\hat{q}$, which satisfy the commutation relation $[\hat{q}, \hat{\Phi}] = -i$. Because of this, any localization of charge within the wire results in quantum fluctuations of the superconducting phase. This duality allows for quantum tunneling of the phase across the potential barrier, enabling QPS even in the absence of thermal energy.

The first phenomenological model of quantum phase slips was introduced by Giordano [Gio88], inspired by macroscopic quantum tunneling in Josephson junctions. By replacing the thermal energy scale $k_B T$ with a zero-point energy $\hbar/\tau_r$, he obtained a tunneling rate of the Arrhenius form with fitting parameters. While this captured the qualitative idea of quantum tunneling of the phase, it underestimated experimental rates by several orders of magnitude.

A more systematic framework was developed by Golubev and Zaikin [ZGvOZ97] using an effective action approach for dirty superconductors. The total QPS action was separated into a core part, associated with the local suppression of the order parameter, and a hydrodynamic part, describing long-range phase fluctuations. They derived a tunneling rate of the form

$$\Gamma_{\text{QPS}} \propto \frac{R_q}{R_n} \frac{L_w}{\xi} \exp\left(-\alpha \frac{R_q L_w}{R_n \xi}\right), \tag{5.48}$$

where $R_q = h/4e^2$ is the quantum resistance, R_n the normal-state resistance, L_w the wire length, and ξ the coherence length. The parameter α is a dimensionless constant of order unity that collects model-dependent numerical factors and is often treated as a weak, sample-dependent fitting parameter.

This theory predicts a strong exponential sensitivity to R_n and L_w, in line with experiments on superconducting nanowires. Extensions including capacitive effects and finite-temperature corrections further improve agreement with data and are widely used to model QPS-driven superconductor–insulator transitions.

5.2.1 QPS element as dual of Josephson junction

In previous sections, phase slips were discussed as isolated, random events characterized by a tunneling rate. However, when these events occur coherently, the system enters a fundamentally different regime. This concept of coherent quantum phase slips was introduced by Büchler et al. [BGB04]. Shortly after, Mooij and Nazarov [MN06] proposed a duality between the well-known Josephson junctions and these so-called QPS junctions. The idea is based on the fact that charge and phase are quantum conjugate variables. This symmetry allows the dynamics of one system to be directly mapped to the other by interchanging phase with charge, and vice versa.

A Josephson junction typically consists of two superconductors separated by a thin insulating barrier. Cooper pairs can tunnel through this barrier, with a coupling energy given by the Josephson energy E_J. Associated with this setup is a charging energy $E_C = (2e)^2/2C$, where C is the junction capacitance. The ratio E_J/E_C determines whether the system behaves more like an inductor (large E_J) or a capacitor (large E_C).

In contrast, a QPS junction is formed by a narrow superconducting wire, thin enough that phase slips can occur. Each phase slip corresponds to the tunneling of a flux quantum Φ_0 through the wire, characterized by a phase slip energy E_S. The dual to the charging energy in the Josephson case is the inductive energy $E_L = \Phi_0^2/2L$, where L is the wire inductance.

In the regime $E_J \gg E_C$, the phase across a Josephson junction is well-defined, allowing a supercurrent to flow up to a critical current $I_c = 2\pi E_J/\Phi_0$. This is mirrored in a QPS junction when $E_S \gg E_L$: the charge becomes well-defined, and a critical voltage $V_C = 2\pi E_S/2e$ emerges, beyond which coherent charge transport is suppressed. In the opposite limit ($E_J \ll E_C$ or $E_S \ll E_L$), the roles reverse, with charge quantization leading to Coulomb blockade in Josephson junctions, and phase coherence enabling supercurrents in QPS junctions.

The Josephson current-phase relation is

$$I = I_c \sin(\varphi), \tag{5.49}$$

which leads to a nonlinear inductance

$$L_J = \frac{\Phi_0}{2\pi I_c \cos(\varphi)}. \tag{5.50}$$

In the QPS case, the dual relation is a voltage-charge dependence:

$$V = V_C \sin(2\pi q), \tag{5.51}$$

with the corresponding nonlinear kinetic capacitance given by

$$C_{\text{kin}} = \frac{2e}{2\pi V_C \cos(2\pi q)}. \tag{5.52}$$

This duality extends to entire circuits. For example, the Cooper pair box dominated by E_C, exhibits charge quantization on a superconducting island. Its Hamiltonian is

$$H_{\text{CPB}} = E_C(N - n_g)^2 - \frac{E_J}{2}\sum_N \left(|N+1\rangle\langle N| + \text{h.c.}\right), \tag{5.53}$$

with $n_g = CV/2e$ being the gate-induced charge.

The dual circuit, the phase slip box, consists of a superconducting loop with inductance L interrupted by a QPS junction. The number of flux quanta N in the loop is quantized, and the energy depends on the deviation from the external flux Φ:

$$H_{\text{QPS}} = E_L(N - f)^2 - \frac{E_S}{2}\sum_N \left(|N+1\rangle\langle N| + \text{h.c.}\right), \tag{5.54}$$

where $f = \Phi/\Phi_0$ is the reduced flux. The roles of E_C, E_J, and n_g are replaced by E_L, E_S, and f respectively, showing the direct duality:

$$E_C \leftrightarrow E_L, \quad E_J \leftrightarrow E_S, \quad n_g \leftrightarrow f. \tag{5.55}$$

This mapping can be extended further. Mooij and Nazarov showed that any Josephson-based circuit can be transformed into a QPS-based one by exchanging parameters:

$$E_J \to E_S, \quad E_C \to E_L, \quad R_Q^{-1}V \leftrightarrow I, \quad R_Q^{-2}Z(\omega) \leftrightarrow Y(\omega), \tag{5.56}$$

where R_Q is the quantum resistance, Z the impedance, and Y the admittance.

For instance, the familiar RCSJ model of a current-biased Josephson junction involves a parallel resistor and capacitor. Its dual is a voltage-biased QPS junction with a series resistor and

inductance. The dynamics of both systems can be described by differential equations. For the Josephson case:

$$I(t) = I_c \sin(\varphi) + \frac{\Phi_0}{2\pi}\left(C\frac{d^2\varphi}{dt^2} + \frac{1}{R}\frac{d\varphi}{dt}\right), \tag{5.57}$$

and for the QPS case:

$$V(t) = V_C \sin(2\pi q) + 2e\left(L\frac{d^2q}{dt^2} + R\frac{dq}{dt}\right). \tag{5.58}$$

Introducing normalized time $t' = \omega_p t$ and defining plasma frequencies

$$\omega_p^J = \sqrt{\frac{2E_J E_C}{\hbar^2}}, \quad \omega_p^{\mathrm{QPS}} = \sqrt{\frac{2E_S E_L}{\hbar^2}}, \tag{5.59}$$

along with the dimensionless damping parameters (McCumber parameters)

$$\beta_c^J = \frac{2\pi R^2 C I_c}{\Phi_0}, \quad \beta_c^{\mathrm{QPS}} = \frac{2\pi L V_C}{2eR^2}, \tag{5.60}$$

the equations become:

$$\frac{I(t')}{I_c} = \sin(\varphi) + \frac{d^2\varphi}{dt'^2} + \frac{1}{\sqrt{\beta_c^J}}\frac{d\varphi}{dt'}, \tag{5.61}$$

$$\frac{V(t')}{V_C} = \sin(2\pi q) + \frac{d^2q}{dt'^2} + \frac{1}{\sqrt{\beta_c^{\mathrm{QPS}}}}\frac{dq}{dt'}. \tag{5.62}$$

These equations describe particles moving in tilted periodic potentials. For the Josephson case, the phase particle moves in

$$U_J(\varphi) = -E_J\left(\frac{I}{I_c}\varphi + \cos\varphi\right), \tag{5.63}$$

while in the QPS case, the charge particle experiences

$$U_{\mathrm{QPS}}(q) = -E_S\left(\frac{V}{V_C}2\pi q + \cos(2\pi q)\right). \tag{5.64}$$

The dynamics in these washboard potentials capture the essence of both systems: below threshold, oscillations occur with the plasma frequency; above threshold, the system enters a running state, producing voltage (for Josephson) or current (for QPS). The damping parameters β_c control the transition between these regimes.

Dual Shapiro steps in QPS junctions. Dual Shapiro steps arise in the charge-dominated regime of ultrasmall Josephson junctions, where the charging energy E_C is comparable to or larger than the Josephson energy E_J.

In the conventional regime (Subsection 5.1.4), where $E_J \gg E_C$, the phase can be treated as a classical variable, and the system is described by a tilted washboard potential periodic in ϕ:

$$U(\phi) = -E_J\cos(\phi) - \frac{\hbar I}{2e}\phi. \tag{5.65}$$

Applying a microwave drive of frequency f modulates this potential, producing phase-locked transport of flux quanta. This gives rise to quantized voltage steps in the I-V characteristic, known as Shapiro steps:

$$V_n = n\frac{hf}{2e}, \quad n \in \mathbb{Z}. \tag{5.66}$$

In the charge-dominated regime, where $E_J/E_C \lesssim 1$, strong phase fluctuations localize the charge, and the system is described by a potential periodic in charge Q:

$$U(Q) \simeq -E_C \cos\left(\pi\frac{Q}{e}\right) - VQ. \tag{5.67}$$

A DC current bias induces Bloch oscillations, which are voltage oscillations dual to the AC Josephson effect:

$$V(t) = V_C \sin\left(\frac{2\pi It}{2e}\right), \tag{5.68}$$

where $V_C = \pi E_C/e$ is the critical voltage. When a microwave drive of frequency f is applied, these Bloch oscillations synchronize with the drive, producing quantized current steps:

$$I_n = n\,2ef, \quad n \in \mathbb{Z}. \tag{5.69}$$

More on this in Chapter 6.

CHAPTER 6

Classical numerical simulations of quantum phase-slip circuits

Contributions and acknowledgments. *I thank the summer interns Uri Sharell and Alinda Gerçek for their contributions in developing the code for the numerical simulations.*

6.1 Josephson circuit duality

Duality in physics describes a situation where two different systems, or two different regimes of the same system, are related by interchanging key variables, such as position and its conjugate momentum. When the relevant parameters have a proper mapping, one can infer the behavior of one system by analyzing its dual. In special cases, this transformation maps a system onto itself, a property known as self-duality: the harmonic oscillator is an example, with exact self-duality due to the symmetry between position and momentum. More often, duality relates asymptotic behaviors in distinct parameter regimes, becoming a tool to study one regime when the other is analytically or experimentally more accessible.

Josephson junction circuits can be a playground for the study of the charge and phase duality [GH10]. In particular, the resistively and capacitively shunted junction (RCSJ) model (Fig. 6.1.a) describes a current-biased Josephson junction with Josephson energy E_J shunted by a capacitor C and a resistor R. Its dual description (Fig. 6.1.b) is given by the capacitively shunted junction[1] in series with a resistor and an inductor, where the junction is voltage biased, shunted by the same capacitor C, and connected in series with R and L. In this sense, the two circuits are dual: current bias is exchanged with voltage bias, and capacitive elements are mapped to inductive ones.

This approximate self-duality [YNHM19; Bun21; GC24] establishes a correspondence between the small-junction limit ($E_J \ll E_C$) and the large-junction limit ($E_J \gg E_C$), i.e. the regime where Cooper-pair tunneling in charge-space dominates can be related to the complementary regime governed by flux-tunneling, or equivalently, phase slips. In this scenario it is possible to infer the dynamcs of charge studying that of phase and viceversa.

This is an approximate self-duality because only at low energies the two circuits exhibit an exact duality; moreover the role of the shunting circuit, and as a consequence of the boundary

[1] A Josephson junction is always unavoidably shunted by a capacitance due to its physical construction.

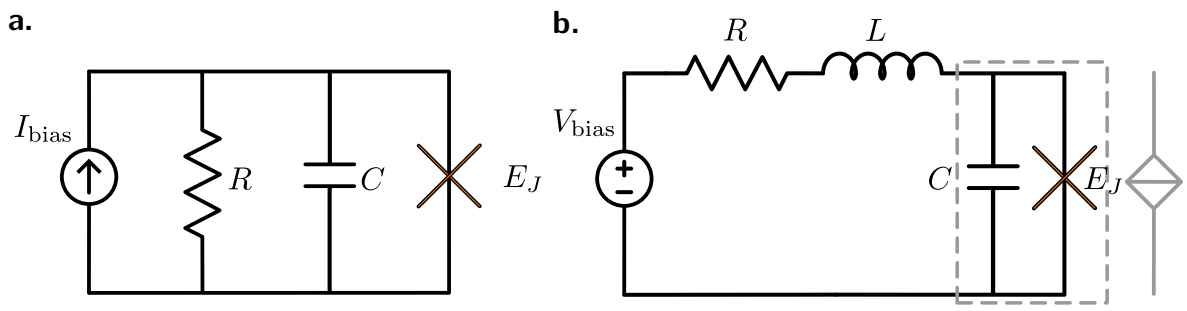

Figure 6.1: **Josephson dual circuits. a.** A current-biased Josephson junction (indicated by a cross) with bias current I_b. The junction, defined by the Josephson energy E_J, is shunted by a capacitor C and a resistor R. **b.** A voltage-biased Josephson junction with applied bias voltage V_b. The junction is shunted by a capacitor C and connected in series with an inductor L and a resistor R. In the dual regime the Josephson junction approximates the phase slip element, in gray.

conditions on the quantum variables, has a primary role. The treatment of variables as either compact or extended in Josephson junctions remains a long-debated issue [PRE25] and continues to cause inconsistencies between theoretical models and experimental findings.

In fluxonium-like superconducting qubits, the low energy spectrum of a quantum phase slip box [AIK+12] is approximated in the limit of high shunting inductances and dominating charging energies ($E_L \ll E_C, E_J \ll E_C$) [ALK+24; MLC+24]. Similarly, in circuits with high-impedance in DC (so at low energy), in the presence of dissipation as a resistor or as an infinitely long transmission line, a Josephson junction and a phase-slip junction become effectively indistinguishable [GC24]. However the latter is still an open topic in the field.

Dissipative phase transition. In quantum circuits, dissipation plays a central role and must be carefully modeled. A common strategy is to represent the environment (such as resistors or transmission lines) as a bath of harmonic oscillators, which can often be mapped onto noninteracting bosons. The most used theoretical framework to describe dissipation in Josephson circuits is the Caldeira-Leggett model [CL81]. Here, a Josephson junction is coupled to an infinite set of harmonic oscillators, each representing an harmonic mode of a resistive environment.

A central prediction of the Caldeira-Leggett model is that such a system undergoes a quantum phase transition between a superconducting and insulating state, known as the Schmid-Bulgadaev transition [Sch83; Bul84]. This occurs when the effective resistance of the environment reaches a critical value $R = R_Q$, where R_Q is the resistance quantum for Cooper pairs. For $R < R_Q$, the junction exhibits superconducting behavior (phase localized), while for $R > R_Q$, it becomes insulating (charge localized).

An important consequence of charge quantization is the compactness of the superconducting phase. The number of Cooper pairs on an island, n, can only take integer values. Since n and the superconducting phase φ are conjugate observables with the commutation relation $[n, \varphi] = i$, discreteness of n enforces that the phase is defined modulo 2π. In other words, the operator $e^{i\varphi}$ acts as a ladder operator that changes $n \to n+1$, so shifting $\varphi \to \varphi + 2\pi$ leaves the physical state unchanged. Thus, charge quantization implies that the superconducting phase is a compact variable, restricted to the interval $\varphi \in [0, 2\pi)$.

In many approximate models, for example when adding a large linear inductive shunt, charge quantization is neglected and n is treated as continuous. In this case, φ effectively loses its compactness and behaves as a non-compact variable taking values on the real line. Although this approximation can simplify calculations, it also removes important physical effects, such as the role of the gate charge n_g, which becomes physically relevant again once charge quantization is restored [KR24].

This shows how articulated this problem is and there is still not an ultimate clear way to address it, neither experimentally nor theoretically. Although the Schmid-Bulgadaev transition is supported by numerous theoretical works, both experimental confirmation and aspects of its theoretical interpretation remain subjects of ongoing debate [MBIS+20; HS21; MBIS+21; MSOA22; SFS23; MSOA23; KR24].

Circuits duality. In this section, the focus is not on a detailed analysis, but rather on presenting a simplified and intuitive overview. The main goal is to numerically study the dual circuit of the Josephson junction (Fig. 6.1.b), with the long-term goal of modeling and eventually realizing an experiment consisting of a single junction in series with a large inductor (ideally a geometric superinductor), operating in regimes that display the corresponding dual physics. First experimental attempts reported in Ref. [Per21] were were unable to provide clear evidence, motivating a step back to the simplified numerical study presented here.

The time evolution of superconducting quantum circuits, including both current-biased Josephson junctions and their dual counterparts, voltage-biased phase-slip junctions, can be described by the same differential equation:

$$\nu = y\dot{n} + \nu_0 \sin(2\pi n) + \tau\ddot{n}. \tag{6.1}$$

This unified form captures the core dynamics of both systems when expressed in terms of appropriately normalized variables. The dynamics of the current-biased Josephson circuit can be modeled as a fictitious phase particle moving in a potential landscape, with an effective mass given by the capacitance C. The dual system, based on a voltage-biased phase-slip junction, involves a charge particle, whose dynamics are similarly governed by an inductive mass L. The definitions of these variables, which differ between the flux-based and charge-based circuits, are summarized in Table 6.1.

By choosing the correct substitutions, we recover familiar circuit models for each case. For the Josephson junction, using the normalized flux variables leads to the well-known resistively and capacitively shunted junction (RCSJ) model, as detailed in Table 6.2. In the dual case of the coherent quantum phase-slip (CQPS) junction, the same equation describes the voltage-biased system when charge-based variables are used, as shown in Table 6.3.

The full mapping between the two systems, the key parameters, governing equations, and energy scales, is summarized in Table 6.4, highlighting the deep duality between these superconducting elements.

6.2 Motivation of classical numerical simulations

The classical simulations of the phase-slip junction circuit presented here are based on the report "On optimal circuit for CQPS current standard" by Oleg Astafiev[2].

[2] https://cordis.europa.eu/project/id/862660/results

Symbol	Josephson junction	Phase-slip junction	Unit
n	Φ/Φ_0 (normalized flux)	Q/Q_0 (normalized charge)	dimensionless
ν	I/Q_0 (normalized current)	V/Φ_0 (normalized voltage)	Hz
y	R/R_Q (normalized resistance)	R_Q/R (normalized admittance)	dimensionless
τ	$R_Q C$ (RC time)	L/R_Q (L/R time)	s
ν_0	I_C/Q_0	V_S/Φ_0	Hz

Table 6.1: **Normalized variable definitions for Josephson and CQPS junctions.**

Quantity	Expression
Supercurrent	$I = I_C \sin\phi$
Josephson energy	$E_J = \dfrac{\hbar I_C}{Q_0}$
Dynamic equation	$I = \dfrac{\dot{\Phi}}{R} + I_C \sin\left(\dfrac{2\pi\Phi}{\Phi_0}\right) + C\ddot{\Phi}$

Table 6.2: **Relations for the Josephson junction circuit.**

Quantity	Expression
Supervoltage	$V = V_S \sin(2\pi n)$
Phase-slip energy	$E_S = \dfrac{\hbar V_S}{\Phi_0}$
Dynamic equation	$V = \dfrac{\dot{Q}}{G} + V_S \sin\left(\dfrac{2\pi Q}{Q_0}\right) + L\ddot{Q}$

Table 6.3: **Relations for the phase-slip junction circuit.**

Josephson junction	Phase-slip junction
Flux Φ	Charge Q
Phase ϕ	$2\pi n$ (normalized charge)
Current I	Voltage V
Capacitance C	Inductance L
Resistance R	Conductance $G = 1/R$
Flux quantum Φ_0	Charge quantum $Q_0 = 2e$
Josephson energy E_J	Phase-slip energy E_S

Table 6.4: **Duality mapping between Josephson and CQPS junctions.**

The code provided in that work was reproduced and extended to different circuit layouts in order to create a tool that is both easy to use and intuitive for exploring circuit designs. The aim is not to determine optimal device parameters, but rather to provide a design aid: a simple way to test ideas, compare with experimental results reported in the literature, assess how well these results can be reproduced, and gain a clearer understanding of the constraints and possibilities of practical circuits.

In particular, the simulations make it possible to test the inductance values achievable with geometric superinductors, as well as the E_J and E_C values attainable with Josephson junctions instead of nanowires, and to estimate the expected size of the dual Shapiro steps.

By running the simulations over a broad range of parameters, it becomes possible to search for additional parameters correlations and build intuition on how different design choices affect

the system.

6.2.1 Numerical implementation in Mathematica

The dynamics of the CQPS device are governed by the nonlinear differential equation (Eq. 6.1), which was implemented and solved numerically in Mathematica. The external voltage applied to the circuit is modeled as a sum of a DC bias and a microwave drive,

$$V(t) = V_{\mathrm{dc}} + V_{\mathrm{ac}} \cos(\omega t), \tag{6.2}$$

where V_{dc} is the static bias and V_{ac} the amplitude of the AC excitation at frequency $\omega/2\pi = f$. The simulations proceed in three steps:

1. Input: for each set of input values $(V_{\mathrm{dc}}, V_{\mathrm{ac}}, V_C, R, L, C_C)$, the dynamics equation is integrated numerically.
2. Time Evolution: the code computes the normalized current $\dot{n}(t)$ and voltage $V(t)$ as functions of time. Transients are discarded, and only the steady-state oscillatory regime is used for analysis.
3. Output: the time average $\langle \dot{n} \rangle$ is calculated and converted into a physical current using

   $$I = \frac{2e}{T} \langle \dot{n} \rangle,$$

   with $T = 1/f$ the microwave period. By sweeping V_{dc} from 0 to $V_{\mathrm{dc,max}}$, the IV characteristic is reconstructed, reproducing what is experimentally measurable .

This simulation reproduces both the blockade at low bias and the quantized current steps in the presence of microwaves, and provides a versatile tool for analyzing how circuit parameters influence coherence and observability of quantum phase slips.

- Current blockade and dissipative branch: without microwave excitation ($V_{\mathrm{ac}} = 0$), the system exhibits a perfect current blockade for $V_{\mathrm{dc}} < V_C$. Beyond this threshold, the I-V curve becomes linear, with slope given by the series resistance R. This behavior directly reflects the duality of coherent phase slips with the Josephson effect.
- Dual Shapiro steps under microwaves: when a microwave drive is applied ($V_{\mathrm{ac}} > 0$), the I-V curve acquires a ladder of quantized current plateaus, the dual Shapiro steps. These steps occur at

  $$I_n = n \cdot 2ef, \qquad n \in \mathbb{Z}. \tag{6.3}$$

  Because $2e$ and f are fundamental and precisely measurable (atomic clocks), these plateaus provide a route to a quantum current standard.

6.2.2 Key findings: roles of L, R, and C_p

The simulations carried out in the report of Astafiev reveal several design rules for QPS circuits:

- Series Inductance (L). The report emphasizes a non-trivial but crucial point: a large series inductance is essential. Just as a large shunt capacitance in a Josephson junction suppresses phase fluctuations, here the inductance plays the dual role of suppressing charge fluctuations.

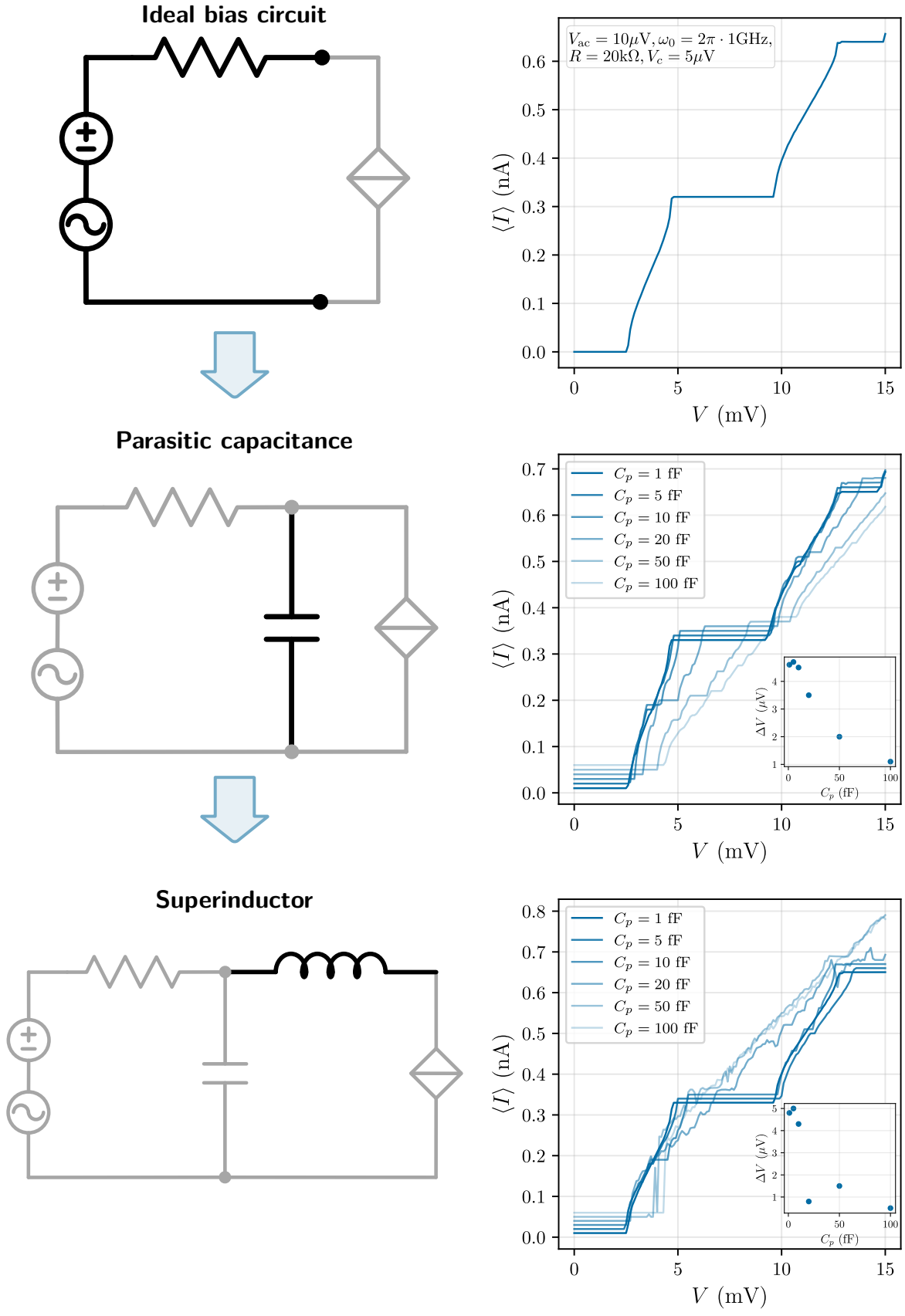

Figure 6.2: **Effect of circuits components on the size of the first dual Shapiro step.**

- Series Resistance (R). The value of R is critical for step visibility. If R is too small, the first Shapiro step lies within the blockade regime and is thus unobservable. The general condition for clear step observation is

$$R \geq \frac{V_C}{2e \cdot f}. \tag{6.4}$$

  With sufficiently large R, the steps appear on the dissipative branch, accessible to experiment.

- Shunting Capacitance (C_p). Real devices inevitably exhibit parasitic capacitance in parallel with the CQPS junction. The CQPS element itself has an intrinsic kinetic capacitance,

$$C_C = \frac{2e}{2\pi V_C}, \tag{6.5}$$

  which for $V_C = 5\ \mu\mathrm{V}$ is about $10\ \mathrm{fF}$. Simulations demonstrate that as long as $C_p \ll C_C$, the quantized steps remain intact. However, when $C_p \gtrsim C_C$ (e.g., $20 - 100\ \mathrm{fF}$), the plateaus become smeared and eventually vanish. The design rule is therefore to minimize parasitic capacitance such that $C_p < C_C$.

These interdependencies are summarized visually in Fig. 6.2. The presence of a parasitic capacitor suppresses the amplitude of the first inverse Shapiro step, while a sufficiently large superinductor can restore quantization, provided that C_p remains below the intrinsic kinetic capacitance.

6.3 Numerical results and conclusions

A substantial part of the work consisted in reproducing the Mathematica code implemented by Astafiev and adapting it to circuits of increasing complexity. Starting from the idealized QPS element biased by a perfect voltage source, successive elements were added to make the model closer to experimental reality (Fig. 6.2). This progressive refinement allowed to evaluate how each element modifies the observable I-V characteristics and, in particular, the quantized dual Shapiro steps under microwave irradiation.

One of the most important take home message, already emphasized in Astafiev's report, is the detrimental role of parasitic capacitance [ARH18]. On the one hand, a large shunting capacitance can smear out the quantized steps and suppress coherent transport. On the other hand, a deliberately engineered capacitance can be exploited as a coupling element to feed the microwave drive into the circuit. This design choice motivated us to test how the I-V characteristics depend on the way the AC component of the bias is coupled it.

In this regard, we compared two cases: (i) driving the system through a capacitor connected in parallel to the superinductor and QPS junction (Fig. 6.3 left column), and (ii) injecting the drive through the series resistor and inductor (Fig. 6.3 right column). Interestingly, the simulations reveal that the amplitude of the first inverse Shapiro step does not scale monotonically with the drive amplitude V_{ac} in both cases, but instead depends strongly on the injection pathway. As shown in Fig. 6.3, when the drive is applied through the $R + L$ branch, the first plateau reaches a larger amplitude at a smaller V_{ac}, but then decreases rapidly in an oscillatory fashion as the drive is further increased. In contrast, capacitive coupling requires a larger V_{ac} to achieve the same plateau amplitude, but the steps remain more stable as the drive is increased.

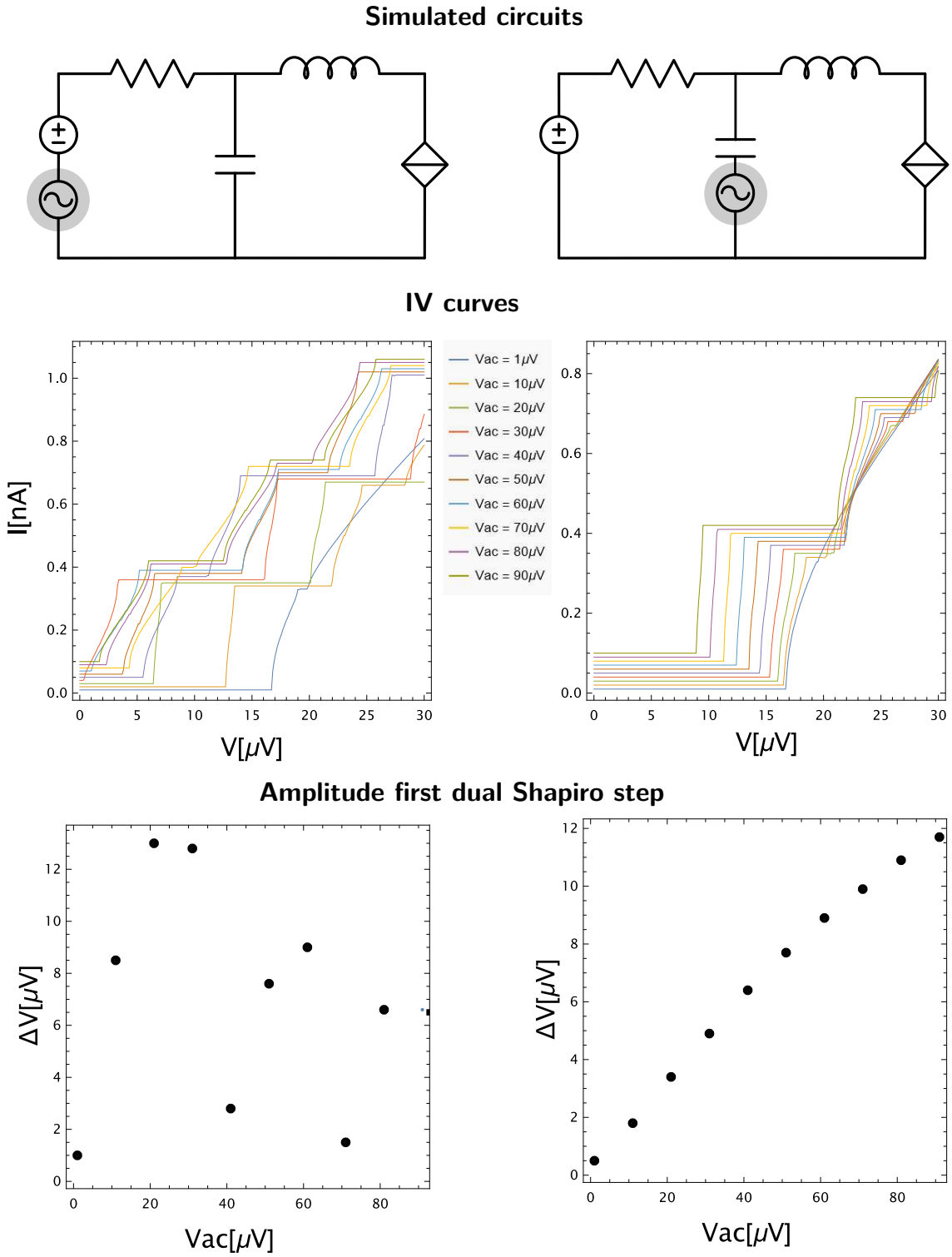

Figure 6.3: **Simulated I-V characteristics under different microwave coupling schemes. Left column.** AC drive (in gray) applied through the $R+L$ branch. **Right column.** AC drive (in gray) applied capacitively. The comparison highlights how the coupling method modifies the amplitude and robustness of the dual Shapiro steps. The values use in these simulations are: $V_C = 16\ \mu\text{V}$, $R = 30\ \text{k}\Omega$, $C_p = 1\ \text{fF}$ and $L = 500\ \text{nH}$.

This observation is particularly relevant for experimental implementations. Since microwave power dissipation is one of the main sources of overheating in low-temperature devices, being able to reach sizeable current steps with smaller V_{AC} is highly beneficial. On the other hand, the oscillatory suppression at higher drive amplitudes may pose a challenge for robustness. Therefore, the choice of microwave injection scheme becomes an important design parameter alongside R, L, and C_p.

In the literature, different groups have employed different strategies for coupling the microwave field:

- Refs. [SKD+22; SKD+24] apply the microwave signal through an on-chip capacitor connected to a split superinductor, with the drive entering through the smaller branch and thereby coupling to the QPS element.
- Ref. [CCG+23] injects the microwave field through through a bias-tee connected to the superinductor.
- Ref. [KKG+24] couples on-chip the drive directly to the QPS junction itself.

Our simulations reproduce the qualitative differences between these approaches and provide a theoretical framework to understand their impact on step amplitude and stability.

Outlook. The approach followed in this work relied on classical simulations of QPS-based circuits, progressively including realistic components such as parasitic capacitance and large inductances. While this provided useful intuition on the role of different circuit parameters and the way microwave injection affects the I-V characteristics, the perspective has shifted significantly in light of more recent theoretical advances. In particular, the work in Ref. [BGC24] has demonstrated that a fully quantum treatment is essential to capture the subtle physics of the dual Shapiro steps and, as a consequence, to determine the optimal set of parameters for their observation.

Unlike earlier analyses based on approximate charge-phase duality and classical RCSJ-like models, Ref. [BGC24] developed a circuit-QED theory where the environment is described as a finite-size transmission line resonator. This quantum description allowsto account not only for the discrete multimode structure of the environment, but also for the multi-band dynamics of the Josephson element itself. Most crucially, it is shown that the synchronization mechanism responsible for the dual Shapiro steps survives even beyond the single-band approximation. This result is highly relevant, as it suggests that dual steps can persist in experimentally realistic regimes where higher bands cannot be ignored.

A central message is also that the optimal parameter regime for observing dual steps differs from naive duality-based expectations. In particular, while the transmon regime ($E_J \gg E_C$) is theoretically simplest, it leads to exponentially small current steps. Instead, it is found that a moderate ratio $E_J/E_C \approx 5$–10 offers the best compromise, producing larger, experimentally accessible steps. Another key finding is the absolute necessity of very high environmental impedance ($Z \gtrsim 10R_Q$) in order to suppress charge fluctuations: unlike the direct Shapiro steps, which are robust against noise, the dual steps are extremely sensitive to both quantum and thermal fluctuations. The truncated Wigner approximation analysis further highlights that even vacuum fluctuations at zero temperature can wash out the steps unless the impedance is sufficiently large. Finally, because the relevant energy scale is the inductive energy E_L, which is typically very small, the dual steps require ultra-low temperatures for stability.

Taken together, these results provide a more realistic picture of the experimental challenges and possibilities. They also suggest why the classical simulations carried out here were not pushed further: while they offer useful first-order intuition, they cannot fully address the quantum noise and multi-band effects that ultimately determine the existence and robustness of the dual Shapiro steps.

6.4 Insights from the first experimental observations of quantized current steps

The observation and practical use of quantized current steps are limited by a range of experimental challenges. The goal of this section is to summarize what understood from the literature in terms of limitations and proposed improvements.

Broadening and smearing out of steps. Landau–Zener tunneling (LZT) between Bloch bands, which becomes relevant when $E_J \sim E_C$, can induce switching between superconducting and resistive states, thereby washing out the quantized plateaus [CCG+23]. Thermal noise from resistors, enhanced by both bias currents and microwave drive, further introduces finite slopes in the current-voltage characteristics and destroys quantization at elevated temperatures [CCG+23]. Heating effects are particularly detrimental: for instance, microwave drives can raise the electron temperature from ~ 40 mK to nearly ~ 250 mK [KKG+24].

Device and environmental constraints. Resistive environments contribute strong Johnson–Nyquist noise and additional heating, which destabilize the plateaus [KKG+24]. Stray capacitances between the junction and surrounding circuit elements lower the effective charging energy [SKD+22; SKD+24], while higher-order steps are often absent because LZT destroys the coherence of Bloch oscillations [CCG+23]. Current quantization has been observed only within narrow Josephson-junction parameter ranges, specifically $E_J/E_C \gtrsim 2$, $V_C^* \in [0.5, 5]$ μV, and $I_C^* \gtrsim 10$ nA [SKD+22; SKD+24]. Moreover, nanowire devices suffer from low fabrication yield and strong variability in parameters compared to junction-based devices [SKD+22; SKD+24].

Accuracy and metrological challenges. Even when steps are visible, current plateaus are generally not flat, and in noise-dominated regimes their amplitudes follow squared Bessel functions rather than first-order predictions [CCG+23]. The accuracy of quantized currents in nanowires or JJ remains significantly below that of single-electron pumps, which currently reach uncertainties on the order of ~ 0.2 ppm [KKG+24]. Despite steady progress, no robust metrological demonstration of dual Shapiro steps has yet been achieved [KKG+24].

Part III

Josephson chains across the superconductor-to-insulator transition

CHAPTER 7

Models for Josephson junction chains physics

Contributions and acknowledgments. *I thank Lucia Vigliotti for clarifying the derivation of the expressions in Section 7.2.*

Depending on the energy scale, the behavior of a Josephson junction chain (also referred to as a one-dimensional Josephson junction array) is more accurately described by different effective models. At high frequencies or high energies, the discrete circuit description, also known as Macroscopic Quantum Model, is required, where each junction's charging and Josephson energies set the characteristic modes and their dispersion. In contrast, at low frequencies or long wavelengths (compared to the chain lattice spacing), the system can be described by an effective Luttinger liquid Hamiltonian: its collective plasmon modes behave like gapless bosonic excitations with interaction strength set by the ratio between Josephson and charging energies.

A one-dimensional Josephson junction array acts as a versatile quantum simulator, reproducing canonical many-body models such as the two-dimensional classical XY model and the Bose-Hubbard model, and enabling experimental access to phenomena such as superfluid-insulator transitions.

In Section 7.2, the Hamiltonian of a Josephson junction chain is reviewed using the discrete formalism, with an emphasis on how the distance of the ground plane, whether close to or far from the chain, influences both the dispersion relation and the Kerr nonlinearity. The formulas refer to a Josephson junction chain that is galvanically coupled to a transmission line in a through-line configuration. In Section 7.3, the continuum case is briefly introduced in the form of a Luttinger liquid. Finally, in Section 7.4, analogies to two classical models, the two-dimensional XY model and the Bose–Hubbard model, are discussed, along with the types of physics that can be explored.

All these models are well established in the literature, and presenting them side by side highlights the connections between approaches, especially since different references often adopt different conventions.

7.1 1D systems

The following section is based on Ref. [Gia03].

Interacting one-dimensional (1D) systems exhibit unique quantum phenomena that cannot be described using traditional methods developed for higher dimensions. In two or three dimensions, Landau's Fermi-liquid theory [Lan56] provides a successful framework for understanding interacting fermionic systems. It treats interactions perturbatively, mapping a complex many-body problem into a gas of weakly interacting quasiparticles, essentially electrons with renormalized effective parameters.

This approach fails in one dimension. In higher dimensions, single-particle excitations can propagate relatively freely, with mean free paths much larger than the interparticle spacing or even the system size. In contrast, in 1D systems, particles are constrained to move along a single line, making collisions with neighbors unavoidable. Consequently, a single-particle excitation inevitably disturbs the surrounding particles, transferring energy and momentum through the entire system. Well-defined single-particle excitations therefore do not exist, and the dynamics are governed entirely by collective modes.

In a Fermi gas, the simplest excitations are particle–hole pairs. A particle–hole pair is formed when an occupied state below the Fermi surface becomes unoccupied, leaving behind a hole, while a previously unoccupied state above the Fermi surface becomes occupied, representing the particle. This construction conserves both energy and momentum, and defines the fundamental building blocks of low-energy excitations. The set of all such possible excitations for a given momentum transfer q defines the particle–hole spectrum.

In two and three dimensions, the Fermi surface is a continuous curve or surface. This continuity implies that, for almost any momentum transfer q, there exist occupied and unoccupied states with arbitrarily small energy separation. Hence, the particle–hole spectrum reaches zero energy for a continuous range of q. This results in a dense set of low-energy excitations, which in turn provides many scattering channels and reduces quasiparticle lifetimes. Although quasiparticles in higher-dimensional systems remain well defined near the Fermi surface, they generally possess finite lifetimes.

The situation in one dimension is qualitatively different. The Fermi surface consists of only two discrete points at $+k_F$ and $-k_F$. Zero-energy particle–hole excitations are possible only when the momentum transfer is exactly $q = 2k_F$. Thus, the particle–hole spectrum touches zero energy at a single momentum value, in contrast to the extended range present in higher dimensions. The restricted phase space for scattering leads to exceptionally long-lived excitations. Moreover, these excitations exhibit an effective bosonic character, despite being composed of fermions.

The bosonic nature of long-lived particle–hole excitations gives rise to coherent collective phenomena such as charge-density and spin-density waves. This forms the basis of the Luttinger liquid [Tom50; Lut63; ML65] description, which replaces the Fermi liquid paradigm in one dimension. In this framework, bosonization [Gia03] provides the appropriate language for expressing the low-energy physics in terms of collective bosonic modes, capturing the essential properties of 1D interacting systems.

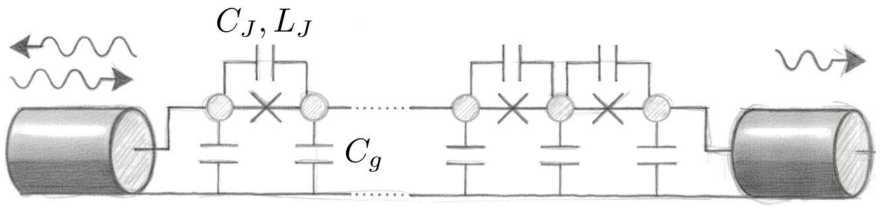

Figure 7.1: **Schematic of a Josephson junction chain.** Each junction has Josephson inductance L_J and capacitance C_J, while each superconducting island is coupled to ground through a capacitance C_g. Adapted from Ref. [YGH21].

7.2 Discrete 1D Josephson junction array model: Macroscopic Quantum Model

The following section closely follows the approach described in Refs. [KNW+18; KNW+23].

A one-dimensional chain composed of N superconducting islands connected via Josephson junctions is considered, with both ends coupled to a transmission line. Each island is assumed to be sufficiently small compared to the superconducting coherence length, allowing its quantum state to be described by a single superconducting phase variable θ_n.

Coupling between neighboring islands occurs through both Cooper-pair tunneling and electrostatic interactions. The tunneling is mediated by the Josephson effect, with energy scale set by the Josephson energy E_J, which is related to the inductance L_J (previously labeled L_{J0} in Eq. 5.7) of each junction by

$$E_J = \left(\frac{\hbar}{2e}\right)^2 \cdot \frac{1}{L_J}. \tag{7.1}$$

This term introduces a nonlinear coupling that depends on the phase difference between adjacent islands.

Electrostatic interactions are described by a capacitance matrix $C_n m$ that incorporates both the junction capacitance C_J between neighboring islands and the self-capacitance C_g of each island to the ground. The charge Q_n on each island is canonically conjugate to the phase θ_n, with commutation relations given by $[\theta_n, Q_m] = i2e\delta_{n,m}$, with $\delta_{n.m}$ being the Kronecker delta.

A schematic representation of the system, including the superconducting islands, Josephson junctions, and capacitances, is shown in Fig. 7.1.

7.2.1 Linear Hamiltonian

The total Hamiltonian describing the system is [KNW+18]

$$H = \frac{1}{2}\sum_{n,m=1}^{N-1} Q_n C_n^{-1} m Q_m - E_J \sum_{n=1}^{N-2} \cos(\theta_{n+1} - \theta_n) - E_J \cos(\theta_1) - E_J \cos(\theta_{N-1}), \tag{7.2}$$

where the first term represents the electrostatic (charging) energy stored in the capacitive network, and the cosine terms account for Josephson tunneling between adjacent islands and between the endpoints and the external circuit. To impose open boundary conditions, the phases at the endpoints are fixed to $\theta_0 = \theta_N = 0$. These conditions define the ends of the physical chain and ensure the correct treatment of the edge junctions.

Capacitive term. The structure of the capacitance matrix $\mathbf{C}$ changes depending on how strongly the island charges are screened [KNW+18]. Its exact form is set by the electrostatic environment of the chain, mainly how close the ground plane is, including nearby dielectrics, gates, and the chosen boundary conditions. The two relevant cases, where the chains are either close or far from the ground plain, are now considered.

When the Josephson chain is placed near a ground plane, each superconducting island is capacitively coupled to the ground through a gate capacitance C_g, which helps to locally screen excess charge. With this screening mechanism in place, the capacitance matrix of the chain takes a simple form [KNW+18]:

$$\mathbf{C}_{\text{close ground}} = \begin{pmatrix} 2C_J + C_g & -C_J & 0 & \dots \\ -C_J & 2C_J + C_g & -C_J & \dots \\ 0 & -C_J & 2C_J + C_g & \dots \\ \vdots & \vdots & \vdots & \ddots \end{pmatrix}. \tag{7.3}$$

This is a tridiagonal matrix of size $(N-1) \times (N-1)$, where the diagonal elements are all equal to $2C_J + C_g$, and the only non-zero off-diagonal entries are $-C_J$, appearing just above and below the diagonal. This structure reflects the fact that, in this approximation, each island interacts electrostatically only with its nearest neighbors. A derivation for this case can also be found in Ref. [WKD+15].

In contrast to the locally screened case, significant differences arise when the ground plane is positioned far from the superconducting chain, far meaning at a distance comparable to, or even larger than, the electromagnetic mode wavelengths supported by the system [KNW+18]. Under these conditions, the screening of the island charges Q_n by the ground plane becomes non-local. A single island's electric field can extend over many neighboring sites before being effectively screened. As a result, the Coulomb interaction develops a long-range character.

To account for these effects, the capacitance matrix must be extended beyond the tridiagonal form used in the local screening case. The resulting matrix takes the form [KNW+18]:

$$\mathbf{C}_{\text{distant ground}} = \begin{pmatrix} 2C_J + C_{g,11} & -C_J + C_{g,12} & C_{g,13} & & & \dots \\ -C_J + C_{g,21} & 2C_J + C_{g,22} & -C_J + C_{g,23} & & & \dots \\ C_{g,31} & -C_J + C_{g,32} & 2C_J + C_{g,33} & -C_J + C_{g,34} & C_{g,35} & \dots \\ \vdots & \vdots & \vdots & \vdots & \vdots & \ddots \end{pmatrix}. \tag{7.4}$$

This matrix includes not only the usual nearest-neighbor coupling terms (the coefficients along the diagonal) but also additional contributions $C_{g,nm}$ that represents long-range interactions mediated by the distant ground plane. The matrix is no longer tridiagonal, and many entries away from the diagonal are non-zero. Consequently, its inverse $\mathbf{C}^{-1}_{\text{distant ground}}$, required for computing the system's charging energy, cannot be obtained analytically and has to be evaluated numerically.

Although the model appears more complex, the number of adjustable parameters remains the same as in the local screening case, since the overall ground capacitance C_g is often used as a fitting parameter. The increased chain–ground distance just acts as a short-distance cutoff in the Coulomb potential, while the remaining interaction is determined by the chain's geometry. As reported in Ref. [KNW+18], when the ground plane is far from the chain this model yields significantly better agreement with experimental observations than the simpler local screening model, particularly for the low-frequency modes.

Inductive term. When the Josephson energy is much larger than the characteristic charging energy, the phase differences between neighboring islands, $\theta_{n+1} - \theta_n$, remain small and the nonlinear Josephson potential can be expanded as a power series in these small phase differences

$$\cos(\theta_n - \theta_m) \approx \frac{1}{2}(\theta_n - \theta_m)^2. \tag{7.5}$$

Replacing the nonlinear cosine potential with a quadratic term each Josephson junction can be approximated as a harmonic element. This makes the analysis of collective modes and circuit quantization more tractable: the total Hamiltonian becomes quadratic $H^{(2)}$ in both charge and phase variables, and is given by

$$H^{(2)} = \frac{1}{2}\sum_{n,m=1}^{N-1} Q_n C_{nm}^{-1} Q_m + \frac{E_J}{2}\sum_{n=1}^{N-2}(\theta_{n+1} - \theta_n)^2 + \frac{E_J}{2}\theta_1^2 + \frac{E_J}{2}\theta_{N-1}^2. \tag{7.6}$$

7.2.2 Dispersion relation

To determine the eigenfrequencies of the chain, the phase and charge operators are expressed in terms of a complete set of normal modes:

$$\theta_n = \sum_{k=1}^{N-1} \psi_k(n)\theta_k, \qquad Q_n = \sum_{k=1}^{N-1} \psi_k(n) Q_k, \tag{7.7}$$

where the mode functions $\psi_k(n)$ form an orthonormal basis of sinusoidal waves that satisfy open boundary conditions at the ends of the chain. These mode functions are used to diagonalize the spatial dependence of the system, allowing the decoupling of collective excitations into independent harmonic modes.

Substituting this expansion into the quadratic Hamiltonian (Eq. 7.6) leads to a fully diagonal form:

$$H^{(2)} = \sum_{k=1}^{N-1}\left(\frac{Q_k^2}{2C_k} + \frac{\theta_k^2}{2L_k}\right), \tag{7.8}$$

where each mode k behaves as a harmonic oscillator characterized by an effective capacitance C_k and inductance L_k.

Within this harmonic approximation, the phase operator acts analogously to a position variable, while the charge corresponds to its conjugate momentum. The spectrum of allowed oscillation frequencies (the normal modes), is then given by

$$\omega_k = \omega_p \sqrt{\frac{1 - \cos\left(\frac{\pi k}{N}\right)}{\frac{C_g}{2C_J} + 1 - \cos\left(\frac{\pi k}{N}\right)}}, \tag{7.9}$$

where the plasma frequency $\omega_p(\text{rad/s}) = \sqrt{2E_J E_C}/\hbar$ sets the characteristic energy scale of the chain, with the charging energy defined as $E_C = (2e)^2/(2C_J)$ and $E_g = (2e)^2/(2C_g)$. Wave vectors usually have dimension [length]$^{-1}$, but they are dimensionless in this notation ($\mathrm{k} = \pi k/N, k$ positive integer), since lengths are expressed in units of the lattice spacing $a = \ell/N$, with ℓ the length of the chain.

This linearized description is valid when the Josephson energy E_J dominates over the charging energy E_C, ensuring that phase fluctuations between neighboring islands remain small and

justifying the expansion of the cosine potential to quadratic order (Eq. 7.5). In this regime, the chain behaves like a set of coupled harmonic oscillators, and the dispersion relation Eq. 7.9 captures the frequency dependence of the collective modes. In the limit where $k \ll N$, cosine can be linearized as

$$\cos\left(\frac{\pi k}{N}\right) \approx 1 - \frac{1}{2}\left(\frac{\pi k}{N}\right)^2 + \dots \tag{7.10}$$

leading to

$$\omega_k \approx \omega_p \sqrt{\frac{\frac{1}{2}\left(\frac{\pi k}{N}\right)^2}{\frac{E_c}{2E_g} + \frac{1}{2}\left(\frac{\pi k}{N}\right)^2}} = \sqrt{\frac{2E_J E_C}{\hbar^2}\frac{\frac{1}{2}\left(\frac{\pi k}{N}\right)^2}{\frac{E_C}{2E_g} + \frac{1}{2}\left(\frac{\pi k}{N}\right)^2}} = \frac{\pi k}{N}\sqrt{\frac{2E_J E_g}{\hbar^2}\frac{1}{\left(1 + \frac{E_g}{E_C}\left(\frac{\pi k}{N}\right)^2\right)}}. \tag{7.11}$$

Introducing the velocity $v(\text{rad/s}) = \sqrt{2E_J E_g}/\hbar$,

$$\omega_k = \frac{\frac{\pi k}{N} v}{\sqrt{\left(1 + \frac{v^2}{\omega_p^2}\left(\frac{\pi k}{N}\right)^2\right)}} = \frac{\mathrm{k} v}{\sqrt{\left(1 + \frac{v^2}{\omega_p^2}\mathrm{k}^2\right)}}. \tag{7.12}$$

Restoring proper lengths via a gives

$$\omega_k = \frac{\frac{\mathrm{k}}{a} v a}{\sqrt{\left(1 + \frac{v^2 a^2}{\omega_p^2}\left(\frac{\mathrm{k}}{a}\right)^2\right)}} = \frac{\tilde{\mathrm{k}}\tilde{v}}{\sqrt{\left(1 + \frac{\tilde{v}^2}{\omega_p^2}\tilde{\mathrm{k}}^2\right)}}, \tag{7.13}$$

where $\tilde{v} = va$, and $\tilde{\mathrm{k}} = \pi k/\ell$. This matches the notations used, for example, in Ref. [HG19], where lengths are not rescaled by a from the beginning. When extracting velocity from fits versus mode numbers (k and not $\tilde{\mathrm{k}}$), the appropriate equation must be used.

From the dispersion relation, three regimes can be identified:

- For $\mathrm{k} \ll \sqrt{E_C/E_g}$, the dispersion relation is linear, and the quantity v corresponds to the phase velocity of the electromagnetic modes propagating along the transmission line.
- When $\mathrm{k} \sim \sqrt{E_C/E_g}$, the influence of the in-line capacitance causes the dispersion relation to deviate from linearity. This identifies $\sqrt{E_C/E_g}$ as the characteristic length scale over which Coulomb interactions between sites become effectively screened.
- For $\mathrm{k} \gg \sqrt{E_C/E_g}$, the wave frequency approaches its maximum value, the plasma frequency ω_p. This frequency corresponds to the natural resonance of the junctions forming the transmission line. At ω_p, all junctions oscillate collectively, and wave propagation is no longer supported.

7.2.3 Second quantization

To transition from the classical description of the chain's collective modes to a fully quantum mechanical framework, the harmonic oscillator analogy is once again employed. Each normal

mode of the system can be quantized by promoting the classical phase and charge variables to operators that satisfy canonical commutation relations. Specifically, the phase operator for mode k can be expressed in terms of bosonic creation and annihilation operators as [KNW+18]

$$\theta_k = 2e\sqrt{\frac{1}{2\hbar C_k \omega_k}}\left(\hat{a}_k + \hat{a}_k^\dagger\right), \tag{7.14}$$

where $\hat{a}_k^\dagger$ and $\hat{a}_k$ are the raising and lowering operators, respectively, for the harmonic oscillator associated with mode k. The prefactor ensures the correct normalization consistent with the canonical commutation relations between phase and charge operators.

Using the expansion of the local phase operators in the normal mode basis,

$$\theta_n = \sum_{k=1}^{N-1} \psi_k(n)\theta_k, \tag{7.15}$$

the spatially resolved phase operators can be written as

$$\theta_n = 2e\sum_{k=1}^{N-1} \psi_k(n)\sqrt{\frac{1}{2\hbar C_k \omega_k}}\left(\hat{a}_k + \hat{a}_k^\dagger\right). \tag{7.16}$$

This quantization procedure naturally leads to the second-quantized form of the Hamiltonian $H^{(2)}$, which describes a set of independent quantum harmonic oscillators:

$$H^{(2)} = \sum_{k=1}^{N-1} \hbar\omega_k \left(\hat{a}_k^\dagger \hat{a}_k + \frac{1}{2}\right). \tag{7.17}$$

Here, each mode k behaves as a quantum harmonic oscillator with energy quanta $\hbar\omega_k$, and the operators $\hat{a}_k^\dagger$ and $\hat{a}_k$ create and annihilate these excitations, respectively. This formalism provides a convenient starting point for analyzing quantum properties such as photon number states, coherent states, and the effects of nonlinearities beyond the harmonic approximation.

7.2.4 Kerr coefficients

To account for interactions between different electromagnetic modes in the chain, it is necessary to move beyond the linear approximation and include the leading nonlinear correction to the Josephson potential. Expanding the cosine potential to fourth order in the phase difference yields a quartic term of the form

$$H^{(4)} = -\frac{E_J}{4!}\sum_{n=1}^{N-2}(\theta_{n+1} - \theta_n)^4, \tag{7.18}$$

which captures the first anharmonic contribution responsible for mode–mode interactions. This term gives rise to important physical effects such as frequency shifts that depend on occupation number, commonly referred to as self-Kerr and cross-Kerr interactions.

Including this quartic correction, the second-quantized Hamiltonian can be written as

$$H^{(2)} + H^{(4)} = \sum_k \omega_k' \hat{a}_k^\dagger \hat{a}_k - \frac{1}{2}\sum_k \mathcal{K}_{k,k}\hat{a}_k^\dagger \hat{a}_k \hat{a}_k^\dagger \hat{a}_k - \frac{1}{2}\sum_{k,p\neq k} \mathcal{K}_{k,p}\hat{a}_k^\dagger \hat{a}_k \hat{a}_p^\dagger \hat{a}_p. \tag{7.19}$$

Here, the first term describes the harmonic modes with renormalized frequencies ω'_k, which include frequency shifts arising from vacuum fluctuations (i.e., the zero-photon limit of the quartic term) [KNW+18]. The second term corresponds to the self-Kerr interaction, in which the frequency of a mode shifts depending on its own photon occupation. The third term describes the cross-Kerr interaction, which introduces mutual frequency shifts between different modes as a function of their respective photon numbers.

The strength of these nonlinear couplings is captured by the Kerr coefficients $\mathcal{K}_{k,p}$, which take the form [KNW+18; KNW+23]:

$$\mathcal{K}_{k,p} = \left(\frac{1}{2} - \frac{\delta_{k,p}}{8}\right) \frac{\omega_k \omega_p}{2NE_J}. \tag{7.20}$$

This expression shows that both self-Kerr ($k = p$) and cross-Kerr ($k \neq p$) terms scale inversely with the Josephson energy E_J and linearly with the product of the corresponding mode frequencies. Notably, the self-Kerr coefficient is slightly reduced due to the additional numerical factor $\delta_{k,p}/8$, reflecting the enhanced symmetry in that case.

7.3 Continuous 1D Josephson junction array model: Luttinger liquid

The discussion in this section follows Ref. [HG19].

The low-energy physics of one-dimensional Josephson junction chains is captured by the Luttinger liquid framework. Instead of particle-like excitations, the system supports collective density and phase fluctuations, which can be described by bosonic fields.

As derived in Eq. 7.13, in Josephson junction chains, the plasmon modes have dispersion

$$\omega_k = \frac{\tilde{v}\tilde{\mathrm{k}}}{\sqrt{1 + (\tilde{v}\tilde{\mathrm{k}}/\omega_p)^2}},$$

with $\tilde{v}$ the plasmon velocity and ω_p the cutoff frequency in rad/s. For angular frequencies $\omega_{\tilde{\mathrm{k}}} \ll \omega_p$, i.e. at low energies where the dispersion is approximately linear, the system reduces to a harmonic string Hamiltonian[1]

$$H_0 = \int dx \left[\frac{\pi \tilde{v} K}{2\hbar}\Pi^2 + \frac{\hbar \tilde{v}}{2\pi K}(\partial_x \phi)^2\right], \tag{7.21}$$

where K is the Luttinger parameter that encodes the interaction strength, ϕ is the coarse-grained phase field and $\Pi = -(\hbar/\pi)\partial_x \theta$ is its conjugate momentum. These fields connect directly to physical observables: the particle density along the chain is expressed as $\rho(x) = -(1/\pi)\partial_x \phi(x)$, while the particle current density is related to Π.

The Luttinger interaction parameter K, also known as superfluid stiffness, is set by circuit parameters. In Josephson chains it can be written as

[1] To maintain consistency with the variables used in Sec. 7.2 following Ref. [BPG+17], the Hamiltonian in Eq. 7.21 adopts a different notation compared to Ref. [HG19]: $q \to \tilde{v}$, $\varphi \to \theta$, and $\theta \to \phi$.

$$K = \pi\sqrt{\frac{E_J}{2E_g}}, \qquad K = \frac{\pi\hbar}{4e^2 Z_C}, \tag{7.22}$$

where E_J is the Josephson coupling, E_g is the effective ground capacitance energy, and Z_C is the (low-frequency) characteristic impedance of the chain. The value of K determines the balance between charge localization and phase coherence: $K < 1$ corresponds to effectively repulsive interactions and insulating tendencies, while $K > 1$ favors superconducting coherence.

Thus, the Luttinger liquid model provides the natural effective description of Josephson junction chains at low energies, where the Hamiltonian Eq. 7.21 encodes how quantum fluctuations, interactions, and impedance shape transport and phase transitions in one dimension.

The mapping between the low-frequency behavior of Josephson junction chains and the Luttinger liquid model was experimentally demonstrated in Ref. [CAK+17] (a nice summary can be found in Ref. [BCD+25]). To account for phase-slip rates, finite-temperature effects, and charge disorder, new theoretical frameworks and predictions have been developed in Refs. [BPG+17; HG19].

7.4 2D-XY and Bose-Hubbard models

The study of one-dimensional Josephson junction arrays is driven by their ability to host a variety of quantum phases and to allow controlled exploration of the transitions between them using fully engineerable devices. Two key theoretical models, which can be implemented and tested using these arrays, are introduced in Subsection 7.4.1, the 2D-XY model, and Subsection 7.4.2, the Bose–Hubbard model.

Although these models describe the same physical system and can be mapped onto each other, they are often presented using different languages, making distinctions between them mostly a matter of convention. For example, XY-like models are commonly used to discuss Berezinskii-Kosterlitz-Thouless (BKT) physics, whereas Bose-Hubbard-type models are typically associated with Mott lobes and quantum phase transitions. Despite these differences in terminology, both frameworks capture the same underlying physics.

In conclusion, these models provide a general framework for understanding the phase diagrams of one-dimensional Josephson junction arrays. However, real systems may exhibit richer behavior due to effects such as disorder, long-range interactions, dissipation, or deliberately engineered circuit geometries and topologies.

This section follows Ref. [Wil19].

7.4.1 2D-XY model in 1D Josephson junction arrays

A Josephson junction array with negligible charging energy can be mapped to the classical two-dimensional XY model with Hamiltonian

$$H = -E_J \sum_{\langle i,j \rangle} \cos(\phi_i - \phi_j). \tag{7.23}$$

Since the Hamiltonian depends only on phase differences, a global shift $\phi_i \to \phi_i + d\phi$ leaves the system invariant, indicating a continuous symmetry.

The correlations behave differently in the high- and low-temperature regimes. At high temperature, i.e. in the disordered case, the correlation decays exponentially,

$$\langle \cos(\phi_r - \phi_0) \rangle \sim e^{-r/\xi}, \qquad \text{with } \xi \sim \frac{1}{\ln(2/J)}, \tag{7.24}$$

with $J = E_J/(k_B T)$, indicating short-range order. At low temperature, $J \to \infty$ as $T \to 0$, so strong fluctuations in ϕ are penalized and global coherence is favored; the correlation then decays algebraically,

$$\langle \cos(\phi_r - \phi_0) \rangle \sim \left(\frac{a}{r}\right)^{1/(2\pi J)}, \tag{7.25}$$

indicating quasi-long-range order.

Although the Mermin-Wagner theorem forbids spontaneous breaking of continuous symmetry and true long-range order in systems of dimension two or lower, the XY model still supports a topological phase transition with no symmetry breaking, in which the high- and low-temperature phases are distinguished by differences in topology. This is an example of a Berezinskii–Kosterlitz–Thouless (BKT) transition.

The phase at each position in a system is a single-valued quantity but is defined modulo 2π. This means that while the phase itself is well-defined, it can wind by an integer multiple of 2π, i.e., the phase at a point can be written as $\phi + 2\pi n$ with $n \in \mathbb{Z}$.

A phase configuration with $n = 0$ everywhere corresponds to the uniformly ordered state, where the phase is coherent across the system. In contrast, a configuration where the phase winds around a certain position corresponds to a topological defect, known as a vortex. Vortices are discrete objects; one cannot continuously transform a configuration with a vortex into the uniform state without a discontinuous change. This is because the winding number n is topologically protected: it is an integer that counts the number of times the phase wraps around 2π along a closed loop, and integers cannot change continuously.

The behavior of vortices depends strongly on temperature. At low temperature, creating vortices is energetically costly. The system favors $n = 0$ configurations, which are phase-coherent and uniformly ordered, supporting superconductivity. In this regime, quantum fluctuations of charge are significant due to the uncertainty principle, allowing for supercurrent flow without dissipation.

At high temperature, thermal fluctuations can favor vortex creation, leading to phase disorder. Vortices interact through a logarithmic potential, reminiscent of Coulomb interactions in two dimensions. This is analogous to the energy of a Josephson junction array in the limit where the charging energy dominates. In this case, the inverse of the capacitance matrix, which determines the interaction between charges, also behaves logarithmically at large distances, giving rise to similar long-range interactions between topological excitations.

The interaction between vortices is logarithmic, so the model maps onto a two-dimensional Coulomb gas and can also be described by the sine–Gordon theory. In fact, in two dimensions, the XY model, the sine–Gordon model, and the Coulomb plasma provide equivalent descriptions of the same underlying physics, highlighting the duality between phase and charge representations and the topological nature of vortices.

In Josephson chains, this picture emerges naturally: when $E_J/E_C \ll 1$, the system is charge dominated and can be described as a Coulomb plasma of localized Cooper pairs, whereas for $E_J/E_C \gg 1$, phase coherence dominates and the system maps onto a Coulomb gas

of vortices. At a formal level, the one-dimensional quantum Josephson junction array at zero temperature maps onto the two-dimensional classical XY model, where the additional dimension corresponds to imaginary time. In this mapping, the spatial coupling is controlled by E_J, while the temporal coupling is set by the charging energy E_C. Consequently, the superconductor-insulator transition in a one-dimensional array falls into the universality class of the BKT transition, with the ratio E_J/E_C at $T = 0$ K determining whether the system exhibits phase coherence or charge localization. At higher temperatures, the phase diagram becomes more intricate (see Ref. [BPG+17; MSSM+23]).

For further details see Ref. [Fv01].

7.4.2 Bose-Hubbard model

In addition to the XY model, one-dimensional Josephson junction arrays can also be described by the Bose–Hubbard model, which captures the physics of interacting bosons on a lattice. The Hamiltonian is

$$H_{\mathrm{BH}} = \frac{U}{2}\sum_i \hat{n}_i(\hat{n}_i - 1) - \mu\sum_i \hat{n}_i - t\sum_{\langle i,j\rangle} \hat{b}_i^\dagger \hat{b}_j, \tag{7.26}$$

where $\hat{b}_i^\dagger$ and $\hat{b}_i$ are boson creation and annihilation operators, $\hat{n}_i = \hat{b}_i^\dagger \hat{b}_i$ is the number operator, U is the on-site interaction energy, μ is the chemical potential, and t is the hopping amplitude between neighboring sites.

In this version of the Bose-Hubbard model, interactions are restricted to on-site terms but in one-dimensional Josephson arrays, th electrostatic interactions between islands can remain significant for distances $r \lesssim \Lambda$, decaying as $e^{-r/\Lambda}$, with Λ being the interaction length depending on the circuit parameters.

The Hamiltonian in Eq. 7.26 provides a good approximation for a Josephson chain in the limit $C_J/C_G \to 0$, where the capacitance matrix becomes diagonal and only on-site interactions contribute to the Hamiltonian, and the mapping is $U = 2E_C,\ t = E_J/2,$ and $\mu = E_C(1+2f)$, with f being the offset charge.

More generally, to include interactions with arbitrary range Λ, an additional term must be added

$$\sum_{i\neq j} C_{ij}^{-1} n_i n_j, \tag{7.27}$$

which makes the effective chemical potential site-dependent. This reflects the influence of the full capacitance matrix. In practice, Josephson junction arrays are not perfectly homogeneous, so U and μ can vary from site to site.

The phase diagram of the Bose–Hubbard model at zero temperature is When tunneling is absent ($t = 0$), the ground state is insulating with a fixed integer number of bosons per site. As μ is varied, one finds successive insulating states with different fillings. At finite t, these insulating regions expand into "Mott lobes", separated by a superfluid phase where bosons delocalize and phase coherence develops.

In two or more dimensions, mean-field theory gives the correct qualitative picture of these Mott lobes. In one dimension, mean-field theory is not accurate, but the same overall structure survives: alternating Mott insulators and superfluids, controlled by the balance of U and t.

The transition between these phases is a quantum phase transition, driven not by temperature but by the competition between charging energy and tunneling. Because charge and phase are conjugate variables, strong charge localization ($U \gg t$) leads to large phase fluctuations and an insulating state, while strong tunneling ($t \gg U$) delocalizes charge and stabilizes long-range phase coherence in the superfluid. The interplay of discreteness and coherence produces the characteristic lobe-shaped phase diagram.

Thus, Josephson arrays realize the Bose–Hubbard physics in a natural way: charging energy corresponds to on-site repulsion, Josephson energy corresponds to hopping, and offset charges shift the chemical potential.

CHAPTER 8

Josephson chains measurements results

Disclaimer. *The results and conclusions presented here are preliminary, as data analysis and interpretation were still ongoing at the time of writing. In particular, for the microwave measurements, a spurious coupling between two devices was identified during the analysis, which limits the extent of the conclusions that can be drawn at this stage. Further work is required to acquire additional data, refine the analysis and develop a more comprehensive understanding of the observed phenomena.*

Contribution and acknowledgments. *I would like to thank Andrew P. Higginbotham for his support as an external supervisor. His guidance was especially valuable while getting the new DC measurement setup up and running. I also appreciate his suggestions regarding relevant literature and his insightful contributions during discussions of the results. Thanks to Georgios Kastaros for the low noise electronics IVVI[1] used in preliminary DC measurements on this setup [Per21]. I am grateful to Manuel Houzet and Leonid Glazman for taking the time to brainstorm about our results in the picture of their paper (Ref. [HG19]), which helped clarify several aspects relevant to this work. I would also like to thank Matilda Peruzzo for her work on installing the RF and DC lines in the dilution refrigerator "Fermi". Finally, I thank Areg Avtandilyan for his help with measurements, discussions and preliminary data analysis during his rotation in the group from April to June 2025.*

8.1 Overview and Motivation

One-dimensional Josephson junction arrays exhibit a rich variety of phenomena in both their DC transport [ELJ+13; VSR+15; CAK+17] and RF response [MPK+12; MGM+18; BVSH25], as well as under simultaneous DC and RF driving [CCG+23], determined by the interplay between the Josephson coupling energy E_J and the charging energies E_C and E_g.

DC behaviour. When the Josephson energy dominates, these arrays behave as highly conductive system. On the contrary, when the Josephson energy is comparable to or smaller than the charging energy, the arrays enter an insulating regime characterized by Coulomb blockade and thermally activated processes [VSR+15; CAK+17].

[1] https://qtwork.tudelft.nl/~schouten/ivvi/index-ivvi.htm

In the insulating regime, current remains suppressed at zero temperature until the bias voltage exceeds a threshold: early works attributed this switching to the nucleation and propagation of charge solitons [HD96], but later experiments showed that the threshold scales linearly with array length and depends on the Josephson energy [HA0; AAH01], pointing instead to depinning of collective charge configurations in the presence of strong charge disorder [VSR+15].

RF behaviour. Josephson junction arrays sustain plasma modes, collective electromagnetic excitations corresponding to small oscillations of the superconducting phase, which can be viewed as quantized electromagnetic waves confined to the array. Their properties are set by the interplay between the Josephson coupling energy E_J, the charging energy E_C, and the ground capacitance energy E_g, the latter controlling the Coulomb screening length and thereby shaping the mode dispersion (see Section 7.2).

When $E_J \gg E_C$, the plasma modes are well-defined, weakly damped, and propagate along the chain with a phase velocity set by the array inductance L_J and the total capacitance per site. On the contrary, when $E_J \lesssim E_C$, quantum phase fluctuations become strong and the mode spectrum can be renormalized or even gapped due to phase-slip processes. In this regime, the chain behaves as a high-impedance medium, and the plasma modes may experience substantial damping or localization [KMG+19; HG19; WS19], due to inelstic scatteing from phase-slip events or charge-disorder induced localization.

This view parallels the "depinning" picture from DC transport: instead of charge configurations being pinned, here the plasma modes themselves can become pinned or fragmented by inhomogeneities in the capacitance network, leading to a suppression of transmission at certain frequencies [YGH21] and mode-dependent quality factors [HG19].

DC+RF bahaviour. When a Josephson junction chain is driven simultaneously by a DC bias and an RF signal, the two drives interact through the nonlinear Josephson current-phase relation, producing transport signatures that reflect both slow charge motion and fast plasma dynamics. One of the most iconic manifestations of this interplay is phase locking between the DC-driven dynamics and the RF excitation.

In the superconducting regime, where $E_J \gg E_C, E_g$, this phase locking leads to the appearance of Shapiro steps in the I-V characteristics: plateaus at quantized voltages $V_n = n(hf_{\mathrm{RF}}/2e)$, with f_{RF} the RF frequency [Sha63]. Shapiro steps are of great importance in metrology, as they provide a direct link between frequency and voltage, enabling primary voltage standards [BH04; BBK+25].

In the opposite, insulating regime, where $E_J \ll E_C, E_g$, the dual Shapiro steps are expected: quantized current plateaus $I_n = n(2ef_{\mathrm{RF}})$ arising from coherent tunneling of single Cooper pairs under RF drive. These dual steps are of metrological interest for the realization of a current standard complementary to the Josephson voltage standard [SAK+24]. First experimental oberservations of dual Shapiro steps have been reported [SKD+22; CCG+23; SKD+24; KKG+24], but a comprehensive understanding of the optimal parameter regimes, coherence requirements, and limitations is still lacking [ARH18; BGC24] (see also Chapter 6).

Motivation for the experiments in this chapter. The measurements in this chapter were motivated by previous results [MSSM+23] in Andrew Higginbotham's group, which investigated how temperature affects coherence in a one-dimensional Josephson junction array.

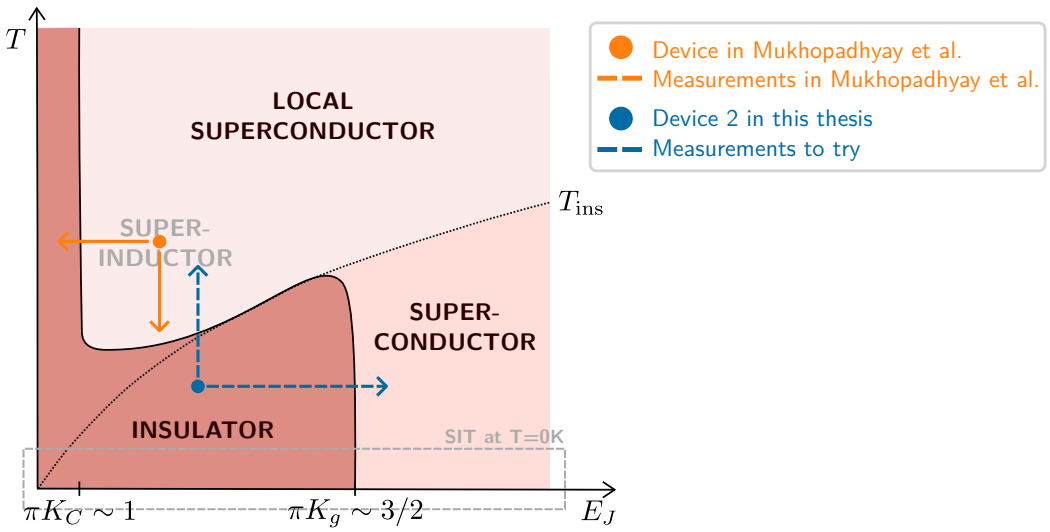

Figure 8.1: **Proposed phase diagram E_J vs. T.** Reproduced from Ref. [MSSM+23]. The diagram illustrates superconducting and insulating phases as functions of the Josephson energy E_J and temperature T. The dashed line represents the threshold temperature T_{ins} that separates regimes of long-range (Superconductor) and short-range behavior (Local Superconductor). For $T < T_{\text{ins}}$, the system is described by the long-range superfluid stiffness K_g, with the superconductor-insulator transition occurring when $\pi K_g \approx 3/2$. For $T > T_{\text{ins}}$, the short-range superfluid stiffness K_C governs the behavior, and the transition appears at $\pi K_C \approx 1$. The solid black curve indicates the crossover from a superconductor to insulator. The orange arrow indicate the parameters spaced studied in Ref. [MSSM+23], the blue dashed line two of the possible direction motivation of the measurements in this chapter. The gray dashed box at the bottom the simple SIT phase diagram at $T = 0$ K highlighted as a comparison to the more rich at higher temperature.

In their study, the array expected to show an increasing resistance decreasing the temperature instead exhibited a drop reminiscent of superconductivity, saturating at low temperatures (temperature sweep measurement indicated by the orange arrow pointing down in Fig. 8.1). The most probable reason was that the transition temperature T_{ins} was below the minimum temperature reachable in the setup. Applying a strong enough magnetic field, so changing the Josephson energy of the array, allowed to crossover to another region of the insulating state (orange arrow pointing left in Fig. 8.1), now showing an increasing resistance decreasing temperature. This can be understood in the new proposed phase diagram E_J vs. T in Fig. 8.1 where a new region "Superinductor" ($E_g \gg E_J \gg E_C$) with local superconducting behavior appears at finite temperature. This can be understood as thermal fluctuations melting the insulating phase, giving rise to the superconducting behavior. Or in other words non monotonic renormalization of the phase slips rate with temperature [BPG+17]. The new phase diagram that takes in consideration finite temperature consequences would so solve the incosistency problem posed by the superinductor: a regime that based on the SIT theory at $T = 0$ K and probed in DC was supposed to lay on the insulating side of the transition but that is regularly used in superconducting qubits [MKGD09; PMN+20], so showing a superconducting behavior.

Building on these results, two main research directions emerge. The first is to explore the insulating–superconducting transition (SIT) in a regime below the crossover insulating temperature T_{ins} (also proposed in the SI of Ref. [MSSM+23]). In Fig. 8.1 it is indicated by the blue dashed arrow pointing right. The second direction is to study the SIT as a function

of temperature by fabricating devices in the insulating regime with a moderate T_{ins}, such that it does not mask or broaden the superconducting response, vertical dashed blue arrow in Fig. 8.1. This approach allows probing both DC and RF behavior and understanding how superconducting modes evolve in a device insulating in DC.

Another option would be to study what happens at the high frequency behaviur of a Josephson chain moving accross the SIT. In particular, the fate of RF modes in the insulating regime remains unclear: earlier studies on high-impedance chains [KMG+19] report a constant internal quality factor as a function of mode frequency but lacked a demonstration of DC insulating behavior (no Coulomb blockade observed in DC). Theoretical proposals [HG19] suggest that in a superinductor, the system could show a frequency-dependent SIT: no modes at low frequency, gradually giving way to regularly spaced modes at higher frequencies. Experimentally testing this prediction could provide direct insight into the dynamics of insulating Josephson arrays.

Finally, studying DC and RF response on the same device offers a unique opportunity to investigate dual Shapiro physics (introduced in Chapter 6, connecting nontrivial superconducting behavior with microwave response. Overall, the interplay of SIT, RF modes in insulators, and dual Shapiro physics were the central motivation for the experiments, guiding the exploration toward the most promising regimes.

8.2 Experimental Methods

8.2.1 Device Design

Each Josephson junction chain is $1.0576\ \mathrm{mm}$ long, measured from the end of the taper on the coplanar waveguide (Fig. 8.2.a). The CAD layout is designed with 500 Dolan bridges, each $0.25\ \mu\mathrm{m}$ long (Fig. 8.2.b), with an additional $20\ \mathrm{nm}$ gap on either side. The segments between the bridges, which define the island lengths, are $1.816\ \mu\mathrm{m}$ long (Fig. 8.2.b). The segments at the two ends of the chain form large junctions that are not considered part of the array. Therefore, for $N = 500$ Dolan bridges, the total number of junctions in the array is $N_{\mathrm{JJ}} = (2 \cdot N + 1) - 2 = 999$. These parameters are the same for all devices; the only differences are the width and spacing to ground.

No DC-SQUID chains were used, and no magnetic field was applied in order to allow for a clean interpretation of the results. This choice was particularly motivated by prior observations, such as in Ref. [CAK+17] where DC-SQUID arrays exhibited a blockade threshold voltage significantly different from that predicted and observed in standard JJ chains. This discrepancy was attributed to flux trapping in the SQUID loops, which complicates interpretation.

Sample A (Fig. 8.2.c) consists of three devices: an insulator (Device 6), a superconducting wire (Device 4) and a superinductor (Device 5, Fig. 8.2.d) with dimensions closely matching those of the superinductor in Ref. [MSSM+23], but with approximately 20% fewer junctions. Additionally, all the device was galvanically connected (in contrast to the original capacitive coupling), and a shorter version was realized for DC transport measurements. Sample B (Fig. 8.2.f) includes five devices of which three connected to the measurements setup: a transmission line used as a baseline (Device 1), an insulator (Device 2, Fig. 8.2.e), and a Josephson chain (Device 3) similar to Device 2 but made by larger junctions. Device 7 and 8 are not connected. A summary of the relevant geometric parameters and characterstic energies are provided in Table 8.1 and Table 8.4 respectively.

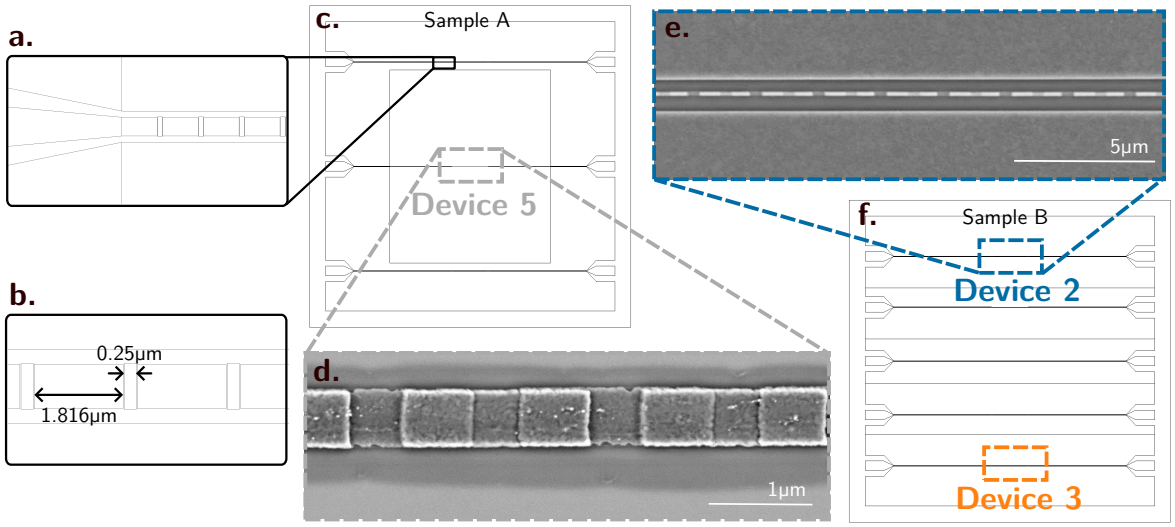

Figure 8.2: **CAD layout and SEM images of Josephson chains devices.** **a.** Each Josephson junction chain has a length of $1.0576\ \mathrm{mm}$, measured from the end of the taper on the coplanar waveguide. **b.** Enlarged CAD layout of the array, designed with $N = 500$ Dolan bridges of length $0.25\ \mu\mathrm{m}$; the island segments are $1.816\ \mu\mathrm{m}$ long. **c.** CAD layout of Sample A, consisting of three devices. **d.** SEM image of the superinductor (Device 5) of Sample A. **e.** SEM image of the Josephson junction chain of Sample B (Device 2), designed as an insulator in DC. **f.** CAD layout of Sample B, which contains five devices, three of which (Devices 1–3) are connected to the measurement setup.

Sample	Width (μm)	Spacing to GND (μm)	Island size (μm)	JJ size (μm)	Device spacing (mm)
Sample A - CAD file: SIT006.dxf					
Device 6 (Ins)	0.1 (0.06)	0.5 (0.57)	(1.67×0.1)	(0.64×0.1)	$\mathrm{D6 - D5 = 4\ mm}$
Device 5 (superL)	0.5 (0.46)	~ 3000	(1.67×0.5)	(0.64×0.5)	-
Device 4 (SuperC)	1 (0.96)	0.28 (0.32)	(1.67×1)	(0.64×1)	$\mathrm{D4 - D5 = 4\ mm}$
Sample B - CAD file: SIT007.dxf					
Device 2	0.16 (0.12)	0.52 (0.54)	(1.67×0.16)	(0.64×0.16)	$\mathrm{D2 - D7 = 1.6\ mm}$
Device 7	0.28 (0.24)	0.46 (0.48)	(1.67×0.28)	(0.64×0.28)	$\mathrm{D7 - D1 = 1.7\ mm}$
Device 1 (Short)	10	6	-	-	$\mathrm{D1 - D8 = 1.7\ mm}$
Device 8	0.22 (0.18)	0.55 (0.58)	(1.67×0.22)	(0.64×0.22)	$\mathrm{D8 - D3 = 1.6\ mm}$
Device 3	0.34 (0.3)	0.55 (0.58)	(1.67×0.34)	(0.64×0.34)	-

Table 8.1: **Dimensions of the Josephson chains.** Values in brackets correspond to the design parameters from the CAD file; values outside the brackets are the expected dimensions based on dose tests. No SEM images of the measured devices are available, and due to e-beam lithography instabilities during fabrication, these values may differ from the actual ones. The last column shows the distance between devices, included to assess possible crosstalk effects in the data. The rows highlighted in gray represent the devices measured and presented in this chapter.

No SEM images of the measured devices were taken before to measurement, in order to avoid electron beam-induced damage that can break the oxide and short some junctions. However, SEM images of similarly fabricated test structures are available and provide representative dimensions and geometries. To minimize slotline modes there are few on-chip bonds over the transmission line connecting bond pads to Josephson devices; each bond pad was connected using three parallel wire bonds for impedance matching and the sample GND is connected to PCB GND with many other wires.

8.2.2 Device fabrication

Steps highlighted in gray indicate optional cleaning processes.

Process	Steps	Notes
Wafer preparation	Tape Dice	
Substrate cleaning	ACE, 21 °C, uc power 9, 5 min IPA, 21 °C, uc power 9, 5 min N2 blow dry Plasma ashing BOE, tank, 10 sec DI Water, becker, 5 sec DI Water, tank, 5 sec N2 blow dry	
Spin and bake e-beam resist	Prebake, 120°C, 1min Spin, MMA EL13, 3.5 krpm, 1 min (acceleration 1 krpm/s) Bake, 170 °C, 3 min Spin, PMMA 950k 4%, 4 krpm, 1 min (acceleration 1 krpm/s) Bake, 170 °C, 3 min	
E-Beam Flow Prep	CAD file preparation Beamer flow file preparation	
E-Beam Patterning	JJ, 0.8 or 1 nm beam, dose 4 × 90-110 μC/cm^2 with 3D PEC (base dose of 1 and 0.4 for undercut box). Coplanar-waveguide and Ground plane, 100 - 250 nm beam, dose 330-350 μC/cm^2 with 3D PEC	
Development	water:IPA (1:3), 21 °C, 2 min IPA, 21 °C, 10 sec N2 blow dry	
Evaporation	Cleaning Ti gittering, 5 min, 0.2 nm/s Al evaporation, 40 nm, 1 nm/s, tilted between 15 and 35 deg Static oxidation 5 min, 5 mbar Al evaporation, 80 nm, 1 nm/s, tilted after a 180 deg rotation of the holder between 15 and 35 deg Static oxidation 2 min, 10 mbar	
Liftoff	DMSO, in a becker immersed in a water bath on a hot plate at 145 °C, 1 h DMSO, in a becker immersed in a water bath on a hot plate at 145 °C, 1 h ACE, 21 °C, 30 sec IPA, 21 °C, 30 sec N2 blow dry	

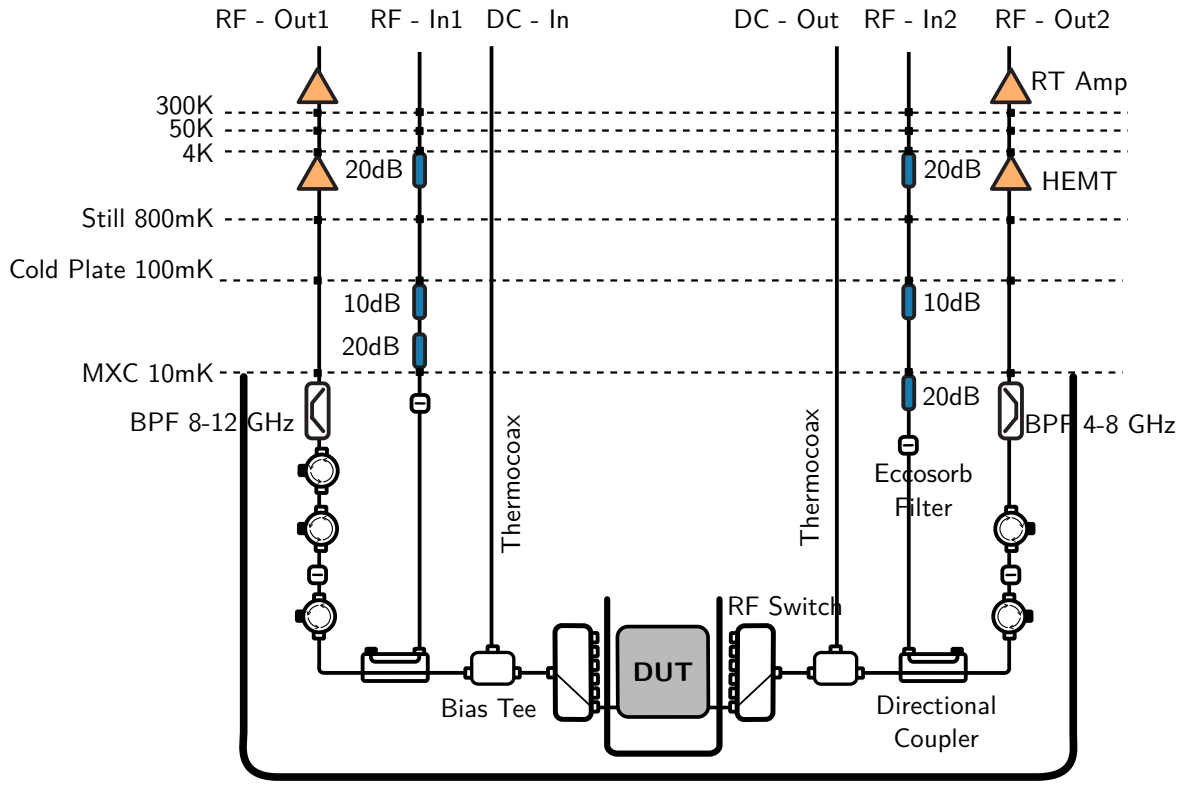

Figure 8.3: **Measurement setup.**

8.2.3 Measurement setup

DC transport measurement setup. All DC transport measurements employ a voltage-bias configuration, schematically illustrated in Fig. 8.3. The bias voltage originates from a Yokogawa GS2000 source. For differential resistance measurements, a lock-in amplifier (Stanford Research Instruments) provides the AC excitation. Combination of the lock-in output with the Yokogawa output occurs through a resistor network with $R_{\mathrm{LI}} = 10\ \mathrm{k}\Omega$ in the lock-in path and $R_{\mathrm{Yoko}} = 100\ \Omega$ in the Yokogawa path. Both resistors are inside Pomona boxes to ensure mechanical protection and shielding.

Measurement DC lines. The measurement lines consist of Thermocoax NC AC RT–MXC cables with twisted-pair center conductors. These lines provide both signal transmission and distributed low-pass filtering for suppression of high-frequency noise. Nominal specifications are: length $3 \pm 5\%\ \mathrm{m}$, outer diameter $0.5 \pm 5\%\ \mathrm{mm}$, resistance $R = 155 \pm 5\%\ \Omega$, and capacitance $C = 562 \pm 5\%\ \mathrm{pF}$. No additional filtering elements precede the Thermocoax cables.

Series resistor and low-pass cutoff. At the mixing chamber (MXC) end of the Thermocoax lines, a $2\ \mathrm{k}\Omega$ resistor in series with the signal path is mounted on a PCB thermally anchored to the MXC, approximately $1\ \mathrm{m}$ from the sample. This arrangement improves thermalization and sets a lower cutoff frequency for the input path. The low-pass filter results from the

combined resistance of the Thermocoax and the series resistor together with the cable capacitance, yielding a total resistance $R_{\text{total}} = 2.15\ \text{k}\Omega$. The -3 dB cutoff frequency is then $f_{\text{cutoff},-3\ \text{dB}} = (2\pi RC)^{-1} \approx 131.7\ \text{kHz}$.

Johnson-Nyquist noise. The RMS voltage noise of a resistor over bandwidth Δf follows $V_{\text{n,rms}} = \sqrt{4k_B T R \Delta f}$. At $T = 10\ \text{mK}$, the Johnson–Nyquist noise corresponds to $V_{\text{n,rms}} \approx 34.45\ \text{pV}/\sqrt{\text{Hz}}$.

RF and DC signal combination. Combination of RF and DC signals occurs via a bias-tee (Anritsu) feeding a 1 to 6 mechanical switch (Radiall). Each switch output routes to an individual device connected through PCB enclosed within a two-part copper cavity. The lower half contains a shallow milled recess without through-penetration, increasing the fundamental resonance frequency of the cavity modes and reducing interference with device-related modes. The upper lid provides mechanical support and preserves a stable electromagnetic environment.

For Sample A, the superinductor design requires a ground plane $3\ \text{mm}$ away while the top lid is only $0.5\ \text{mm}$ above. To accommodate this requirement, a full through-cutout matching the chip size ($\approx 10\ \text{mm} \times 10\ \text{mm}$) is present. The copper cavity attaches to a cold finger connected to the MXC and resides inside a mu-metal shield to reduce magnetic noise.

Current measurement. Current readout employs a current-to-voltage converter (Basel Instruments) with transimpedance gain $10^7\ \text{V/A}$. While higher gains up to $10^9\ \text{V/A}$ are technically possible, the present configuration consistently uses $10^7\ \text{V/A}$. The signal then passes through a low-pass filter with either $100\ \text{Hz}$ or $300\ \text{Hz}$ cutoff before further amplification. A digital multimeter (Keysight) records the voltage with averaging over 10 power-line cycles (NPLC), corresponding to an integration time of approximately $0.2\ \text{ms}$.

Microwave signal path. Microwave excitation travels from room temperature to the sample via dedicated coaxial lines and combines with the DC bias at the bias-tees. Total attenuation in the cryostat amounts to $70\ \text{dB}$ ($50\ \text{dB}$ from attenuators $+\ 20\ \text{dB}$ from the side port of the directional coupler). Eccosorb filters are present on both input and output lines (input: in-house made [Red22]; output: commercial model). The usual $12\ \text{GHz}$ low-pass filter (K&L) in the input is omitted to allow measurements up to $20\ \text{GHz}$. No circulators are present; a directional coupler is used instead.

Output 1 contains three isolators (Memstar, 8–$12\ \text{GHz}$), a band-pass filter (BPF), and a LNF HEMT amplifier. Output 2 contains two isolators (LNF, 4–$8\ \text{GHz}$), a BPF, and a LNF HEMT amplifier. A room-temperature amplifier, common to both outputs, is swapped between them depending on the active measurement channel.

RF spectroscopy. RF spectroscopy employs a vector network analyzer (VNA), either a Keysight PNA or a R&S ZNB1, and an RF source from R&S.

DC grounding. Several grounding configurations are evaluated to interface the lock-in amplifier with the rest of the measurement chain. The adopted scheme uses star grounding, with the refrigerator frame as the sole ground reference and all instruments floating relative to earth, connected only to this point. Instruments unable to float from the main ground, particularly the lock-in amplifier, operate via an isolation power generator to prevent ground loops.

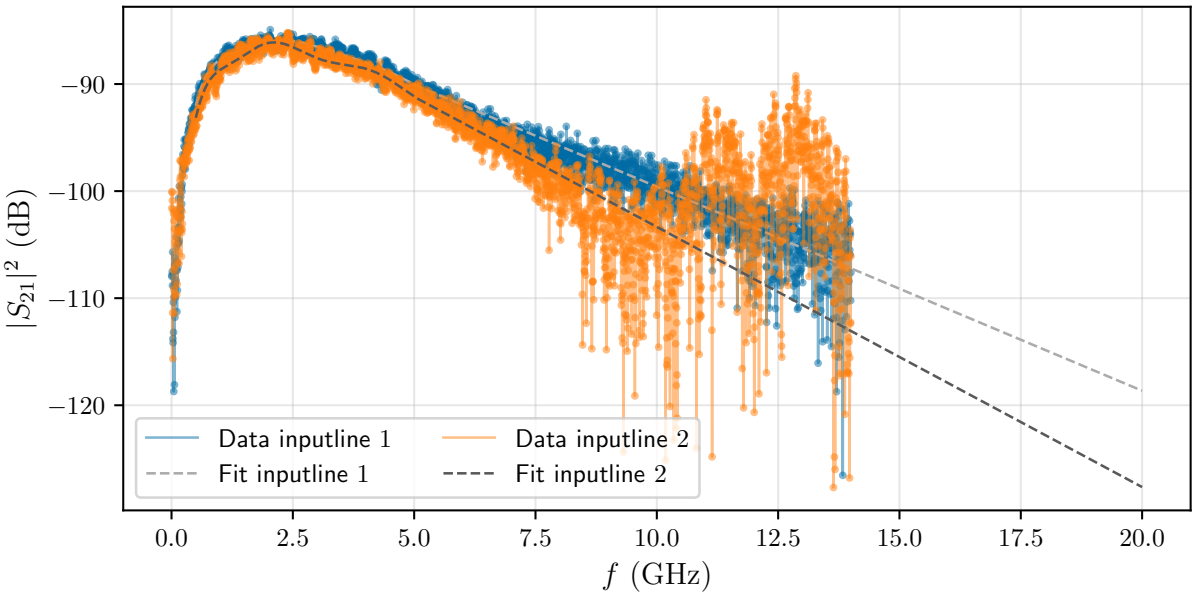

Figure 8.4: **Input-line attenuation.** Input-line 1 baseline: attenuation from the room-temperature cable and the 70 dB (50 dB attenuator + 20 dB side port of the directional coupler) inside the cryostat. The downturn below 3 GHz corresponds to the contribution of the side port of the directional coupler inside the refrigerator. Beyond this range, the fit is linear (in log scale) to account for the cable's frequency-dependent loss. Input-line 2 baseline: same specs as Input-line 1. The unexpected behavior above 10 GHz needs further investigation.

8.2.4 Baselines characterization

RF inputlines attenuation. The baselines of the two microwave (RF) input lines in the experimental setup were characterized to account for frequency-dependent attenuation. These lines transmit the signal from the vector network analyzer (VNA) to the SMA connectors immediately following the mechanical RF switch. Attenuation was measured at room temperature across the frequency range from 300 kHz to 14 GHz, covering the VNA operating range.

Between 300 kHz and 3 GHz, the data exhibit a downturn caused by the directional coupler's coupling port. For frequencies above 14 GHz, attenuation was extrapolated, assuming a steady trend at higher frequencies where direct measurements were not available. This extends the baseline estimate up to 20 GHz.

Fig. 8.4 shows the measured attenuation along with the interpolation and linear extrapolation. These baselines are important for the photon number calculation and comparison of reflection and transmission measurements among devices. Inputline 2 exhibits a feature around 12 GHz, absent in previous cooldowns. Further investigation is required to confirm its origin.

RF baselines. The four RF baselines (Fig. 8.5) characterize the transmission and reflection paths within the measurement setup. Measurements were performed at low temperature (MXC temperature 10 mK, one day after reaching base temperature) using a VNA. The dataset includes reflection (S_{11}, S_{22}) and transmission (S_{21}, S_{12}) scattering parameters, allowing quantification of frequency-dependent attenuation and gain along the signal paths, as well as identification of asymmetries or component-induced variations. The measurement ranges are

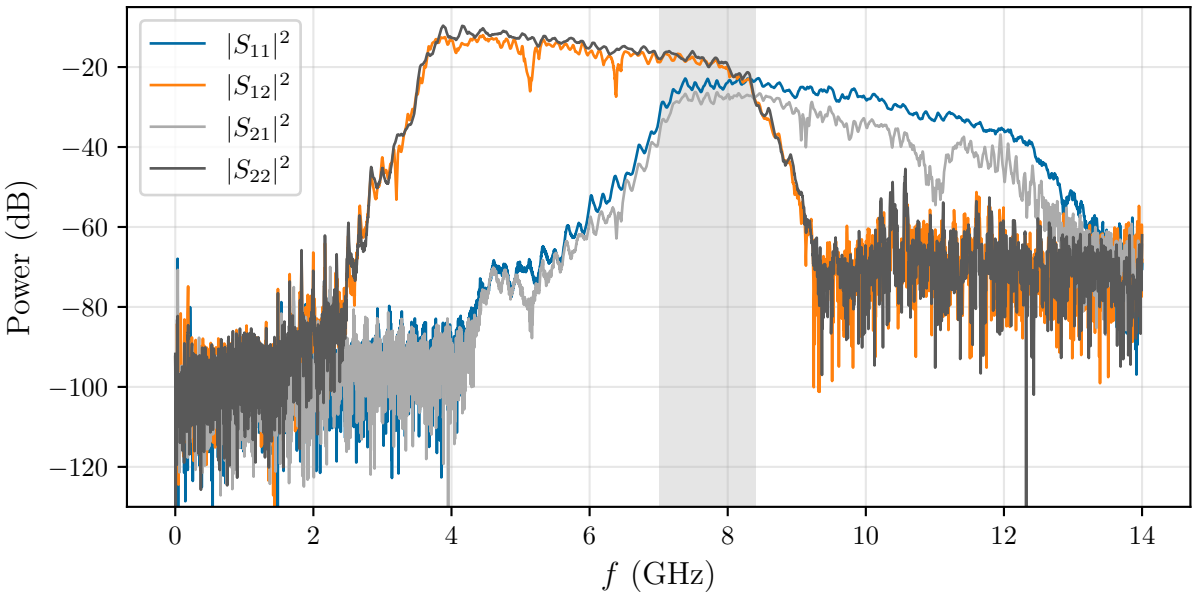

Figure 8.5: **Room-temperature RF baselines.** S_{11} and S_{22} are measured with the RF switch in the "reset" state (all signal reflected). S_{12} and S_{21} are measured with the switch connected to Device 1 on-chip, a $50\ \Omega$ matched coplanar waveguide. The measurements characterize the frequency-dependent attenuation and gain of the four measurements paths in the setup. The gray area marks the frequency range in which all four S-parameters can be extracted for a resonance mode present in this region. The directional coupler adds a constant 20 dB attenuation. In one-tone measurements, the room-temperature directional coupler is not used, so the blue baselines serve as the reference. In two-tone spectroscopy, the VNA is connected to the side port, making the orange curve the reference attenuation for the signal, while the pump passes through the through-port of the directional coupler, making the blue baseline the reference.

set by the output line bandpass filters and isolators: Outputline 1 spans $8 - 12$ GHz, while Outputline 2 spans $4 - 8$ GHz.

The reflection coefficient S_{11}, measured with the RF switch in the "reset" position (input disconnected from any output), corresponds to the Inputline 1 $\rightarrow$ Outputline 1 path. Similarly, S_{22} under the same "reset" condition corresponds to the Inputline 2 $\rightarrow$ Outputline 2 path. Differences between these reflection measurements arise from slight variations in nominally identical components, such as connectors, attenuators, and cables in the input lines, and from different isolators and cryogenic High Electron Mobility Transistor (HEMT) amplifiers in the output lines. Each output line has a different cryogenic HEMT, introducing unique gain and noise characteristics, while the room-temperature amplifier following the cryostat is identical for both lines.

The forward transmission coefficient S_{12}, measured through a 50 Ω matched coplanar waveguide (Device 1) on the chip, captures the baseline for the Inputline 1 $\rightarrow$ Outputline 2 path. The reverse transmission coefficient S_{21} corresponds to the Inputline 2 $\rightarrow$ Outputline 1 path, also measured through Device 1. Both S_{12} and S_{21} exhibit small resonances with a free spectral range of approximately 1 GHz. These transmission baselines provide essential information for identifying potential non-reciprocities or direction-dependent losses introduced by the setup, including the switch and amplifiers.

Together, the reflection and transmission baselines serve as critical references for future device

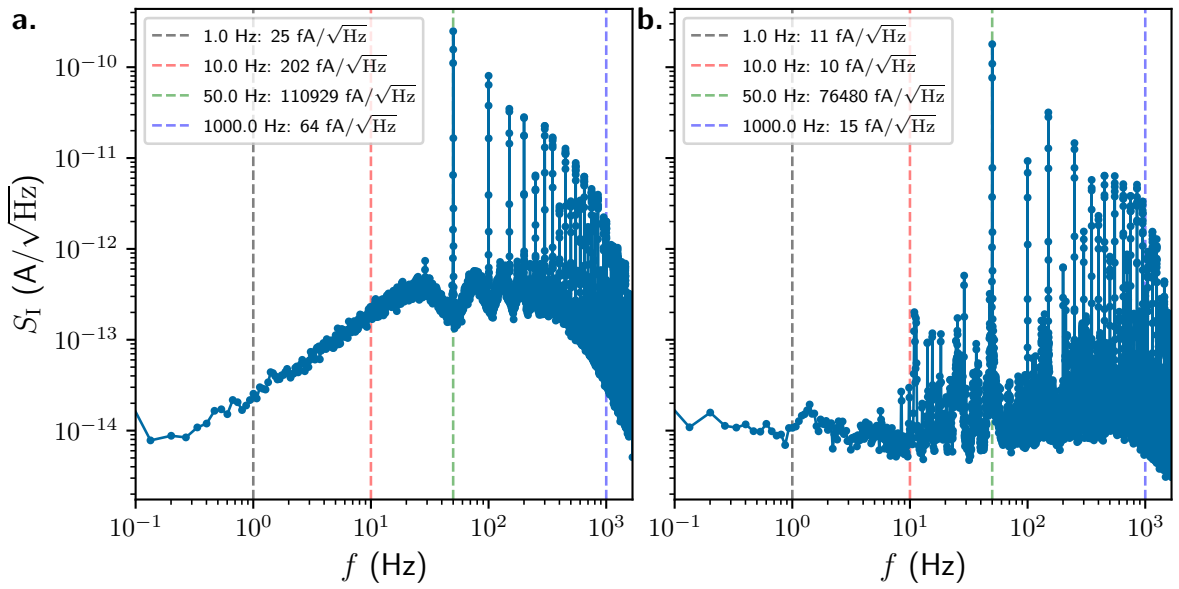

Figure 8.6: **Low-frequency noise.** Low-frequency noise spectral density measured from Device 2 under insulating conditions. The data were averaged using Welch's method from more than 10 independent time traces. Peaks at 50 Hz and harmonics indicate residual electromagnetic interference from the environment. **a.** Measurement configuration: DC cable connected to Yokogawa ON, output OFF, HEMTs OFF; **b.** DC cable not connected to Yokogawa, HEMTs OFF.

characterization, enabling accurate de-embedding of setup-related attenuation and gain, and providing insight into the performance and symmetry of individual RF components in the measurement chain.

Electronic Noise. This paragraph presents the characterization of the DC response and low-frequency noise performance of the measurement setup. These quantities are critical for assessing the effective thermalization, grounding, and shielding quality of the wiring from room temperature to the sample.

DC Baseline. Device 1, a $50\ \Omega$-matched coplanar waveguide on chip, was measured under voltage bias at low temperature to serve as a calibration reference for determining the series resistance in the DC lines. The current-voltage characteristic exhibits a linear (in log scale) slope corresponding to the total resistance between the DC source and the sample. The extracted resistance is consistent with the expected contribution from the mixing-chamber resistors, twisted-pair wiring, and filtering elements. This measured baseline agrees well with the expected value and provides a reference for interpreting transport measurements on other devices.

Low-Frequency Noise. Figure 8.6 presents the low-frequency noise spectral density measured from Device 2, a sample exhibiting an insulating behavior at DC. In this configuration, both RF switches are connected to Device 2, ensuring isolation from external circuit paths and amplifiers.

The voltage fluctuations were recorded using a high-resolution digital multimeter (DMM), configured for high-speed time-domain acquisition. For accurate noise characterization, multiple time traces ($N > 10$) were acquired sequentially and processed using Welch's method for

Parameter	Notation	Formula
Junction capacitance	C_J	$(2e)^2/(2E_C)$
Junction capacitance to ground	C_g	$(2e)^2/(2E_g)$
Junction inductance	L_J	$(\hbar/2e)^2/E_J$
Impedance	Z_C	$\sqrt{L_J/C_g}$
Local superfluid phase stiffness	K_C	$\sqrt{E_J/(2E_C)}$
Global superfluid phase stiffness	K_g	$\sqrt{E_J/(2E_g)}$
Plasma frequency	f_P	$\sqrt{2E_JE_C}/h$
Charge screening length	Λ	$\sqrt{E_g/E_C}$
Bloch bandwidth (also Phase slip rate)	$W(\text{or }\Gamma)$	$16\sqrt{E_JE_C/\pi}\,(2E_J/E_C)^{1/4}\,e^{-\sqrt{32E_J/E_C}}$

Table 8.3: **Formulas for relevant parameters.** Formulas used to extract and calculate relevant parameters from the measurements. The formulas used for the Josephson charging energy and the charging energy to ground are a factor of 4 larger than those commonly adopted in the superconducting qubit community.

power spectral density (PSD) estimation. This approach averages over several independent realizations of the noise signal to reduce variance in the estimated spectrum. The data acquisition code is based on a code kindly provided by Anton Bubis.

Key DMM settings for optimal time resolution included:

- `autozero = OFF` and `autorange = OFF`, to avoid delays introduced by automatic calibration and range switching,
- `NPLC = 0.02`, reducing integration time and increasing bandwidth,
- `timetrace_npts = 50000`, to acquire long time-domain sequences,
- Sampling interval set to the hardware-limited minimum.

The maximum sampling rate achieved corresponds to a Nyquist frequency of approximately $\sim 25\,\mathrm{kHz}$, and the frequency resolution in the FFT was better than $1\,\mathrm{Hz}$, enabling fine spectral features to be resolved.

From this analysis, prominent peaks at $50\,\mathrm{Hz}$ and its harmonics are still visible in the spectra, indicating coupling to the power-line environment. Compared to state-of-the-art noise measurement setups, this level of interference is relatively high and highlights the need for further improvements in filtering, shielding, and ground isolation within the setup.

8.3 DC transport characterization

8.3.1 IVC large bias: ohmic behavior

The Josephson energy and critical current of the junctions were extracted from their normal-state resistance measured under high voltage bias. For these calculations, a superconducting gap of aluminum $\Delta(0) = 0.4\ \mathrm{mV}$ was assumed. Junction capacitance to ground was determined using two complementary approaches. First, a fit to the dispersion relation obtained via microwave spectroscopy provided one estimate. Second, SEM imaging of the junctions enabled a geometrical estimate using a standard specific capacitance of 45–$48\ \mathrm{fF}/\mu\mathrm{m}^2$ [Wei14]

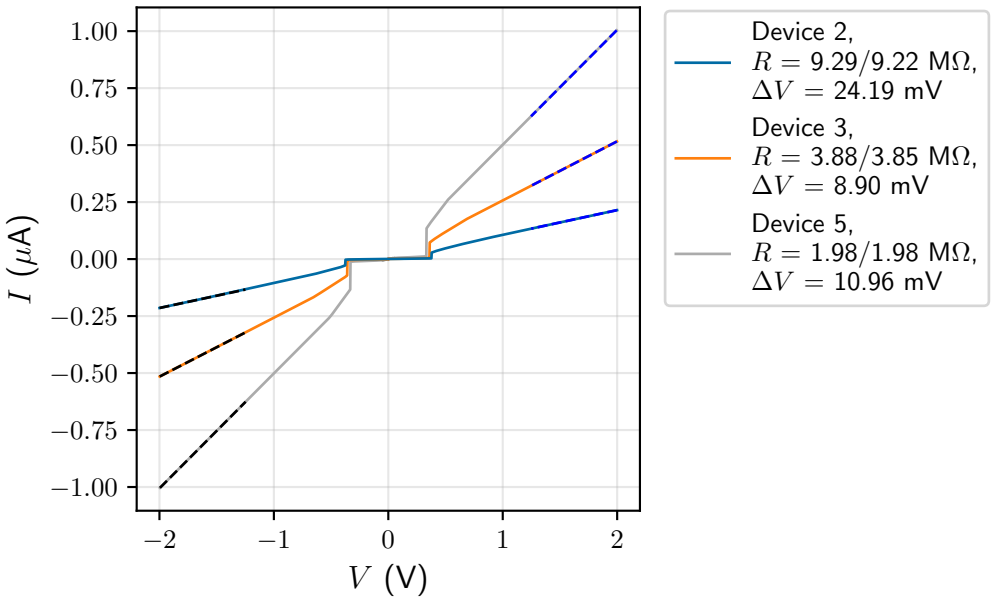

Figure 8.7: **IVC - Large bias.** The solid curves show the measured I-V traces, while the dashed lines are linear fits to the high-bias resistive branches (black: lower branch, blue: upper branch). At sufficiently high bias voltages ($V \geq N \cdot 2\Delta$), the aluminum islands forming the Josephson junctions enter the normal state, where the I-V response becomes linear and dominated by quasiparticle transport. In this regime, the slope reflects the normal-state resistance R_N, which is related to the Josephson energy through the Ambegaokar–Baratoff relation. Reliable determination of R_N requires sampling well above the transition threshold, ensuring an accurate estimate of E_J. The extracted resistances and voltage offsets, obtained by extrapolating the fits to zero current, are reported in the legend.

[MSSM+23]. As a consistency check, the voltage offset observed in the high-voltage regime was also used to estimate the capacitance.

The current-voltage (IV) characteristics of the three devices measured under a voltage bias configuration are presented in Fig.8.7. These curves have been corrected for the voltage drop across the series resistance in the measurement circuit, which includes inline resistors, cable resistance, and the input impedance of the measurement instruments. The total estimated resistance of the setup is approximately $R_{\text{circuit}} = 4.3\ \text{k}\Omega$, as determined from measurements on Device 1, which is a short transmission line used as a reference.

$$V = V_{\text{bias}} - I \cdot R_{\text{circuit}} \tag{8.1}$$

At large bias voltages, when $V \geq N \cdot 2\Delta$, the aluminum islands forming the Josephson junctions transition into the normal state. In this regime, the I-V characteristics become linear and reflect the resistive behavior of the chain, dominated by quasiparticle transport. The slope of the I-V curve in this high-bias regime is described by the Ambegaokar-Baratoff relation:

$$I_c R_N = \frac{\pi \Delta(T)}{2e} \tanh\left(\frac{\Delta(T)}{2k_B T}\right) \tag{8.2}$$

To accurately determine the normal-state resistance and thereby extract the Josephson energy, it is essential to sample the I-V curve at sufficiently high bias voltages where the slope has

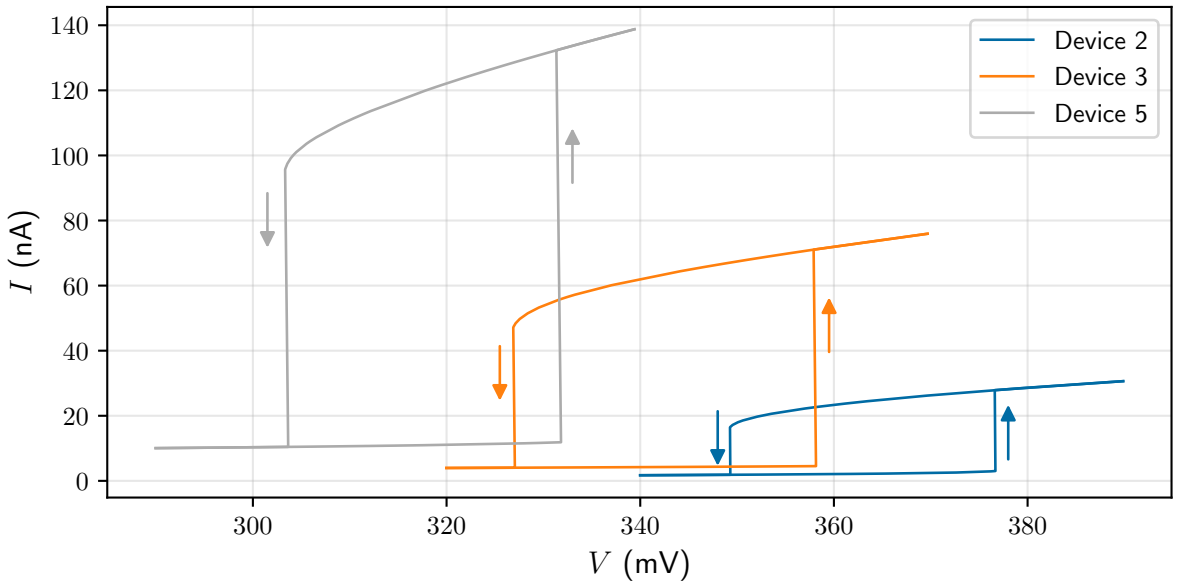

Figure 8.8: $\boldsymbol{V_{\mathrm{gap}}}$ **hysteresis.** Zoom-in of the I-V characteristics around the switching point, where the superconducting and resistive branches meet. The switching voltages observed allow us to estimate the average superconducting energy gap Δ of the aluminum electrodes. The observed device-to-device variations are attributed to heating effects, as supported by the spacing of supercurrent peaks (Fig. 8.9.b) that indicate $\Delta(0) \approx 0.4$ mV, largely independent of the measured V_{gap}.

fully saturated. Sampling too close to the transition threshold may result in an overestimated slope and therefore an underestimated E_J.

From the switching voltages observed in the IV sweeps, we can estimate the average superconducting energy gap Δ of the aluminum electrodes. This value is averaged because the two aluminum layers (formed via double-angle evaporation) have slightly different thicknesses, leading to different gap values. The dependence of the superconducting gap on film thickness is given by [MAC22]:

$$\Delta(t) = 43.5\ \mathrm{GHz} + \frac{145\ \mathrm{GHz}}{t\ [\mathrm{nm}]} \tag{8.3}$$

From the high-bias regime of the up-sweep IV traces, we extract the effective normal-state voltage corresponding to 2Δ for each device. Additionally, Fig.8.7 shows the raw IV characteristics for all three devices in the high-bias regime, while Fig.8.8 provides a zoomed-in view to highlight the hysteresis around the switching point.

The large difference observed in extracted parameters between devices can be attributed to heating: the voltage spacing between supercurrent peaks (Fig. 8.9 inset) indicate a $\Delta(0) \approx 0.4$ mV for all devices. The V_{gap} scaling doesn't match with the Joule heating from the resistances. The temperature of the three devices (from the expressions of $\Delta(T)$, Eqs. 3.11, 3.12), at these voltage bias would be around $T_{\mathrm{Device2}} \approx 104$ mK, $T_{\mathrm{Device3}} \approx 164$ mK and $T_{\mathrm{Device5}} \approx 254$ mK.

V_{off} is obtained by measuring the I-V curve at $V \gg e/(2C_\Sigma)$, fitting the linear high-bias region, and extrapolating the tangent back to the $I = 0$ axis. From $V_{\mathrm{off}} \simeq e/(2C_\Sigma)$, the charging energy follows as $E_C = e\,V_{\mathrm{off}}$. Physically, the offset arises because the total current

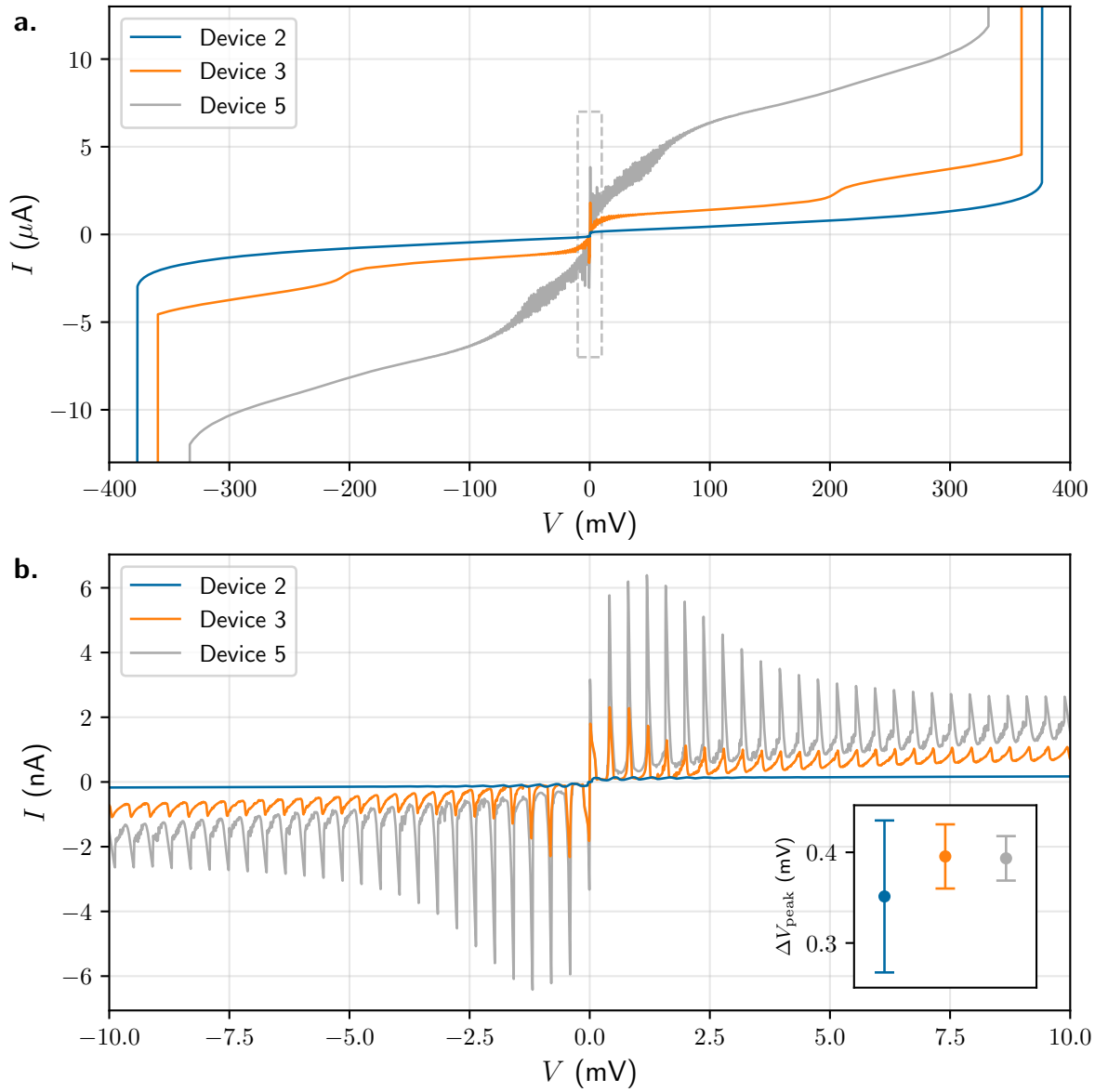

Figure 8.9: **IVC - Itermediate bias. a.** I-V characteristic of the three devices under study, focused on the subgap region features. Device 3 showing a change in slope around ± 200 mV, approximately half of the superconducting gap. **b.** Sequence of peaks appearing on the low-voltage branch of the I-V curve for Devices 2, 3, and 5. Devices 3 and 5 display peaks at the same voltage locations, while Device 2 shows a shift of about 50 μV. The peak spacing and width are consistent across devices, while their amplitude depends on the superconducting/insulating character of the chain. The inset shows the spacing between the peaks reported in panel **b.**.

includes both the tunneling current and the displacement current that charges the junction capacitance. At low bias, this capacitive charging must first supply the electrostatic energy E_C needed to add an electron to the island, shifting the entire I-V curve by V_{off}. Values of E_C are reported in Table 8.3.

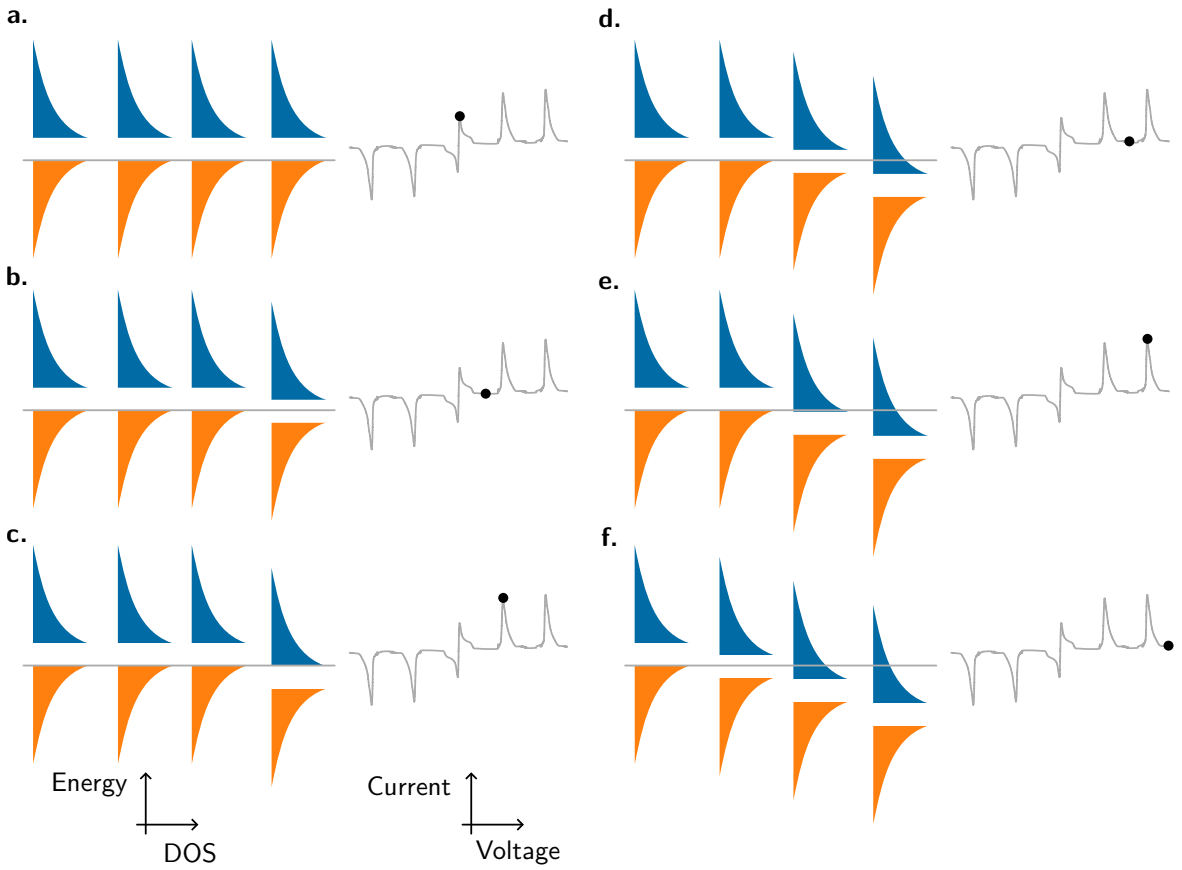

Figure 8.10: **Sub-gap peaks in a Josephson superconducting chain.** The observed sub-gap peaks in the I-V characteristics arise from a chain of junctions, where voltage drops localize across individual junctions. At zero bias (**a.**), aligned energy levels enable coherent Cooper-pair tunneling, producing a supercurrent peak. As the bias increases, quasi-particle tunneling becomes allowed at successive junctions, generating peaks at $V = 2\Delta/e$ (**c.**), $4\Delta/e$ (**e.**), etc., which can be seen as replicas of the zero-bias supercurrent peak. Adapted from Ref. [Wei14].

8.3.2 IVC intermediate bias: subgap region

A sequence of peaks is observed on the low-voltage branch of the I-V characteristic (Fig. 8.9.b). Similar features have been reported in Refs. [Pop11; CCG+23; MSSM+23], where the peaks appear in the sub-gap region, although the underlying mechanism remains unclear.

Device 3 and 5 show peaks at the same voltage location, while Device 2 shows them roughly $50\ \mu\mathrm{V}$ shifted (Fig. 8.11). The peak spacing and width remain the same, while the amplitude varies, being larger in the more superconducting regime and becoming shallower in the insulating regime under DC bias.

Around $\pm 200\ \mathrm{mV}$, roughly half of the superconducting gap, Device 3 exhibits a noticeable change in slope of the I-V curve (Fig. 8.9.a).

The emergence of these peaks in the low-current regime can be understood by considering a system composed of some tunnel junctions, four in the sketch in Fig. 8.10. The density of states of both the leads and the superconducting islands includes electron-like quasi-particle states (orange) and hole-like quasi-particle states (blue), separated by an energy gap of 2Δ.

Applying a voltage across a junction introduces an energy difference between its two sides. At

zero applied voltage, the energy levels of all junctions are aligned, allowing coherent Cooper-pair tunneling through the entire chain and resulting in a peak in the current-voltage characteristic (Fig. 8.10.a).

For voltages below $2\Delta/e$, the voltage drop localizes across a single junction. The position of this drop can occur at any junction in the chain. Under these conditions, Cooper-pair tunneling is suppressed and no supercurrent flows. Quasi-particle tunneling is also blocked due to the absence of available states in the lead at the junction with the voltage drop, producing a current minimum in the I-V curve (Fig. 8.10.b).

When the applied voltage exceeds $2\Delta/e$, quasi-particle tunneling becomes energetically allowed across the junction with the voltage drop. This enables a supercurrent to flow through the remaining three junctions, while a normal tunneling current passes through the biased junction. As a result, a peak appears in the I-V characteristic at $V = 2\Delta/e$ (Fig. 8.10.c).

As the voltage further increases and the critical current of the three-junction chain is exceeded, another junction acquires the voltage drop, temporarily suppressing the supercurrent. At $V = 4\Delta/e$, an additional peak emerges (Fig. 8.10.e). This process repeats, with each successive peak corresponding to one more junction entering the tunneling regime.

In summary, the observed peaks in the sub-gap region of the I-V characteristics can be interpreted as successive replicas of the supercurrent peak near zero bias, reflecting the interplay between Cooper-pair tunneling and quasi-particle tunneling across individual junctions. The origin of the change in slope around ± 200 mV, roughly half of the gap, remains an open question, consistent with observations in Refs. [Pop11; CCG+23; MSSM+23].

8.3.3 IVC zero bias: Coulomb blockade and supercurrent

At low bias voltages near zero, the Devices 3 and 5 exhibit a superconducting branch while Device 2 a Coulomb blockade of Cooper pairs, visible as a gap around zero voltage in the I-V characteristics (Fig. 8.11).

Supercurrent. The finite supercurrent peak at zero voltage for Devices 3 and 5 indicates of coherent Cooper pair tunneling through the entire chain. The height of the supercurrent peak . The residual resistance is of $3.41\ \Omega$/junction for Device 3 and of $1.65\ \Omega$/junction for Device 5. The shoulder appearing around $125\ \mu$V is also observed in Ref. [KSH+24], where the authors also provide a circuit model to fit this feature. The origin is a resonance in the circuit. For Device 2 the residual resistance of the first peak after the blockade is $8\ \Omega$/junction.

Coulomb blockade. The Coulomb blockade observed in Device 2 originates from the interplay between the Josephson coupling energy and the charging energy. In chains of Josephson junctions, the effective threshold voltage for Cooper-pair transport depends on the full capacitance matrix of the junction array, including screening effects from neighboring junctions and the electromagnetic environment.

Figure 8.12(b) shows the statistics of the switching voltage, together with the extraction method from the I-V curve shown in Fig. 8.12(a) for Device 2 at three different temperatures. Each histogram contains 500 switching events, recorded while sweeping the bias voltage upwards. With increasing temperature, the mean value of the histogram shifts toward lower voltages, while the distribution narrows, in qualitative agreement with the behavior reported in

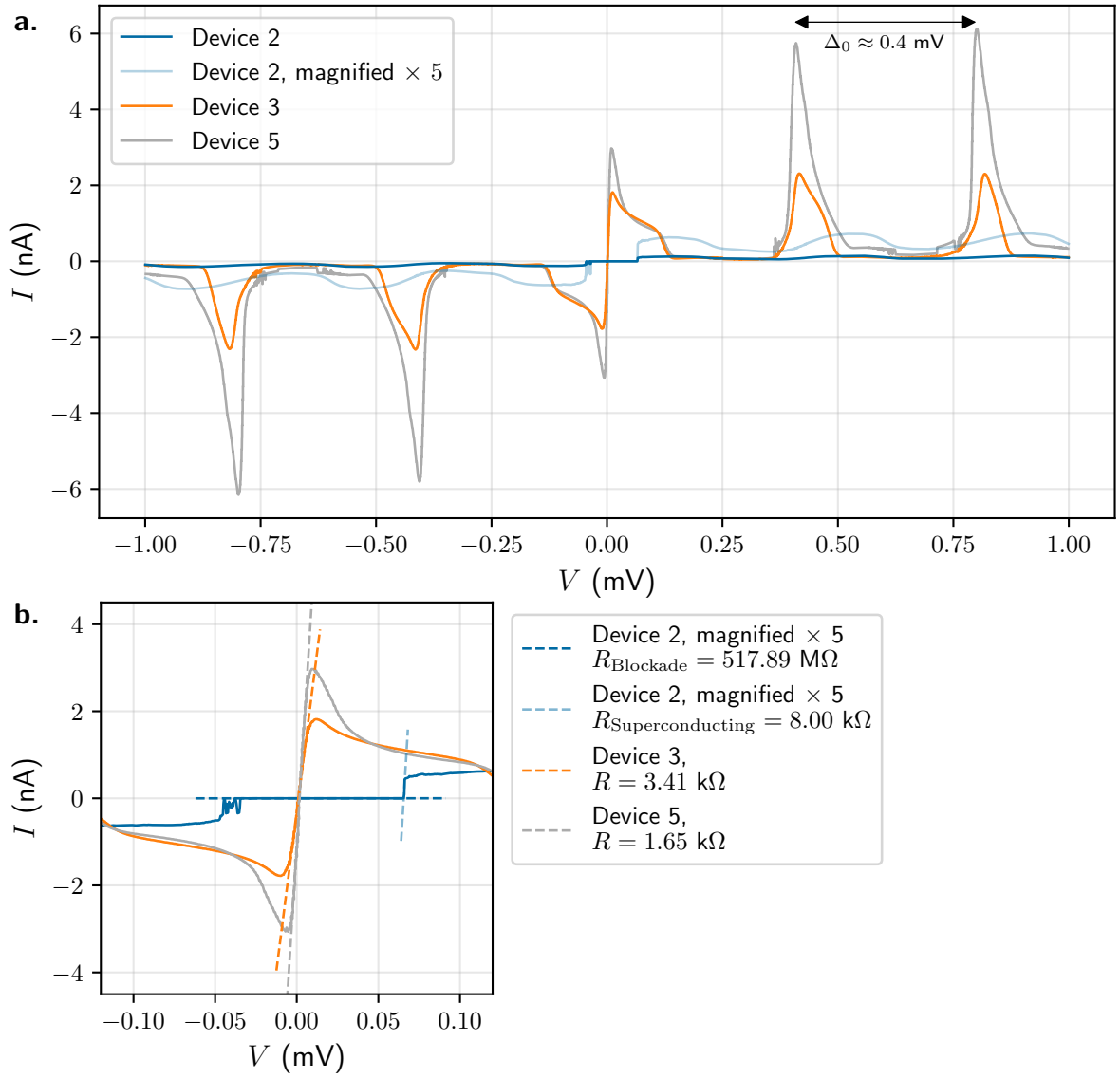

Figure 8.11: **IVC - low bias. a.** Low-voltage I-V characteristics of Devices 2, 3, and 5. Devices 3 and 5 display a superconducting branch with a finite supercurrent peak at zero bias, consistent with coherent Cooper-pair tunneling through the entire chain. Device 2, in contrast, exhibits a Coulomb blockade of Cooper pairs, visible as a gap around zero voltage. A shoulder feature around 125 μV is observed in Devices 3 and 5, consistent with a resonance reported in Ref. [KSH+24]. **b.** Linear fits to the resistive part of the low-bias features. The extracted residual resistances are reported in the legend.

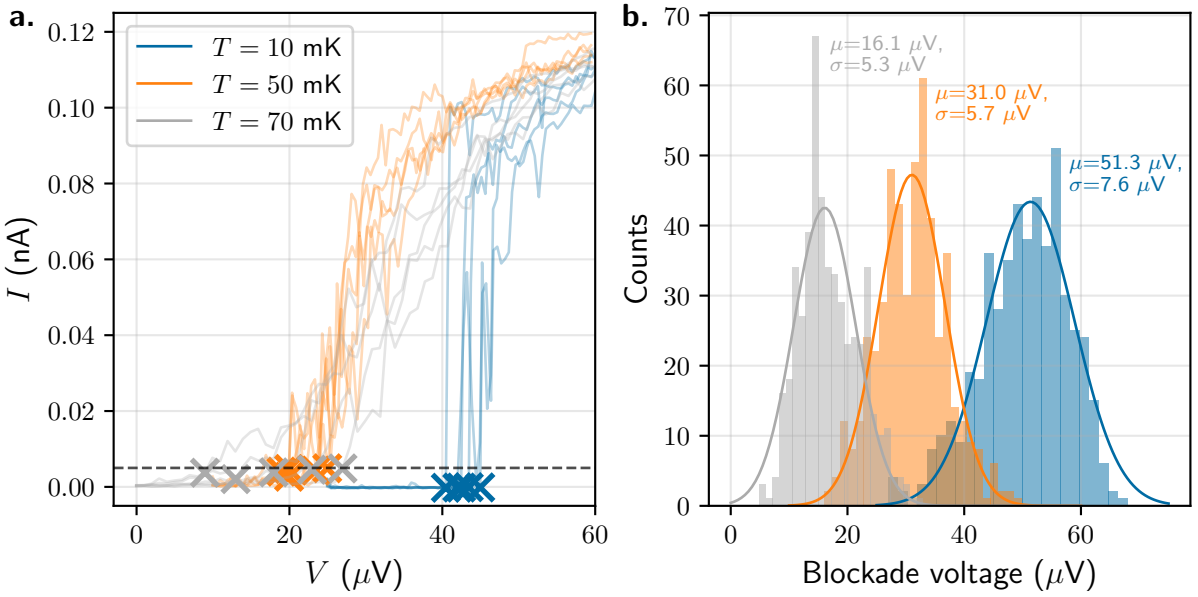

Figure 8.12: **Switching voltage statistics of Device 2. a.** Current–voltage characteristics of Device 2 at different temperatures. The red crosses indicate the extracted blockade voltage values used for the statistical analysis. **b.** Histograms of the switching voltage obtained from 500 upward sweeps of the bias for three representative temperatures. As the temperature increases, the average switching voltage shifts toward lower values and the distribution becomes narrower, in qualitative agreement with Ref. [AH03].

Ref. [AH03]. These observations also suggest that the switching statistics follow a Poissonian distribution.

The zero-bias resistance R_0 as a function of temperature for Device 2 is obtained from the differential conductance measured via a lock-in technique. The lock-in parameters for this measurement are $f_{\mathrm{LI}} = 17.3333$ Hz, $A_{\mathrm{LI}} = 1$ μV, sensitivity $= 100$ μV, $\tau = 1$ s, filter slope $= 18$ dB/oct.

Figure 8.13.a shows $R_0(T)$ for Device 2. Panels .b to .e illustrate the measurement procedure at four different temperatures: 9 mK, 52 mK, 98 mK, and 152 mK. For each temperature point up to 200 mK, 16 I-V curves are recorded (reduced to 8 curves above 200 mK). The subpanels labeled $\#1$ show the raw I–V curves. The subpanels labeled $\#2$ present the X and Y quadratures measured by the lock-in amplifier. From these, both the differential resistance obtained from the in-phase quadrature and the absolute magnitude of the impedance are extracted; the in-phase quadrature generally exhibits lower noise. Finally, the subpanels labeled $\#3$ show the measured lock-in phase. In an ideal lock-in measurement, the phase remains constant; however, in cases (c) and (d), it becomes unstable near zero bias, most likely because the measurement frequency exceeds the RC cutoff of the setup and device. For the insulating state of this device, the RC time constant corresponds to a frequency of about 0.3 Hz. The extracted resistance values are consistent with those obtained from the slope of the I–V curves, as shown in Fig. 8.11(b).

The saturation of $R_0(T)$ at low temperatures suggests that the device does not fully thermalize below approximately 50 mK. The evolution from the normal state at high temperature to the insulating state at low temperature, indicated by the resistance increasing as the temperature decreases, exhibits an initial drop in resistance before rising again below 150 mK. This behavior

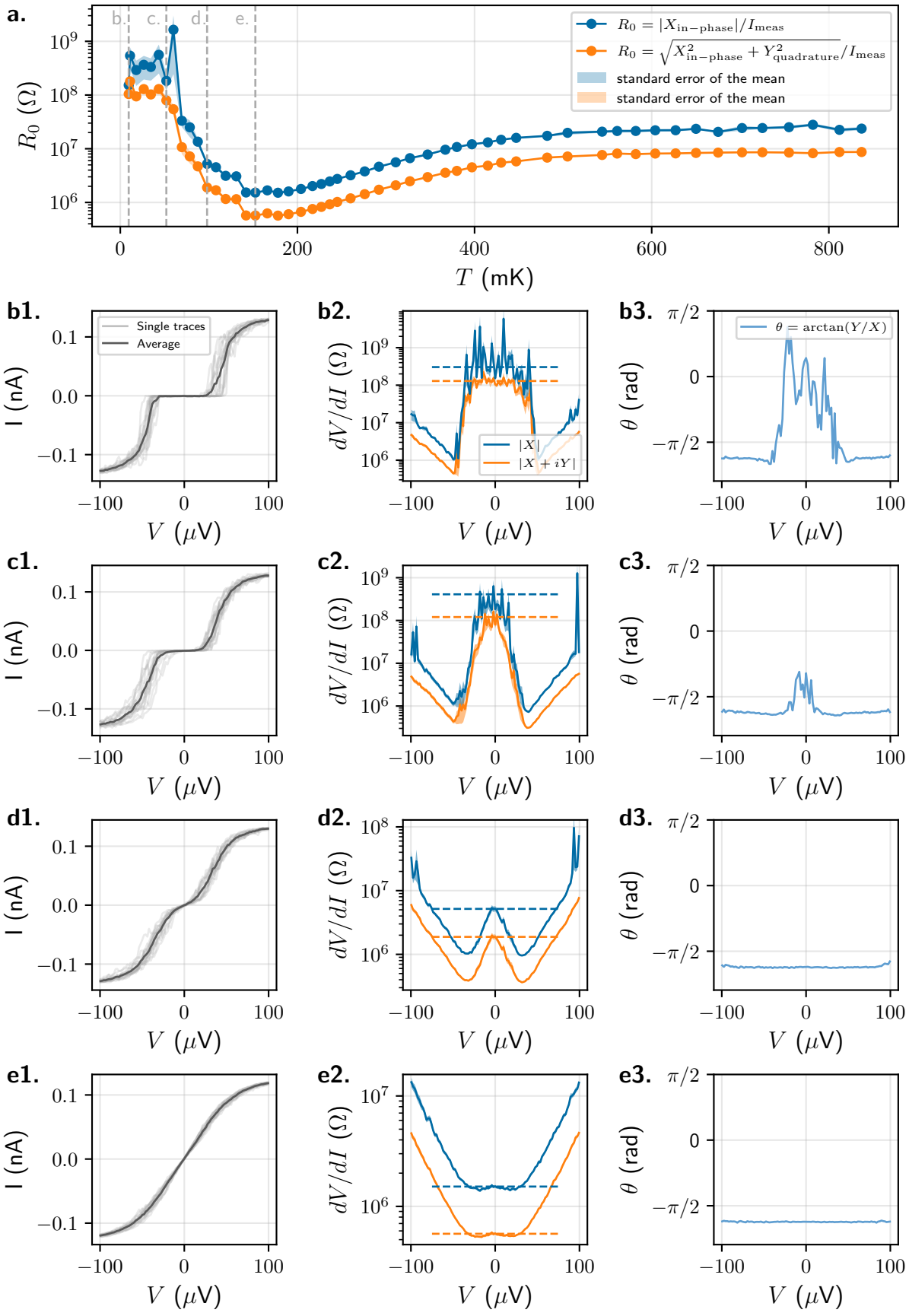

Figure 8.13: **Zero bias resistance vs temperature Device 2.**

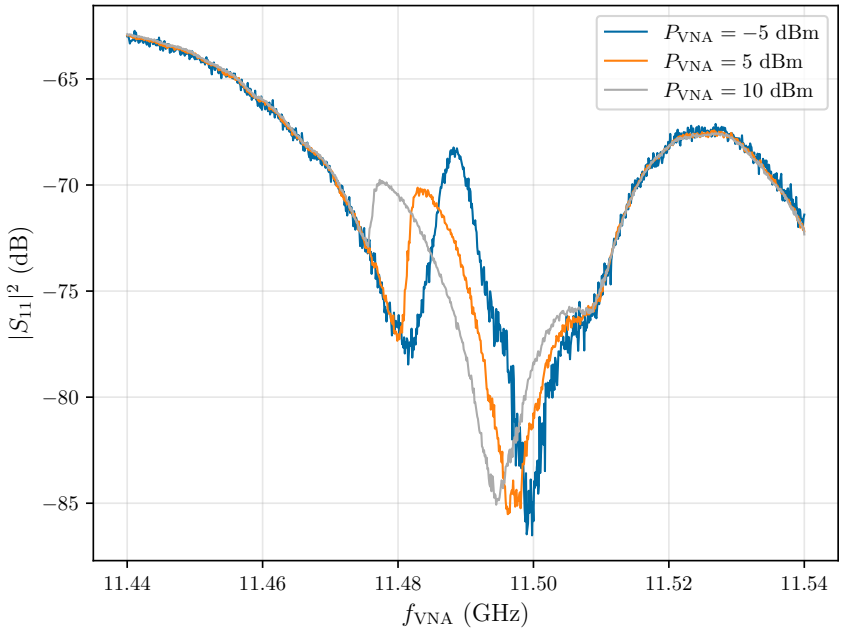

Figure 8.14: **Probe tone of Device 2.**

can be qualitatively[2] understood as a consequence of the renormalization of phase-slip events with temperature, as predicted in Ref. [BPG+17]. It also indicates that Device 2 lies within the proposed phase diagram between the vertical boundaries defined by $\pi K_C \approx 1$ and $\pi K_g \approx 3/2$, corresponding to the region where it was originally designed to be.

8.4 Microwave spectroscopy

8.4.1 Single Tone

The response of Device 2 was measured in both reflection and transmission over the frequency range 4–12 GHz. Power-dependent features were observed only in reflection, between 10 and 12 GHz. In particular, the mode at ~ 11.492 GHz (Fig. 8.14) was selected as the probe tone for the two-tone spectroscopy.

8.4.2 Two Tone

Two-tone spectroscopy is a measurement method used to detect electromagnetic modes that lie outside the frequency range accessible by single-tone measurements. In this setup, single-tone spectroscopy is limited by the bandwidth of the circulators and band-pass filters (BPF), which restricts the measurable range to approximately 4 GHz–12 GHz. By introducing a second probe tone while monitoring the system response at a fixed readout frequency within this band, two-tone spectroscopy reveals resonances at frequencies far below or above the single-tone range, allowing characterization of modes that would otherwise remain inaccessible.

[2]While the upturn of $R_0(T)$ at low temperatures is predicted by theory [LG11; BPG+17], these models are limited to the perturbative treatment of quantum phase slips and are therefore not directly applicable to the present regime.

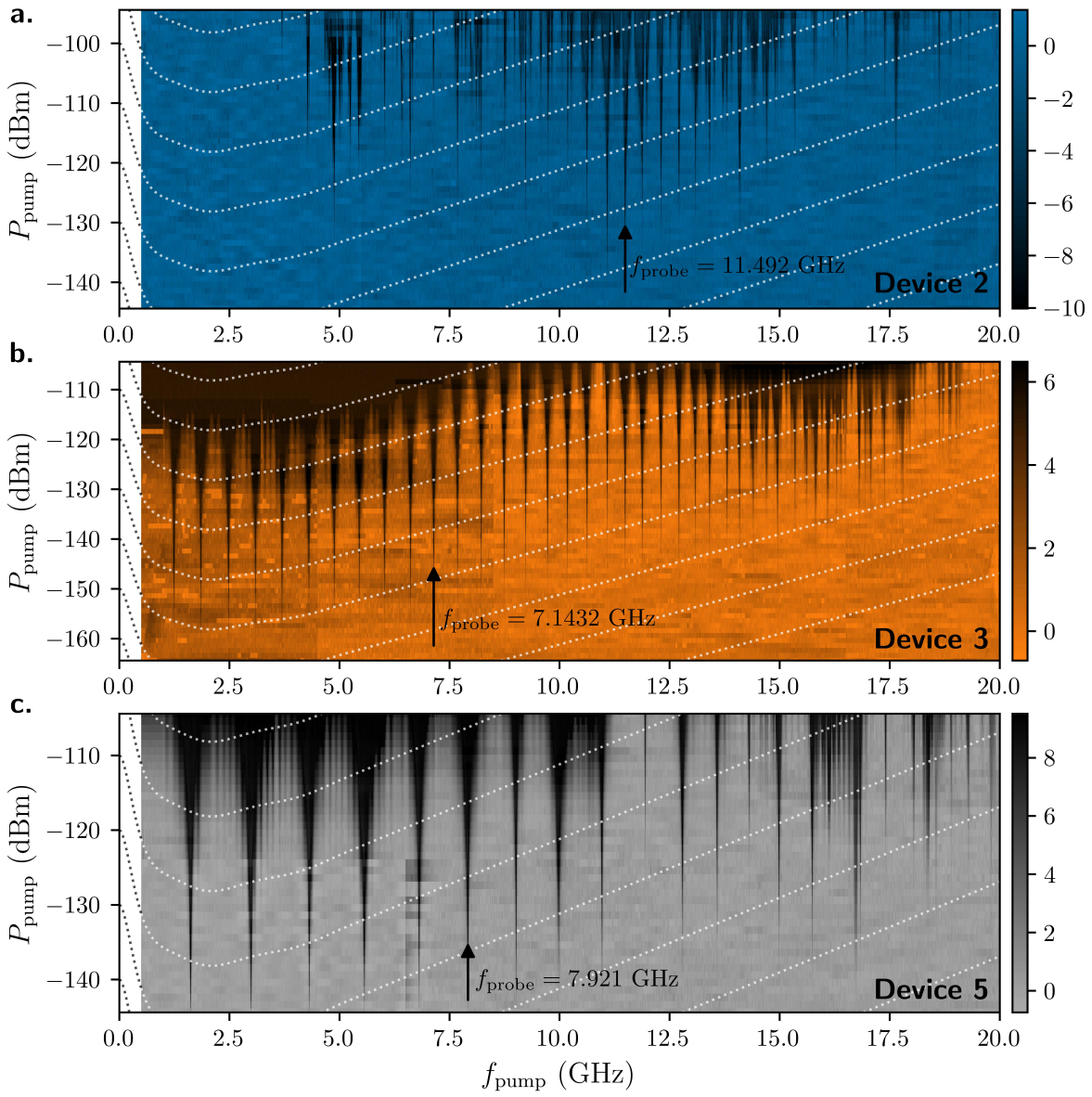

Figure 8.15: **Pump input 1.** Two-tone spectroscopy versus pump power for the three devices. The probe tone frequency is indicated in each subplot by a black arrow. Dashed isolines represent lines of constant applied power, accounting for attenuation in the input line. For Devices 2 and 5, the probe tone is applied from Input 1 (position $x = 0$ on the device), while for Device 3 it is applied from Input 2 (position $x = \ell$). The pump is applied through Input Line 1 for all devices. Individual traces are clipped between the 1st and 99th percentiles to remove pump-induced resonance effects on the probe that could distort the colormap scale. Following this, the baseline is subtracted so that the plotted data represent only the depths of dips or peaks.

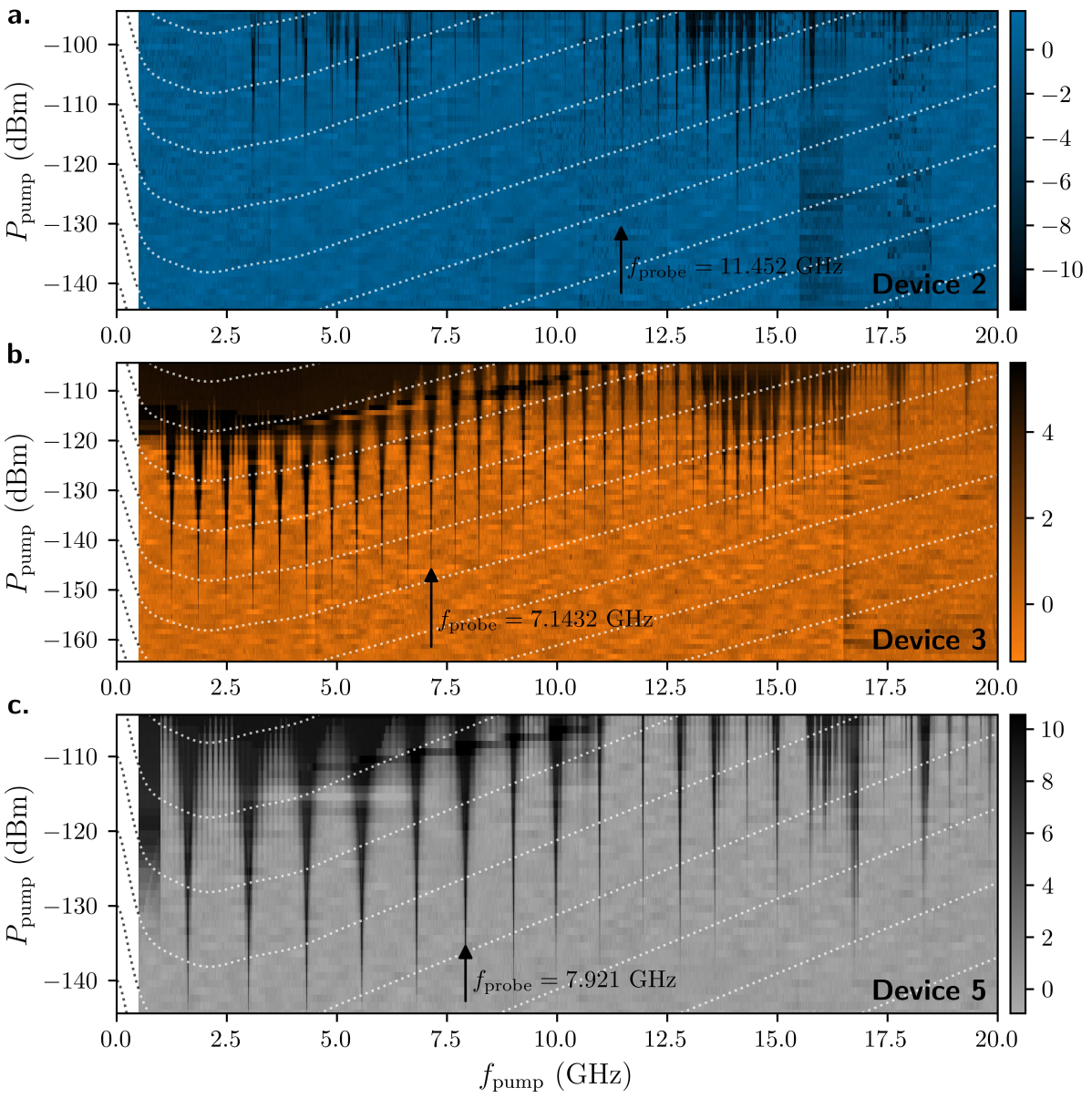

Figure 8.16: **Pump input 2.** Two-tone spectroscopy versus pump power for the three devices. The probe tone frequency is indicated in each subplot by a black arrow. Dashed isolines represent lines of constant applied power, accounting for attenuation in the input line. For Devices 2 and 5, the probe tone is applied from Input 1 (position $x = 0$ on the device), while for Device 3 it is applied from Input 2 (position $x = \ell$). The pump is applied through Input Line 2 for all devices. Individual traces are clipped between the 1st and 99th percentiles to remove pump-induced resonance effects on the probe that could distort the colormap scale. Following this, the baseline is subtracted so that the plotted data represent only the depths of dips or peaks.

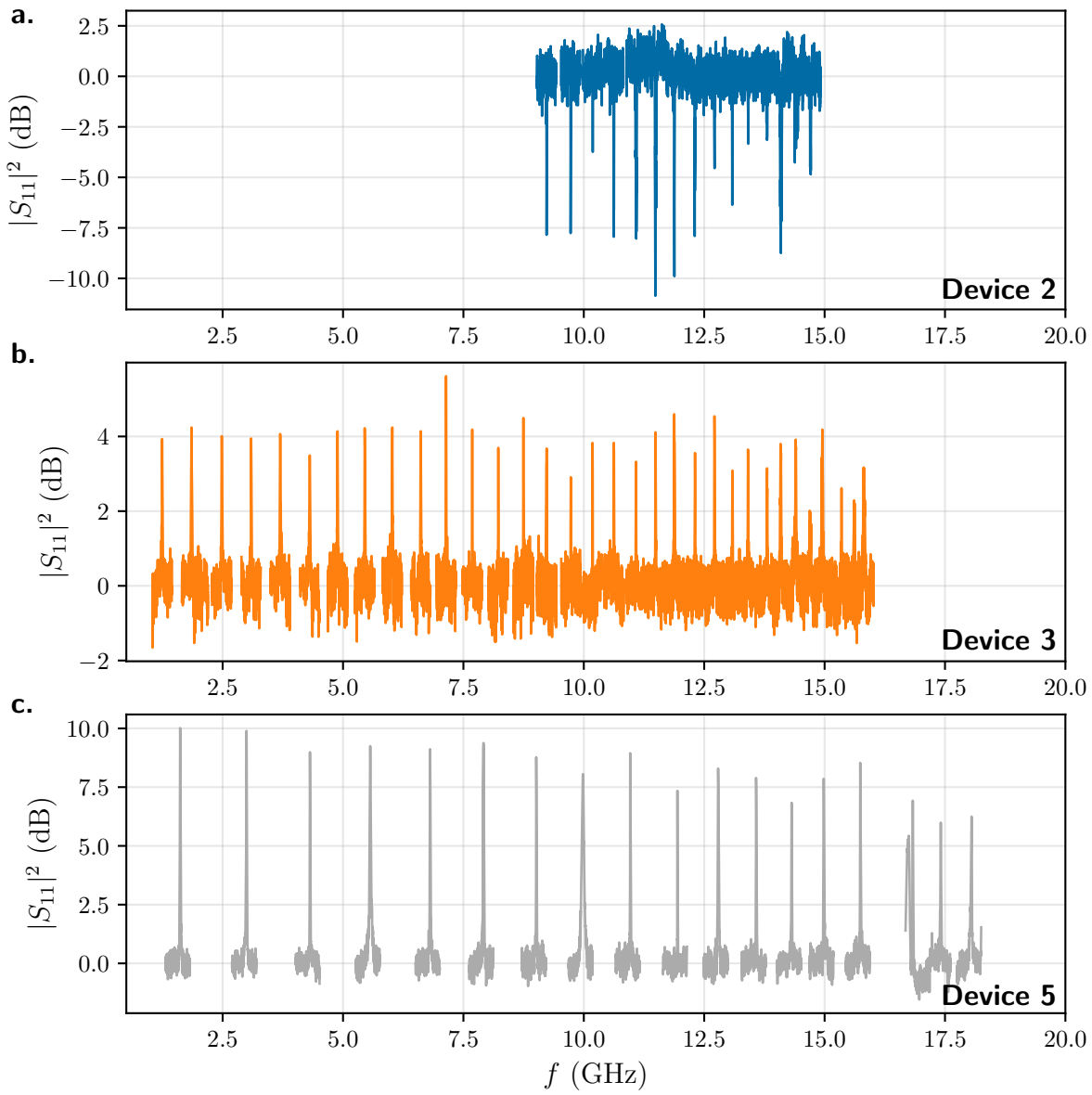

Figure 8.17: **Two-tone microwave spectroscopy showing probe-tone reflection power $|S_{11}|^2$ as a function of pump-tone frequency f.** The probe tone is fixed at the resonant frequency, which differs for each device (see Fig. 8.15). Each plasma-mode resonance is plotted at a different power level because the baseline and nonlinear coupling effects appear at widely varying powers (see Fig. 8.15). Device 2 (panel **a.**) exhibits clear modes distinguishable from high-power multi photon modes only between 9 and 15 GHz. These modes coincide with those of Device 3 (panel **b.**), suggesting possible crosstalk between the two devices.

In Josephson-junction chains, this technique takes advantage of the weak nonlinearity of the junctions. The quartic term in the Josephson potential produces a cross-Kerr interaction between different standing-wave modes. This interaction shifts the resonant frequency of a monitored mode in proportion to the photon number in another pumped mode. The frequency shift can be estimated as

$$\Delta f_{\mathrm{probe}} \approx n_{\mathrm{pump}} \cdot \frac{f_{\mathrm{probe}}\, f_{\mathrm{pump}}}{N E_J}, \tag{8.4}$$

where n_{pump} is the photon number in the pumped mode, f_{probe} and f_{pump} are the probe and pump frequencies, N is the number of junctions, and E_J is the Josephson energy.

Experimentally, a readout tone is fixed on the slope of a chosen resonance, where the transmission changes most rapidly with frequency, and a second probe tone is swept over a wide frequency range. When the probe tone excites a collective mode, the cross-Kerr effect induces a measurable shift in the readout resonance, seen as a dip or peak in the readout transmission magnitude.

This method also enables RF power calibration: by comparing the measured frequency shift with the known Kerr coefficient, the photon number in the mode can be extracted. In these measurements, the pump tone power was varied from $-30\ \mathrm{dBm}$ to $+20\ \mathrm{dBm}$ at the cryostat input. The actual power delivered to each mode depends on the frequency-dependent attenuation in the input line and on the coupling to that mode. Using this approach, standing-wave modes were probed across a wide frequency range, from $500\ \mathrm{MHz}$ to $20\ \mathrm{GHz}$.

Figs. 8.15 and 8.16 show the two-tone spectroscopy spectra versus pump power for the three devices, when pumping from input 1 (position $x = 0$) or from input 2 (position $x = \ell$). The VNA is applied through input 1 for Devices 2 and 5, and through input 2 for Device 3. This choice depends on the probe mode used and the type of measurement performed; all measurements are in reflection.

Devices 3 and 5 display a regular spectrum from low to high frequency, consistent with the expected behavior of a superconducting transmission line. In contrast, Device 2 exhibits a richer and more complex spectrum: no modes are observed below $3\ \mathrm{GHz}$; between 3 and $9\ \mathrm{GHz}$ modes appear at irregular pump powers and are accompanied by several side peaks; above $9\ \mathrm{GHz}$ up to $15\ \mathrm{GHz}$ the modes become more regularly spaced. At first glance, this behavior strongly resembles the signature of charge density waves (CDWs) pinned by disorder, as predicted in Ref. [HG19]: resonances with $\omega \ll \omega_*$ are suppressed; for $\omega_{\mathrm{cr}} \ll \omega \ll \omega_*$ disorder effects dominate; and for $\omega \gg \omega_{\mathrm{cr}}$ the system recovers the regular mode structure of a clean superconducting transmission line.

When pumping from opposite ends of the chain (Fig. 8.15.a and Fig. 8.16.a), slight differences appear in the low-frequency spectrum, consistent with the possibility that certain modes are localized predominantly on one side of the junction chain.

A closer comparison between Device 2 and Device 3, obtained by plotting the single modes of Device 2 irrespective of the pump power at which they appear, revealed that these modes have exactly the same resonant frequencies as those observed in Device 3 (Fig. 8.17). This observation motivated the cross-coupling test described in Section 8.5.

8.4.3 Dispersion relation

To determine the parameters of the chain, namely the capacitances C_J, C_g, and the inductance L_J, the fit of the dispersion relation via two-tone spectroscopy. The measured data as a

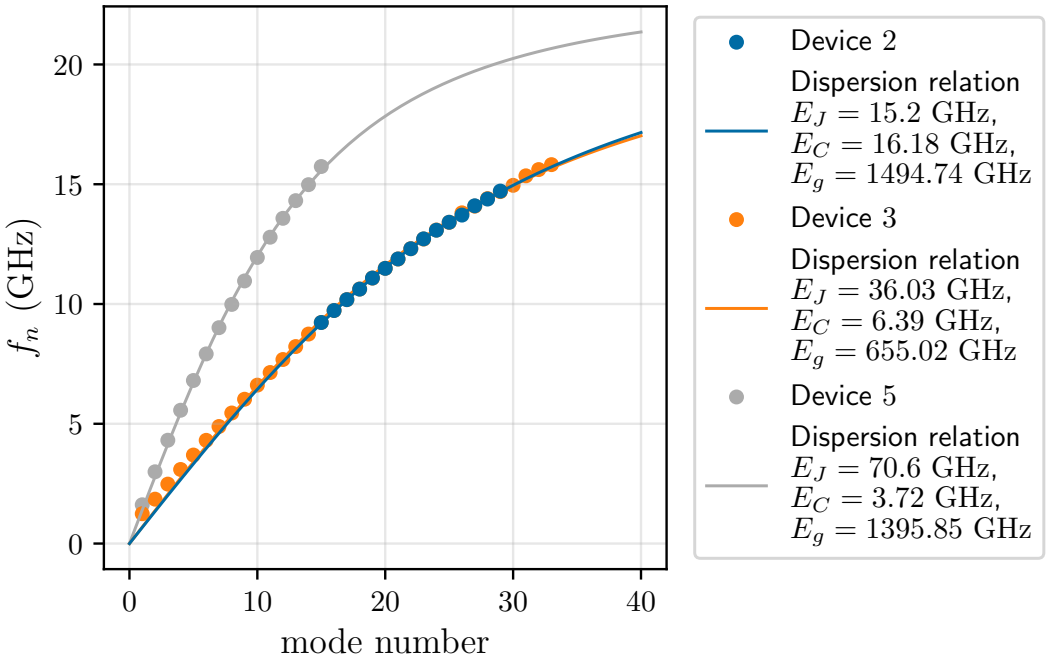

Figure 8.18: **Dispersion relations**. The Josephson energy E_J is extracted from the dissipative branch of the I–V curve using the Ambegaokar–Baratoff relation. The charging energies E_C and E_g are obtained by fitting the measured dispersion data using the analytical expression from Krupko. The dots indicate the data points used in the fitting procedure. For Device 5, a more accurate fit could be achieved using the model from Ref. [WKD+15], which accounts for the absence of ground-plane screening so long range interactions. In the case of Device 2, the fundamental mode is not visible; the mode indices were inferred based on the approximate spacing between adjacent modes. For Device 3, all modes except the fundamental are observed.

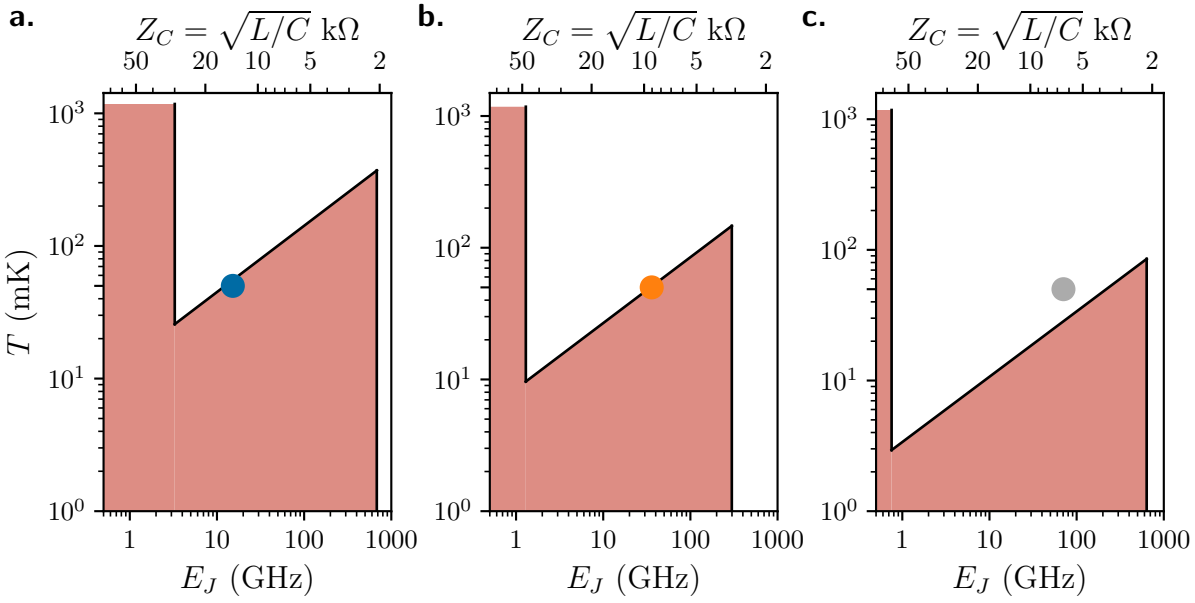

Figure 8.19: **Phase diagram of measured devices.** Based on the extracted parameters in Table 8.4 the three devices are placed on the proposed phase diagram (Ref. [MSSM+23]). **a.** Device 2; **b.** Device 3 and **c.** Device 5.

	Device 2	Device 3	Device 5
N_{JJ}	999	999	999
Expected Area$_{\mathrm{JJ}}$ (μm^2)	0.1024	0.2176	0.32
$R_{\mathrm{N}}/N_{\mathrm{JJ}}$ (kΩ)	9.26	3.87	1.98
R_0/N_{JJ} (Ω)	5.18×10^3	3.41	1.65
I_C/Area$_{\mathrm{JJ}}$ (nA/μm^2)	301.5	339.5	451
L_J (nH)	10.66	4.455	2.279
E_J (GHz)	15.334	36.691	71.714
E_J (K)	0.736	1.761	3.442
E_C (GHz) Geometry	$15.3762 - 16.814$	$7.418 - 7.913$	$5.044 - 5.381$
E_C (GHz) V offset	23.42	8.617	10.611
E_C (GHz) Fit	16.180 ± 0.169	6.386 ± 0.212	3.716 ± 0.138
E_g (GHz) Fit	1494.740 ± 7.760	655.025 ± 12.734	1395.848 ± 24.844
E_J/E_C	0.948	5.746	19.299
C_J (fF)	4.789	12.133	20.851
C_g (aF)	51.836	118.287	55.508
Z_C (kΩ)	14.340	6.136	6.408
$\omega_p/2\pi$ (GHz)	22.276	21.648	23.086
K_C	0.688	1.695	3.106
K_g	0.072	0.167	0.160
Λ	9.61	10.128	19.381
W(or Γ) (Hz)	$6.770 \cdot 10^8$	$3.287 \cdot 10^5$	5.922

Table 8.4: **Extracted parameters.** Parameters obtained from the measurements are reported. By definition, the values for the Josephson charging energy and the charging energy to ground are a factor of 4 larger than those commonly adopted in the superconducting qubit community. The charging energy E_C was independently verified using two additional methods. The values of E_C used to calculate C_J, f_p, K_C, and W are those obtained from fitting the dispersion relation. The value of E_C extracted from the junction geometry uses capacitance densities of 45 fF/μm^2 and 48 fF/μm^2, as reported in Refs. [WKD+15]. The device area corresponds to the expected value from a dose test run with the same geometry and parameters as the measured devices. Due to e-beam instabilities during fabrication, these values may vary.

function of mode number is presented in Fig. 8.18. For small wavevectors ($k \ll 1$), the system exhibits a linear dispersion described by $\omega_k = k/\sqrt{L_J C_g}$. In contrast, for $k > \sqrt{C_g/C}$, the dispersion flattens and approaches the plasma frequency, given by $\omega_p = 1/\sqrt{L_J(C_J + C_g/4)}$. These limiting behaviors provide a means to extract C_g and C_J, once L_J is known.

The results are summarized in Table 8.4 using the definitions in Table 8.3.

8.5 Investigation of cross-coupling between Device 2 and 3

During the analysis of the data, the overlap between the plasmon frequencies of Device 2 and Device 3 appeared suspicious, motivating an investigation of possible cross-coupling between these two devices. Both devices are located on the same chip, separated by approximately 6 mm. They are the only two connected devices on this chip, while two additional devices

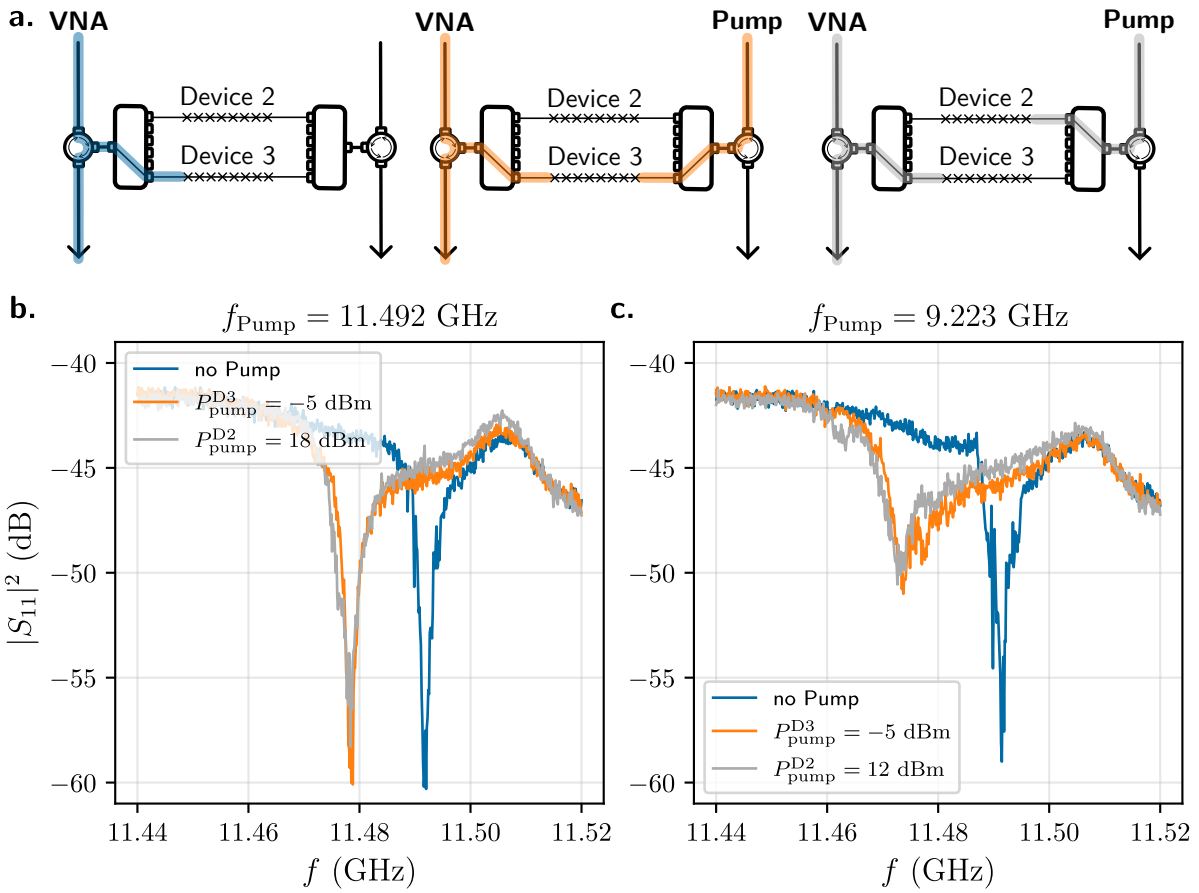

Figure 8.20: **Test II: cross-driving Device 3 via Device 2. a.** Simplified sketch of the measurements. **b.** Mode at 11.492 GHz response with no pump (blue), pump applied directly to Device 3 (orange), and pump applied to Device 2 (gray). Pumping Device 2 requires roughly 20 dB more power to achieve the same self-Kerr shift as direct pumping of Device 3. **c.** Similar measurement for another mode at 9.23 GHz, highlighting cross-Kerr effects, confirming the behavior observed in panel **b.**.

are unconnected and were never measured. The energies E_C and E_g for Device 2 have been independently confirmed, as reported in Table 8.3, and are not solely derived from fits to the two-tone spectroscopy dispersion relation. Alternative approaches, such as extracting these parameters from HFSS simulation (E_g) or from the device's geometric capacitance and IVC resistive branches offset (E_C), provide consistent results. The apparent coincidence in resonance frequencies requires further investigation; current evidence so far confirms cross-coupling, although it may not fully exclude that Device 2 doesn't show microwave modes.

Three tests were conducted to check RF switch integrity and the effects of pumping on device modes.

Test I: Switch integrity. All switch ports were set to "reset", physically disconnecting the devices on one side. A power sweep of the pump was performed at the frequency of the mode while monitoring the same mode with the VNA in reflection (Input 1 $\rightarrow$ Output 1). The switch was observed to operate correctly, without leakage, with no obvious shift or distortion of the mode.

Test II: Driving Device 3 mode via Device 2. The mode of Device 3 at 11.492 GHz was monitored in reflection on Input 1 $\rightarrow$ Output 1 while the pump was applied either directly to

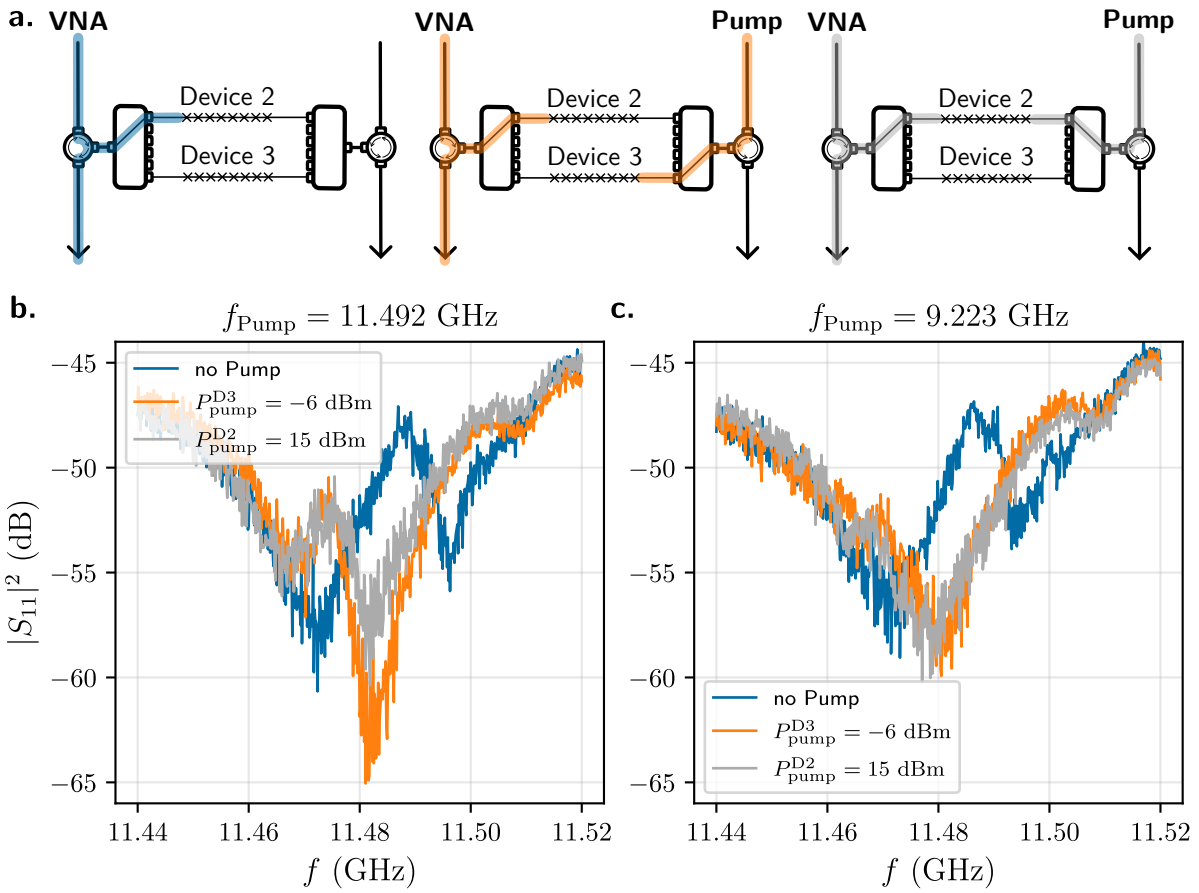

Figure 8.21: **Test III: Cross-driving Device 2 via Device 3. a.** Simplified sketch of the measurements. **b.** Mode at 11.492 GHz response with no pump (blue), pump applied directly to Device 3 (orange), and pump applied to Device 2 (gray). Pumping Device 2 requires roughly 20 dB more power to achieve the same self-Kerr shift as direct pumping of Device 3. **c.** Similar measurement for another mode at 9.23 GHz, highlighting cross-Kerr effects, confirming the behavior observed in panel **b.** and Fig. 8.20.

Device 3 or to Device 2, as in Fig. 8.20.b . Both configurations allowed driving the mode, but pumping Device 2 required approximately 20 dB more power to achieve the same self-Kerr shift as pumping Device 3 directly. Similar measurement pumping on another mode at 9.223 GHz, probing cross-Kerr effects, showed consistent results, as in Fig. 8.20.c.

Test III: Reciprocal test. The same mode in Device 2 at 11.492 GHz was monitored while pumping either Device 3 or Device 2. Pumping Device 3 at the same frequency produced a comparable mode shift, whereas driving from Device 2 required approximately 20 dB more power to achieve the same effect, the same as *Test II*, as reported in Fig. 8.21.b. The same trend was observed pumping on another mode at 9.223 GHz, as in Fig. 8.21.c.

In conclusion, all the modes initially attributed to the insulating device (Device 2) highly likely correspond to Device 3. However, further investigation is required to determine whether any spectroscopic features are uniquely associated with Device 2.

8.6 Conclusion and Outlook

Chapter 8 presented the DC and RF characterization of three Josephson junction (JJ) chains having the same total length, number of junctions, and island length, but differing in island width and spacing to ground. These design variations place them in three distinct regimes: superinducting (Device 5), slightly more insulating (Device 3), and even deeper into the insulating state (Device 2). Fig. 8.19 shows the three devices in the proposed phase diagram, assuming a temperature of $50\ \mathrm{mK}$

Because this chapter was written while both the data analysis and the measurements were still ongoing, the conclusions presented here are not final.

The DC characterization revealed that Devices 3 and 5 exhibit a superconducting peak at zero bias, followed by additional superconducting peaks spaced by $\Delta \approx 0.4\ \mathrm{mV}$. Device 2, in contrast, showed a Coulomb blockade at zero bias, followed by a few smeared superconducting peaks. This behavior places Device 2 at an interesting boundary of the superconductor–insulator transition (SIT). To my knowledge, no other device consisting solely of a chain of single Josephson junctions has shown the simultaneous presence of current blockade at zero bias and superconducting peaks at finite voltage; in the literature, only one device based on DC-SQUIDs, when properly tuned, has exhibited similar behavior. That device was fabricated in the group of David Haviland and measured at KIT within the group of Alexey Ustinov; the result, unpublished to my knowledge, appears only as Fig. 5 in the report https://www.cfn.kit.edu/downloads/research_b_nano_electronics/B306-Report.pdf.

The measurement of RF modes in a device showing Coulomb blockade has, to my knowledge, never been reported before. Devices studied in Ref. [KMG+19] with high impedance do not show a blockade. However, due to crosstalk between Devices 3 and 2, no clear conclusion can be drawn at this stage. The fact that these two devices couple to each other means that Device 2 can probably host superconducting modes, but no stronger statement can be made without further study. Any conclusion requires additional investigation.

In the near future, the priority is to eliminate this crosstalk, possibly by cleaving Sample B. This would allow us to test whether the RF modes can be directly observed in Device 2. Sample B also contains other devices with slightly different geometries that may be less insulating but still display Coulomb blockade in their I–V curves. The goal would be to identify a device slightly more superconducting while retaining current blockade at DC.

The observation of RF modes in a DC-insulating device is an active research topic, also explored in other group that characterize disordered material. Groups such as N. Roch (Institut Néel CNRS), B. Sacépé (Institut Néel CNRS), and C. Strunk (University of Regensburg) are working in this direction, but have not found conclusive evidence so far. Josephson junction arrays provide an attractive alternative for this line of research because their three relevant energy scales can be independently tuned and engineered.

In addition, as already mentioned in the introductory Chapter 8.1, Josephson junction transmission lines offer an interesting platform to study the infrared (IR) SIT and the SIT as a function of temperature. For the IR SIT, the design requires the T_{ins} to be high enough so that a superconducting device below that threshold can be tuned to the insulating regime by applying a perpendicular magnetic field, as demonstrated in Ref. [MSSM+23]. To observe the SIT as a function of temperature, the opposite condition is required: T_{ins} must be sufficiently low so that increasing the temperature does not excessively broaden the modes through thermal population.

Another promising direction for these devices is to study the effects of simultaneous DC and RF biasing. This raises questions such as: What is the effect on RF modes of operating at zero bias (blockade) versus at a superconducting peak? Conversely, how does an RF bias affect DC transport, particularly from the perspective of dual-Shapiro physics? Which operating regime offers the best conditions for observing such effects? If pumping at one of the modes is required, how effectively can the RF signal couple into the device?

Bibliography

[AAH01] Peter Agren, Karin Andersson, and David B. Haviland. Kinetic Inductance and Coulomb Blockade in One Dimensional Josephson Junction Arrays. *Journal of Low Temperature Physics*, 124(1–2):291–304, July 2001. URL: http://dx.doi.org/10.1023/A:1017594322332, doi:10.1023/a:1017594322332.

[AAWP+18] Patricio Arrangoiz-Arriola, E. Alex Wollack, Marek Pechal, Jeremy D. Witmer, Jeff T. Hill, and Amir H. Safavi-Naeini. Coupling a Superconducting Quantum Circuit to a Phononic Crystal Defect Cavity. *Phys. Rev. X*, 8:031007, Jul 2018. URL: https://link.aps.org/doi/10.1103/PhysRevX.8.031007, doi:10.1103/PhysRevX.8.031007.

[AB63a] Vinay Ambegaokar and Alexis Baratoff. Tunneling Between Superconductors. *Phys. Rev. Lett.*, 10:486–489, Jun 1963. URL: https://link.aps.org/doi/10.1103/PhysRevLett.10.486, doi:10.1103/PhysRevLett.10.486.

[AB63b] Vinay Ambegaokar and Alexis Baratoff. Tunneling Between Superconductors. *Phys. Rev. Lett.*, 11:104–104, Jul 1963. URL: https://link.aps.org/doi/10.1103/PhysRevLett.11.104, doi:10.1103/PhysRevLett.11.104.

[ADD+06] A. André, D. DeMille, J. M. Doyle, M. D. Lukin, S. E. Maxwell, P. Rabl, R. J. Schoelkopf, and P. Zoller. A coherent all-electrical interface between polar molecules and mesoscopic superconducting resonators. *Nature Physics*, 2(9):636–642, August 2006. URL: http://dx.doi.org/10.1038/nphys386, doi:10.1038/nphys386.

[AGL+19] Kaveh Ahadi, Luca Galletti, Yuntian Li, Salva Salmani-Rezaie, Wangzhou Wu, and Susanne Stemmer. Enhancing superconductivity in $SrTiO_3$ films with strain. *Science Advances*, 5(4), April 2019. URL: http://dx.doi.org/10.1126/sciadv.aaw0120, doi:10.1126/sciadv.aaw0120.

[AGZ08] K.Yu. Arutyunov, D.S. Golubev, and A.D. Zaikin. Superconductivity in one dimension. *Physics Reports*, 464(1):1–70, 2008. URL: https://www.sciencedirect.com/science/article/pii/S0370157308001609, doi:10.1016/j.physrep.2008.04.009.

[AH69] Vinay Ambegaokar and BI Halperin. Voltage due to thermal noise in the dc Josephson effect. *Physical Review Letters*, 22(25):1364, 1969.

[AH03] K. Andersson and D. B. Haviland. Escape from a zero-current state in a one-dimensional array of Josephson junctions. *Physical Review B*, 67(9), March 2003. URL: http://dx.doi.org/10.1103/PhysRevB.67.092507, doi:10.1103/physrevb.67.092507.

[AIK+12] O. V. Astafiev, L. B. Ioffe, S. Kafanov, Yu. A. Pashkin, K. Yu. Arutyunov, D. Shahar, O. Cohen, and J. S. Tsai. Coherent quantum phase slip. *Nature*, 484(7394):355–358, April 2012. URL: http://dx.doi.org/10.1038/nature10930, doi:10.1038/nature10930.

[ALK+24] Waël Ardati, Sébastien Léger, Shelender Kumar, Vishnu Narayanan Suresh, Dorian Nicolas, Cyril Mori, Francesca D'Esposito, Tereza Vakhtel, Olivier Buisson, Quentin Ficheux, and Nicolas Roch. Using Bifluxon Tunneling to Protect the Fluxonium Qubit. *Phys. Rev. X*, 14:041014, Oct 2024. URL: https://link.aps.org/doi/10.1103/PhysRevX.14.041014, doi:10.1103/PhysRevX.14.041014.

[Ann10] Anthony Joseph Annunziata. *Single-Photon Detection, Kinetic Inductance, and Non-Equilibrium Dynamics in Niobium and Niobium Nitride Superconducting Nanowires*. Ph.d. dissertation, Yale University, New Haven, CT, 2010. Dissertation Director: Professor Daniel E. Prober. URL: https://proberlab.yale.edu/sites/default/files/files/Annunziata_Thesis.pdf.

[APE03] A. Anthore, H. Pothier, and D. Esteve. Density of States in a Superconductor Carrying a Supercurrent. *Phys. Rev. Lett.*, 90:127001, Mar 2003. URL: https://link.aps.org/doi/10.1103/PhysRevLett.90.127001, doi:10.1103/PhysRevLett.90.127001.

[ARH18] Lisa Arndt, Ananda Roy, and Fabian Hassler. Dual shapiro steps of a phase-slip junction in the presence of a parasitic capacitance. *Phys. Rev. B*, 98:014525, Jul 2018. URL: https://link.aps.org/doi/10.1103/PhysRevB.98.014525, doi:10.1103/PhysRevB.98.014525.

[ASB89] S.M. Anlage, H.J. Snortland, and M.R. Beasley. A current controlled variable delay superconducting transmission line. *IEEE Transactions on Magnetics*, 25(2):1388–1391, March 1989. URL: http://dx.doi.org/10.1109/20.92554, doi:10.1109/20.92554.

[ASF+10] Anthony J Annunziata, Daniel F Santavicca, Luigi Frunzio, Gianluigi Catelani, Michael J Rooks, Aviad Frydman, and Daniel E Prober. Tunable superconducting nanoinductors. *Nanotechnology*, 21(44):445202, October 2010. URL: http://dx.doi.org/10.1088/0957-4484/21/44/445202, doi:10.1088/0957-4484/21/44/445202.

[AWB+20] G. Arnold, M. Wulf, S. Barzanjeh, E. S. Redchenko, A. Rueda, W. J. Hease, F. Hassani, and J. M. Fink. Converting microwave and telecom photons with a silicon photonic nanomechanical interface. *Nature Communications*, 11(1), September 2020. URL: http://dx.doi.org/10.1038/s41467-020-18269-z, doi:10.1038/s41467-020-18269-z.

[AZL85] DV Averin, AB Zorin, and KK Likharev. Bloch oscillations in small Josephson junctions. *Sov. Phys. JETP*, 61(2):407–413, 1985.

[BBK+25] R. Behr, S. Bauer, M. Kraus, O. Kieler, Y. Pimsut, and L. Palafox. Accurate measurements with Josephson-based quantum voltage standards. *Measurement: Sensors*, 38:101427, 2025. Proceedings of the XXIV IMEKO World Congress. URL: https://www.sciencedirect.com/science/article/pii/S2665917424004033, doi:10.1016/j.measen.2024.101427.

[BCD+25] Isabelle Bouchoule, Roberta Citro, Tim Duty, Thierry Giamarchi, Randall G. Hulet, Martin Klanjsek, Edmond Orignac, and Bent Weber. Platforms for the realization and characterization of Tomonaga-Luttinger liquids, 2025. URL: https://arxiv.org/abs/2501.12097, arXiv:2501.12097.

[BCS57a] J. Bardeen, L. N. Cooper, and J. R. Schrieffer. Microscopic Theory of Superconductivity. *Phys. Rev.*, 106:162–164, Apr 1957. URL: https://link.aps.org/doi/10.1103/PhysRev.106.162, doi:10.1103/PhysRev.106.162.

[BCS57b] J. Bardeen, L. N. Cooper, and J. R. Schrieffer. Theory of Superconductivity. *Phys. Rev.*, 108:1175–1204, Dec 1957. URL: https://link.aps.org/doi/10.1103/PhysRev.108.1175, doi:10.1103/PhysRev.108.1175.

[BDV+20] Jochen Braumüller, Leon Ding, Antti P. Vepsäläinen, Youngkyu Sung, Morten Kjaergaard, Tim Menke, Roni Winik, David Kim, Bethany M. Niedzielski, Alexander Melville, Jonilyn L. Yoder, Cyrus F. Hirjibehedin, Terry P. Orlando, Simon Gustavsson, and William D. Oliver. Characterizing and Optimizing Qubit Coherence Based on SQUID Geometry. *Phys. Rev. Appl.*, 13:054079, May 2020. URL: https://link.aps.org/doi/10.1103/PhysRevApplied.13.054079, doi:10.1103/PhysRevApplied.13.054079.

[BGB04] H. P. Büchler, V. B. Geshkenbein, and G. Blatter. Quantum Fluctuations in Thin Superconducting Wires of Finite Length. *Phys. Rev. Lett.*, 92:067007, Feb 2004. URL: https://link.aps.org/doi/10.1103/PhysRevLett.92.067007, doi:10.1103/PhysRevLett.92.067007.

[BGC24] Federico Borletto, Luca Giacomelli, and Cristiano Ciuti. Circuit quantum electrodynamics of direct and dual Shapiro steps with finite-size-transmission-line resonators. *Phys. Rev. Appl.*, 22:054061, Nov 2024. URL: https://link.aps.org/doi/10.1103/PhysRevApplied.22.054061, doi:10.1103/PhysRevApplied.22.054061.

[BGGW21] Alexandre Blais, Arne L. Grimsmo, S. M. Girvin, and Andreas Wallraff. Circuit quantum electrodynamics. *Rev. Mod. Phys.*, 93:025005, May 2021. URL: https://link.aps.org/doi/10.1103/RevModPhys.93.025005, doi:10.1103/RevModPhys.93.025005.

[BGMP20] Guido Burkard, Michael J. Gullans, Xiao Mi, and Jason R. Petta. Superconductor–semiconductor hybrid-circuit quantum electrodynamics. *Nature*

Reviews Physics, 2(3):129–140, January 2020. URL: http://dx.doi.org/10.1038/s42254-019-0135-2, doi:10.1038/s42254-019-0135-2.

[BGS+17a] Sal J. Bosman, Mario F. Gely, Vibhor Singh, Daniel Bothner, Andres Castellanos-Gomez, and Gary A. Steele. Approaching ultrastrong coupling in transmon circuit QED using a high-impedance resonator. *Phys. Rev. B*, 95:224515, Jun 2017. URL: https://link.aps.org/doi/10.1103/PhysRevB.95.224515, doi:10.1103/PhysRevB.95.224515.

[BGS+17b] Sal J. Bosman, Mario F. Gely, Vibhor Singh, Alessandro Bruno, Daniel Bothner, and Gary A. Steele. Multi-mode ultra-strong coupling in circuit quantum electrodynamics. *npj Quantum Information*, 3(1), October 2017. URL: http://dx.doi.org/10.1038/s41534-017-0046-y, doi:10.1038/s41534-017-0046-y.

[BH04] S.P. Benz and C.A. Hamilton. Application of the Josephson effect to voltage metrology. *Proceedings of the IEEE*, 92(10):1617–1629, 2004. doi:10.1109/JPROC.2004.833671.

[BHW+04] Alexandre Blais, Ren-Shou Huang, Andreas Wallraff, S. M. Girvin, and R. J. Schoelkopf. Cavity quantum electrodynamics for superconducting electrical circuits: An architecture for quantum computation. *Phys. Rev. A*, 69:062320, Jun 2004. URL: https://link.aps.org/doi/10.1103/PhysRevA.69.062320, doi:10.1103/PhysRevA.69.062320.

[BLZ01] Paul Bunyk, Konstantin Likharev, and Dmitry Zinoviev. RSFQ technology: Physics and devices. *International Journal of High Speed Electronics and Systems*, 11(01):257–305, 2001. arXiv:https://doi.org/10.1142/S012915640100085X, doi:10.1142/S012915640100085X.

[BPG+17] M. Bard, I. V. Protopopov, I. V. Gornyi, A. Shnirman, and A. D. Mirlin. Superconductor-insulator transition in disordered Josephson-junction chains. *Phys. Rev. B*, 96:064514, Aug 2017. URL: https://link.aps.org/doi/10.1103/PhysRevB.96.064514, doi:10.1103/PhysRevB.96.064514.

[BSI+12] M. T. Bell, I. A. Sadovskyy, L. B. Ioffe, A. Yu. Kitaev, and M. E. Gershenson. Quantum Superinductor with Tunable Nonlinearity. *Phys. Rev. Lett.*, 109:137003, Sep 2012. URL: https://link.aps.org/doi/10.1103/PhysRevLett.109.137003, doi:10.1103/PhysRevLett.109.137003.

[BSK+17] J. Burnett, J. Sagar, O. W. Kennedy, P. A. Warburton, and J. C. Fenton. Low-Loss Superconducting Nanowire Circuits Using a Neon Focused Ion Beam. *Phys. Rev. Appl.*, 8:014039, Jul 2017. URL: https://link.aps.org/doi/10.1103/PhysRevApplied.8.014039, doi:10.1103/PhysRevApplied.8.014039.

[Bul84] S. A. Bulgadaev. Phase transition in a one-dimensional system with a long-range interaction. *JETP Lett.*, 39:315–319, 1984. ZhETF Pis'ma 39, 264–267 (1984).

[Bun21] Alexey Bunkov. *Current-voltage characteristic of quantum phase-slip junctions*. PhD thesis, 2021. URL: https://scholar.google.com/citations?view_op=view_citation&hl=ru&user=Wi5r95sAAAAJ&citation_for_view=Wi5r95sAAAAJ:u5HHmVD_uO8C.

[BVJ+98] V. Bouchiat, D. Vion, P. Joyez, D. Esteve, and M. H. Devoret. Quantum Coherence with a Single Cooper Pair. *Physica Scripta*, T76(1):165, 1998. URL: http://dx.doi.org/10.1238/Physica.Topical.076a00165, doi:10.1238/physica.topical.076a00165.

[BVSH25] Anton V. Bubis, Lucia Vigliotti, Maksym Serbyn, and Andrew P. Higginbotham. Nonequilibrium plasmon fluid in a Josephson junction chain, 2025. URL: https://arxiv.org/abs/2504.09721, arXiv:2504.09721.

[CAK+17] Karin Cedergren, Roger Ackroyd, Sergey Kafanov, Nicolas Vogt, Alexander Shnirman, and Timothy Duty. Insulating Josephson Junction Chains as Pinned Luttinger Liquids. *Phys. Rev. Lett.*, 119:167701, Oct 2017. URL: https://link.aps.org/doi/10.1103/PhysRevLett.119.167701, doi:10.1103/PhysRevLett.119.167701.

[CBL07] M. A. Castellanos-Beltran and K. W. Lehnert. Widely tunable parametric amplifier based on a superconducting quantum interference device array resonator. *Applied Physics Letters*, 91(8), August 2007. URL: http://dx.doi.org/10.1063/1.2773988, doi:10.1063/1.2773988.

[CC97] Erli Chen and S.Y. Chou. Characteristics of coplanar transmission lines on multilayer substrates: modeling and experiments. *IEEE Transactions on Microwave Theory and Techniques*, 45(6):939–945, 1997. doi:10.1109/22.588606.

[CCD+88] John Clarke, Andrew N. Cleland, Michel H. Devoret, Daniel Esteve, and John M. Martinis. Quantum Mechanics of a Macroscopic Variable: The Phase Difference of a Josephson Junction. *Science*, 239(4843):992–997, February 1988. URL: http://dx.doi.org/10.1126/science.239.4843.992, doi:10.1126/science.239.4843.992.

[CCG+23] Nicolò Crescini, Samuel Cailleaux, Wiebke Guichard, Cécile Naud, Olivier Buisson, Kater W. Murch, and Nicolas Roch. Evidence of dual Shapiro steps in a Josephson junction array. *Nature Physics*, 19(6):851–856, March 2023. URL: http://dx.doi.org/10.1038/s41567-023-01961-4, doi:10.1038/s41567-023-01961-4.

[CEP69] P. N. Chubov, V. V. Eremenko, and Y. A. Pilipenko. Dependence of the critical temperature and energy gap on the thickness of superconducting aluminum films. *Sov. Phys. JETP*, 28(2):389, 1969.

[CGHH06a] S. Corlevi, W. Guichard, F. W. J. Hekking, and D. B. Haviland. Coulomb blockade of Cooper pair tunneling and parity effects in the Cooper pair transistor. *Phys. Rev. B*, 74:224505, Dec 2006. URL: https://link.aps.org/doi/10.1103/PhysRevB.74.224505, doi:10.1103/PhysRevB.74.224505.

[CGHH06b] S. Corlevi, W. Guichard, F. W. J. Hekking, and D. B. Haviland. Phase-Charge Duality of a Josephson Junction in a Fluctuating Electromagnetic Environment. *Phys. Rev. Lett.*, 97:096802, Aug 2006. URL: https://link.aps.org/doi/10.1103/PhysRevLett.97.096802, doi:10.1103/PhysRevLett.97.096802.

[CL81] A. O. Caldeira and A. J. Leggett. Influence of Dissipation on Quantum Tunneling in Macroscopic Systems. *Phys. Rev. Lett.*, 46:211–214, Jan 1981. URL: https://link.aps.org/doi/10.1103/PhysRevLett.46.211, doi:10.1103/PhysRevLett.46.211.

[CLB+20] A. A. Clerk, K. W. Lehnert, P. Bertet, J. R. Petta, and Y. Nakamura. Hybrid quantum systems with circuit quantum electrodynamics. *Nature Physics*, 16(3):257–267, March 2020. URL: http://dx.doi.org/10.1038/s41567-020-0797-9, doi:10.1038/s41567-020-0797-9.

[CMD+23] Kevin D. Crowley, Russell A. McLellan, Aveek Dutta, Nana Shumiya, Alexander P. M. Place, Xuan Hoang Le, Youqi Gang, Trisha Madhavan, Matthew P. Bland, Ray Chang, Nishaad Khedkar, Yiming Cady Feng, Esha A. Umbarkar, Xin Gui, Lila V. H. Rodgers, Yichen Jia, Mayer M. Feldman, Stephen A. Lyon, Mingzhao Liu, Robert J. Cava, Andrew A. Houck, and Nathalie P. de Leon. Disentangling Losses in Tantalum Superconducting Circuits. *Phys. Rev. X*, 13:041005, Oct 2023. URL: https://link.aps.org/doi/10.1103/PhysRevX.13.041005, doi:10.1103/PhysRevX.13.041005.

[CPF+22] Qi-Ming Chen, Matti Partanen, Florian Fesquet, Kedar E. Honasoge, Fabian Kronowetter, Yuki Nojiri, Michael Renger, Kirill G. Fedorov, Achim Marx, Frank Deppe, and Rudolf Gross. Scattering coefficients of superconducting microwave resonators. II. System-bath approach. *Phys. Rev. B*, 106:214506, Dec 2022. URL: https://link.aps.org/doi/10.1103/PhysRevB.106.214506, doi:10.1103/PhysRevB.106.214506.

[CPP+22] Qi-Ming Chen, Meike Pfeiffer, Matti Partanen, Florian Fesquet, Kedar E. Honasoge, Fabian Kronowetter, Yuki Nojiri, Michael Renger, Kirill G. Fedorov, Achim Marx, Frank Deppe, and Rudolf Gross. Scattering coefficients of superconducting microwave resonators. I. Transfer matrix approach. *Phys. Rev. B*, 106:214505, Dec 2022. URL: https://link.aps.org/doi/10.1103/PhysRevB.106.214505, doi:10.1103/PhysRevB.106.214505.

[CSM+25] Ray D. Chang, Nana Shumiya, Russell A. McLellan, Yifan Zhang, Matthew P. Bland, Faranak Bahrami, Junsik Mun, Chenyu Zhou, Kim Kisslinger, Guangming Cheng, Basil M. Smitham, Alexander C. Pakpour-Tabrizi, Nan Yao, Yimei Zhu, Mingzhao Liu, Robert J. Cava, Sarang Gopalakrishnan, Andrew A. Houck, and Nathalie P. de Leon. Eliminating Surface Oxides of Superconducting Circuits with Noble Metal Encapsulation. *Physical Review Letters*, 134(9), March 2025. URL: http://dx.doi.org/10.1103/PhysRevLett.134.097001, doi:10.1103/physrevlett.134.097001.

[d'A14] Antonio d'Addabbo. *Applications of Kinetic Inductance Detectors to Astronomy and Particle Physics*. Theses, Université de Grenoble ; Università degli studi La Sapienza (Rome), October 2014. URL: https://theses.hal.science/tel-01368000.

[DCH+21] Akash V. Dixit, Srivatsan Chakram, Kevin He, Ankur Agrawal, Ravi K. Naik, David I. Schuster, and Aaron Chou. Searching for Dark Matter with a Superconducting Qubit. *Phys. Rev. Lett.*, 126:141302, Apr 2021. URL: https://link.aps.org/doi/10.1103/PhysRevLett.126.141302, doi:10.1103/PhysRevLett.126.141302.

[dG14] Sebastian Erik de Graaf. *Fractal superconducting resonators for the interrogation of two-level systems*. PhD thesis, Chalmers University of Technology, 2014. URL: https://research.chalmers.se/en/publication/190808.

[DGS07] M.H. Devoret, Steven Girvin, and Robert Schoelkopf. Circuit-QED: How strong can the coupling between a Josephson junction atom and a transmission line resonator be? *Annalen der Physik*, 519(10–11):767–779, October 2007. URL: http://dx.doi.org/10.1002/andp.200751910-1109, doi:10.1002/andp.200751910-1109.

[DM04] Michel H. Devoret and John M. Martinis. Implementing Qubits with Superconducting Integrated Circuits. *Quantum Information Processing*, 3(1–5):163–203, October 2004. URL: http://dx.doi.org/10.1007/s11128-004-3101-5, doi:10.1007/s11128-004-3101-5.

[DN61] Robert Doll and Martin Näbauer. Experimental proof of magnetic flux quantization in a superconducting ring. *Physical Review Letters*, 7(2):51, 1961.

[Ear19] Nathan Don Earnest. *Engineering Light-Matter Interactions with Metastable States in a Heavy Fluxonium*. PhD dissertation, The University of Chicago, Chicago, Illinois, March 2019. URL: https://schusterlab.stanford.edu/static/pdfs/Earnest_thesis.pdf.

[ELJ+13] Adem Ergül, Jack Lidmar, Jan Johansson, Yağız Azizoğlu, David Schaeffer, and David B Haviland. Localizing quantum phase slips in one-dimensional Josephson junction chains. *New Journal of Physics*, 15(9):095014, September 2013. URL: http://dx.doi.org/10.1088/1367-2630/15/9/095014, doi:10.1088/1367-2630/15/9/095014.

[FAdP+23] S. Frasca, I.N. Arabadzhiev, S.Y. Bros de Puechredon, F. Oppliger, V. Jouanny, R. Musio, M. Scigliuzzo, F. Minganti, P. Scarlino, and E. Charbon. NbN films with high kinetic inductance for high-quality compact superconducting resonators. *Phys. Rev. Appl.*, 20:044021, Oct 2023. URL: https://link.aps.org/doi/10.1103/PhysRevApplied.20.044021, doi:10.1103/PhysRevApplied.20.044021.

[Fan61] U. Fano. Effects of Configuration Interaction on Intensities and Phase Shifts. *Phys. Rev.*, 124:1866–1878, Dec 1961. URL: https://link.aps.org/doi/10.1103/PhysRev.124.1866, doi:10.1103/PhysRev.124.1866.

[FDLR+19] P. Forn-Díaz, L. Lamata, E. Rico, J. Kono, and E. Solano. Ultrastrong coupling regimes of light-matter interaction. *Rev. Mod. Phys.*, 91:025005, Jun 2019. URL: https://link.aps.org/doi/10.1103/RevModPhys.91.025005, doi:10.1103/RevModPhys.91.025005.

[FI18] M. V. Feigel'man and L. B. Ioffe. Microwave Properties of Superconductors Close to the Superconductor-Insulator Transition. *Phys. Rev. Lett.*, 120:037004, Jan 2018. URL: https://link.aps.org/doi/10.1103/PhysRevLett.120.037004, doi:10.1103/PhysRevLett.120.037004.

[FKMDL+19] Anton Frisk Kockum, Adam Miranowicz, Simone De Liberato, Salvatore Savasta, and Franco Nori. Ultrastrong coupling between light and matter. *Nature Reviews Physics*, 1(1):19–40, January 2019. URL: http://dx.doi.org/10.1038/s42254-018-0006-2, doi:10.1038/s42254-018-0006-2.

[FKP+16] J. M. Fink, M. Kalaee, A. Pitanti, R. Norte, L. Heinzle, M. Davanço, K. Srinivasan, and O. Painter. Quantum electromechanics on silicon nitride nanomembranes. *Nature Communications*, 7(1), August 2016. URL: http://dx.doi.org/10.1038/ncomms12396, doi:10.1038/ncomms12396.

[FSM+24] N. Foroozani, B. Sarabi, S. H. Moseley, T. Stevenson, E. J. Wollack, O. Noroozian, and K. D. Osborn. Dual-resonator kinetic inductance detector for distinction between signal and $1/f$ frequency noise. *Phys. Rev. Appl.*, 21:014009, Jan 2024. URL: https://link.aps.org/doi/10.1103/PhysRevApplied.21.014009, doi:10.1103/PhysRevApplied.21.014009.

[Fv01] Rosario Fazio and Herre van der Zant. Quantum phase transitions and vortex dynamics in superconducting networks. *Physics Reports*, 355(4):235–334, 2001. URL: https://www.sciencedirect.com/science/article/pii/S0370157301000229, doi:10.1016/S0370-1573(01)00022-9.

[Gao08] Jiansong Gao. *The Physics of Superconducting Microwave Resonators*. Dissertation (ph.d.), California Institute of Technology, 2008. CaltechTHESIS. URL: https://resolver.caltech.edu/CaltechETD:etd-06092008-235549, doi:10.7907/RAT0-VM75.

[GC85] C. W. Gardiner and M. J. Collett. Input and output in damped quantum systems: Quantum stochastic differential equations and the master equation. *Phys. Rev. A*, 31:3761–3774, Jun 1985. URL: https://link.aps.org/doi/10.1103/PhysRevA.31.3761, doi:10.1103/PhysRevA.31.3761.

[GC24] Luca Giacomelli and Cristiano Ciuti. Emergent quantum phase transition of a Josephson junction coupled to a high-impedance multimode resonator. *Nature Communications*, 15(1), June 2024. URL: http://dx.doi.org/10.1038/s41467-024-48558-w, doi:10.1038/s41467-024-48558-w.

[GDPK+21] András Gyenis, Agustin Di Paolo, Jens Koch, Alexandre Blais, Andrew A. Houck, and David I. Schuster. Moving beyond the Transmon: Noise-Protected Superconducting Quantum Circuits. *PRX Quantum*, 2:030101, Sep 2021. URL: https://link.aps.org/doi/10.1103/PRXQuantum.2.030101, doi:10.1103/PRXQuantum.2.030101.

[GFB+08] M. Göppl, A. Fragner, M. Baur, R. Bianchetti, S. Filipp, J. M. Fink, P. J. Leek, G. Puebla, L. Steffen, and A. Wallraff. Coplanar waveguide resonators for circuit quantum electrodynamics. *Journal of Applied Physics*, 104(11), December 2008. URL: http://dx.doi.org/10.1063/1.3010859, doi:10.1063/1.3010859.

[GH10] W. Guichard and F. W. J. Hekking. Phase-charge duality in Josephson junction circuits: Role of inertia and effect of microwave irradiation. *Phys. Rev. B*, 81:064508, Feb 2010. URL: https://link.aps.org/doi/10.1103/PhysRevB.81.064508, doi:10.1103/PhysRevB.81.064508.

[Gia03] Thierry Giamarchi. *Quantum Physics in One Dimension*. International Series of Monographs on Physics. Clarendon Press, Oxford, England, November 2003.

[Gio88] N. Giordano. Evidence for Macroscopic Quantum Tunneling in One-Dimensional Superconductors. *Phys. Rev. Lett.*, 61:2137–2140, Oct 1988. URL: https://link.aps.org/doi/10.1103/PhysRevLett.61.2137, doi:10.1103/PhysRevLett.61.2137.

[GKD+19] Mario F. Gely, Marios Kounalakis, Christian Dickel, Jacob Dalle, Rémy Vatré, Brian Baker, Mark D. Jenkins, and Gary A. Steele. Observation and stabilization of photonic Fock states in a hot radio-frequency resonator. *Science*, 363(6431):1072–1075, March 2019. URL: http://dx.doi.org/10.1126/science.aaw3101, doi:10.1126/science.aaw3101.

[GKI04] A. A. Golubov, M. Yu. Kupriyanov, and E. Il'ichev. The current-phase relation in josephson junctions. *Rev. Mod. Phys.*, 76:411–469, Apr 2004. URL: https://link.aps.org/doi/10.1103/RevModPhys.76.411, doi:10.1103/RevModPhys.76.411.

[GKM+17] Xiu Gu, Anton Frisk Kockum, Adam Miranowicz, Yu xi Liu, and Franco Nori. Microwave photonics with superconducting quantum circuits. *Physics Reports*, 718-719:1–102, 2017. Microwave photonics with superconducting quantum circuits. URL: https://www.sciencedirect.com/science/article/pii/S0370157317303290, doi:10.1016/j.physrep.2017.10.002.

[GL50] V. L. Ginzburg and L. D. Landau. On the Theory of Superconductivity. *Zh. Eksp. Teor. Fiz.*, 20:1064–1082, 1950. In Russian.

[GLK95] S. Gevorgian, L.J.P. Linner, and E.L. Kollberg. CAD models for shielded multilayered CPW. *IEEE Transactions on Microwave Theory and Techniques*, 43(4):772–779, 1995. doi:10.1109/22.375223.

[GMDP+21] András Gyenis, Pranav S. Mundada, Agustin Di Paolo, Thomas M. Hazard, Xinyuan You, David I. Schuster, Jens Koch, Alexandre Blais, and Andrew A. Houck. Experimental Realization of a Protected Superconducting Circuit Derived from the 0–π Qubit. *PRX Quantum*, 2:010339, Mar 2021. URL: https://link.aps.org/doi/10.1103/PRXQuantum.2.010339, doi:10.1103/PRXQuantum.2.010339.

[Gor59] Lev Petrovich Gor'kov. Microscopic derivation of the Ginzburg-Landau equations in the theory of superconductivity. *Sov. Phys. JETP*, 9(6):1364–1367, 1959.

[GPK+22] Samuel Goldstein, Guy Pardo, Naftali Kirsh, Niklas Gaiser, Ciprian Padurariu, Björn Kubala, Joachim Ankerhold, and Nadav Katz. Compact itinerant microwave photonics with superconducting high-kinetic inductance microstrips. *New Journal of Physics*, 24(2):023022, February 2022. URL: http://dx.doi.org/10.1088/1367-2630/ac45cc, doi:10.1088/1367-2630/ac45cc.

[GS19] Ernst O. Göbel and Uwe Siegner, editors. *The New International System of Units (SI): Quantum Metrology and Quantum Standards*. Wiley-VCH, Weinheim, Germany, 2019. URL: https://www.wiley.com/en-us/The+New+International+System+of+Units+(SI)-p-9783527814497, doi:10.1002/9783527814497.

[GT57] R. E. Glover and M. Tinkham. Conductivity of Superconducting Films for Photon Energies between 0.3 and $40kT_c$. *Phys. Rev.*, 108:243–256, Oct 1957. URL: https://link.aps.org/doi/10.1103/PhysRev.108.243, doi:10.1103/PhysRev.108.243.

[GZ08] Dmitri S Golubev and Andrei D Zaikin. Thermally activated phase slips in superconducting nanowires. *Physical Review B—Condensed Matter and Materials Physics*, 78(14):144502, 2008.

[GZV+08] J. Gao, J. Zmuidzinas, A. Vayonakis, P. Day, B. Mazin, and H. Leduc. Equivalence of the Effects on the Complex Conductivity of Superconductor due to Temperature Change and External Pair Breaking. *Journal of Low Temperature Physics*, 151(1–2):557–563, January 2008. URL: http://dx.doi.org/10.1007/s10909-007-9688-z, doi:10.1007/s10909-007-9688-z.

[HA0] David B. Haviland, Karin Andersson, and Peter Ågren. Superconducting and Insulating Behavior in One-Dimensional Josephson Junction Arrays. *Journal of Low Temperature Physics*, 118(5–6):733–749, March 2000. URL: http://dx.doi.org/10.1023/A:1004603814529, doi:10.1023/a:1004603814529.

[HB24] Farid Hassani Bijarbooneh. *Superconducting qubits capable of dynamic switching between protected and high-speed control regimes*. PhD thesis, 2024. URL: https://research-explorer.ista.ac.at/record/17133, doi:10.15479/AT:ISTA:17133.

[HD96] David B. Haviland and Per Delsing. Cooper-pair charge solitons: The electrodynamics of localized charge in a superconductor. *Phys. Rev. B*, 54:R6857–R6860, Sep 1996. URL: https://link.aps.org/doi/10.1103/PhysRevB.54.R6857, doi:10.1103/PhysRevB.54.R6857.

[Hei25] W. Heisenberg. Über quantentheoretische Umdeutung kinematischer und mechanischer Beziehungen. *Zeitschrift für Physik*, 33(1):879–893, December 1925. URL: http://dx.doi.org/10.1007/BF01328377, doi:10.1007/bf01328377.

[HG19] Manuel Houzet and Leonid I. Glazman. Microwave Spectroscopy of a Weakly Pinned Charge Density Wave in a Superinductor. *Phys. Rev. Lett.*, 122:237701, Jun 2019. URL: https://link.aps.org/doi/10.1103/PhysRevLett.122.237701, doi:10.1103/PhysRevLett.122.237701.

[HGWC86] Mark Halpern, Herbert P. Gush, Edward Wishnow, and Vittorio De Cosmo. Far infrared transmission of dielectrics at cryogenic and room temperatures: glass, Fluorogold, Eccosorb, Stycast, and various plastics. *Appl. Opt.*, 25(4):565–570, Feb 1986. URL: https://opg.optica.org/ao/abstract.cfm?URI=ao-25-4-565, doi:10.1364/AO.25.000565.

[Hil13] Jeffrey Thomas Hill. *Nonlinear Optics and Wavelength Translation Via Cavity-Optomechanics*. Dissertation (ph.d.), California Institute of Technology, 2013. URL: https://resolver.caltech.edu/CaltechTHESIS:05312013-144103500, doi:10.7907/DKW6-TF64.

[HKDC91] D. B Haviland, L. S Kuzmin, P Delsing, and T Claeson. Observation of the Coulomb Blockade of Cooper Pair Tunnelling in Single Josephson Junctions. *Europhysics Letters (EPL)*, 16(1):103–108, September 1991. URL: http://dx.doi.org/10.1209/0295-5075/16/1/018, doi:10.1209/0295-5075/16/1/018.

[HPK+23] F. Hassani, M. Peruzzo, L. N. Kapoor, A. Trioni, M. Zemlicka, and J. M. Fink. Inductively shunted transmons exhibit noise insensitive plasmon states and a fluxon decay exceeding 3 hours. *Nature Communications*, 14(1), July 2023. URL: http://dx.doi.org/10.1038/s41467-023-39656-2, doi:10.1038/s41467-023-39656-2.

[HRA+16] Jerris W. Hooker, Vijaykumar Ramaswamy, Rajendra K. Arora, Arthur S. Edison, and William W. Brey. Effects of Dielectric Substrates and Ground Planes on Resonance Frequency of Archimedean Spirals. *IEEE Transactions on Applied Superconductivity*, 26(3):1–4, 2016. doi:10.1109/TASC.2016.2531007.

[HS21] Pertti J. Hakonen and Edouard B. Sonin. Comment on "Absence of a Dissipative Quantum Phase Transition in Josephson Junctions". *Phys. Rev. X*, 11:018001, Mar 2021. URL: https://link.aps.org/doi/10.1103/PhysRevX.11.018001, doi:10.1103/PhysRevX.11.018001.

[HSG+07] A. A. Houck, D. I. Schuster, J. M. Gambetta, J. A. Schreier, B. R. Johnson, J. M. Chow, L. Frunzio, J. Majer, M. H. Devoret, S. M. Girvin, and R. J. Schoelkopf. Generating single microwave photons in a circuit. *Nature*, 449(7160):328–331, September 2007. URL: http://dx.doi.org/10.1038/nature06126, doi:10.1038/nature06126.

[HTK12] Andrew A. Houck, Hakan E. Türeci, and Jens Koch. On-chip quantum simulation with superconducting circuits. *Nature Physics*, 8(4):292–299, April 2012. URL: http://dx.doi.org/10.1038/nphys2251, doi:10.1038/nphys2251.

[HW21] Iftikhar Hussain and Dong-Kyun Woo. Self-Inductance Calculation of the Archimedean Spiral Coil. *Energies*, 15(1):253, December 2021. URL: http://dx.doi.org/10.3390/en15010253, doi:10.3390/en15010253.

[HWA+08] Max Hofheinz, E. M. Weig, M. Ansmann, Radoslaw C. Bialczak, Erik Lucero, M. Neeley, A. D. O'Connell, H. Wang, John M. Martinis, and A. N. Cleland. Generation of Fock states in a superconducting quantum circuit. *Nature*, 454(7202):310–314, July 2008. URL: http://dx.doi.org/10.1038/nature07136, doi:10.1038/nature07136.

[IZ69] YM Ivanchenko and LA Zil'Berman. The Josephson effect in small tunnel contacts. *Soviet Phys. JETP*, 28, 1969.

[JCN+25] Christian Jünger, Trevor Chistolini, Long B. Nguyen, Hyunseong Kim, Larry Chen, Thomas Ersevim, William Livingston, Gerwin Koolstra, David I. Santiago, and Irfan Siddiqi. Implementation of scalable suspended superinductors. *Applied Physics Letters*, 126(4), January 2025. URL: http://dx.doi.org/10.1063/5.0250341, doi:10.1063/5.0250341.

[JNG21] Atharv Joshi, Kyungjoo Noh, and Yvonne Y Gao. Quantum information processing with bosonic qubits in circuit QED. *Quantum Science and Technology*, 6(3):033001, April 2021. URL: http://dx.doi.org/10.1088/2058-9565/abe989, doi:10.1088/2058-9565/abe989.

[Jos62] B.D. Josephson. Possible new effects in superconductive tunnelling. *Physics Letters*, 1(7):251–253, July 1962. URL: http://dx.doi.org/10.1016/0031-9163(62)91369-0, doi:10.1016/0031-9163(62)91369-0.

[JRBE+25] Marián Janík, Kevin Roux, Carla Borja-Espinosa, Oliver Sagi, Abdulhamid Baghdadi, Thomas Adletzberger, Stefano Calcaterra, Marc Botifoll, Alba Garzón Manjón, Jordi Arbiol, Daniel Chrastina, Giovanni Isella, Ioan M. Pop, and Georgios Katsaros. Strong charge-photon coupling in planar germanium enabled by granular aluminium superinductors. *Nature Communications*, 16(1), March 2025. URL: http://dx.doi.org/10.1038/s41467-025-57252-4, doi:10.1038/s41467-025-57252-4.

[JXGRR16] Tuomas Jaako, Ze-Liang Xiang, Juan José Garcia-Ripoll, and Peter Rabl. Ultrastrong-coupling phenomena beyond the Dicke model. *Phys. Rev. A*, 94:033850, Sep 2016. URL: https://link.aps.org/doi/10.1103/PhysRevA.94.033850, doi:10.1103/PhysRevA.94.033850.

[Kal] Quantum electromechanics of a hypersonic crystal.

[KBDG24] Xanda C. Kolesnikow, Raditya W. Bomantara, Andrew C. Doherty, and Arne L. Grimsmo. Gottesman-Kitaev-Preskill State Preparation Using Periodic Driving. *Phys. Rev. Lett.*, 132:130605, Mar 2024. URL: https://link.aps.org/doi/10.1103/PhysRevLett.132.130605, doi:10.1103/PhysRevLett.132.130605.

[KCB+24] Mary Kreidel, Xuanjing Chu, Jesse Balgley, Abhinandan Antony, Nishchhal Verma, Julian Ingham, Leonardo Ranzani, Raquel Queiroz, Robert M. Westervelt, James Hone, and Kin Chung Fong. Measuring kinetic inductance and superfluid stiffness of two-dimensional superconductors using high-quality transmission-line resonators. *Physical Review Research*, 6(4), December 2024. URL: http://dx.doi.org/10.1103/PhysRevResearch.6.043245, doi:10.1103/physrevresearch.6.043245.

[KGB+25] G. Koolstra, E.O. Glen, N.R. Beysengulov, H. Byeon, K.E. Castoria, M. Sammon, B. Dizdar, C.S. Wang, D.I. Schuster, S.A. Lyon, J. Pollanen, and D.G. Rees. High-impedance resonators for strong coupling to an electron on helium. *Phys. Rev. Appl.*, 23:024001, Feb 2025. URL: https://link.aps.org/doi/10.1103/PhysRevApplied.23.024001, doi:10.1103/PhysRevApplied.23.024001.

[KH91] L. S. Kuzmin and D. B. Haviland. Observation of the Bloch oscillations in an ultrasmall Josephson junction. *Phys. Rev. Lett.*, 67:2890–2893, Nov 1991. URL: https://link.aps.org/doi/10.1103/PhysRevLett.67.2890, doi:10.1103/PhysRevLett.67.2890.

[KHZ+20] Konstantin Kalashnikov, Wen Ting Hsieh, Wenyuan Zhang, Wen-Sen Lu, Plamen Kamenov, Agustin Di Paolo, Alexandre Blais, Michael E. Gershenson, and Matthew Bell. Bifluxon: Fluxon-Parity-Protected Superconducting Qubit. *PRX Quantum*, 1:010307, Sep 2020. URL: https://link.aps.org/doi/10.1103/PRXQuantum.1.010307, doi:10.1103/PRXQuantum.1.010307.

[Kis13] Egor Kiselev. Design and Measurement of Superconducting Spiral Microwave Resonators. Bachelor thesis, Physikalisches Institut, Karlsruhe Institute of Technology (KIT), Karlsruhe, Germany, aug 2013. URL: https://www.phi.kit.edu/publications/BA/2013_Kiselev.pdf.

[KKG+24] Fabian Kaap, Christoph Kissling, Victor Gaydamachenko, Lukas Grünhaupt, and Sergey Lotkhov. Demonstration of dual Shapiro steps in small Josephson junctions. *Nature Communications*, 15(1), October 2024. URL: http://dx.doi.org/10.1038/s41467-024-53011-z, doi:10.1038/s41467-024-53011-z.

[KLK+20] Plamen Kamenov, Wen-Sen Lu, Konstantin Kalashnikov, Thomas DiNapoli, Matthew T. Bell, and Michael E. Gershenson. Granular Aluminum Meandered Superinductors for Quantum Circuits. *Phys. Rev. Appl.*, 13:054051, May 2020. URL: https://link.aps.org/doi/10.1103/PhysRevApplied.13.054051, doi:10.1103/PhysRevApplied.13.054051.

[KMDG09] Jens Koch, V. Manucharyan, M. H. Devoret, and L. I. Glazman. Charging Effects in the Inductively Shunted Josephson Junction. *Phys. Rev. Lett.*, 103:217004, Nov 2009. URL: https://link.aps.org/doi/10.1103/PhysRevLett.103.217004, doi:10.1103/PhysRevLett.103.217004.

[KMG+19] R. Kuzmin, R. Mencia, N. Grabon, N. Mehta, Y.-H. Lin, and V. E. Manucharyan. Quantum electrodynamics of a superconductor–insulator phase transition. *Nature Physics*, 15(9):930–934, June 2019. URL: http://dx.doi.org/10.1038/s41567-019-0553-1, doi:10.1038/s41567-019-0553-1.

[KN19] Anton Frisk Kockum and Franco Nori. *Quantum Bits with Josephson Junctions*, pages 703–741. Springer International Publishing, Cham, 2019. doi:10.1007/978-3-030-20726-7_17.

[KNW+18] Yu. Krupko, V. D. Nguyen, T. Weißl, É. Dumur, J. Puertas, R. Dassonneville, C. Naud, F. W. J. Hekking, D. M. Basko, O. Buisson, N. Roch, and W. Hasch-Guichard. Kerr nonlinearity in a superconducting Josephson metamaterial. *Phys. Rev. B*, 98:094516, Sep 2018. URL: https://link.aps.org/doi/10.1103/PhysRevB.98.094516, doi:10.1103/PhysRevB.98.094516.

[KNW+23] Yu. Krupko, V. D. Nguyen, T. Weißl, É. Dumur, J. Puertas, R. Dassonneville, C. Naud, F. W. J. Hekking, D. M. Basko, O. Buisson, N. Roch, and W. Hasch-Guichard. Erratum: Kerr nonlinearity in a superconducting Josephson metamaterial [Phys. Rev. B 98, 094516 (2018)]. *Phys. Rev. B*, 108:219904, Dec 2023. URL: https://link.aps.org/doi/10.1103/PhysRevB.108.219904, doi:10.1103/PhysRevB.108.219904.

[KR24] O. Kashuba and R.-P. Riwar. Limitations of Caldeira-Leggett model for description of phase transitions in superconducting circuits. *Phys. Rev. B*, 110:184505, Nov 2024. URL: https://link.aps.org/doi/10.1103/PhysRevB.110.184505, doi:10.1103/PhysRevB.110.184505.

[KSB+16] P. Kumar, S. Sendelbach, M. A. Beck, J. W. Freeland, Zhe Wang, Hui Wang, Clare C. Yu, R. Q. Wu, D. P. Pappas, and R. McDermott. Origin and Reduction of $1/f$ Magnetic Flux Noise in Superconducting Devices. *Phys. Rev. Appl.*, 6:041001, Oct 2016. URL: https://link.aps.org/doi/10.1103/PhysRevApplied.6.041001, doi:10.1103/PhysRevApplied.6.041001.

[KSH+24] Bayan Karimi, Gorm Ole Steffensen, Andrew P. Higginbotham, Charles M. Marcus, Alfredo Levy Yeyati, and Jukka P. Pekola. Bolometric detection of Josephson radiation. *Nature Nanotechnology*, 19(11):1613–1618, August 2024. URL: http://dx.doi.org/10.1038/s41565-024-01770-7, doi:10.1038/s41565-024-01770-7.

[KSP+25] Mahya Khorramshahi, Martin Spiecker, Patrick Paluch, Simon Geisert, Nicolas Gosling, Nicolas Zapata, Lucas Brauch, Christian Kuebel, Simone

Dehm, Ralph Krupke, Wolfgang Wernsdorfer, Ioan M. Pop, and Thomas Reisinger. High Impedance Granular Aluminum Ring Resonators, 2025. URL: https://arxiv.org/abs/2506.07761, arXiv:2506.07761.

[KVHC82] Roger H. Koch, D. J. Van Harlingen, and John Clarke. Measurements of quantum noise in resistively shunted Josephson junctions. *Phys. Rev. B*, 26:74–87, Jul 1982. URL: https://link.aps.org/doi/10.1103/PhysRevB.26.74, doi:10.1103/PhysRevB.26.74.

[KVMM24] Heidi Kivijärvi, Arto Viitanen, Timm Mörstedt, and Mikko Möttönen. Noise-induced quantum-circuit refrigeration, 2024. URL: https://arxiv.org/abs/2412.05886, arXiv:2412.05886.

[KYG+07] Jens Koch, Terri M. Yu, Jay Gambetta, A. A. Houck, D. I. Schuster, J. Majer, Alexandre Blais, M. H. Devoret, S. M. Girvin, and R. J. Schoelkopf. Charge-insensitive qubit design derived from the Cooper pair box. *Phys. Rev. A*, 76:042319, Oct 2007. URL: https://link.aps.org/doi/10.1103/PhysRevA.76.042319, doi:10.1103/PhysRevA.76.042319.

[KYS19] Gerwin Koolstra, Ge Yang, and David I. Schuster. Coupling a single electron on superfluid helium to a superconducting resonator. *Nature Communications*, 10(1), November 2019. URL: http://dx.doi.org/10.1038/s41467-019-13335-7, doi:10.1038/s41467-019-13335-7.

[KZA+20] K. L. Krewer, W. Zhang, J. Arabski, G. Schmerber, E. Beaurepaire, M. Bonn, and D. Turchinovich. Thickness-dependent electron momentum relaxation times in iron films. *Applied Physics Letters*, 116(10):102406, 03 2020. arXiv:https://pubs.aip.org/aip/apl/article-pdf/doi/10.1063/1.5142479/16718303/102406_1_online.pdf, doi:10.1063/1.5142479.

[KZL+21] Emanuel Knehr, Mario Ziegler, Sven Linzen, Konstantin Ilin, Patrick Schanz, Jonathan Plentz, Marco Diegel, Heidemarie Schmidt, Evgeni Il'ichev, and Michael Siegel. Wafer-level uniformity of atomic-layer-deposited niobium nitride thin films for quantum devices. *Journal of Vacuum Science Technology A*, 39(5):052401, 07 2021. arXiv:https://pubs.aip.org/avs/jva/article-pdf/doi/10.1116/6.0001126/14046716/052401_1_online.pdf, doi:10.1116/6.0001126.

[L+25] Trevyn F. Q. Larson et al. Localized quasiparticles in a fluxonium with quasi-two-dimensional amorphous kinetic inductors. 4 2025. arXiv:2504.07950.

[LA67] James S Langer and Vinay Ambegaokar. Intrinsic resistive transition in narrow superconducting channels. *Physical Review*, 164(2):498, 1967.

[Lan37] L. D. Landau. On the theory of phase transitions. *Zh. Eksp. Teor. Fiz.*, 7:19–32, 1937. doi:10.1016/B978-0-08-010586-4.50034-1.

[Lan56] L. D. Landau. The Theory of a Fermi Liquid. *Zh. Eksp. Teor. Fiz.*, 30(6):1058, 1956.

[LBZN03] S. V. Lotkhov, S. A. Bogoslovsky, A. B. Zorin, and J. Niemeyer. Cooper Pair Cotunneling in Single Charge Transistors with Dissipative Electromagnetic Environment. *Phys. Rev. Lett.*, 91:197002, Nov 2003. URL: https://link.aps.org/doi/10.1103/PhysRevLett.91.197002, doi:10.1103/PhysRevLett.91.197002.

[Leg80] A. J. Leggett. Macroscopic Quantum Systems and the Quantum Theory of Measurement. *Progress of Theoretical Physics Supplement*, 69:80–100, 03 1980. arXiv:https://academic.oup.com/ptps/article-pdf/doi/10.1143/PTP.69.80/5356381/69-80.pdf, doi:10.1143/PTP.69.80.

[LG11] Alejandro M. Lobos and Thierry Giamarchi. Superconductor-to-insulator transition in linear arrays of Josephson junctions capacitively coupled to metallic films. *Phys. Rev. B*, 84:024523, Jul 2011. URL: https://link.aps.org/doi/10.1103/PhysRevB.84.024523, doi:10.1103/PhysRevB.84.024523.

[Lit67] William A. Little. Decay of Persistent Currents in Small Superconductors. *Phys. Rev.*, 156:396–403, Apr 1967. URL: https://link.aps.org/doi/10.1103/PhysRev.156.396, doi:10.1103/PhysRev.156.396.

[LS91] K.K. Likharev and V.K. Semenov. RSFQ logic/memory family: a new Josephson-junction technology for sub-terahertz-clock-frequency digital systems. *IEEE Transactions on Applied Superconductivity*, 1(1):3–28, 1991. doi:10.1109/77.80745.

[Lut63] J. M. Luttinger. An Exactly Soluble Model of a Many-Fermion System. *Journal of Mathematical Physics*, 4(9):1154–1162, 09 1963. arXiv:https://pubs.aip.org/aip/jmp/article-pdf/4/9/1154/19057386/1154_1_online.pdf, doi:10.1063/1.1704046.

[LZA+17] S Linzen, M Ziegler, O V Astafiev, M Schmelz, U Hübner, M Diegel, E Il'ichev, and H-G Meyer. Structural and electrical properties of ultrathin niobium nitride films grown by atomic layer deposition. *Superconductor Science and Technology*, 30(3):035010, January 2017. URL: http://dx.doi.org/10.1088/1361-6668/aa572a, doi:10.1088/1361-6668/aa572a.

[M+25] Paul Manset et al. Hyperinductance based on stacked Josephson junctions. 5 2025. arXiv:2505.02764.

[MAA+14] N. Maleeva, N. N. Abramov, A. S. Averkin, M. V. Fistul, A. Karpov, A. P. Zhuravel, and A. V. Ustinov. Electrodynamics of a planar Archimedean spiral resonator, 2014. URL: https://arxiv.org/abs/1411.5823, arXiv:1411.5823.

[MAA+15] N. Maleeva, A. Averkin, N. N. Abramov, M. V. Fistul, A. Karpov, A. P. Zhuravel, and A. V. Ustinov. Electrodynamics of planar Archimedean spiral resonator. *Journal of Applied Physics*, 118(3):033902, 07 2015. arXiv:https://pubs.aip.org/aip/jap/article-pdf/doi/1

0.1063/1.4923305/15164644/033902_1_online.pdf, doi:10.1063/1.4923305.

[MAC22] Giampiero Marchegiani, Luigi Amico, and Gianluigi Catelani. Quasiparticles in Superconducting Qubits with Asymmetric Junctions. *PRX Quantum*, 3:040338, Dec 2022. URL: https://link.aps.org/doi/10.1103/PRXQuantum.3.040338, doi:10.1103/PRXQuantum.3.040338.

[Man12] Vladimir Eduardovich Manucharyan. *Superinductance*. PhD thesis, Yale University, May 2012. URL: https://bpb-us-w2.wpmucdn.com/campuspress.yale.edu/dist/2/3627/files/2021/07/Manucharyan-Vladimir-Superinductance-Yale-2012.pdf.

[Maz05] Benjamin A. Mazin. *Microwave kinetic inductance detectors*. PhD thesis, 2005. URL: https://resolver.caltech.edu/CaltechETD:etd-10042004-120707, doi:10.7907/GZ72-V784.

[MBIS+20] A. Murani, N. Bourlet, H. le Sueur, F. Portier, C. Altimiras, D. Esteve, H. Grabert, J. Stockburger, J. Ankerhold, and P. Joyez. Absence of a Dissipative Quantum Phase Transition in Josephson Junctions. *Phys. Rev. X*, 10:021003, Apr 2020. URL: https://link.aps.org/doi/10.1103/PhysRevX.10.021003, doi:10.1103/PhysRevX.10.021003.

[MBIS+21] A. Murani, N. Bourlet, H. le Sueur, F. Portier, C. Altimiras, D. Esteve, H. Grabert, J. Stockburger, J. Ankerhold, and P. Joyez. Reply to "Comment on 'Absence of a Dissipative Quantum Phase Transition in Josephson Junctions"'. *Phys. Rev. X*, 11:018002, Mar 2021. URL: https://link.aps.org/doi/10.1103/PhysRevX.11.018002, doi:10.1103/PhysRevX.11.018002.

[MBM02] J. B. Majer, J. R. Butcher, and J. E. Mooij. Simple phase bias for superconducting circuits. *Applied Physics Letters*, 80(19):3638–3640, May 2002. URL: http://dx.doi.org/10.1063/1.1478150, doi:10.1063/1.1478150.

[MBP+18] X. Mi, M. Benito, S. Putz, D. M. Zajac, J. M. Taylor, Guido Burkard, and J. R. Petta. A coherent spin–photon interface in silicon. *Nature*, 555(7698):599–603, February 2018. URL: http://dx.doi.org/10.1038/nature25769, doi:10.1038/nature25769.

[McC68] D. E. McCumber. Effect of ac Impedance on dc Voltage-Current Characteristics of Superconductor Weak-Link Junctions. *Journal of Applied Physics*, 39(7):3113–3118, 06 1968. arXiv:https://pubs.aip.org/aip/jap/article-pdf/39/7/3113/18346890/3113_1_online.pdf, doi:10.1063/1.1656743.

[MCG+07] J. Majer, J. M. Chow, J. M. Gambetta, Jens Koch, B. R. Johnson, J. A. Schreier, L. Frunzio, D. I. Schuster, A. A. Houck, A. Wallraff, A. Blais, M. H. Devoret, S. M. Girvin, and R. J. Schoelkopf. Coupling superconducting qubits via a cavity bus. *Nature*, 449(7161):443–447, September 2007. URL: http://dx.doi.org/10.1038/nature06184, doi:10.1038/nature06184.

[MD02] H. Mabuchi and A. C. Doherty. Cavity Quantum Electrodynamics: Coherence in Context. *Science*, 298(5597):1372–1377, 2002. URL: https://www.science.org/doi/abs/10.1126/science.1078446, arXiv:https://www.science.org/doi/pdf/10.1126/science.1078446, doi:10.1126/science.1078446.

[MDC85] John M. Martinis, Michel H. Devoret, and John Clarke. Energy-Level Quantization in the Zero-Voltage State of a Current-Biased Josephson Junction. *Phys. Rev. Lett.*, 55:1543–1546, Oct 1985. URL: https://link.aps.org/doi/10.1103/PhysRevLett.55.1543, doi:10.1103/PhysRevLett.55.1543.

[Mes69] Meservey, R. and Tedrow, P. M. Measurements of the Kinetic Inductance of Superconducting Linear Structures. *Journal of Applied Physics*, 40(5):2028–2034, 04 1969. arXiv:https://pubs.aip.org/aip/jap/article-pdf/40/5/2028/18350463/2028_1_online.pdf, doi:10.1063/1.1657905.

[MFK+14] N. Maleeva, M. V. Fistul, A. Karpov, A. P. Zhuravel, A. Averkin, P. Jung, and A. V. Ustinov. Electrodynamics of a ring-shaped spiral resonator. *Journal of Applied Physics*, 115(6):064910, 02 2014. arXiv:https://pubs.aip.org/aip/jap/article-pdf/doi/10.1063/1.4863835/13380381/064910_1_online.pdf, doi:10.1063/1.4863835.

[MGK+18] N. Maleeva, L. Grünhaupt, T. Klein, F. Levy-Bertrand, O. Dupre, M. Calvo, F. Valenti, P. Winkel, F. Friedrich, W. Wernsdorfer, A. V. Ustinov, H. Rotzinger, A. Monfardini, M. V. Fistul, and I. M. Pop. Circuit quantum electrodynamics of granular aluminum resonators. *Nature Communications*, 9(1), September 2018. URL: http://dx.doi.org/10.1038/s41467-018-06386-9, doi:10.1038/s41467-018-06386-9.

[MGM+18] P. R. Muppalla, O. Gargiulo, S. I. Mirzaei, B. Prasanna Venkatesh, M. L. Juan, L. Grünhaupt, I. M. Pop, and G. Kirchmair. Bistability in a mesoscopic Josephson junction array resonator. *Phys. Rev. B*, 97:024518, Jan 2018. URL: https://link.aps.org/doi/10.1103/PhysRevB.97.024518, doi:10.1103/PhysRevB.97.024518.

[MH70] D. E. McCumber and B. I. Halperin. Time Scale of Intrinsic Resistive Fluctuations in Thin Superconducting Wires. *Phys. Rev. B*, 1:1054–1070, Feb 1970. URL: https://link.aps.org/doi/10.1103/PhysRevB.1.1054, doi:10.1103/PhysRevB.1.1054.

[MH05] J E Mooij and C J P M Harmans. Phase-slip flux qubits. *New Journal of Physics*, 7:219–219, October 2005. URL: http://dx.doi.org/10.1088/1367-2630/7/1/219, doi:10.1088/1367-2630/7/1/219.

[MKF+18] Mohammad Mirhosseini, Eunjong Kim, Vinicius S. Ferreira, Mahmoud Kalaee, Alp Sipahigil, Andrew J. Keller, and Oskar Painter. Superconducting metamaterials for waveguide quantum electrodynamics. *Nature Communications*, 9(1), September 2018. URL: http://dx.doi.org/10.1038/s41467-018-06142-z, doi:10.1038/s41467-018-06142-z.

[MKGD09] Vladimir E. Manucharyan, Jens Koch, Leonid I. Glazman, and Michel H. Devoret. Fluxonium: Single Cooper-Pair Circuit Free of Charge Offsets. *Science*, 326(5949):113–116, October 2009. URL: http://dx.doi.org/10.1126/science.1175552, doi:10.1126/science.1175552.

[MKM+25] Mihirangi Medahinne, Yadav P. Kandel, Suraj Thapa Magar, Elizabeth Champion, John M. Nichol, and Machiel S. Blok. Magnetic-field-tolerant superconducting spiral resonators for circuit quantum electrodynamics. *Phys. Rev. Appl.*, 23:014070, Jan 2025. URL: https://link.aps.org/doi/10.1103/PhysRevApplied.23.014070, doi:10.1103/PhysRevApplied.23.014070.

[ML65] Daniel C. Mattis and Elliott H. Lieb. Exact Solution of a Many-Fermion System and Its Associated Boson Field. *Journal of Mathematical Physics*, 6(2):304–312, 02 1965. arXiv:https://pubs.aip.org/aip/jmp/article-pdf/6/2/304/19083264/304_1_online.pdf, doi:10.1063/1.1704281.

[MLC+24] Raymond A. Mencia, Wei-Ju Lin, Hyunheung Cho, Maxim G. Vavilov, and Vladimir E. Manucharyan. Integer Fluxonium Qubit. *PRX Quantum*, 5:040318, Nov 2024. URL: https://link.aps.org/doi/10.1103/PRXQuantum.5.040318, doi:10.1103/PRXQuantum.5.040318.

[MLG02] K. A. Matveev, A. I. Larkin, and L. I. Glazman. Persistent Current in Superconducting Nanorings. *Phys. Rev. Lett.*, 89:096802, Aug 2002. URL: https://link.aps.org/doi/10.1103/PhysRevLett.89.096802, doi:10.1103/PhysRevLett.89.096802.

[MN06] J. E. Mooij and Yu. V. Nazarov. Superconducting nanowires as quantum phase-slip junctions. *Nature Physics*, 2(3):169–172, February 2006. URL: http://dx.doi.org/10.1038/nphys234, doi:10.1038/nphys234.

[MNAU02] John M. Martinis, S. Nam, J. Aumentado, and C. Urbina. Rabi Oscillations in a Large Josephson-Junction Qubit. *Phys. Rev. Lett.*, 89:117901, Aug 2002. URL: https://link.aps.org/doi/10.1103/PhysRevLett.89.117901, doi:10.1103/PhysRevLett.89.117901.

[MNB+12] A. Megrant, C. Neill, R. Barends, B. Chiaro, Yu Chen, L. Feigl, J. Kelly, Erik Lucero, Matteo Mariantoni, P. J. J. O'Malley, D. Sank, A. Vainsencher, J. Wenner, T. C. White, Y. Yin, J. Zhao, C. J. PalmstrÃ¸m, John M. Martinis, and A. N. Cleland. Planar superconducting resonators with internal quality factors above one million. *Applied Physics Letters*, 100(11):113510, 03 2012. arXiv:https://pubs.aip.org/aip/apl/article-pdf/doi/10.1063/1.3693409/13262211/113510_1_online.pdf, doi:10.1063/1.3693409.

[MO33] W. Meissner and R. Ochsenfeld. Ein neuer Effekt bei Eintritt der Supraleitfähigkeit. *Die Naturwissenschaften*, 21(44):787–788, November

1933. URL: http://dx.doi.org/10.1007/BF01504252, doi:10.1007/bf01504252.

[Moh99] Mohan, S.S. and del Mar Hershenson, M. and Boyd, S.P. and Lee, T.H. Simple accurate expressions for planar spiral inductances. *IEEE Journal of Solid-State Circuits*, 34(10):1419–1424, 1999. doi:10.1109/4.792620.

[MOH+15] C. Macklin, K. O'Brien, D. Hover, M. E. Schwartz, V. Bolkhovsky, X. Zhang, W. D. Oliver, and I. Siddiqi. A near–quantum-limited Josephson traveling-wave parametric amplifier. *Science*, 350(6258):307–310, October 2015. URL: http://dx.doi.org/10.1126/science.aaa8525, doi:10.1126/science.aaa8525.

[MOL+99] J. E. Mooij, T. P. Orlando, L. Levitov, Lin Tian, Caspar H. van der Wal, and Seth Lloyd. Josephson Persistent-Current Qubit. *Science*, 285(5430):1036–1039, August 1999. URL: http://dx.doi.org/10.1126/science.285.5430.1036, doi:10.1126/science.285.5430.1036.

[MPK+12] Nicholas A. Masluk, Ioan M. Pop, Archana Kamal, Zlatko K. Minev, and Michel H. Devoret. Microwave Characterization of Josephson Junction Arrays: Implementing a Low Loss Superinductance. *Phys. Rev. Lett.*, 109:137002, Sep 2012. URL: https://link.aps.org/doi/10.1103/PhysRevLett.109.137002, doi:10.1103/PhysRevLett.109.137002.

[MPP+22] G. C. Ménard, A. Peugeot, C. Padurariu, C. Rolland, B. Kubala, Y. Mukharsky, Z. Iftikhar, C. Altimiras, P. Roche, H. le Sueur, P. Joyez, D. Vion, D. Esteve, J. Ankerhold, and F. Portier. Emission of Photon Multiplets by a dc-Biased Superconducting Circuit. *Phys. Rev. X*, 12:021006, Apr 2022. URL: https://link.aps.org/doi/10.1103/PhysRevX.12.021006, doi:10.1103/PhysRevX.12.021006.

[MSOA22] Kanta Masuki, Hiroyuki Sudo, Masaki Oshikawa, and Yuto Ashida. Absence versus Presence of Dissipative Quantum Phase Transition in Josephson Junctions. *Phys. Rev. Lett.*, 129:087001, Aug 2022. URL: https://link.aps.org/doi/10.1103/PhysRevLett.129.087001, doi:10.1103/PhysRevLett.129.087001.

[MSOA23] Kanta Masuki, Hiroyuki Sudo, Masaki Oshikawa, and Yuto Ashida. Masuki et al. Reply:. *Phys. Rev. Lett.*, 131:199702, Nov 2023. URL: https://link.aps.org/doi/10.1103/PhysRevLett.131.199702, doi:10.1103/PhysRevLett.131.199702.

[MSSM+23] S. Mukhopadhyay, J. Senior, J. Saez-Mollejo, D. Puglia, M. Zemlicka, J. M. Fink, and A. P. Higginbotham. Superconductivity from a melted insulator in Josephson junction arrays. *Nature Physics*, 19(11):1630–1635, August 2023. URL: http://dx.doi.org/10.1038/s41567-023-02161-w, doi:10.1038/s41567-023-02161-w.

[Mur21] Conal E. Murray. Material matters in superconducting qubits. *Materials Science and Engineering: R: Reports*, 146:100646, 2021. URL: https:

//www.sciencedirect.com/science/article/pii/S092779X21000413, doi:10.1016/j.mser.2021.100646.

[MVS+13] F. Marsili, V. B. Verma, J. A. Stern, S. Harrington, A. E. Lita, T. Gerrits, I. Vayshenker, B. Baek, M. D. Shaw, R. P. Mirin, and S. W. Nam. Detecting single infrared photons with 93 *Nature Photonics*, 7(3):210–214, February 2013. URL: http://dx.doi.org/10.1038/nphoton.2013.13, doi:10.1038/nphoton.2013.13.

[MVV+22] Timm Fabian Mörstedt, Arto Viitanen, Vasilii Vadimov, Vasilii Sevriuk, Matti Partanen, Eric Hyyppä, Gianluigi Catelani, Matti Silveri, Kuan Yen Tan, and Mikko Möttönen. Recent Developments in Quantum-Circuit Refrigeration. *Annalen der Physik*, 534(7), May 2022. URL: http://dx.doi.org/10.1002/andp.202100543, doi:10.1002/andp.202100543.

[MY20] Ari Mizel and Yariv Yanay. Right-sizing fluxonium against charge noise. *Phys. Rev. B*, 102:014512, Jul 2020. URL: https://link.aps.org/doi/10.1103/PhysRevB.102.014512, doi:10.1103/PhysRevB.102.014512.

[NB17] D. V. Nguyen and D. M. Basko. Inhomogeneous Josephson junction chains: a superconducting meta-material for superinductance optimization. *The European Physical Journal Special Topics*, 226(7):1499–1514, May 2017. URL: http://dx.doi.org/10.1140/epjst/e2016-60278-4, doi:10.1140/epjst/e2016-60278-4.

[NCT97] Y. Nakamura, C. D. Chen, and J. S. Tsai. Spectroscopy of Energy-Level Splitting between Two Macroscopic Quantum States of Charge Coherently Superposed by Josephson Coupling. *Phys. Rev. Lett.*, 79:2328–2331, Sep 1997. URL: https://link.aps.org/doi/10.1103/PhysRevLett.79.2328, doi:10.1103/PhysRevLett.79.2328.

[NPT99] Y. Nakamura, Yu. A. Pashkin, and J. S. Tsai. Coherent control of macroscopic quantum states in a single-Cooper-pair box. *Nature*, 398(6730):786–788, April 1999. URL: http://dx.doi.org/10.1038/19718, doi:10.1038/19718.

[NPV+12] Simon E. Nigg, Hanhee Paik, Brian Vlastakis, Gerhard Kirchmair, S. Shankar, Luigi Frunzio, M. H. Devoret, R. J. Schoelkopf, and S. M. Girvin. Black-Box Superconducting Circuit Quantization. *Phys. Rev. Lett.*, 108:240502, Jun 2012. URL: https://link.aps.org/doi/10.1103/PhysRevLett.108.240502, doi:10.1103/PhysRevLett.108.240502.

[OMT+99] T. P. Orlando, J. E. Mooij, Lin Tian, Caspar H. van der Wal, L. S. Levitov, Seth Lloyd, and J. J. Mazo. Superconducting persistent-current qubit. *Phys. Rev. B*, 60:15398–15413, Dec 1999. URL: https://link.aps.org/doi/10.1103/PhysRevB.60.15398, doi:10.1103/PhysRevB.60.15398.

[Onn11] H. K. Onnes. The Superconductivity of Mercury. *Communications from the Physical Laboratory of the University of Leiden*, (122-124), 1911.

[PCvHK25] Cheeranjeev Purmessur, Kaicheung Chow, Bernard van Heck, and Angela Kou. Operation of a high-frequency, phase-slip qubit. 2 2025. arXiv:2502.07043.

[Per21] Matilda Peruzzo. *Geometric superinductors and their applications in circuit quantum electrodynamics*. PhD thesis, 2021. URL: https://research-explorer.app.ist.ac.at/record/9920, doi:10.15479/AT:ISTA:9920.

[PHS+21] M. Peruzzo, F. Hassani, G. Szep, A. Trioni, E. Redchenko, M. Zemlicka, and J. M. Fink. Geometric Superinductance Qubits: Controlling Phase Delocalization across a Single Josephson Junction. *PRX Quantum*, 2:040341, Nov 2021. URL: https://link.aps.org/doi/10.1103/PRXQuantum.2.040341, doi:10.1103/PRXQuantum.2.040341.

[PMN+20] Ivan V. Pechenezhskiy, Raymond A. Mencia, Long B. Nguyen, Yen-Hsiang Lin, and Vladimir E. Manucharyan. The superconducting quasicharge qubit. *Nature*, 585(7825):368–371, September 2020. URL: http://dx.doi.org/10.1038/s41586-020-2687-9, doi:10.1038/s41586-020-2687-9.

[Pop11] Ioan Mihai Pop. *Sauts quantiques de phase dans des chaînes de jonctions Josephson*. Theses, Université de Grenoble, February 2011. URL: https://theses.hal.science/tel-00586075.

[Poz12] David M. Pozar. *Microwave Engineering*. Wiley, Hoboken, NJ, 4th edition, 2012.

[PPH+99] J. S. Penttilä, Ü. Parts, P. J. Hakonen, M. A. Paalanen, and E. B. Sonin. "Superconductor-Insulator Transition" in a Single Josephson Junction. *Phys. Rev. Lett.*, 82:1004–1007, Feb 1999. URL: https://link.aps.org/doi/10.1103/PhysRevLett.82.1004, doi:10.1103/PhysRevLett.82.1004.

[PRE25] A. Parra-Rodriguez and I. L. Egusquiza. Exact Quantization of Nonreciprocal Quasilumped Electrical Networks. *Phys. Rev. X*, 15:011072, Mar 2025. URL: https://link.aps.org/doi/10.1103/PhysRevX.15.011072, doi:10.1103/PhysRevX.15.011072.

[Pro15] Sebastian Probst. resonator_tools: A Python library to fit complex resonator scattering data. https://github.com/sebastianprobst/resonator_tools, 2015.

[PTH+20] M. Peruzzo*, A. Trioni*, F. Hassani, M. Zemlicka, and J. M. Fink. Surpassing the Resistance Quantum with a Geometric Superinductor. *Phys. Rev. Appl.*, 14:044055, Oct 2020. URL: https://link.aps.org/doi/10.1103/PhysRevApplied.14.044055, doi:10.1103/PhysRevApplied.14.044055.

[RDD+06] P. Rabl, D. DeMille, J. M. Doyle, M. D. Lukin, R. J. Schoelkopf, and P. Zoller. Hybrid Quantum Processors: Molecular Ensembles as Quantum Memory for Solid State Circuits. *Phys. Rev. Lett.*, 97:033003, Jul 2006. URL: https:

//link.aps.org/doi/10.1103/PhysRevLett.97.033003, doi:10.1103/PhysRevLett.97.033003.

[Red22] Elena Redchenko. *Controllable states of superconducting Qubit ensembles*. PhD thesis, 2022. URL: https://research-explorer.app.ist.ac.at/record/12366, doi:10.15479/AT:ISTA:12132.

[Reg23] Ulysse Reglade. abcd_rf_fit: A Python library for optimal resonator fit. https://github.com/UlysseREGLADE/abcd_rf_fit, 2023.

[RGS+23] D. Rieger, S. Günzler, M. Spiecker, A. Nambisan, W. Wernsdorfer, and I.M. Pop. Fano Interference in Microwave Resonator Measurements. *Phys. Rev. Appl.*, 20:014059, Jul 2023. URL: https://link.aps.org/doi/10.1103/PhysRevApplied.20.014059, doi:10.1103/PhysRevApplied.20.014059.

[RHDP+24] Mallika T. Randeria, Thomas M. Hazard, Agustin Di Paolo, Kate Azar, Max Hays, Leon Ding, Junyoung An, Michael Gingras, Bethany M. Niedzielski, Hannah Stickler, Jeffrey A. Grover, Jonilyn L. Yoder, Mollie E. Schwartz, William D. Oliver, and Kyle Serniak. Dephasing in Fluxonium Qubits from Coherent Quantum Phase Slips. *PRX Quantum*, 5:030341, Aug 2024. URL: https://link.aps.org/doi/10.1103/PRXQuantum.5.030341, doi:10.1103/PRXQuantum.5.030341.

[Ros08] E. B. Rosa. The self and mutual-inductances of linear conductors. *Bulletin of the Bureau of Standards*, 4(2):301, January 1908. URL: http://dx.doi.org/10.6028/bulletin.088, doi:10.6028/bulletin.088.

[RPA+16] Matthew Reagor, Wolfgang Pfaff, Christopher Axline, Reinier W. Heeres, Nissim Ofek, Katrina Sliwa, Eric Holland, Chen Wang, Jacob Blumoff, Kevin Chou, Michael J. Hatridge, Luigi Frunzio, Michel H. Devoret, Liang Jiang, and Robert J. Schoelkopf. Quantum memory with millisecond coherence in circuit QED. *Phys. Rev. B*, 94:014506, Jul 2016. URL: https://link.aps.org/doi/10.1103/PhysRevB.94.014506, doi:10.1103/PhysRevB.94.014506.

[SAK+24] Rais S. Shaikhaidarov, Ilya Antonov, Kyung Ho Kim, Artem Shesterikov, Sven Linzen, Evgeni V. Il'ichev, Vladimir N Antonov, and Oleg V Astafiev. Feasibility of the Josephson voltage and current standards on a single chip. *Applied Physics Letters*, 125(12):122602, 09 2024. arXiv:https://pubs.aip.org/aip/apl/article-pdf/doi/10.1063/5.0221404/20163382/122602_1_5.0221404.pdf, doi:10.1063/5.0221404.

[SBS+16] N. Samkharadze, A. Bruno, P. Scarlino, G. Zheng, D. P. DiVincenzo, L. DiCarlo, and L. M. K. Vandersypen. High-Kinetic-Inductance Superconducting Nanowire Resonators for Circuit QED in a Magnetic Field. *Phys. Rev. Appl.*, 5:044004, Apr 2016. URL: https://link.aps.org/doi/10.1103/PhysRevApplied.5.044004, doi:10.1103/PhysRevApplied.5.044004.

[Sch26] E. Schrödinger. Quantisierung als Eigenwertproblem. *Annalen der Physik*, 384(4):361–376, January 1926. URL: http://dx.doi.org/10.1002/andp.19263840404, doi:10.1002/andp.19263840404.

[Sch83] Albert Schmid. Diffusion and Localization in a Dissipative Quantum System. *Phys. Rev. Lett.*, 51:1506–1509, Oct 1983. URL: https://link.aps.org/doi/10.1103/PhysRevLett.51.1506, doi:10.1103/PhysRevLett.51.1506.

[Sch07] David Isaac Schuster. *Circuit Quantum Electrodynamics*. PhD thesis, Yale University, 2007. URL: https://rsl.yale.edu/sites/default/files/2024-08/2007-RSL-Thesis-David-Schuster.pdf.

[SFD+10] D. I. Schuster, A. Fragner, M. I. Dykman, S. A. Lyon, and R. J. Schoelkopf. Proposal for Manipulating and Detecting Spin and Orbital States of Trapped Electrons on Helium Using Cavity Quantum Electrodynamics. *Phys. Rev. Lett.*, 105:040503, Jul 2010. URL: https://link.aps.org/doi/10.1103/PhysRevLett.105.040503, doi:10.1103/PhysRevLett.105.040503.

[SFS23] Théo Sépulcre, Serge Florens, and Izak Snyman. Comment on "Absence versus Presence of Dissipative Quantum Phase Transition in Josephson Junctions". *Phys. Rev. Lett.*, 131:199701, Nov 2023. URL: https://link.aps.org/doi/10.1103/PhysRevLett.131.199701, doi:10.1103/PhysRevLett.131.199701.

[SGJ+13] M J Schwarz, J Goetz, Z Jiang, T Niemczyk, F Deppe, A Marx, and R Gross. Gradiometric flux qubits with a tunable gap. *New Journal of Physics*, 15(4):045001, April 2013. URL: http://dx.doi.org/10.1088/1367-2630/15/4/045001, doi:10.1088/1367-2630/15/4/045001.

[Sha63] Sidney Shapiro. Josephson Currents in Superconducting Tunneling: The Effect of Microwaves and Other Observations. *Phys. Rev. Lett.*, 11:80–82, Jul 1963. URL: https://link.aps.org/doi/10.1103/PhysRevLett.11.80, doi:10.1103/PhysRevLett.11.80.

[She66] Thomas P. Sheahen. Rules for the Energy Gap and Critical Field of Superconductors. *Phys. Rev.*, 149:368–370, Sep 1966. URL: https://link.aps.org/doi/10.1103/PhysRev.149.368, doi:10.1103/PhysRev.149.368.

[SHR+22] Rishabh Sahu, William Hease, Alfredo Rueda, Georg Arnold, Liu Qiu, and Johannes M. Fink. Quantum-enabled operation of a microwave-optical interface. *Nature Communications*, 13(1), March 2022. URL: http://dx.doi.org/10.1038/s41467-022-28924-2, doi:10.1038/s41467-022-28924-2.

[SHS+07] D. I. Schuster, A. A. Houck, J. A. Schreier, A. Wallraff, J. M. Gambetta, A. Blais, L. Frunzio, J. Majer, B. Johnson, M. H. Devoret, S. M. Girvin, and R. J. Schoelkopf. Resolving photon number states in a superconducting circuit. *Nature*, 445(7127):515–518, February 2007. URL: http://dx.doi.org/10.1038/nature05461, doi:10.1038/nature05461.

[SJC+01] A. Steinbach, P. Joyez, A. Cottet, D. Esteve, M. H. Devoret, M. E. Huber, and John M. Martinis. Direct Measurement of the Josephson Supercurrent in an Ultrasmall Josephson Junction. *Phys. Rev. Lett.*, 87:137003, Sep 2001. URL: https://link.aps.org/doi/10.1103/PhysRevLett.87.137003, doi:10.1103/PhysRevLett.87.137003.

[SKD+22] Rais S. Shaikhaidarov, Kyung Ho Kim, Jacob W. Dunstan, Ilya V. Antonov, Sven Linzen, Mario Ziegler, Dmitry S. Golubev, Vladimir N. Antonov, Evgeni V. Il'ichev, and Oleg V. Astafiev. Quantized current steps due to the a.c. coherent quantum phase-slip effect. *Nature*, 608(7921):45–49, July 2022. URL: http://dx.doi.org/10.1038/s41586-022-04947-z, doi:10.1038/s41586-022-04947-z.

[SKD+24] Rais S. Shaikhaidarov, Kyung Ho Kim, Jacob Dunstan, Ilya Antonov, Dmitry Golubev, Vladimir N. Antonov, and Oleg V. Astafiev. Quantized current steps due to the synchronization of microwaves with Bloch oscillations in small Josephson junctions. *Nature Communications*, 15(1), October 2024. URL: http://dx.doi.org/10.1038/s41467-024-53600-y, doi:10.1038/s41467-024-53600-y.

[SKE+21] S. Shu, N. Klimovich, B. H. Eom, A. D. Beyer, R. Basu Thakur, H. G. Leduc, and P. K. Day. Nonlinearity and wide-band parametric amplification in a (Nb,Ti)N microstrip transmission line. *Phys. Rev. Res.*, 3:023184, Jun 2021. URL: https://link.aps.org/doi/10.1103/PhysRevResearch.3.023184, doi:10.1103/PhysRevResearch.3.023184.

[SKX+20] W. C. Smith, A. Kou, X. Xiao, U. Vool, and M. H. Devoret. Superconducting circuit protected by two-Cooper-pair tunneling. *npj Quantum Information*, 6(1), January 2020. URL: http://dx.doi.org/10.1038/s41534-019-0231-2, doi:10.1038/s41534-019-0231-2.

[Som21] Arnold Sommerfeld. *Atombau und Spektrallinien*. Friedr. Vieweg & Sohn, Braunschweig, 2 edition, 1921. URL: https://archive.org/details/atombauundspekt00sommgoog/page/240/mode/2up?ref=ol&view=theater.

[SPG+25] Yogesh Kumar Srivastava, Teng Chen Ietro Pang, Manoj Gupta, Manukumara Manjappa, Piyush Agarwal, Jérôme Lesueur, and Ranjan Singh. YBa2Cu3O7 as a high-temperature superinductor. *Nature Materials*, 24(6):883–890, February 2025. URL: http://dx.doi.org/10.1038/s41563-024-02107-4, doi:10.1038/s41563-024-02107-4.

[SRCR25] Shraddha Singh, Gil Refael, Aashish Clerk, and Emma Rosenfeld. Impact of Josephson junction array modes on fluxonium readout, 2025. URL: https://arxiv.org/abs/2412.14788, arXiv:2412.14788.

[SSK+17] A. Stockklauser, P. Scarlino, J. V. Koski, S. Gasparinetti, C. K. Andersen, C. Reichl, W. Wegscheider, T. Ihn, K. Ensslin, and A. Wallraff. Strong Coupling Cavity QED with Gate-Defined Double Quantum Dots Enabled by a High Impedance Resonator. *Phys. Rev. X*, 7:011030, Mar 2017. URL: https://link.aps.org/doi/10.1103/PhysRevX.7.011030, doi:10.1103/PhysRevX.7.011030.

[SSL+25] L.-A. Sellem, A. Sarlette, Z. Leghtas, M. Mirrahimi, P. Rouchon, and P. Campagne-Ibarcq. Dissipative Protection of a GKP Qubit in a High-Impedance Superconducting Circuit Driven by a Microwave Frequency Comb. *Physical Review X*, 15(1), January 2025. URL: http://dx.doi.org/10.1103/PhysRevX.15.011011, doi:10.1103/physrevx.15.011011.

[Ste68] W. C. Stewart. CURRENT-VOLTAGE CHARACTERISTICS OF JOSEPHSON JUNCTIONS. *Applied Physics Letters*, 12(8):277–280, 04 1968. arXiv:https://pubs.aip.org/aip/apl/article-pdf/12/8/277/18421008/277_1_online.pdf, doi:10.1063/1.1651991.

[SVM+22] W. C. Smith, M. Villiers, A. Marquet, J. Palomo, M. R. Delbecq, T. Kontos, P. Campagne-Ibarcq, B. Douçot, and Z. Leghtas. Magnifying Quantum Phase Fluctuations with Cooper-Pair Pairing. *Phys. Rev. X*, 12:021002, Apr 2022. URL: https://link.aps.org/doi/10.1103/PhysRevX.12.021002, doi:10.1103/PhysRevX.12.021002.

[SWB+05] D. I. Schuster, A. Wallraff, A. Blais, L. Frunzio, R.-S. Huang, J. Majer, S. M. Girvin, and R. J. Schoelkopf. ac Stark Shift and Dephasing of a Superconducting Qubit Strongly Coupled to a Cavity Field. *Phys. Rev. Lett.*, 94:123602, Mar 2005. URL: https://link.aps.org/doi/10.1103/PhysRevLett.94.123602, doi:10.1103/PhysRevLett.94.123602.

[TCCGdPM+25] Alba Torras-Coloma, Luca Cozzolino, Ariadna Gómez-del Pulgar-Martínez, Elia Bertoldo, and P. Forn-Díaz. Superinductor-based ultrastrong coupling in a superconducting circuit. 7 2025. arXiv:2507.09339.

[Tin04] M. Tinkham. *Introduction to Superconductivity*. Dover Books on Physics Series. Dover Publications, 2004. URL: https://books.google.at/books?id=VpUk3NfwDIkC.

[Tom50] Sin-itiro Tomonaga. Remarks on Bloch's Method of Sound Waves applied to Many-Fermion Problems. *Progress of Theoretical Physics*, 5(4):544–569, 07 1950. arXiv:https://academic.oup.com/ptp/article-pdf/5/4/544/5430161/5-4-544.pdf, doi:10.1143/ptp/5.4.544.

[TSH+25] Yusuke Tominaga, Shotaro Shirai, Yuji Hishida, Hirotaka Terai, and Atsushi Noguchi. Intrinsic quality factors approaching 10 million in superconducting planar resonators enabled by spiral geometry. *EPJ Quant. Technol.*, 12(1):60, 2025. arXiv:2502.17901, doi:10.1140/epjqt/s40507-025-00367-w.

[VAC+02] D. Vion, A. Aassime, A. Cottet, P. Joyez, H. Pothier, C. Urbina, D. Esteve, and M. H. Devoret. Manipulating the Quantum State of an Electrical Circuit. *Science*, 296(5569):886–889, May 2002. URL: http://dx.doi.org/10.1126/science.1069372, doi:10.1126/science.1069372.

[VC15] Giovanni Viola and Gianluigi Catelani. Collective modes in the fluxonium qubit. *Phys. Rev. B*, 92:224511, Dec 2015. URL: https://link.aps.org/doi/10.1103/PhysRevB.92.224511, doi:10.1103/PhysRevB.92.224511.

[VD17] Uri Vool and Michel Devoret. Introduction to quantum electromagnetic circuits. *International Journal of Circuit Theory and Applications*, 45(7):897–934, June 2017. URL: http://dx.doi.org/10.1002/cta.2359, doi:10.1002/cta.2359.

[VDCK15] J. J. Viennot, M. C. Dartiailh, A. Cottet, and T. Kontos. Coherent coupling of a single spin to microwave cavity photons. *Science*, 349(6246):408–411, July 2015. URL: http://dx.doi.org/10.1126/science.aaa3786, doi:10.1126/science.aaa3786.

[VEK+16] M. R. Vissers, R. P. Erickson, H.-S. Ku, Leila Vale, Xian Wu, G. C. Hilton, and D. P. Pappas. Low-noise kinetic inductance traveling-wave amplifier using three-wave mixing. *Applied Physics Letters*, 108(1):012601, 01 2016. arXiv:https://pubs.aip.org/aip/apl/article-pdf/doi/10.1063/1.4937922/12854602/012601_1_online.pdf, doi:10.1063/1.4937922.

[VMT+24] Arto Viitanen, Timm Mörstedt, Wallace S. Teixeira, Maaria Tiiri, Jukka Räbinä, Matti Silveri, and Mikko Möttönen. Quantum-circuit refrigeration of a superconducting microwave resonator well below a single quantum. *Phys. Rev. Res.*, 6:023262, Jun 2024. URL: https://link.aps.org/doi/10.1103/PhysRevResearch.6.023262, doi:10.1103/PhysRevResearch.6.023262.

[VSJ+21] Arto Viitanen, Matti Silveri, Máté Jenei, Vasilii Sevriuk, Kuan Y. Tan, Matti Partanen, Jan Goetz, Leif Grönberg, Vasilii Vadimov, Valtteri Lahtinen, and Mikko Möttönen. Photon-number-dependent effective Lamb shift. *Phys. Rev. Res.*, 3:033126, Aug 2021. URL: https://link.aps.org/doi/10.1103/PhysRevResearch.3.033126, doi:10.1103/PhysRevResearch.3.033126.

[VSR+15] Nicolas Vogt, Roland Schäfer, Hannes Rotzinger, Wanyin Cui, Andreas Fiebig, Alexander Shnirman, and Alexey V. Ustinov. One-dimensional Josephson junction arrays: Lifting the Coulomb blockade by depinning. *Phys. Rev. B*, 92:045435, Jul 2015. URL: https://link.aps.org/doi/10.1103/PhysRevB.92.045435, doi:10.1103/PhysRevB.92.045435.

[VW81] Richard F. Voss and Richard A. Webb. Macroscopic Quantum Tunneling in 1-μm Nb Josephson Junctions. *Phys. Rev. Lett.*, 47:265–268, Jul 1981. URL: https://link.aps.org/doi/10.1103/PhysRevLett.47.265, doi:10.1103/PhysRevLett.47.265.

[Wei14] Thomas Weissl. *Quantum phase and charge in Josephson junction chains*. Theses, Université de Grenoble, October 2014. URL: https://theses.hal.science/tel-01369020.

[Wes20] Johannes Wesseler. Tunable Superinductance from Parallel Josephson Junction Arrays. Master's thesis, Friedrich-Alexander-Universität Erlangen-Nürnberg, 2020. Supervisor: Michael J. Hartmann, private communication.

[WH03] Michio Watanabe and David B. Haviland. Quantum effects in small-capacitance single Josephson junctions. *Phys. Rev. B*, 67:094505, Mar 2003. URL: https://link.aps.org/doi/10.1103/PhysRevB.67.094505, doi:10.1103/PhysRevB.67.094505.

[Wil19] Samuel A. Wilkinson. *Quasicharge models of Josephson junction arrays*. PhD thesis, RMIT University, January 2019. URL: https://core.ac.uk/download/pdf/200210184.pdf.

[WKD+15] T. Weißl, B. Küng, E. Dumur, A. K. Feofanov, I. Matei, C. Naud, O. Buisson, F. W. J. Hekking, and W. Guichard. Kerr coefficients of plasma resonances in Josephson junction chains. *Phys. Rev. B*, 92:104508, Sep 2015. URL: https://link.aps.org/doi/10.1103/PhysRevB.92.104508, doi:10.1103/PhysRevB.92.104508.

[WMRG14] D. S. Wisbey, A. Martin, A. Reinisch, and J. Gao. New Method for Determining the Quality Factor and Resonance Frequency of Superconducting Micro-Resonators from Sonnet Simulations. *Journal of Low Temperature Physics*, 176(3–4):538–544, May 2014. URL: http://dx.doi.org/10.1007/s10909-014-1099-3, doi:10.1007/s10909-014-1099-3.

[WO19] Joel I-Jan Wang and William D. Oliver. An aluminium superinductor. *Nature Materials*, 18(8):775–776, July 2019. URL: http://dx.doi.org/10.1038/s41563-019-0401-9, doi:10.1038/s41563-019-0401-9.

[WS19] Huan-Kuang Wu and Jay D. Sau. Theory of coherent phase modes in insulating Josephson junction chains. *Phys. Rev. B*, 99:214509, Jun 2019. URL: https://link.aps.org/doi/10.1103/PhysRevB.99.214509, doi:10.1103/PhysRevB.99.214509.

[WSB+04] A. Wallraff, D. I. Schuster, A. Blais, L. Frunzio, R.-S. Huang, J. Majer, S. Kumar, S. M. Girvin, and R. J. Schoelkopf. Strong coupling of a single photon to a superconducting qubit using circuit quantum electrodynamics. *Nature*, 431(7005):162–167, September 2004. URL: http://dx.doi.org/10.1038/nature02851, doi:10.1038/nature02851.

[XAYN13] Ze-Liang Xiang, Sahel Ashhab, J. Q. You, and Franco Nori. Hybrid quantum circuits: Superconducting circuits interacting with other quantum systems. *Rev. Mod. Phys.*, 85:623–653, Apr 2013. URL: https://link.aps.org/doi/10.1103/RevModPhys.85.623, doi:10.1103/RevModPhys.85.623.

[XHF+19] Mingrui Xu, Xu Han, Wei Fu, Chang-Ling Zou, and Hong X. Tang. Frequency-tunable high-Q superconducting resonators via wireless control of nonlinear kinetic inductance. *Applied Physics Letters*, 114(19):192601, 05 2019. arXiv:https://pubs.aip.org/aip/apl/article-pdf/doi/10.1063/1.5098466/13624960/192601_1_online.pdf, doi:10.1063/1.5098466.

[YGH21] Tsuyoshi Yamamoto, Leonid I. Glazman, and Manuel Houzet. Transmission of waves through a pinned elastic medium. *Phys. Rev. B*, 103:224211, Jun 2021. URL: https://link.aps.org/doi/10.1103/PhysRevB.103.224211, doi:10.1103/PhysRevB.103.224211.

[YGK+16] Fei Yan, Simon Gustavsson, Archana Kamal, Jeffrey Birenbaum, Adam P Sears, David Hover, Ted J. Gudmundsen, Danna Rosenberg, Gabriel Samach, S Weber, Jonilyn L. Yoder, Terry P. Orlando, John Clarke, Andrew J. Kerman, and William D. Oliver. The flux qubit revisited to enhance coherence and reproducibility. *Nature Communications*, 7(1), November 2016. URL: http://dx.doi.org/10.1038/ncomms12964, doi:10.1038/ncomms12964.

[YNHM19] M. Yoneda, M. Niwa, N. Hirata, and M. Motohashi. Duality between coherent quantum phase-slip and the Josephson junction in nanowires by dual Hamiltonian method. *International Journal of Modern Physics B*, 33(25):1950291, 2019. arXiv:https://doi.org/10.1142/S0217979219502916, doi:10.1142/S0217979219502916.

[ZBS+18] Alexander P. Zhuravel, Seokjin Bae, Sergey N. Shevchenko, Alexander N. Omelyanchouk, Alexander V. Lukashenko, Alexey V. Ustinov, and Steven M. Anlage. Imaging the paramagnetic nonlinear Meissner effect in nodal gap superconductors. *Phys. Rev. B*, 97:054504, Feb 2018. URL: https://link.aps.org/doi/10.1103/PhysRevB.97.054504, doi:10.1103/PhysRevB.97.054504.

[ZGK+13] Alexander P. Zhuravel, B. G. Ghamsari, C. Kurter, P. Jung, S. Remillard, J. Abrahams, A. V. Lukashenko, Alexey V. Ustinov, and Steven M. Anlage. Imaging the Anisotropic Nonlinear Meissner Effect in Nodal $YBa_2Cu_3O_{7-\delta}$ Thin-Film Superconductors. *Phys. Rev. Lett.*, 110:087002, Feb 2013. URL: https://link.aps.org/doi/10.1103/PhysRevLett.110.087002, doi:10.1103/PhysRevLett.110.087002.

[ZGvOZ97] Andrei D. Zaikin, Dmitrii S. Golubev, Anne van Otterlo, and Gergely T. Zimányi. Quantum Phase Slips and Transport in Ultrathin Superconducting Wires. *Phys. Rev. Lett.*, 78:1552–1555, Feb 1997. URL: https://link.aps.org/doi/10.1103/PhysRevLett.78.1552, doi:10.1103/PhysRevLett.78.1552.

[ZRP+23] M. Zemlicka, E. Redchenko, M. Peruzzo, F. Hassani, A. Trioni, S. Barzanjeh, and J. M. Fink. Compact vacuum-gap transmon qubits: Selective and sensitive probes for superconductor surface losses. *Phys. Rev. Appl.*, 20:044054, Oct 2023. URL: https://link.aps.org/doi/10.1103/PhysRevApplied.20.044054, doi:10.1103/PhysRevApplied.20.044054.

APPENDIX A

Archimedean spiral length

An Archimedean spiral is described in polar coordinates by

$$r(\theta) = a + b\theta, \tag{A.1}$$

where a is the initial radius and b determines the spacing between turns. The infinitesimal arc length is given by

$$ds = \sqrt{\left(\frac{dr}{d\theta}\right)^2 + r(\theta)^2}\, d\theta. \tag{A.2}$$

Since

$$\frac{dr}{d\theta} = b, \tag{A.3}$$

the total length between angles θ_1 and θ_2 is

$$\ell = \int_{\theta_1}^{\theta_2} \sqrt{b^2 + (a + b\theta)^2}\, d\theta. \tag{A.4}$$

The integral

$$\int \sqrt{b^2 + (a + b\theta)^2}\, d\theta \tag{A.5}$$

can be solved analytically to yield

$$\ell = \frac{1}{2b}\left[(a + b\theta)\sqrt{(a + b\theta)^2 + b^2} + b^2 \ln\left(a + b\theta + \sqrt{(a + b\theta)^2 + b^2}\right)\right]_{\theta_1}^{\theta_2}. \tag{A.6}$$

For a spiral with pitch p (distance between successive turns), the radial equation can be written as

$$r(\theta) = R_i + \frac{p}{2\pi}\,\theta, \tag{A.7}$$

where R_i is the inner radius. In this case:

$$a = R_i, \quad b = \frac{p}{2\pi}. \tag{A.8}$$

The angular limits corresponding to the inner and outer radii are

$$\theta_i = \frac{2\pi R_i}{p}, \quad \theta_e = \frac{2\pi R_e}{p}. \tag{A.9}$$

Substituting into the general solution and simplifying gives

$$\ell = \frac{p}{2\pi}\left[\frac{\theta_e}{2}\sqrt{\theta_e^2+1} + \frac{1}{2}\ln\left(\theta_e + \sqrt{\theta_e^2+1}\right) - \frac{\theta_i}{2}\sqrt{\theta_i^2+1} - \frac{1}{2}\ln\left(\theta_i + \sqrt{\theta_i^2+1}\right)\right]. \quad \text{(A.10)}$$

If the spiral is specified by its pitch p, number of turns n, and inner diameter d_i:

$$R_i = \frac{d_i}{2}, \quad R_e = R_i + np, \quad \text{(A.11)}$$

and the angular limits become

$$\theta_i = \frac{\pi d_i}{p}, \quad \theta_e = \frac{\pi d_o}{p}, \quad d_o = d_i + 2np. \quad \text{(A.12)}$$

The length ℓ in this case is obtained from Eq. A.10 with these definitions of θ_i and θ_e.

APPENDIX B

Solution of Eq. 4.17

Mathematica implementation of the numerical root-finding procedure used to solve Eq. 4.17 for the eigenfrequencies of an Archimedean spiral resonator, following Ref. [MAA+15].

Simplified expression of β

$p = \text{pitch} * 10^{-6}$; (*m, distance between two adjacent turns*)
$c = \frac{\text{c0}}{\sqrt{\epsilon\text{eff}}}$; (*m/s, effective speed of light*)
$\text{Ro} = \frac{\text{do}*10^{-6}}{2}$ (*m, external radius of the spiral*)
$\alpha = \frac{p}{2\pi \text{Ro}}$;

$\int_{\sqrt{v}}^{\infty} \text{BesselJ}[1, ux]\, du$

$$\boxed{\frac{\text{BesselJ}\left[0,\sqrt{v}x\right]}{x} \text{ if } \text{Re}[v] > 0 \&\& \text{Im}[v] == 0 \&\& \text{Re}[x] > 0 \&\& \text{Im}[x] == 0}$$

$\int_0^{\infty} \frac{\text{BesselJ}\left[0,\sqrt{v}x\right]}{x} \text{BesselJ}[1, x] dx$

$$\boxed{\frac{2v\text{EllipticE}\left[\frac{1}{v}\right] - 2(-1+v)\text{EllipticK}\left[\frac{1}{v}\right]}{\pi\sqrt{v}} \text{ if } \text{Re}[v] > 1 \&\& \text{Im}[v] == 0}$$

$\int_0^{\infty} \text{BesselJ}\left[1, \sqrt{v}x\right] \text{BesselJ}[1, x] dx$

$$\boxed{\frac{2(-\text{EllipticE}[v] + \text{EllipticK}[v])}{\pi\sqrt{v}} \text{ if } 0 < \text{Re}[v] < 1 \&\& \text{Im}[v] == 0}$$

$\text{g1}[\text{v\_}] := \text{Ro}\sqrt{v}\frac{2\left(v\text{EllipticE}\left[\frac{1}{v}\right] - (-1+v)\text{EllipticK}\left[\frac{1}{v}\right]\right)}{\pi\sqrt{v}}$;
$\text{K0}[\text{v\_}] := \text{Ro}v\frac{2(-\text{EllipticE}[v] + \text{EllipticK}[v])}{\pi\sqrt{v}}$;
$\beta[\text{n\_}] := \text{NIntegrate}\left[\frac{\text{K0}[v]}{\text{g1}[v]} v^{-2} \text{Sin}[\pi n v], \{v, 0, 1\}\right]$;

Initial Value

xmin=0.000001; xmax=1; step=0.02;
$\text{S}[\text{a\_}] := \text{Sum}\left[\frac{(-1)^m m\beta[m]}{-m^2+a}, \{m, 1, 10\}\right] - \pi$;
$\text{Sdiscrete} = \text{Table}[S[i], \{i, \text{xmin}, \text{xmax}, \text{step}\}]$;
$\text{arange} = \text{Range}[\text{xmin}, \text{xmax}, \text{step}]$;

```
(*Find proper initial value*)
Stable = Flatten[Sdiscrete];
alldata = {arange, Stable}^T;
initialvalue0 = alldata[[Position[Re[Stable], Min[Re[Stable]]][[1]][[1]]]];
initialvalue = initialvalue0[[1]];
ListLinePlot[Re[alldata], Frame → True, FrameLabel → {a, "Re[S]"}]
```

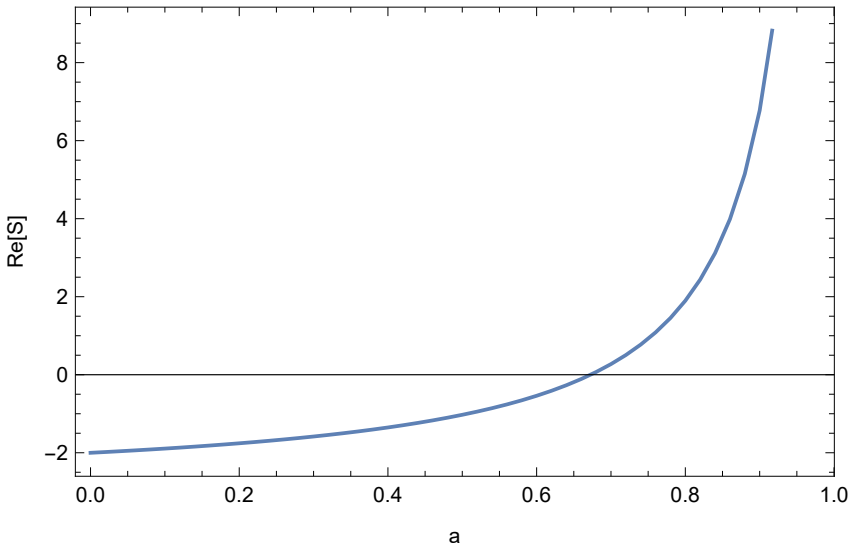

Solution of the Equation 18

```
S[a_]:=Sum[(-1)^m mβ[m]/(-m^2+a), {m, 1, 10^3}] - π;
equation = FindRoot[S[a] == 0, {a, initialvalue}];
solution = a/.equation[[1]]
```

$$0.655029 - 0.139597i$$

```
√Re[solution]
```

$$0.809338$$

APPENDIX C

Inductance and capacitance between two parallel straight wires

For two straight parallel cylindrical conductors of length ℓ, radius a, and center-to-center spacing d, the inductance is given by

$$L = \frac{\mu_0\,\ell}{\pi}\,\operatorname{arccosh}\!\left(\frac{d}{2a}\right), \tag{C.1}$$

where μ_0 is the permeability of free space. Using the identity

$$\operatorname{arccosh}(x) = \ln\!\left(x + \sqrt{x^2-1}\right), \tag{C.2}$$

this can be rewritten as

$$L = \frac{\mu_0\,\ell}{\pi}\,\ln\!\left(\frac{d}{2a} + \sqrt{\left(\frac{d}{2a}\right)^2 - 1}\right). \tag{C.3}$$

In the limit $d \gg a$, the inductance can be approximated by

$$L \approx \frac{\mu_0\,\ell}{\pi}\,\ln\!\left(\frac{d}{a}\right). \tag{C.4}$$

For two parallel cylindrical conductors of radius a, center-to-center distance d, and length ℓ, the capacitance is given by

$$C = \frac{\pi\varepsilon\ell}{\operatorname{arccosh}\!\left(\frac{d}{2a}\right)}, \tag{C.5}$$

where ε is the permittivity of the medium between the conductors. Using the identity

$$\operatorname{arccosh}(x) = \ln\!\left(x + \sqrt{x^2-1}\right), \tag{C.6}$$

this can be rewritten as

$$C = \frac{\pi\varepsilon\ell}{\ln\!\left(\frac{d}{a} + \sqrt{\left(\frac{d}{a}\right)^2 - 1}\right)}. \tag{C.7}$$

In the limit of large separation, $d \gg a$, the capacitance reduces to

$$C \approx \frac{\pi\varepsilon\ell}{\ln\!\left(\frac{d}{a}\right)}. \tag{C.8}$$

APPENDIX D

Vapor HF Etch

This section details the extensive testing of vapor HF (vHF) etching, performed to determine the optimal process for releasing silicon membranes with low-pitch aluminum coils, with pitches down to 0.3 µm. The main challenge was to fully remove silicon dioxide (SiO_2) without affecting the aluminum.

Initially, a recipe using the conditions listed in Table D.1 successfully etched SiO_2, but it also chemically attacked the 0.3 µm-pitch coils, while leaving the 0.5 µm-pitch coils unaffected. These devices were on SOI-BE. Interestingly, a similar recipe applied to a not-backetched 0.4 µm pitch fluxonium sample with holes on the membrane appeared to preserve coils, yet it failed to fully remove SiO_2. The residues observed post-vHF were identified as inorganic, suggesting they were a by-product of the vHF process itself rather than incomplete resist removal.

The subsequent systematic tests, mainly conducted at 21°C with an HF flow of 40 scc, aimed to explore the complex interplay of pressure, time, and water content on etching efficacy and coil integrity. Decisions on the next steps were guided by qualitative insights into parameter effects, as summarized in Table D.2, while Table D.3 provides an overview of the recipes tested and their main outcomes. Test 13, highlighted in gray, is the recipe used for the release of the coil resonators in Ref. [PTH+20], as well as other devices in Ref. [PHS+21].

Temperature (°C)	H_2O (mg)	Time (s)	Pressure (Torr)	HF Flow (scc)
15	2	10,000	12	40

Table D.1: **Initial vapor HF recipe.**

Action	Etch Rate	Uniformity
Increasing HF Flow	Decrease	Increase
Increasing $\mathrm{H_2O}$ Flow	Increase	Decrease
Increase Pressure	Increase	Decrease

Table D.2: **The effect of changing process parameters on etch rate and uniformity.**

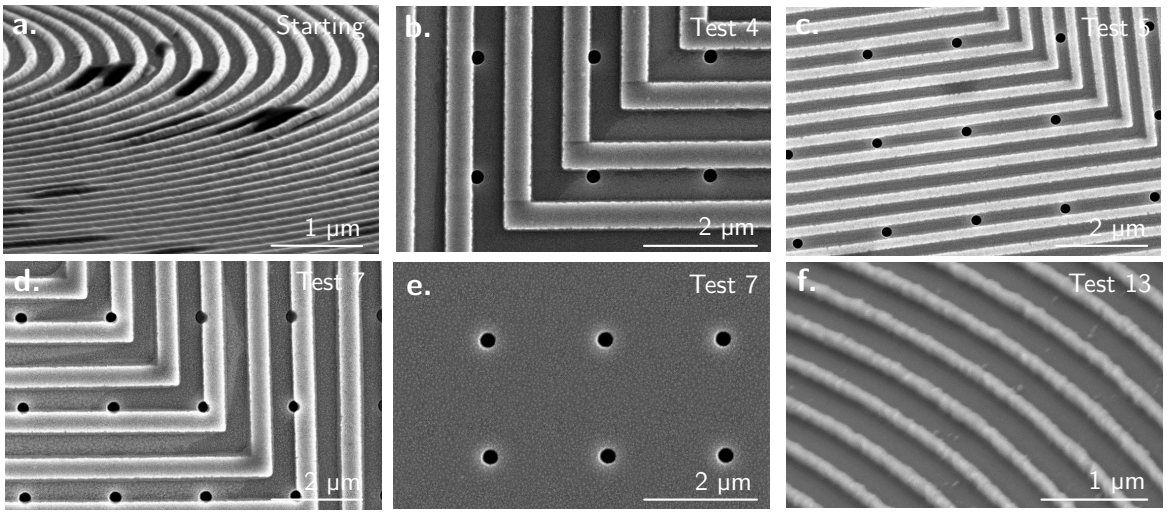

Figure D.1: **SEM images showing the results of some of the tests performed.**

Test	Pressure (Torr)	Time (s)	H_2O (mg)	Observation
1	20 + 22	4,000 + 2,500	2	Very clean, but coils (p=1 µm) affected. Too aggressive. Reduce the pressure of both steps but increase the time.
2	18 + 21	7,500 + 2,500	2	Very clean, but coils (p=0.5 µm) affected.
3a	18	7,500	2	Leftover SiO_2 remained, coils (p=0.5 µm) were OK. No visible Al affected.
3b	3a + 20	3a + 1,000	2	Test 3a continued, adding a second step at higher pressure to remove the oxide. Oxide fully removed, but nanobeam and coils (p=0.5 µm) slightly damaged.
4	18 + 20	7,500 + 500	2	Since after Test 3a the coils were good, we decide to shorten the second step. Shadows on coils (p=1 µm), some SiO_2 on wafer; membrane backside clean.
5	18 + 19	7,500 + 2,500	2	We saw some shadows on the coils (beginning of the fluorination maybe). We decide to reduce the pressure and increase the time of the second step in order to remove more SiO_2 (longer time) and preserve the coils (lower pressure). More SiO_2 removed, but Al was significantly affected. Time seems to play a very important role.

6	18 + 19	7,500 + 1,500	2	Since time seems to play an important role in the Al fluorination we reduce the length of the second step. Coils (p=1 µm) slightly affected, some SiO_2 residues remained. Membrane clean.
7	18	500 to 4,000	3	Since 18 Torr step with whatever second step doesn't fully remove the SiO_2 without affecting the coils, we change the amount of water and checked after every 500 s. SiO_2 removed after 4,000 s, but Al affected; membrane had spots also distant from Al structures.
8	16	1,000 to 10,000	3	Now we are shorter in time, but still the coils are affected. We try to change the pressure, lowering it. Checked every 1,000 s. SiO_2 removed after 9,000 s – 10,000 s; coils (p=1 µm) showed shadows; surface had spots; SiO_2 remained on the backside of the membrane under the coils.
9	16	10,000	3	Similar to Test 8 but without stopping and checking every 1,000 s: same result, showing that moving sample had no effect.
10a	16	3,600	4	We repeat the recipe given us by the company in 2017. No coils, just a membrane with holes, holes dose 330, development 1 min, ICP F 1 min 55 s; SiO_2 etched without residues or shadows.
10b	16	3,000	4	With coils (p=0.4 and 0.3 µm) on a membrane with holes; SiO_2 residues, coils were slightly affected.

11	16	10,000 to 22,000	2	Reduce the water and increase the time until the SiO_2 is removed and hopefully the coils not affected: checked after 10,000, 14,000, 18,000, 22,000 s. Coils not affected, but some shadows over them. SiO_2 residues on the wafer but only underneath the coil.
12	16	24,000	3	Coils intact, membrane and wafer clean; shadows appeared across sample.
13	16	24,000	2	Since Test 12 is promising, we now test it on a back-etched sample with coils. There are around 2.5 µm SiO_2, and holes on top to release the CPW. Coils, membrane and wafer clean.

Table D.3: **Vapor HF etching tests.**

APPENDIX E

Bosch Si etching

This section compares and evaluates different Bosch recipes for etching $200\ \mu\mathrm{m}$ of silicon using a Cr mask. Test II was found to be successful, achieving the desired etch depth and profile while maintaining good sidewall quality and surface cleanness.

Standard Bosch process. The Standard process from Oxford was carried out using Arkadiusz's recipe, adapted to my design. With 280 steps, we achieved an etch depth of approximately 101.7 µm, which closely aligns with the target of 100 µm. Despite this success in depth, the etched surface exhibited significant micrograss and surface contamination. Interestingly, the sidewalls showed minimal undercutting, indicating good anisotropy in the etch profile. While the depth and vertical profile were satisfactory, surface cleanliness remains a concern (Fig. E.1).

Step	Time (s)	P (mTorr)	C_4F_8 (sccm)	SF_6 (sccm)	T (°C)	RF Power (W)	ICP Power (W)
Gas on	20	25	100	5	5	0	0
Strike	5	25	100	5	5	50	1000
Deposition	4	30	100	5	5	0	1250
Etch 1	4	25	10	100	5	25	1250
Etch 2	3	50	10	100	5	0	1250

Table E.1: **Standard Bosch Recipe from Oxford.** The steps shown in gray are repeated in a loop.

Test I. The Test I (by Ivan Prieto) required over 700 steps to achieve a shallow etch of 3 µm, suggesting a significantly slower etch rate. This version of the process used 25% shorter loop steps, likely in an effort to produce smoother sidewalls. One modification involved operating Etch 2 with lower pressure and ICP power, which appears to reduce isotropic etching, though the reasoning behind this requires further investigation. An additional step was introduced to remove micrograss (Fig. E.2); however, it was ineffective against dirt particles bonded to the grass. Moreover, this step may induce unwanted isotropy, potentially leaving dangling Cr mask remnants that could affect further processing—though this side effect might not always be critical.

Test II. In the Test II process (tested by me), I modified the deposition step duration, aiming to reduce the thickness of the protective layer and thus increase etch exposure. As a result,

Step	Time (s)	P (mTorr)	C_4F_8 (sccm)	SF_6 (sccm)	T (°C)	RF Power (W)	ICP Power (W)
Gas On	20	25	100	5	5	0	0
Strike	5	25	100	5	5	50	1000
Deposition	3	30	100	5	5	0	1000
Etch 1	3	25	10	100	5	25	1000
Etch 2	2	30	10	100	5	0	1000
Step	10' (20')	30	10	100	5	0	1000

Table E.2: **Test I Bosch recipe.** The steps shown in gray are repeated in a loop.

we achieved a depth of 88 µm before the ICP was halted due to an error at around 120 steps. This change successfully reduced micrograss formation, almost eliminating it entirely, though some surface dirt persisted (Fig. E.2). The findings suggest that adjusting deposition time can be an effective strategy to balance etch depth and cleanliness, though further refinement is needed to address remaining contamination.

Step	Time (s)	P (mTorr)	C_4F_8 (sccm)	SF_6 (sccm)	T (°C)	RF Power (W)	ICP Power (W)
Gas On	20	25	100	5	5	0	0
Strike	5	25	100	5	5	50	1000
Deposition	3	30	100	5	5	0	1250
Etch 1	4	25	10	100	5	25	1250
Etch 2	3	50	10	100	5	0	1250

Table E.3: **Test II Bosch recipe.** The steps shown in gray are repeated in a loop.

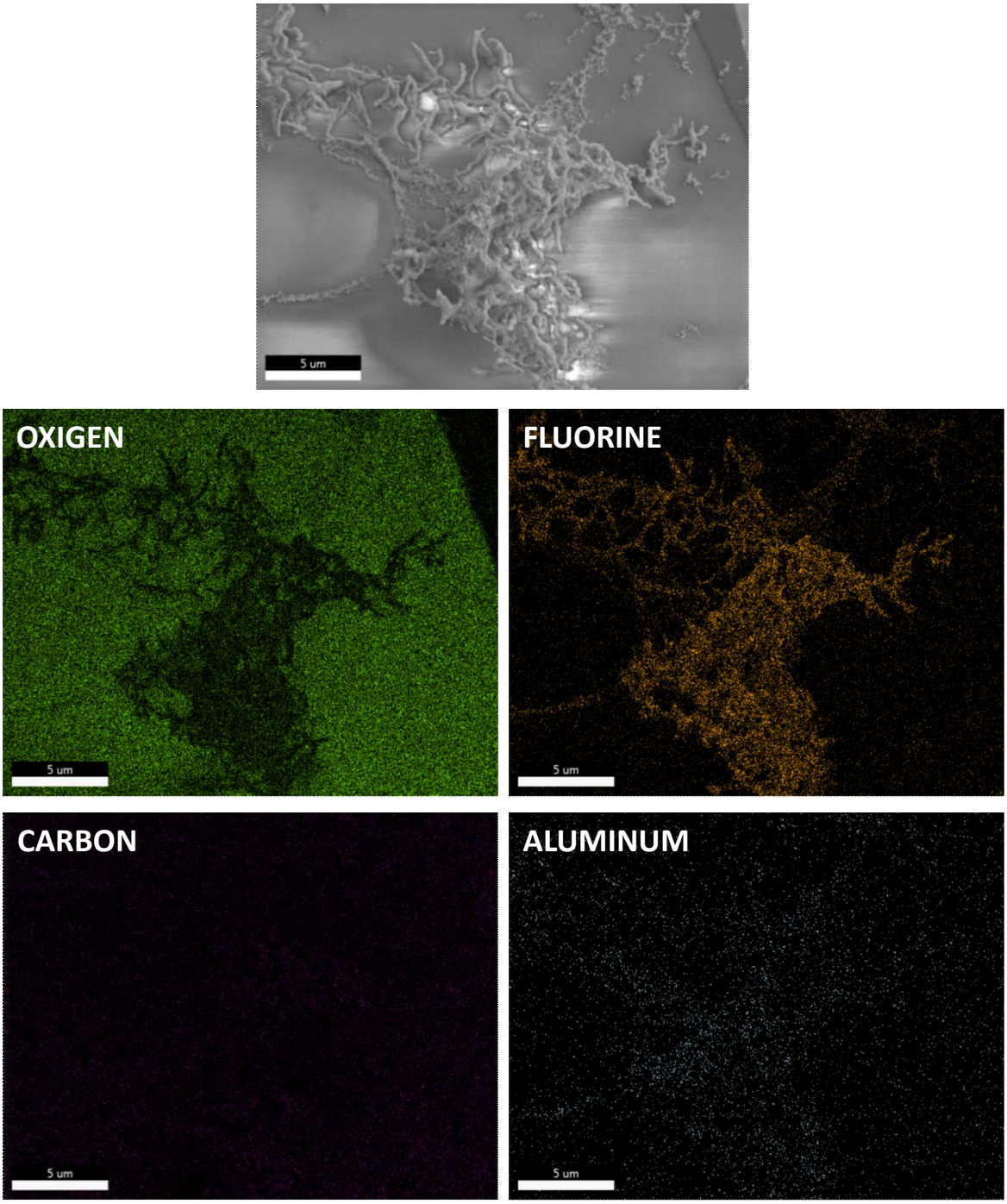

Figure E.1: **EDX analysis of the residues after the standard Bosch process.**

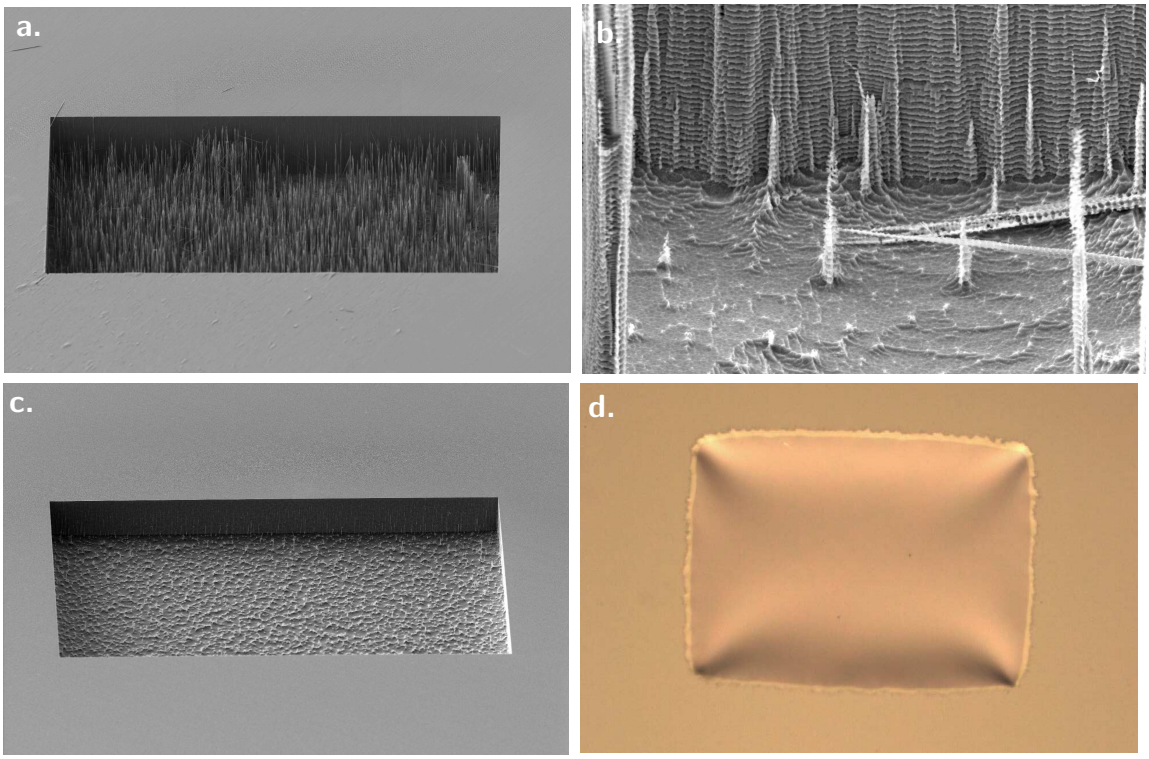

Figure E.2: **Bosch process Test I and II. a., b.** Micrograss formation during Test I; **c.** successful removal with Test II and **d.** clean membrane release.